KINEMATICS, STRUCTURAL MECHANICS, AND DESIGN OF ORIGAMI STRUCTURES WITH SMOOTH FOLDS

A Dissertation

by

EDWIN ALEXANDER PERAZA HERNANDEZ

Submitted to the Office of Graduate and Professional Studies of
Texas A&M University
in partial fulfillment of the requirements for the degree of

DOCTOR OF PHILOSOPHY

Chair of Committee,	Dimitris C. Lagoudas
Co-Chair of Committee,	Darren J. Hartl
Committee Members,	Richard J. Malak
	Ergun Akleman
	Jay R. Walton
Head of Department,	Rodney Bowersox

December 2016

Major Subject: Aerospace Engineering

ABSTRACT

Origami provides novel approaches to the fabrication, assembly, and functionality of engineering structures in various fields such as aerospace, robotics, etc. With the increase in complexity of the geometry and materials for origami structures that provide engineering utility, computational models and design methods for such structures have become essential. Currently available models and design methods for origami structures are generally limited to the idealization of the folds as creases of zeroth-order geometric continuity. Such an idealization is not proper for origami structures having non-negligible thickness or maximum curvature at the folds restricted by material limitations. Thus, for general structures, creased folds of merely zeroth-order geometric continuity are not appropriate representations of structural response and a new approach is needed. The first contribution of this dissertation is a model for the kinematics of origami structures having realistic folds of non-zero surface area and exhibiting higher-order geometric continuity, here termed *smooth folds*. The geometry of the smooth folds and the constraints on their associated kinematic variables are presented. A numerical implementation of the model allowing for kinematic simulation of structures having arbitrary fold patterns is also described. Examples illustrating the capability of the model to capture realistic structural folding response are provided. Subsequently, a method for solving the origami design problem of determining the geometry of a single planar sheet and its pattern of smooth folds that morphs into a given three-dimensional goal shape, discretized as a polygonal mesh, is presented. The design parameterization of the planar sheet and the constraints that allow for a valid pattern of smooth folds and approximation of the goal shape in a known folded configuration are presented. Various testing

examples considering goal shapes of diverse geometries are provided. Afterwards, a model for the structural mechanics of origami continuum bodies with smooth folds is presented. Such a model entails the integration of the presented kinematic model and existing plate theories in order to obtain a structural representation for folds having non-zero thickness and comprised of arbitrary materials. The model is validated against finite element analysis. The last contribution addresses the design and analysis of active material-based self-folding structures that morph via simultaneous folding towards a given three-dimensional goal shape starting from a planar configuration. Implementation examples including shape memory alloy (SMA)-based self-folding structures are provided.

DEDICATION

To the loving memory of my grandfather Jose Miguel Peraza.

And to my parents Maria Esperanza Hernandez and Jose Arturo Peraza for their love and support.

ACKNOWLEDGEMENTS

First and foremost, I would like to thank God for all the blessings that He has given me. I could not have made it to this point without Him and all the help He has provided me during every moment and struggle in my life. Every achievement in my life belongs to Him.

I thank my co-chairs of committee Dr. Dimitris Lagoudas and Dr. Darren Hartl for giving me the opportunity to belong to their research groups. I feel honored to have them as my advisors. Dr. Lagoudas taught me a lot about approaching and solving research problems. I learned a lot from him about critical and scientific thinking during our various research discussions throughout the years. I also thank him for bringing me into his research group when I was a sophomore during my undergraduate studies. I thank Dr. Hartl for deciding to have me as his graduate student, for the countless hours he spent reading the drafts of my research papers line by line, and for having a positive and friendly attitude towards every research topic we discussed.

I would like to thank Dr. Richard Malak, Dr. Ergun Akleman, and Dr. Jay Walton for agreeing to be my committee members. Dr. Malak taught me a lot about design and optimization during the course I took with him during my first semester and also during various meetings throughout these past years. I thank Dr. Akleman for providing me with a different perspective of the various research problems we discussed and for being involved in my research all this time. Dr. Walton has been an amazing teacher and I enjoyed the two math courses I had with him. Everyone provided helpful and insightful feedback during my dissertation defense.

Other persons that have contributed to my growth as a researcher include Dr.

Bjoern Kiefer and Dr. Andreas Menzel. They provided me with their guidance during my two months technical exchange at TU Dortmund. It was also an honor to work with Dr. Robert Skelton on various ideas to integrate origami and tensegrity when he first came to Texas A&M as a visiting faculty fellow.

My sincere gratitude goes to every student from the research groups of Dr. Lagoudas and Dr. Hartl for being both great friends and great colleagues, and for always providing a wonderful work environment. I also want to specifically thank Dr. Brian Lester and Dr. Majid Tabesh for being very helpful when I had any questions regarding courses or research.

The work presented in this dissertation was supported by the National Science Foundation (NSF) and the Air Force Office of Scientific Research (AFOSR) under grant No. EFRI-1240483. I would also like to thank the aforementioned institutions and grant for providing financial support for my research assistantship during my complete graduate studies and for conference travel. I would like to acknowledge the support from the NSF International Institute of Materials for Energy Conversion (IIMEC) award No. 0844082, and the Institute of Mechanics at TU Dortmund during a two months technical exchange at TU Dortmund on the Summer 2014. The support from the NSF IIMEC award No. 0844082 for the summer school that I attended during July 2015 in Thessaloniki, Greece is also gratefully acknowledged.

I would like to thank Texas A&M University and all the professors, staff, and fellow students I have met here for providing an amazing educational environment. It has been the greatest privilege of my life to attend this University for both my undergraduate and graduate studies.

I want to thank my parents Maria Esperanza and Jose Arturo for their unconditional support and affection. They have been my emotional support during all these years and have always been there when I need them the most. I would like to

acknowledge my grandfather Jose Miguel who always encouraged me to do my best for my education.

To my family, friends, professors, and to everyone who has contributed to my personal and professional growth, I would like to thank you with all my heart.

CONTRIBUTORS AND FUNDING SOURCES

Contributors

This work was supported by a dissertation committee consisting of Professor Dimitris Lagoudas of the Department of Aerospace Engineering (co-advisor), Professor Darren Hartl of the Department of Aerospace Engineering (co-advisor), Professor Richard Malak of the Department of Mechanical Engineering, Professor Ergun Akleman of the Department of Visualization, and Professor Jay Walton of the Department of Mathematics.

All work for the dissertation was completed independently by the student.

Funding Sources

This work was made possible in part by the National Science Foundation (NSF) and the Air Force Office of Scientific Research (AFOSR) under grant No. EFRI-1240483.

Its contents are solely the responsibility of the author and do not necessarily represent the official views of NSF or AFOSR.

NOMENCLATURE

$\hat{\boldsymbol{a}}$	Vector having components corresponding to $\hat{a}_1, \ldots, \hat{a}_{N_{\mathcal{F}}}$
A_f	Austenite finish temperature at zero stress
a_i	$i = 1, 2, 3$. Shape memory alloy model parameters associated with the transformation hardening behavior
$\hat{a}_i$	Asymmetry variable of the i^{th} smooth fold
$\mathtt{A}_i$	Total surface area of the rigid faces in the i^{th} edge module prior to face trimming and edge module trimming
a_i^B	Thickness of the i^{th} layer in a bilayer laminate
a_{jk}	Asymmetry variable of the k^{th} smooth fold adjacent to the j^{th} interior fold intersection
$\breve{a}_{jk}$	Asymmetry variable of the k^{th} smooth fold crossed by the path $\breve{\boldsymbol{\gamma}}_j(\eta)$
A_s	Austenite start temperature at zero stress
$\boldsymbol{a}^j$	Vector having components corresponding to $a_{j1}, \ldots, a_{jn_j}$
$\breve{\boldsymbol{a}}^j$	Vector having components corresponding to $\breve{a}_{j1}, \ldots, \breve{a}_{jp_j}$
$\mathbf{b}$	Body force vector
$\mathbf{B}_L^j$	Vectors constructed by concatenating the vectors $\mathbf{b}_L^{j1}, \ldots, \mathbf{b}_L^{jn_j}$
$\breve{\mathbf{B}}_L^j$	Vectors constructed by concatenating the vectors $\breve{\mathbf{b}}_L^{j1}, \ldots, \breve{\mathbf{b}}_L^{jp_j}$
$\mathbf{b}_L^{jk}$	Position vector of the point where the path $\boldsymbol{\gamma}_j(\eta)$ enters the k^{th} fold adjacent to the j^{th} interior fold intersection
$\breve{\mathbf{b}}_L^{jk}$	Position vector of the point where the path $\breve{\boldsymbol{\gamma}}_j(\eta)$ enters the k^{th} fold it crosses
$\mathbf{B}_R^j$	Vectors constructed by concatenating the vectors $\mathbf{b}_R^{j1}, \ldots, \mathbf{b}_R^{jn_j}$
$\breve{\mathbf{B}}_R^j$	Vectors constructed by concatenating the vectors $\breve{\mathbf{b}}_R^{j1}, \ldots, \breve{\mathbf{b}}_R^{jp_j}$

$\mathbf{b}_R^{jk}$	Position vector of the points where the path $\boldsymbol{\gamma}_j(\eta)$ exits the k^{th} fold adjacent to the j^{th} interior fold intersection
$\breve{\mathbf{b}}_R^{jk}$	Position vector of the point where the path $\breve{\boldsymbol{\gamma}}_j(\eta)$ exits the k^{th} fold it crosses
$\mathfrak{b}^{jk}$	Position vectors of the edge module corners associated with the j^{th} interior node of the goal mesh
$\boldsymbol{C}$	Fourth-order stiffness tensor
$\widehat{\mathbf{C}}$	Connectivity matrix relating the vertices to the end-points of each fold centerline
c_0^i	Reference concentration of the i^{th} chemical species
C_i^B	$i = 1, 2$. Non-dimensional constants related to the structural response of a bilayer laminate
$\hat{\mathbf{c}}_{L_j}^i$	End condition of $\hat{\mathbf{c}}^i(\zeta_1)$ for j^{th}-order geometric continuity at $\zeta_1 = -1$
$\bar{\mathbf{c}}_{L_j}^i$	Non-dimensional form of $\hat{\mathbf{c}}_{L_j}^i$
$\hat{\mathbf{c}}_{R_j}^i$	End condition of $\hat{\mathbf{c}}^i(\zeta_1)$ for j^{th}-order geometric continuity at $\zeta_1 = 1$
$\bar{\mathbf{c}}_{R_j}^i$	Non-dimensional form of $\hat{\mathbf{c}}_{R_j}^i$
C^A	Stress influence coefficient of austenite
$\mathbf{C}^{E_I N}$	Connectivity matrix relating the mesh nodes to the interior edges
c^i	Concentration of the i^{th} chemical species
$\mathbf{c}^i(\zeta_1)$	Fold cross-section parametric curve
$\hat{\mathbf{c}}^i(\zeta_1)$	Fold cross-section parametric curve expressed in the basis $\{\hat{\mathbf{e}}_1^i, \hat{\mathbf{e}}_2^i, \hat{\mathbf{e}}_3^i\}$
$\bar{\mathbf{c}}^i(\zeta_1)$	Non-dimensional form of $\hat{\mathbf{c}}^i(\zeta_1)$
$\mathbf{C}^j$	Connectivity matrix used for the identification and ordering of the fold centerlines incident to the j^{th} interior vertex

$\breve{\mathbf{C}}^j$	Connectivity matrix used for the identification and ordering of the folds crossed by the path $\breve{\boldsymbol{\gamma}}_j(\eta)$
C^M	Stress influence coefficient of martensite
${}^j\mathbf{C}^{ME_I}$	Connectivity matrix used for the identification of the interior edges associated with the j^{th} face of the goal mesh
${}^j\mathbf{C}^{MN}$	Connectivity matrix used for the identification of the nodes associated with the j^{th} face of the goal mesh
${}^j\mathbf{C}^{N_IE_I}$	Connectivity matrix used for the identification of the interior edges incident to the j^{th} interior node of the goal mesh
$\boldsymbol{C}^{PS}$	Effective plane stress stiffness matrix
D	Shape memory alloy model parameter associated with the stress dependence of the critical thermodynamical force for transformation
D	Vector having components corresponding to the design variables
$\tilde{d}_i^{jk}$	$i = 1, 2$. Change in length of the k^{th} edge of the j^{th} face in the goal mesh due to face trimming
$\hat{d}_{mn}^i$	$m = 1, 2;\ n = 1, 2$. Changes in length of the edge associated with the i^{th} edge module due to face trimming
$\mathbf{d}^j$	Translation constraint vector associated with the j^{th} interior fold intersection
$\boldsymbol{D}^M$	Third-order tensor of piezomagnetic coefficients
${}^j\boldsymbol{d}^{mn}$	Vector having components corresponding to $d_{mn}^{j1}, \ldots, d_{mn}^{jn_j^{\mathcal{M}}}$
$\hat{\boldsymbol{d}}^{mn}$	Vector having components corresponding to $\hat{d}_{mn}^1, \ldots, \hat{d}_{mn}^{N_{\mathcal{E}}^I}$
$\boldsymbol{D}^P$	Third-order tensor of piezoelectric coefficients
E	Young's modulus
E	Surface area efficiency

$\mathtt{E}$	Approximation error
$\boldsymbol{E}$	Electric field vector
$\mathbf{e}_i$	$i = 1, 2, 3$. Orthonormal vectors used to define the fixed global coordinate system
E_i^B	Young's modulus of the i^{th} layer in a bilayer laminate
$\hat{\mathbf{e}}_j^i$	$j = 1, 2, 3$. Fold-attached orthonormal vectors associated with the i^{th} smooth fold
E^A	Young's modulus of austenite
$\boldsymbol{e}^i$	Second-order tensor of expansion due to concentration of the i^{th} chemical species
E^M	Young's modulus of martensite
$\mathcal{F}_0^i$	Reference configuration of the i^{th} smooth fold
$\mathcal{F}_t^i$	Current configuration of the i^{th} smooth fold
$\mathbf{f}^i$	Force vector of the i^{th} point load
$\mathfrak{F}^i$	Region occupied by the i^{th} smooth fold domain
$\boldsymbol{\mathcal{F}}^i(\zeta_1, \zeta_2)$	Surface parameterization of $\mathcal{F}_t^i$
$\boldsymbol{g}$	Vector associated with the inequality constraints
G_T	Shear modulus of an active torsional element
$\mathbf{g}^{jk}$	Recursively determined vectors accounting for the change in the distance between the smooth folds boundary rulings in a current configuration
G^n	Order of geometric continuity
$\boldsymbol{h}$	Vector associated with the equality constraints
$\boldsymbol{H}$	Magnetic field vector
h_B	Total thickness of a bilayer laminate
$\mathfrak{h}_i$	Thickness of the i^{th} fold domain

$h_{jk}(\zeta_1)$	$k = 0, \ldots, j$. Hermite interpolation polynomials of j^{th}-order
H_{min}	Minimum transformation strain magnitude for full transformation
H_{sat}	Maximum attainable transformation strain magnitude for full transformation
H^{cur}	Transformation strain magnitude for full transformation
$\mathbf{h}^i$	Director vector of the i^{th} smooth fold
$\mathbf{H}^{jk}$	Simplified transformation matrix associated with the k^{th} fold adjacent to the j^{th} interior fold intersection
$\breve{\mathbf{H}}^{jk}$	Simplified transformation matrix associated with the k^{th} fold crossed by the path $\breve{\boldsymbol{\gamma}}_j(\eta)$
$\mathcal{I}_0^i$	Reference configuration of the i^{th} fold intersection
I_i^B	Area moment of inertia of the i^{th} layer in a bilayer laminate
$\mathbf{I}_n$	$\mathbb{R}^{n\times n}$ identity matrix
I_T	Polar second moment of a circular cross-section
$\mathcal{I}_t^i$	Current configuration of the i^{th} fold intersection
k	Transformation strain parameter
K_j	Discrete Gaussian curvature associated with the j^{th} interior vertex
$\mathfrak{L}$	Penalty function associated with kinematic constraints
$\hat{\boldsymbol{l}}$	Vector having components corresponding to the trim lengths $\hat{l}_1, \ldots, \hat{l}_{N_{\mathcal{E}}^I}$
$\hat{l}_i$	Trim length associated with the i^{th} interior edge of the goal mesh
$\tilde{l}_{jk}$	Trim length associated with the k^{th} edge of the j^{th} face of the goal mesh
L_T	Length of an active torsional element
$\tilde{\boldsymbol{l}}^j$	Vector having components corresponding to the trim lengths associated with the j^{th} face $\tilde{l}_{j1}, \ldots, \tilde{l}_{jn_j^C}$

$\mathbf{l}^{jk}$	Vector with start-point and end-point respectively corresponding to the points where the path $\boldsymbol{\gamma}_j(\eta)$ enters and exits the face between the k^{th} and $(k+1)^{\text{th}}$ folds adjacent to the j^{th} interior fold intersection
$\tilde{\mathbf{l}}^{jk}$	Vector $\mathbf{l}^{jk}$ rotated by $-\varphi(\mathbf{m}^{jk})$ about $\mathbf{e}_3$
$\mathbf{L}^{jk}$	Transformation matrix associated with the k^{th} fold adjacent to the j^{th} interior fold intersection
M	Moment resultant
$\mathcal{M}$	Goal mesh
m_B	Ratio of the thickness of the layers in a bilayer laminate
M_B	Moment applied to a bilayer laminate
M_f	Martensite finish temperature at zero stress
M_s	Martensite start temperature at zero stress
M_T	Torque applied to an active torsional element
$\mathcal{M}_\sharp$	Set of trimmed mesh faces
$\mathcal{M}_\sharp^j$	j^{th} face of the set of trimmed mesh faces
$\mathcal{M}^j$	j^{th} face of the goal mesh
$\mathbf{M}^j$	Vector constructed by concatenating the vectors $\mathbf{m}^{j1}, \ldots, \mathbf{m}^{jn_j}$
$\breve{\mathbf{M}}^j$	Vector constructed by concatenating the vectors $\breve{\mathbf{m}}^{j1}, \ldots, \breve{\mathbf{m}}^{jp_j}$
$\mathbf{m}^{jk}$	Vector along the length of the k^{th} fold centerline incident to the j^{th} interior vertex that emanates from such a vertex
$\breve{\mathbf{m}}^{jk}$	Vector along the fold centerline of the k^{th} fold crossed by the path $\breve{\boldsymbol{\gamma}}_j(\eta)$
N	Axial force resultant
N_{adj}	Number of increments in the step associated with adjusting of fold angles
n_B	Ratio of the Young's modulus of the layers in a bilayer laminate

$N_{\mathcal{B}}$	Number of vertices located at the boundary or outside the sheet
N_{dof}	Number of degrees of freedom
$N_{\mathcal{E}}$	Number of edges in the goal mesh
$N_{\mathcal{E}}^{I}$	Number of interior edges in the goal mesh
$N_{\mathcal{E}}^{Ij}$	$j = 0, 1, 2$. Number of interior edges incident to j interior nodes
N_{fol}	Number of increments in the step associated with constant fold angle guess increments
$N_{\mathcal{F}}$	Number of folds in the sheet
$N_{\mathcal{I}}$	Number of fold intersections in the sheet
n_i	$i = 1, 2, 3, 4$. Transformation hardening exponents
n_j	Number of fold centerlines incident to the j^{th} interior vertex
n_j^C	Number of corners of the j^{th} face in the goal mesh
$n_j^{\mathcal{M}}$	Number of faces connected to the the j^{th} interior node in the goal mesh
$N_{\mathcal{M}}$	Number of faces in the goal mesh
$N_{\mathcal{N}}$	Number of nodes in the goal mesh
$N_{\mathcal{N}}^{I}$	Number of interior nodes in the goal mesh
$N_{\mathcal{P}}$	Number of faces in the sheet
$\hat{\mathbf{n}}^{ij}$	$j = 1, 2$. Unit normal vectors of the faces adjacent to the i^{th} interior edge
$\mathbf{n}^{jk}$	Unit normal vector of the k^{th} face adjacent to the j^{th} interior node in the goal mesh
$\bar{\mathbf{n}}^{jk}$	Unit normal vector associated with the k^{th} edge incident to the j^{th} interior node in the goal mesh
$\bar{n}^{\mathcal{M}}$	Average valence of the interior nodes in the goal mesh
$\mathcal{P}_0^i$	Reference configuration of the i^{th} face

P_B	Axial force in the active layer of a bilayer laminate
p_j	Number of folds crossed by $\breve{\boldsymbol{\gamma}}_j(\eta)$
$\hat{\mathbf{p}}_j^i$	$j = 1, 2, 3, 4$. Position vectors of the corner points of the i^{th} smooth fold in the reference configuration
$\mathcal{P}_t^i$	Current configuration of the i^{th} face
$\hat{\mathbf{P}}^j$	$j = 1, 2, 3, 4$. Vectors constructed by concatenating the vectors $\hat{\mathbf{p}}_j^1, \ldots, \hat{\mathbf{p}}_j^{N_{\mathcal{F}}}$
$\mathbf{Q}_i(\phi)$	Transformation matrix in homogeneous coordinates associated with a rotation by ϕ about an axis aligned to $\mathbf{e}_i$
$\boldsymbol{\mathfrak{R}}$	Residual vector
$\hat{r}_1^i, \hat{r}_2^i$	Length parameters associated with the i^{th} smooth fold
R_B	Radius of curvature of a bent bilayer laminate
$\mathbf{R}_i(\phi)$	Transformation matrix associated with a rotation by ϕ about an axis aligned to $\mathbf{e}_i$
r_T	Radius of the circular cross-section of an active torsional element
$\mathbf{R}^j$	Rotation constraint matrix associated with the j^{th} interior fold intersection
$\boldsymbol{\mathfrak{R}}^s$	Vector of residuals associated with fold arc-lengths
$\boldsymbol{\mathfrak{R}}^\theta$	Vector of residuals associated with fold angles
$\boldsymbol{S}$	Fourth-order compliance tensor
$\hat{\mathbf{s}}$	Vector having components corresponding to the fold arc-lengths of the sheet
s_0	Specific entropy at reference state
$\mathcal{S}_0$	Sheet reference configuration
$\hat{s}_i$	Total arc-length of the i^{th} fold cross-section

$\bar{s}_i$	Non-dimensional total arc-length of the i^{th} fold cross-section
$\mathcal{S}_t$	Sheet current configuration
$\mathcal{S}_\star$	Sheet goal configuration
$\boldsymbol{S}^A$	Fourth-order compliance tensor of austenite
$\boldsymbol{S}^M$	Fourth-order compliance tensor of martensite
t	Time parameter
$\mathbf{t}$	Traction vector
$\bar{\mathbf{t}}$	Applied traction vector
T	Absolute temperature
T_0	Reference absolute temperature
$\mathbf{T}(\mathbf{b})$	Transformation matrix in homogeneous coordinates associated with a translation by vector $\mathbf{b}$
$\mathbf{t}^i(\zeta_1)$	Unit tangent vector of the curve $\hat{\mathbf{c}}^i(\zeta_1)$
`tol`	Numerical tolerance
$\mathbf{u}$	Displacement vector
$\bar{\mathbf{u}}$	Applied displacement vector
u_0	Specific internal energy at reference state
$\mathbf{u}^i$	Displacement vector of the point of application of the i^{th} point load
$\mathbf{v}$	Velocity vector
V	Vector constructed by concatenating the position vectors of all the vertices of the sheet
v_f	Volume fraction of SMA wires
$\hat{\mathsf{V}}^1$	Vector constructed by concatenating the position vectors of the fold centerline start-points

$\hat{\mathbf{V}}^2$	Vector constructed by concatenating the position vectors of the fold centerline end-points
$\hat{\mathbf{v}}^{i1}$	Position vector of the vertex from which the i^{th} fold centerline emanates
$\hat{\mathbf{v}}^{i2}$	Position vector of the vertex at which the i^{th} fold centerline ends
$\mathbf{v}^j$	Position vector of the j^{th} vertex
$\hat{\boldsymbol{w}}$	Vector having components corresponding to $\hat{w}_1, \ldots, \hat{w}_{N_{\mathcal{F}}}$
$\hat{\boldsymbol{W}}$	Vector having components corresponding to $\hat{W}_1, \ldots, \hat{W}_{N_{\mathcal{E}}^I}$
w_B	Width of a bilayer laminated beam
W_E	External work exerted by body forces and boundary tractions
$\hat{w}_i$	Current distance between the end-points of the cross-section curve of the i^{th} fold
$\hat{W}_i$	Length design variable of the i^{th} edge module
$\hat{w}_i^0$	Fold width of the i^{th} fold
$\hat{w}_i^{\mathsf{E}0}$	Fold width of the exterior folds in the i^{th} edge module
$\hat{w}_i^{\mathsf{E}\star}$	Distance between the end-points of the cross-section curve of the exterior folds in the i^{th} edge module at the goal configuration
$\hat{w}_i^{\mathsf{I}0}$	Fold width of the interior fold in the i^{th} edge module
$\hat{w}_i^{\mathsf{I}\star}$	Distance between the end-points of the cross-section curve of the interior fold in the i^{th} edge module at the goal configuration
W_I	Internal work
w_{jk}	Distance between the end-points of the cross-section curve of the k^{th} fold adjacent to the j^{th} interior fold intersection
W_{jk}	Length design variable of the k^{th} edge module associated with the j^{th} interior vertex of the goal mesh

$\breve{w}_{jk}$	Distance between the end-points of the cross-section curve of the k^{th} fold crossed by the path $\breve{\boldsymbol{\gamma}}_j(\eta)$
w^0_{jk}	Fold width of the k^{th} fold adjacent to the j^{th} interior fold intersection
$\breve{w}^0_{jk}$	Fold width of the k^{th} fold crossed by the path $\breve{\boldsymbol{\gamma}}_j(\eta)$
$\hat{\boldsymbol{w}}^0$	Vector having components corresponding to $\hat{w}^0_1, \ldots, \hat{w}^0_{N_{\mathcal{F}}}$
$\boldsymbol{w}^{0,j}$	Vector having components corresponding to $w^0_{j1}, \ldots, w^0_{jn_j}$
$\breve{\boldsymbol{w}}^{0,j}$	Vector having components corresponding to $\breve{w}^0_{j1}, \ldots, \breve{w}^0_{jp_j}$
$\boldsymbol{w}^j$	Vector having components corresponding to $w_{j1}, \ldots, w_{jn_j}$
$\boldsymbol{W}^j$	Vector having components corresponding to $W_{j1}, \ldots, W_{jn_j^{\mathcal{M}}}$
$\breve{\boldsymbol{w}}^j$	Vector having components corresponding to $\breve{w}_{j1}, \ldots, \breve{w}_{jp_j}$
$\mathbf{w}^{jk}$	Vector with start-point and end-point corresponding to the points where the path $\boldsymbol{\gamma}_j(\eta)$ crosses the boundary rulings of the k^{th} fold adjacent to the j^{th} interior fold intersection
$\tilde{\mathbf{w}}^{jk}$	Vector $\mathbf{w}^{jk}$ rotated by $-\varphi(\mathbf{m}^{jk})$ about $\mathbf{e}_3$
$\mathbf{x}$	Position vector of a point in the sheet at the current configuration
$\mathbf{X}$	Position vector of a point in the sheet at the reference configuration
$\hat{\mathbf{Y}}$	Vector constructed by concatenating the node position vectors $\hat{\mathbf{y}}^1, \ldots, \hat{\mathbf{y}}^{N_{\mathcal{N}}}$
$\tilde{\mathbf{y}}^{jk}_{\sharp}$	Position vector of the k^{th} corner of the j^{th} face in the set of trimmed mesh faces
$\hat{\mathbf{y}}^i$	Position vector of the i^{th} node in the goal mesh
$\tilde{\mathbf{Y}}^j$	Vector constructed by concatenating the vectors $\tilde{\mathbf{y}}^{j1}, \ldots, \tilde{\mathbf{y}}^{jn_j^C}$
$\tilde{\mathbf{y}}^{jk}$	Position vector of the k^{th} corner of the j^{th} face in the goal mesh
Y^t	Critical thermodynamic driving force for transformation
$\hat{\mathbf{Z}}$	Vector constructed by concatenating the vectors $\hat{\mathbf{z}}^1, \ldots, \hat{\mathbf{z}}^{N^I_{\mathcal{E}}}$

$\hat{\mathbf{z}}^i$	Vector along the length of the i^{th} interior edge of the goal mesh
$\mathbf{Z}^j$	Vector constructed by concatenating the vectors $\mathbf{z}^{j1}, \ldots, \mathbf{z}^{jn_j^{\mathcal{M}}}$
$\mathbf{z}^{jk}$	Vector connecting the j^{th} interior node to its k^{th} adjacent node
$\boldsymbol{\alpha}$	Second-order thermal expansion tensor
α	Thermoelastic expansion coefficient
α_i^B	Thermoelastic expansion coefficient of the i^{th} layer in a bilayer laminate
α_{jk}	Angle between adjacent fold centerlines incident to an interior vertex
$\beta^i_{L_j}$	Shape parameter of $\hat{\mathbf{c}}^i(\zeta_1)$ arising from the end-condition for j^{th}-order geometric continuity at $\zeta_1 = -1$
$\beta^i_{R_j}$	Shape parameter of $\hat{\mathbf{c}}^i(\zeta_1)$ arising from the end-condition for j^{th}-order geometric continuity at $\zeta_1 = 1$
$\boldsymbol{\gamma}_j(\eta)$	Closed path enclosing $\mathcal{I}_0^j$ and crossing the folds adjacent to $\mathcal{I}_0^j$
$\breve{\boldsymbol{\gamma}}_j(\eta)$	Path connecting the fixed face to the j^{th} face
$\boldsymbol{\varepsilon}$	Second-order linearized strain tensor
ε_0	Mid-surface strain
ε_{mn}	Components of the linearized strain tensor in the basis $\{\hat{\mathbf{e}}_1^i, \hat{\mathbf{e}}_2^i, \hat{\mathbf{e}}_3^i\}$
ε^{ACT}	Effective actuation strain
$\boldsymbol{\varepsilon}^{ACT}$	Second-order tensor of actuation strains
$\boldsymbol{\varepsilon}^{EL}$	Second-order tensor of elastic strains
$\boldsymbol{\varepsilon}^{MS}$	Second-order tensor of strains caused by changes in the material microstructure
$\boldsymbol{\varepsilon}^t$	Second-order transformation strain tensor
$\boldsymbol{\varepsilon}^{t0}$	Second-order pre-strain tensor
$\boldsymbol{\varepsilon}^{th}$	Second-order tensor of thermoelastic strains

$\boldsymbol{\varepsilon}^{t-r}$	Second-order transformation strain tensor at the cessation of forward transformation
$\hat{\boldsymbol{\theta}}$	Vector having components corresponding to the fold angles of the sheet
$\hat{\theta}_i$	Fold angle of the i^{th} fold
$\hat{\Theta}_i$	Dihedral angle of the i^{th} interior edge in the goal mesh
$\hat{\theta}_i^L$	Lower bound for the fold angle domain of the i^{th} fold
$\hat{\theta}_i^U$	Upper bound for the fold angle domain of the i^{th} fold
θ_{jk}	Fold angle of the k^{th} fold adjacent to the j^{th} interior fold intersection
$\breve{\theta}_{jk}$	Fold angle of the k^{th} fold crossed by $\breve{\boldsymbol{\gamma}}_j(\eta)$
$\boldsymbol{\theta}^j$	Vector having components corresponding to the fold angles of the folds adjacent to the j^{th} fold intersection
$\breve{\boldsymbol{\theta}}^j$	Vector having components corresponding to the fold angles of the folds crossed by $\breve{\boldsymbol{\gamma}}_j(\eta)$
$\hat{\boldsymbol{\theta}}^{t_f}$	Vector having components corresponding to the fold angles of the sheet in the final configuration
$\hat{\boldsymbol{\theta}}^\star$	Vector having components corresponding to the fold angles of the sheet in the goal configuration
${}^{IN}_{l}\Delta\hat{\boldsymbol{\theta}}$	Input guess change of the fold angles in the l^{th} fold sequence increment
$\kappa(\zeta_1)$	Signed curvature of $\hat{\mathbf{c}}^i(\zeta_1)$
$\hat{\kappa}(\zeta_1)$	Curvature of $\hat{\mathbf{c}}^i(\zeta_1)$
$\bar{\hat{\kappa}}(\zeta_1)$	Non-dimensional curvature of $\hat{\mathbf{c}}^i(\zeta_1)$
$\bar{\kappa}(\zeta_1)$	Non-dimensional signed curvature of $\hat{\mathbf{c}}^i(\zeta_1)$
$\kappa^G(\zeta_1)$	Goal signed curvature of $\hat{\mathbf{c}}^i(\zeta_1)$
$\bar{\kappa}^G(\zeta_1)$	Goal non-dimensional signed curvature of $\hat{\mathbf{c}}^i(\zeta_1)$
λ_B	Penalty weight for residuals from fold angle bounds

λ_d	Penalty weight for residuals from translation constraints
$\mathbf{\Lambda}^t_{fwd}$	Second-order transformation direction tensor for forward transformation
λ_R	Penalty weight for residuals from rotation constraints
$\mathbf{\Lambda}^t_{rev}$	Second-order transformation direction tensor for reverse transformation
$\mathbf{\Lambda}^t$	Second-order transformation direction tensor
ν	Poisson's ratio
ν^A	Poisson's ratio of austenite
ν^M	Poisson's ratio of martensite
ξ	Martensite volume fraction
Ξ	Field variable
$\bar{\Xi}$	Applied field variable
ξ^r	Martensite volume fraction at the cessation of forward transformation
ρ	Mass density
$\boldsymbol{\sigma}$	Second-order Cauchy stress tensor
$\bar{\sigma}$	von Mises stress
σ_{mn}	Components of the Cauchy stress tensor in the basis $\{\hat{\mathbf{e}}^i_1, \hat{\mathbf{e}}^i_2, \hat{\mathbf{e}}^i_3\}$
$\boldsymbol{\sigma'}$	Second order deviatoric stress tensor
σ^{ACT}	Effective actuation stress
$\hat{\tau}^i_j$	$j = 1, 2$. Trim angles of the i^{th} edge module
τ_{jk}	Trim angle of the k^{th} edge module associated with the j^{th} interior node of the goal mesh
Φ^t_{fwd}	Transformation function for forward transformation
ϕ_{jk}	Corner angle of the k^{th} face adjacent to the j^{th} interior node of the goal mesh
$\tilde{\phi}_{jk}$	k^{th} interior corner angle of the j^{th} face in the goal mesh

Φ^t_{rev}	Transformation function for reverse transformation
ϕ_T	Twist angle of an active torsional element
φ_T	Total twist angle of an active torsional element
ϕ'_T	Spatial derivative of twist angle of an active torsional element along the longitudinal axis
Φ^t	Transformation function
$\varphi(\mathbf{y})$	Counterclockwise angle from $\mathbf{e}_1$ to $\mathbf{y} \in \text{span}(\mathbf{e}_1, \mathbf{e}_2)$
χ	Deformation map
$\hat{\boldsymbol{\psi}}$	Vector having components corresponding to $\hat{\psi}_1, \ldots, \hat{\psi}_{N^I_{\mathcal{E}}}$
$\hat{\psi}_i$	Angular design variable of the i^{th} edge module
ψ_{jk}	Angular design variable of the k^{th} edge module associated with the j^{th} interior vertex of the goal mesh
$\boldsymbol{\psi}^j$	Vector having components corresponding to $\psi_{j1}, \ldots, \psi_{jn^{\mathcal{M}}_j}$
Ω	Region occupied by the material body
$\boldsymbol{\omega}_{jkl}$	Vector along the intersection axis of the k^{th} and the l^{th} edge modules associated with j^{th} interior node
$\partial\mathcal{M}$	Boundary of the goal mesh
$\partial\mathcal{M}^I$	Introduced boundary edges
$\partial\mathcal{M}^O$	Boundary edges corresponding to the outer edges of the goal shape discretization
$\partial\mathcal{S}_0$	Boundary of the sheet in the reference configuration
$\partial\Omega$	Boundary of the region occupied by the material body
$\partial\Omega_u$	Boundary of the region occupied by the material body where displacement boundary conditions are applied

$\partial\Omega_\sigma$	Boundary of the region occupied by the material body where traction boundary conditions are applied
$\mathbf{0}_n$	Zero vector in $\mathbb{R}^n$
$\varnothing$	Empty set

TABLE OF CONTENTS

Page

LIST OF FIGURES

FIGURE Page

LIST OF TABLES

1. INTRODUCTION

[1]This section provides a literature review of the topics addressed in the subsequent sections of this dissertation. A review of the classical notions of origami and existing applications of origami in various engineering fields are presented in Section 1.1. Sections 1.1.1–1.1.3 specifically address a subset of existing origami structures termed as *self-folding structures* [3, 12] and the use of *active materials* in their development. Section 1.2 provides a comprehensive review of existing active material-based self-folding structures organized by their physical activation field, namely thermal (Section 1.2.1), chemical (Section 1.2.2), electrical (Section 1.2.3), or magnetic (Section 1.2.4). After reviewing existing and potential applications of origami structures, both with and without self-folding capabilities, Sections 1.3, 1.4, and 1.5 focus on theoretical and computational efforts addressing the kinematics, structural mechanics, and design of origami structures, respectively. The motivation and objectives of the work presented in this dissertation are briefly stated in Section 1.6 and the outline of this dissertation is provided in Section 1.7.

1.1 Origami Structures

Traditionally, the term *origami* has been primarily associated with the ancient art of folding paper. The term origami has the Japanese roots *oru* meaning *folded*, and *kami* meaning *paper* [13, 14]. Its original purpose was not particularly utilitarian, but rather recreational and artistic [15]. Specifically, it was and remains the art of folding sheets of paper into decorative and often intriguing shapes, either abstract

[1]Portions of this section are reprinted or adapted from [3] E. A. Peraza-Hernandez, D. J. Hartl, R. J. Malak Jr, and D. C. Lagoudas. Origami-inspired active structures: a synthesis and review. Smart Materials and Structures, 23(9):094001, 2014. http://dx.doi.org/10.1088/0964-1726/23/9/094001

in form or representative of realistic objects (e.g. plants, animals). In origami, a goal shape is obtained from an initially planar sheet exclusively through *folding*. Traditionally, a *fold* is defined for an idealized sheet having negligible thickness as any deformation (excluding purely rigid body deformations) such that the in-surface distance between any two points in the sheet is preserved and self-intersection does not result [16]. Therefore, stretching and tearing are not permitted [16].

Based on such traditional definitions of origami, researchers discovered in the 1970s that an endless number of shapes could in theory be created using conventional origami (initially planar shape, only *folds* allowed) [14]. These discoveries enabled new approaches for manufacturing, assembling, and morphing of devices and structures based on origami principles. This is evident from the increasing attention mathematicians, scientists, and engineers have given to research on origami during the past four decades [17, 18, 19, 20, 21, 22].

Origami offers engineers novel ways to fabricate, assemble, store, and morph structures. Potential engineering advantages of origami-inspired structures include compact storage/deployment capabilities (e.g. airbags [23, 24]), potential for reconfigurability [25, 26, 27, 28, 29, 30, 31, 32], and reduction in manufacturing complexity [2, 33, 34, 35, 36, 37] (reduced part counts and improved assembly using collapsible/deployable parts). Moreover, origami principles have been utilized across scales through their applications ranging from the nano- and micro-scales [38, 39, 40, 41, 42, 43] to deployable structures for space exploration at the macro scale [44, 45, 46, 47]. Other applications of origami-inspired structures include: various space structures (solar panels, solar sail, telescope lenses [48]), micro-mirrors [49], electronic components [50, 51, 52, 53, 54, 55], robots [1, 56, 57, 58, 59, 60, 61, 62, 63], foldable wings and airplanes [64, 65, 66, 67, 68, 69, 70], foldcore-based structures for improved mechanical properties and impact resistance [71, 72, 73, 74, 75, 76, 77, 78, 79, 80, 81],

crash boxes and other energy absorption systems [82, 83, 84, 85], shelters [86, 87, 88, 89, 90, 91], metamaterials [92, 93, 94, 95, 96, 97, 98, 99, 100], microelectromechanical systems (MEMS) [28, 101, 102, 103, 104, 105, 106, 107, 108, 109], biomedical devices [110, 111, 112, 113, 114, 115], and many others [17, 116, 117]. Representative examples of such engineering applications are shown in Figures 1.1[2] and 1.2.

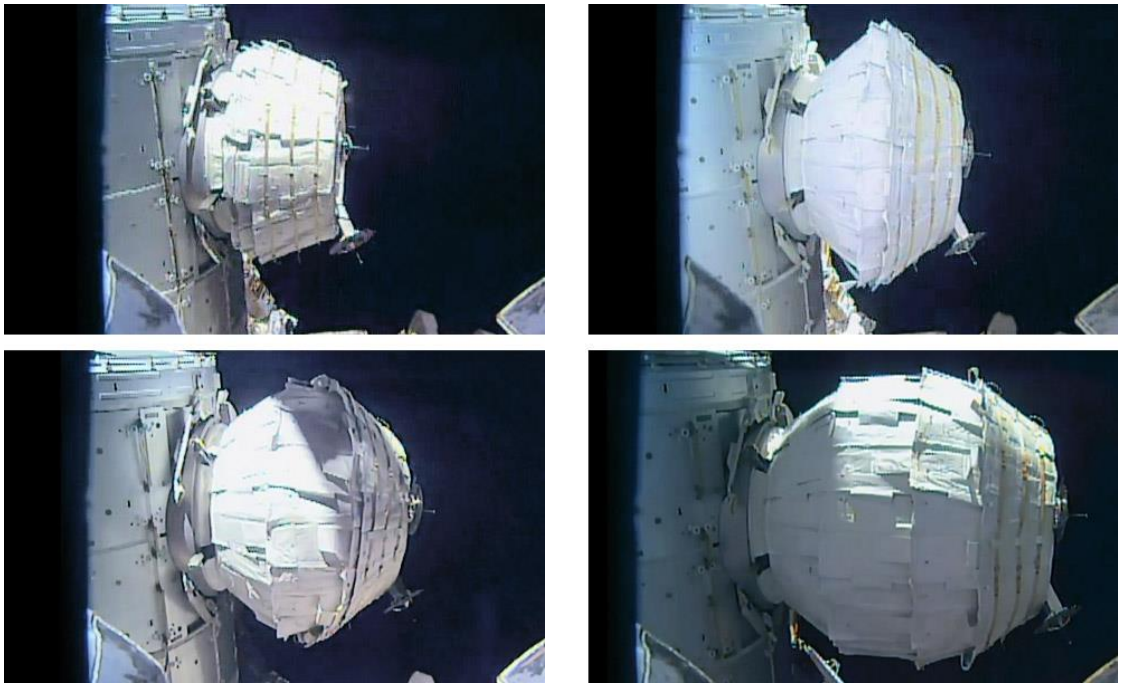

Figure 1.1: Demonstration of unfolding-based expansion of the Bigelow Expandable Activity Module (BEAM). Obtained from: NASA TV.

For certain origami-inspired engineering applications, it is impractical to externally apply the mechanical loads necessary to fold a given structure. This is the case for nano/micro structures or remote applications (e.g. space structures, underwater robotics, invasive biomedical devices). In such circumstances, *self-folding* capabili-

[2] `https://blogs.nasa.gov/spacestation/2016/05/28/beam-expanded-to-full-size/`

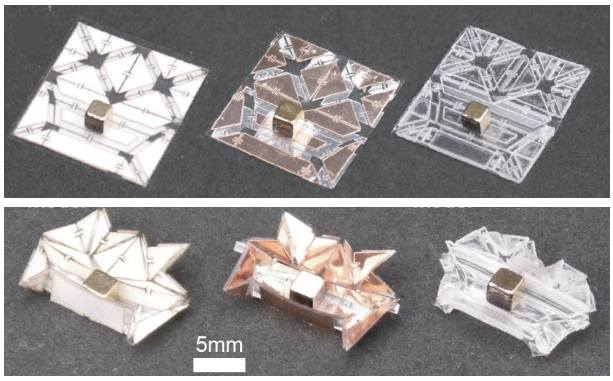

(a) Robotics [1]

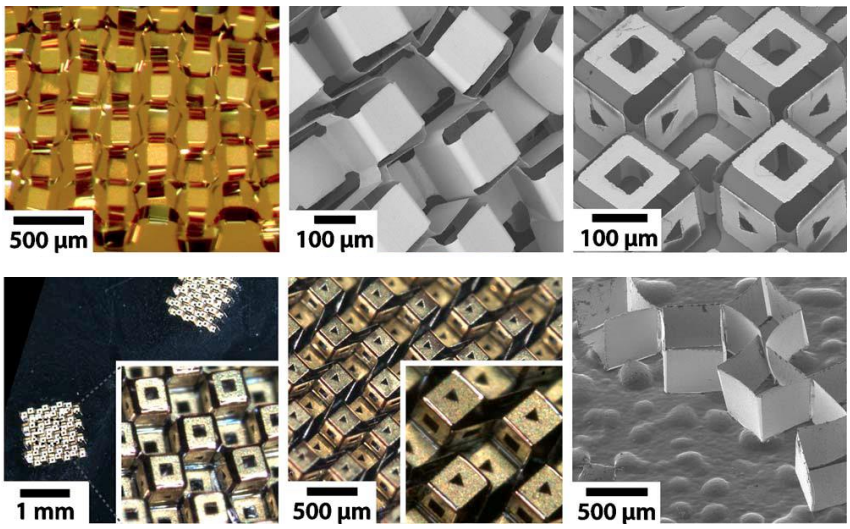

(b) Micro-fabrication and micro-assembly [2]

Figure 1.2: Examples of current and potential applications of origami-inspired structures: (a) Various origami-inspired robot designs that self-fold due to thermal expansion of polyvinyl chloride (PVC) actuating layers (from Figure 1 of [1], © 2015 IEEE, with permission of IEEE, `http://dx.doi.org/10.1109/ICRA.2015.7139386`); (b) Demonstrations of micro-fabrication and micro-assembly utilizing self-folding metallic bilayer and trilayer laminates (reprinted from [2] N. Bassik, G. M. Stern, and D. H. Gracias. Microassembly based on hands free origami with bidirectional curvature. Applied Physics Letters, 95(9):091901, 2009, `http://dx.doi.org/10.1063/1.3212896`, with the permission of AIP Publishing).

ties are essential [3]. A *self-folding* structure is one that has the capability of folding and/or unfolding to and/or from a desired shape without the application of mechanical loads [3, 12]. One approach for the development of self-folding structures is to leverage the use of *active materials* as agents of fold generation [3, 118, 119]. *Active materials* are those that convert various forms of energy into mechanical work [4]. This coupling can be categorized as direct (mechanical response due to field-induced inelastic strains in the active material) or indirect (mechanical response due to field-induced change in stiffness or other properties) [120]. In both cases, active materials allow for the mechanical work required to fold a structure to be obtained through the application of a non-mechanical field (e.g. thermal, electrical, chemical, etc.).

Certain basic concepts of origami should be briefly introduced prior to the discussion of origami structures in the remainder of the section. These concepts are depicted in Figure 1.3. In origami, it is often assumed that the reference configuration of the sheet is planar and having no overlaps [121]. The locations of the folds in such a planar configuration of the sheet are termed as the fold lines [13, 122] (see Figure 1.3(a)). Typically, the fold lines are defined by their end-points, termed as *vertices* [121]. The sheet regions bounded by the fold lines and the boundary of the sheet are known as the *faces*. A fold pattern is a schematic that shows all the fold lines on a sheet. The fold pattern and the folding sequence (Figure 1.3(b)) determine the ultimate shape of the sheet. The deformation of a fold is described by the *fold angle*, defined as π radians less the signed dihedral angle between the faces joined by a fold (which generally are assumed planar) [121]. A mountain fold exhibits non-positive fold angle values while a valley fold exhibits non-negative fold angle values [13]. An extended discussion and mathematical definitions of the aforementioned concepts is presented in Section 2 of this dissertation. The following section describes various approaches for developing self-folding structures.

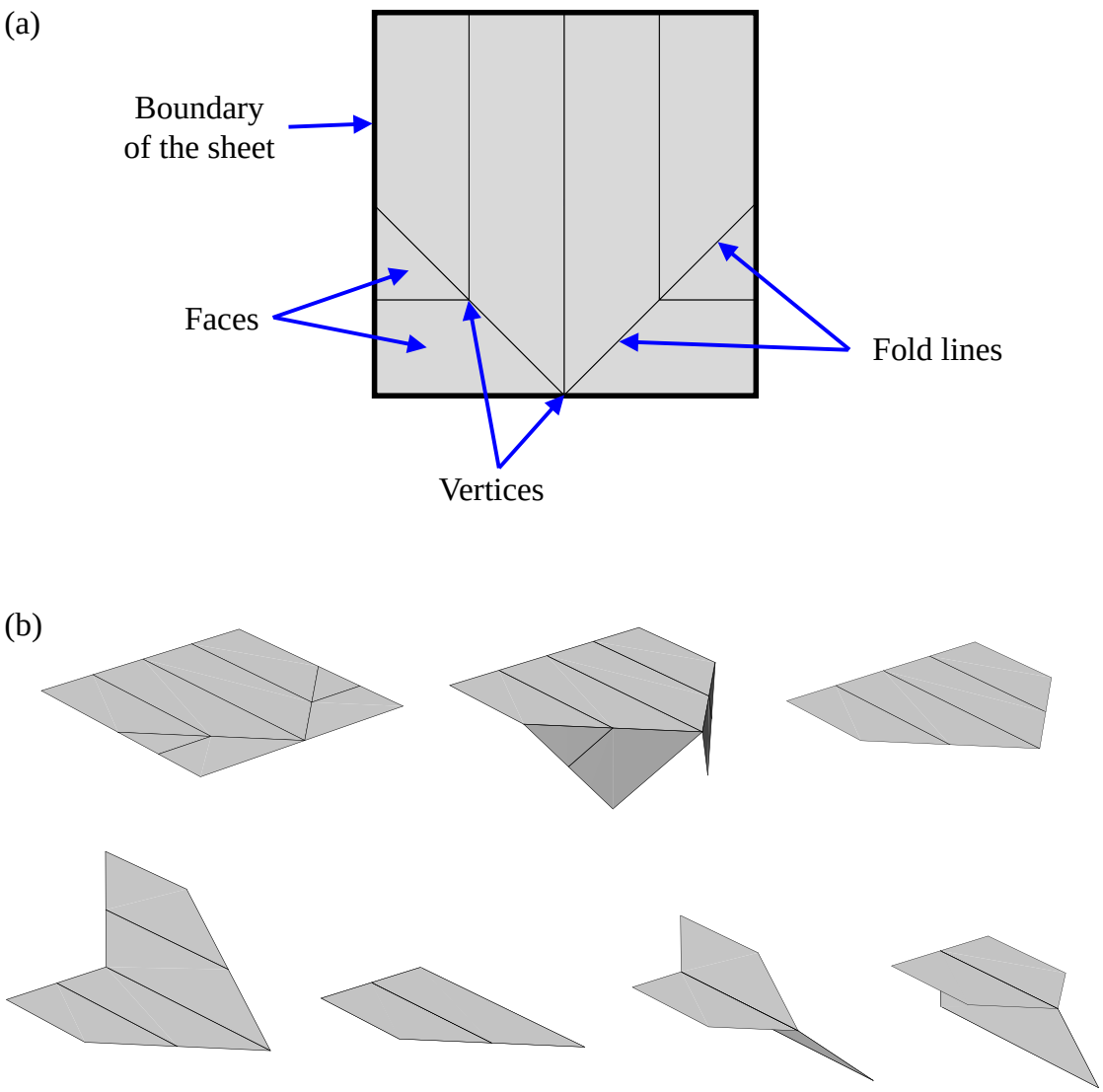

Figure 1.3: Schematic of a simple origami airplane illustrating various concepts of conventional origami: (a) Fold pattern showing fold lines, vertices, faces, and the boundary of the sheet; (b) Various configurations attained by the sheet under a given folding sequence.

1.1.1 Self-folding and Individual Active Fold Concepts

Self-folding is the capability of a structure to fold and/or unfold without the application of external mechanical loads [3]. As stated in the preceding section, active materials can be utilized to develop self-folding structures because such materials inherently convert other forms of energy into the mechanical work that allows for folding and, in some cases, unfolding deformations. Active materials are also typically energy dense and geometrically simple when used as actuators [123, 124, 125]. Physical compactness is an important consideration for self-folding structures since having a planar reference configuration is often essential.

Concepts for developing individual folds using active materials are provided here while particular examples follow in Section 1.2. The concepts are divided into two categories: *hinge type* and *bending type* [3]. Most hinge-type active folds are associated with one of three actuator concepts: (i) Variable length active rod or spring connected to the two faces joined by the hinge (Figure 1.4(a)), (ii) active torsional element attached to the hinge (Figure 1.4(b)), and (iii) active element with preset folded shape attached to the faces joined by the hinge (Figure 1.4(c)). Throughout this section, these fold concepts will be referred to as *extensional*, *torsional*, and *flexural*, respectively.

The extensional concept (Figure 1.4(a)) uses the active material in a rod or spring form with its two ends attached to the faces connected by the hinge. The length of the active element dictates the rotation of the hinge. The torsional concept (Figure 1.4(b)) uses the active material as a torsional spring or rod that provides twist deformation at the hinge. The twist angle of the active material thus directly dictates the rotation of the hinge. In the flexural concept (Figure 1.4(c)), the active material has been manufactured or trained to have a preset folded configuration

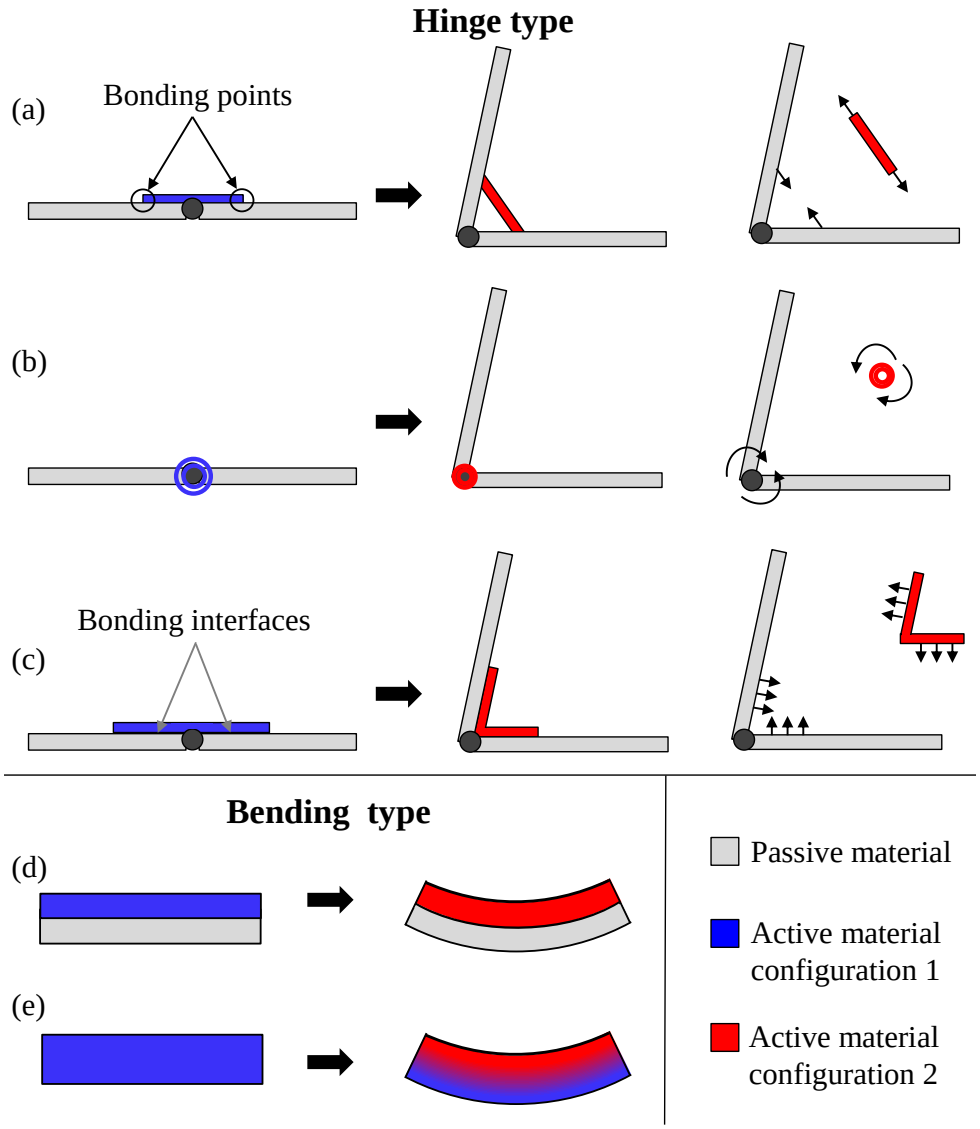

Figure 1.4: Basic concepts for active material-based folds. Hinge type: (a) *Extensional* (variable length active rod or spring connected to the two faces); (b) *Torsional* (active torsional element at the hinge); (c) *Flexural* (active element with preset folded shape). Simplified free body diagrams of the hinge-face structure and the active element are also shown. Bending type: (d) *Multilayer* laminate comprised of active and passive layers (the simplest case of a bilayer having one active and one passive layer is shown); (e) *Single layer* subjected to a graded activation field.

but is then deformed to an initially planar configuration. Upon application of the activation field, the active material returns to its preset folded configuration and being bonded to the faces of the passive material, induces the hinge to do the same.

All concepts can be further improved to allow for both mountain and valley folds by adding corresponding antagonistic active components. In the torsional concept, this can be achieved by attaching two active torsional elements to the hinge that generate twist in opposite directions (e.g. [126]). For the extensional and flexural concepts, it can be achieved by pairs of active elements in opposition to each other (e.g. on opposite sides of the sheet for the extensional concept). However, mechanical restrictions may arise since activation of one active element may subject its associated antagonistic active element to excessive stress or deformation, hindering the folding operation and possibly leading to material failure. Another challenge is that of maintaining both sufficient geometric offset and localized/targeted activation field imposition such that opposing hinge moments do not result.

Other individual fold concepts do not assume the existence of discrete hinge mechanisms but are rather based on bending caused by the actuation of the active material. Such concepts are shown in Figures 1.4(d) and 1.4(e). Unlike the hinge-type fold concepts, the bending-type approaches may offer the advantage of massive foldability [127] (i.e. folds may be generated at any location or orientation at which the driving field is applied, unless mechanically restricted). Conversely, the folds are clearly restricted to pre-determined hinge locations in the hinge-type concepts. In the remainder of the section, the individual fold concept of Figure 1.4(d) is referred to as *multilayer* and that of Figure 1.4(e) as *single layer*.

The multilayer concept considers self-folding using a laminate comprised of active and passive layers (see Figure 1.4(d) for an example of a two-layer laminate with one passive layer and one active layer). A *passive* layer generates negligible mechanical

work compared to the active layer under the application of the activation field. When such a field (thermal, magnetic, etc.) is applied, the active layers are driven to deform, generally axially, while the passive layers are not. This difference in expansion or contraction between the various laminate layers generates bending of the sheet. This concept can allow for both mountain and valley folds in a manner similar to that employed for hinge-type folds. Specifically, three-layer designs with two opposing outer layers of active material separated by a passive material can be used [8]. A significant challenge for such three-layer designs is to isolate the activation field within only one of the two active outer layers. For this purpose, the middle layer may serve in another role as an insulator with respect to the activation field, preventing the field applied to one active layer from reaching the opposing active layer [128].

The single layer concept considers self-folding through bending without hinges using a single active layer subjected to a graded activation field (Figure 1.4(e)). Such a gradient generates a non-uniform distribution of actuation strain throughout the thickness, causing the structure to bend. This design also allows for mountain and valley folds based on the direction of the activation field gradient. However, folding using this approach is generally more difficult as compared to the multilayer concept since it is not practical to maintain gradients in some physical fields (e.g. temperature) at specific locations for a considerable period of time [129].

It should be noted that folding using active materials is not restricted to the five concepts presented in this section. Examples of self-folding structures that use other fold concepts are presented in Section 1.2 (e.g. passive hinged faces with attached magnetic patches that are manipulated by the direction of the magnetic field without requiring bending or stretching of the magnetic patches [130, 131]).

1.1.2 Active Materials for Self-folding Structures

When considering self-folding from a planar reference configuration to a three-dimensional deformed configuration using active material actuation, several critical design drivers should be considered: actuation strain, actuation stress, and the capability of generating and/or manipulating the field that induces deformation in the active material at the chosen scale. This section provides a simple description of the relations among activation field, actuation strain, and actuation stress.

To understand how active self-folding structures are developed, constitutive equations that relate the externally applied fields to the obtained actuation strain are needed. The following simple expression relates the second-order linearized strain tensor $\boldsymbol{\varepsilon}$ to different fields and applies for a wide range of commonly used active materials [4, 132, 133, 134, 135][3]:

$$\boldsymbol{\varepsilon} = \boldsymbol{S}\boldsymbol{\sigma} + \boldsymbol{\alpha}(T - T_0) + \boldsymbol{D}^P\boldsymbol{E} + \boldsymbol{D}^M\boldsymbol{H} + \sum_{i=1}^{n} \boldsymbol{e}^i(c^i - c_0^i) + \boldsymbol{\varepsilon}^{MS}, \tag{1.1}$$

where $\boldsymbol{S}$ is the fourth-order compliance tensor, $\boldsymbol{\sigma}$ is the second-order Cauchy stress tensor, $\boldsymbol{\alpha}$ is the second-order thermal expansion tensor, T is the absolute temperature, T_0 is the reference absolute temperature, $\boldsymbol{D}^P$ is the third-order tensor of piezoelectric coefficients, $\boldsymbol{E}$ is the electric field vector, $\boldsymbol{D}^M$ is the third-order tensor of piezomagnetic coefficients, $\boldsymbol{H}$ is the magnetic field vector, $\boldsymbol{e}^i$ is the second-order tensor of expansion due to concentration of the i^{th} chemical species, c^i is the concentration of the i^{th} chemical species, c_0^i is the reference concentration of the i^{th} chemical species, and $\boldsymbol{\varepsilon}^{MS}$ is the second-order tensor of strains caused by changes in the material micro- and/or nano-structure. This last contribution ($\boldsymbol{\varepsilon}^{MS}$) may be altered due

[3]This additive decomposition of strain is valid only in the case of linearized strains. The work presented in this dissertation considers such a case.

to phase transformation [136, 137, 138], variant reorientation [139, 140], change in the crosslinked structure in certain polymers [141, 142, 143, 144], etc. Such strains are coupled in certain extent to field variables such as $\boldsymbol{\sigma}$, T, $\boldsymbol{H}$, and $\boldsymbol{E}$ depending on the considered material.

The total strain $\boldsymbol{\varepsilon}$ can clearly be separated into two distinct parts: the strain due to elastic deformation $\boldsymbol{\varepsilon}^{EL}$ and the strain due to actuation $\boldsymbol{\varepsilon}^{ACT}$. This separation is given as $\boldsymbol{\varepsilon} = \boldsymbol{\varepsilon}^{EL} + \boldsymbol{\varepsilon}^{ACT}$, where the elastic strain is given by $\boldsymbol{\varepsilon}^{EL} = \boldsymbol{S}\boldsymbol{\sigma}$. Taking this into account, the following expression is obtained for the actuation strain:

$$\boldsymbol{\varepsilon}^{ACT} = \boldsymbol{\alpha}(T - T_0) + \boldsymbol{D}^P\boldsymbol{E} + \boldsymbol{D}^M\boldsymbol{H} + \sum_{i=1}^{n} \boldsymbol{e}^i(c^i - c_0^i) + \boldsymbol{\varepsilon}^{MS}. \tag{1.2}$$

It is observed that there are various possible ways to actuate an active self-folding structure depending on the active material chosen:

- Use direct coupling by applying fields that induce actuation strain without modifying the material micro- and nano-structure (e.g. alter the electric field $\boldsymbol{E}$ to induce actuation strain due to the piezoelectric effect ($\boldsymbol{D}^P\boldsymbol{E}$) or change the temperature to generate thermal expansion or contraction $\boldsymbol{\alpha}(T - T_0)$) .

- Use direct coupling by applying fields to change the micro- and nano-structure of the material and alter $\boldsymbol{\varepsilon}^{MS}$ (e.g. apply temperature changes to induce phase transformation in an SMA and generate/recover transformation strains [4]).

- Use indirect coupling and apply fields that alter certain material properties (e.g. use temperature changes to alter the material compliance $\boldsymbol{S}$ and induce changes in the elastic strains. Examples of indirect coupling are found in [145, 146, 147, 148]).

1.1.3 Comparative Individual Fold Analysis

In order to make simple assessments for the performance of various active materials in the active fold concepts described in Section 1.1.1, the actuation strain and actuation stress for such active materials should be mapped into fold quantitative responses (e.g. bending or torsional moment, fold angle or radius of curvature at the fold). Analytical expressions for quantitative responses of a single active fold can be readily derived for the torsional and multilayer concepts (refer to Figure 1.4) after making certain simplifying assumptions. The derivation of such expressions is summarized in Appendix A for the multilayer concept and in Appendix B for the torsional concept. The influence of secondary material regions or structural components (e.g. sensors, connectors) that might be essential in the full physically realized self-folding structures is not explicitly considered.

Equations relating actuation strain and actuation stress to various fold quantitative parameters are presented in Table 1.1 where R_B is the radius of curvature of a bent multilayer fold, M_B is the bending moment applied to a multilayer fold, φ_T is the total twist angle of an active torsional rod (directly related to the fold angle for the torsional concept), and M_T is the torque applied to an active torsional rod. Those values are directly or inversely proportional to the active material actuation strain ε^{ACT} and actuation stress σ^{ACT}. The other parameters in the equations shown in Table 1.1 directly correspond to geometric and/or material parameters or are derived from them. Considering the multilayer concept, h_B is the total laminate thickness, w_B is the width of a laminated beam, and a_1^B is the thickness of the active layer. The parameters C_1^B and C_2^B are dependent on material and geometric parameters of the layers comprising the laminate and their definitions are provided in Equations (A.5) and (A.6), respectively. Considering the torsional concept, r_T is the radius of

Table 1.1: Relations among actuation stress and actuation strain and various fold quantitative parameters.

Fold concept	Actuation strain assessment	Actuation stress assessment
Multilayer concept (Appendix A)	$\varepsilon^{ACT} = \dfrac{C_1^B h_B}{R_B}$	$\sigma^{ACT} = \dfrac{M_B C_2^B}{w_B h_B a_1^B}$
Torsional concept (Appendix B)	$\varepsilon^{ACT} = \dfrac{\sqrt{3}\, r_T \varphi_T}{3 L_T}$	$\sigma^{ACT} = \dfrac{2\sqrt{3}\, M_T}{\pi r_T^3}$

a torsional rod of circular cross-section and L_T is the length of the rod.

Figure 1.5 and Figure 1.6 provide a comparison of the actuation strain and actuation stress of common active materials [4] and their performance assessment for the multilayer and torsional fold concepts, respectively. The bottom axes of both Figure 1.5 and Figure 1.6 represent the magnitude of the actuation strain ε^{ACT} and the left axes represent the magnitude of the actuation stress σ^{ACT}. The top and right axes of Figure 1.5 show parameters that assess the material performance as an active layer in the multilayer concept (Table 1.1). From the plot shown in this figure, it is observable that ceramic-type active materials (electrostrictive ceramics, magnetostrictive ceramics, and piezoelectric ceramics) may not be suitable for self-folding systems because they would provide bending radii that are orders of magnitude below other common active materials, though they may do so at much higher frequencies [149, 150]. The top and right axes of Figure 1.6 show parameters that assess the material performance in the torsional concept (according to the results of Table 1.1).

Often, actuation stress limitations may be reduced by the usage of compliant mechanisms [151, 152, 153, 154, 155, 156]. For instance, shape memory polymers

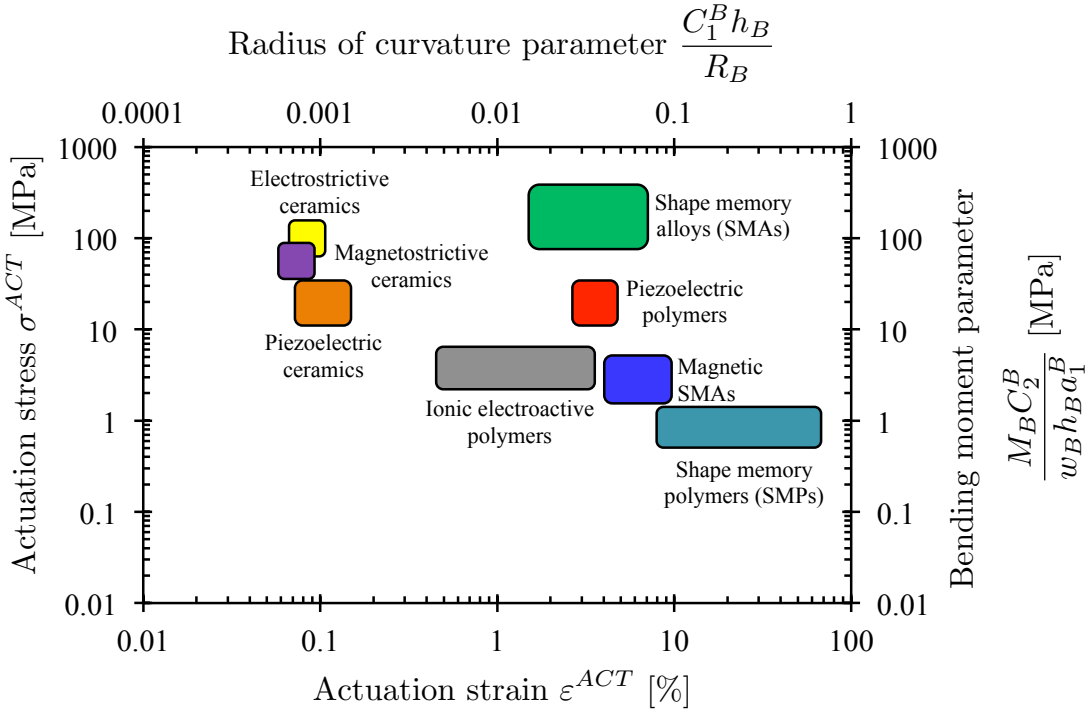

Figure 1.5: Active materials performance for the multilayer fold concept. The diagram shows typical ranges of actuation strain and actuation stress for different common active materials [4]. The top and right axes represent parameters related to the radius of curvature and the bending moment, respectively.

(SMPs) [141, 157, 158], which are shown in Figure 1.5 and Figure 1.6 as having the lowest actuation stress compared to the other common active materials, have been demonstrated to be a suitable active material for self-folding (e.g. [159, 160, 161, 162, 163]).

The assessments in Table 1.1 were determined using simplified analytical models and they serve as simple quantitative estimations of how different materials will perform in active folds under certain idealizations (e.g. the influence of structural components such as connectors and sensors on the folding performance is neglected). To provide with further information regarding the full system integration and capabilities of active materials within self-folding structures, examples of previously

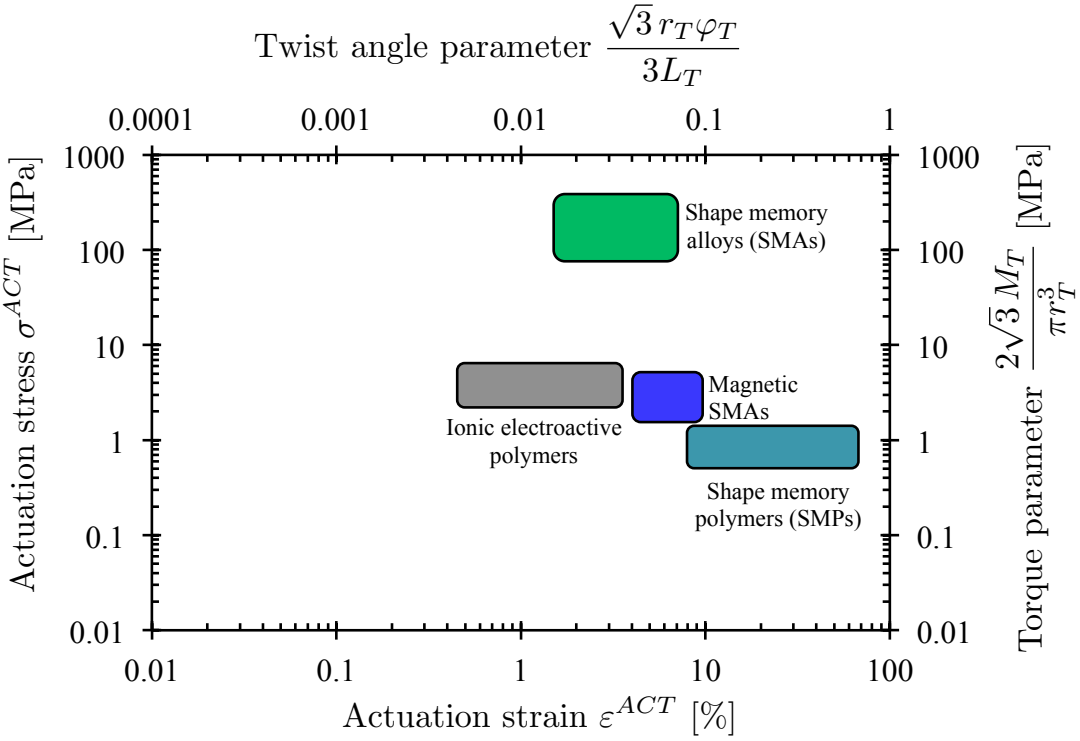

Figure 1.6: Active materials performance for the torsional fold concept. The diagram shows typical ranges of actuation strain and actuation stress for different common active materials [4]. The top and right axes represent parameters related to the twist angle and the applied torque, respectively.

demonstrated systems (either through experimentation or highly detailed numerical simulation) are reviewed in the following section.

1.2 Review of Active Self-folding Structures

Existing examples of self-folding structures classified according to the physical field that induces the folding deformation are described in this section. The goal is to provide a systematic view of the state-of-the-art in this important and evolving area. Thermal, chemical, electrical, and magnetic field-activated self-folding structures are presented. Tables 1.2 through 1.5 summarize the characteristics of the largest classes of self-folding systems considered. Examples of each type are classified in terms of

their fold concept, reversibility of the folds, material system, characteristic sheet thickness, and current or potential applications.

1.2.1 Thermally-activated Self-folding Structures

Table 1.2 provides a classification of various existing self-folding structures that are thermally-activated. The design space for thermally-activated morphing structures is large due to the various methods available for localized supply of heat that include convection, Joule heating, induction heating [164, 165], radiation [166, 167], etc. Although there are several ways to alter the temperature in a structure, the diffusive nature of heat represents a design challenge requiring the consideration of methods for controlling the spatial distribution of temperature over time (e.g. by adding thermal insulators to maintain a high temperature concentrated in localized regions of the self-folding structure).

At the macro-scale, thermally-activated self-folding structures have been based mostly on SMAs and SMPs. Regarding SMAs, Rus and coworkers [5, 168, 202] developed a self-folding structure that consisted of a single sheet having repeated triangular tiles connected by hinges. The pattern of repeated triangular tiles provides flexibility in the number of shapes towards which the sheet can fold. Thin SMA foils shape-set to a folded configuration were used to actuate the hinges (using the flexural fold concept shown in Figure 1.4(c)). Such a structure was shown to be successful through demonstrations of folding towards different conventional origami shapes such as a boat or an airplane (Figure 1.7(a)). An and Rus provided a design and programming guide for self-folding structures of this kind [203].

Another example of SMA-based self-folding structures is the concept of massively foldable laminated sheet [8, 170, 204, 205, 206, 207]. The concept consists of a laminated composite with two outer layers of SMA separated by a compliant and

Table 1.2: Examples of thermally-activated self-folding structures.

Fold concept	Reversible	Material system	Characteristic thickness [μm]	Application	Reference
Flexural	Yes	SMA	500.0	Potential multi-purpose morphing structures	[5, 168]
Multilayer and single layer	Yes	SMA	1000.0	Potential multi-purpose morphing structures	[8, 169, 170, 171]
Other	Yes	SMA	50.0	Stent	[110, 172, 173]
Other	Yes	SMA	100.0	Robotics fabrication	[174, 175]
Extensional	Yes	SMA	1000.0	Robotics	[56, 176]
Flexural	Yes	SMA	1000.0	Robotics	[177]
Extensional, flexural, and multilayer	Yes	SMA	2000.0	Flexible mobile devices	[178]
Multilayer	Yes	SMA	100.0	Flexible mobile devices	[179]
Multilayer	Yes	SMA	500.0	Decorative paper structures	[180, 181, 182]
Multilayer	Yes	SMA and SMP	1000.0	Potential multi-purpose morphing structures	[183]

Table 1.2: Continued.

Fold concept	Reversible	Material system	Characteristic thickness [μm]	Application	Reference
Flexural and multilayer	Yes	SMP	1000.0	Potential multi-purpose morphing structures	[159, 160, 184, 185]
Flexural and multilayer	Yes	SMP	500.0	Novel fabrication methods	[186]
Other	Yes	SMP	500.0	Potential multi-purpose morphing structure	[187]
Single layer	Yes (once)	SMP	250.0	Potential multi-purpose morphing structure	[188, 189, 190]
Multilayer	Yes	SMA	25.0	Microgripper	[191, 192]
Multilayer	Yes	Thermoresponsive polymer	Not available (in the order of 1000.0)	Potential multi-purpose morphing structures	[193]
Multilayer	Yes	Polymer-metal bilayer	5.0	Capture/release small scale devices	[194, 195]
Multilayer	Yes	Thermoresponsive polymer	0.5	Capture/release small scale devices	[196, 197, 198]
Single layer	Yes	Liquid crystal elastomers	50.0	Folding actuators	[199, 200, 201]

thermally insulating layer (e.g. an elastomer). The outer layers of the SMA may consist of thin pre-strained SMA films [127, 170, 208] or meshes of pre-strained SMA wires [8, 10, 209]. With this design, the side of the laminate being heated determines whether a mountain or valley fold would result. It was shown through finite element simulations that structures comprised of this laminate are able to self-fold and form arbitrary three-dimensional structures [169]. Simulations and experimental demonstrations [210] of such a self-folding structure are shown in Figure 1.7(b). More recently, SMA-SMP laminated composites based on this concept have been investigated. Such a shape memory composite is capable of locking in its folded shape upon a heating/cooling cycle [183].

Kuribayashi and coworkers [110, 172] addressed the design, manufacturing, and characterization of a self-deployable origami stent. The stent is comprised of a single SMA foil with pre-engineered mountain and valley folds. The deployment of this stent design can be achieved by utilizing the shape memory effect activated at body temperature or by making use of the pseudoelastic effect [4, 211]. The authors demonstrated that the stent design successfully deploys as expected. Such a prototype is a valuable addition to the extensive list of existing and potential applications of of SMAs in the biomedical field [212, 213, 214].

Self-folding using SMA actuation has also been used for paper animation. Qi and coworkers [180, 181] used SMA wire actuators attached to paper in order to self-fold towards different artistic paper shapes. This study on SMA-actuated paper animation represents another contribution on the topic of active materials-based artwork [215, 216]. Self-folding structures can also be potentially applied to other areas such as flexible display devices [217, 218, 219, 220, 221, 222, 223]. For example Roudaut and coworkers [178] and Gomes and coworkers [179] proposed new flexible display designs for mobile devices that can alter their shape via fold-like deformations

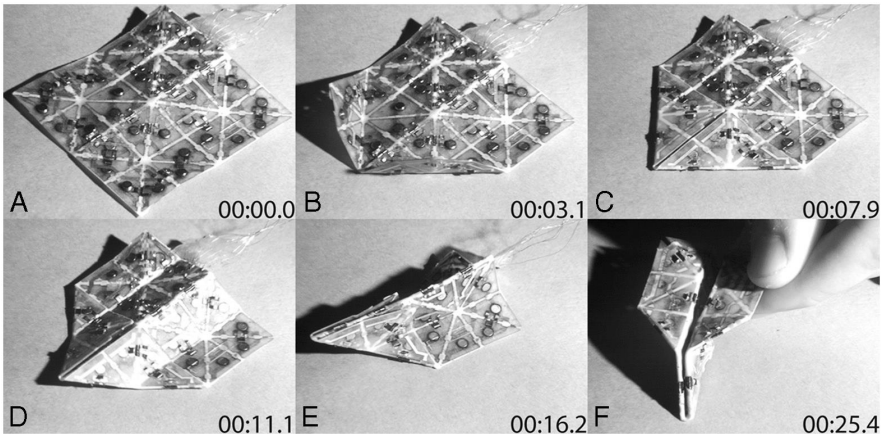

(a)

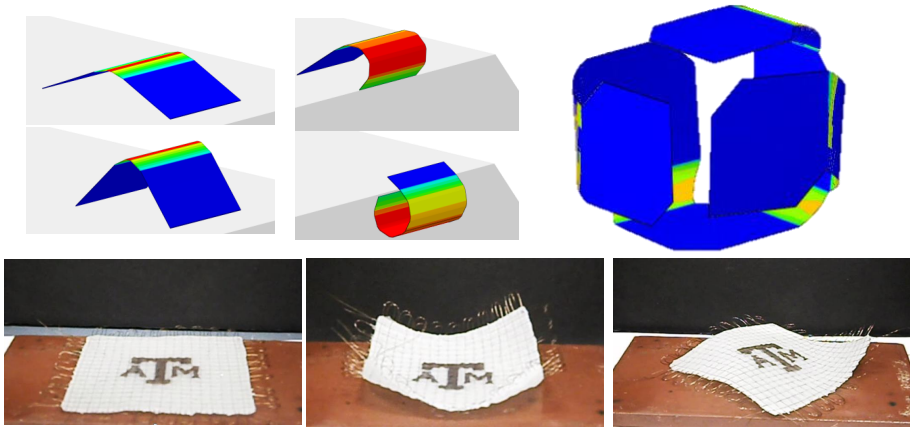

(b)

Figure 1.7: Examples of thermally-activated self-folding structures: (a) Sheet with SMA-actuated hinges. An initially planar sheet folds towards an airplane shape [5] (Reproduced from [5] E. Hawkes, B. An, N. M. Benbernou, H. Tanaka, S. Kim, E. D. Demaine, D. Rus, and R. J. Wood, Programmable matter by folding, Proceedings of the National Academy of Sciences, 107(28):12441–12445, 2010, `http://dx.doi.org/10.1073/pnas.0914069107`, by permission of the Proceedings of the National Academy of Science of the United States of America PNAS); (b) Massively foldable SMA-based laminate including worm and rolling locomotion examples and self-folded cube simulations [6]. Experimental demonstrations of such a sheet concept folding towards a "bowl shape" and an "S-shape" are also shown.

driven by SMA actuation.

Of course, SMAs are not the only option for thermally-activated self-folding structures. Shape memory polymers [224] provide higher actuation strains but lower actuation stresses (see Figures 1.5 and 1.6). One example of thermally-activated self-folding with SMPs is the work of Demaine and coworkers [159, 160]. They developed self-folding hinges comprised of SMP, paper, and resistive circuits. In addition, they presented a model for the torque exerted by such composite hinges that was experimentally validated.

Light sources have also been used to provide heat to thermally-activated self-folding structures based on the conversion of light to heat [129], where the thermal energy is then converted to mechanical work. Liu and coworkers fabricated self-folding structures that employ localized absorption of light cast over a compositionally homogenous sheet of SMP. The uniform externally applied stimulus (i.e. unfocused light) generates a focused folding response via localized designed light absorption [188]. Their approach uses mass-produced materials without the need for multiple fabrication steps, where the folded regions were defined by the presence of black ink patterned via a printing process. The polymer regions located beneath inked areas heat faster than the areas elsewhere and eventually their temperature increases beyond the glass transition temperature of the SMP. After such a temperature is exceeded, these localized SMP regions actuate and the structure bends. The reference planar configuration can be recovered by increasing the temperature of the entire sheet above the SMP glass transition temperature. An extensive review on self-folding polymeric sheets is provided in [225].

There are various examples of thermally-activated self-folding structures at the small scales. For instance, Lee and coworkers designed a microgripper that uses SMA actuation to open and close [191, 192]. Deposited SMA films serve as the outer layers

of the microgrippers, acting as actuators. Applications for the microgripper include assembling small parts for manufacturing, minimally invasive tissue sampling, and remote handling of small particles in extreme environments [191].

As another example, Gracias and coworkers fabricated self-folding structures at the micro-scale able to perform sequential folding through heating of pre-stressed hinges using lasers [193]. Their hinges were comprised of Cr/Au-polymer bilayers. Upon laser radiation, the polymer layer softens and the bilayer bends due to existing pre-stress generated during the bilayer fabrication process. Kalaitzidou and coworkers [194, 195] also developed self-folding polymer-metal bilayer structures. Their self-folding laminated composites were comprised of a polydimethysiloxane (PDMS [226, 227]) layer and an Au layer. The PDMS layer had a thickness of several micrometers while the thickness of the Au layer was in the order of nanometers. Upon changes in temperature, the bilayer folds or unfolds due to dissimilar thermal expansion of the materials in the two layers. They also fabricated a PDMS-silicon carbide (SiC) bilayer with similar behavior to demonstrate that their micro-fabrication approach can be applied using any two materials with dissimilar thermal expansions. The ability of the bilayers to capture, transport, and release different solids was demonstrated indicating their potential application as delivery tubes [195]. A similar concept was adopted by Ionov and coworkers when fabricating self-folding bilayers having one layer of polycaprolactone (PCL) and another layer of poly-(N-isopropylacrylamide) (PNIPAM) [196, 197]. Polycaprolactone is hydrophobic (i.e. tending to repel/reject water [228]) while the absorptivity of PNIMAN can be reversibly changed with temperature by heating/cooling above/below its low critical solution temperature [196]. This temperature dependent behavior allows PNIPAM to swell or collapse in the presence of water driven by changes in temperature.

1.2.2 Chemically-activated Self-folding Structures

Self-folding structures activated by chemical stimulus have also been explored by multiple researchers. Most of these structures are based on the multilayer fold concept and utilize the degradation or swelling behavior of certain polymers under the presence of specific substances or pH level [229, 230]. Examples of these structures are classified in Table 1.3.

One example of self-folding structures activated through chemical stimulus are the microtubes fabricated by Kumar and coworkers [231]. They considered a three-layer laminated composite comprised of PDMS, polystyrene (PS), and poly(4-vinylpyridine) (P4 VP). The folding mechanism of the microtubes was based on the different amount of swelling in their comprising polymer layers. Polystyrene demonstrates minimal water uptake while P4 VP is less hydrophobic and swells in acidic aqueous solutions [231]. A P4 VP layer increases its volume upon swelling and if fixed to a PS layer, it will cause the polymer laminate to fold. Micro- and nano-tubes fabricated through this method are promising for applications including nano-syringes for intra-cellular surgery and nano-jet printing [244]. In another work, Shim and coworkers [238] fabricated robust microcarriers using hydrogel bilayers that exhibit reversible folding behavior. The bilayer composite consisted of a layer of poly(2-hydroxyethyl methacrylate-co-acrylic acid), p(HEMA-co-AA), and a layer of poly(2-hydroxyethyl methacrylate), p(HEMA). Planar structures comprised of this laminated composite were able to fold towards micro-containers by swelling of the p(HEMA-co-AA) layer triggered by changes in pH.

A similar self-folding bilayer approach was adopted by He and coworkers in the fabrication of an oral delivery device [236]. The main part of the device consisted of a finger-like bilayer comprised of pH-sensitive hydrogel based on crosslinked

Table 1.3: Examples of chemically-activated self-folding structures.

Fold concept	Reversible	Material system	Characteristic thickness [μm]	Application	Reference
Multilayer	No	Hydrogel	0.5	Microtubes fabrication for small scale devices	[231, 232, 233, 234]
Multilayer	Yes	Hydrogel	100.0	Potential multi-purpose morphing structures	[235]
Multilayer	No	Hydrogel	20.0	Drug release device	[236, 237]
Multilayer	Yes	Hydrogel	50.0	Micro-containers	[238]
Multilayer	Yes	Hydrogel	5.0	Potential multi-purpose morphing structures	[239]
Torsional and multi-layer	Yes	Hydrogel	200.0	Potential multi-purpose morphing structures	[240]
Multilayer	No	Polymer degradation	Not available (in the order of 100)	Small scale grippers	[241, 242]
Multilayer	No	pH responsive polymer	0.5	Capture/release small scale devices	[243]

poly(methyacrylic acid) (PMAA) which swells significantly when exposed to body fluids, and a second non-swelling layer. Guan and coworkers [239] studied the magnitude of folds achieved by a self-folding bilayer composite as a function of the active layer composition [239]. In such studies, the active swelling layer was prepared with a mixture of poly(ethylene glycol methacrylate) (PEGMA) and poly-(ethylene glycol dimethacrylate) (PEGDMA). By controlling the ratio between the two components of such an active layer, different magnitudes of folding were achieved.

A self-folding gripper that opens and closes by the actuation of polymer hinges was fabricated by Gracias and coworkers [241, 242]. The actuation of the polymer hinges was triggered by their sensitivity to the presence of enzymes, where they utilize two different polymers with two mutually exclusive enzyme sensitivities. The two polymers were placed at hinges in such a way that bending in opposite directions is activated given the appropriate stimulus. When one polymer is selectively degraded by its associated enzyme, the gripper closes. When the other polymer is degraded through the action of its own distinct enzyme, its respective hinge bends and the gripper opens.

1.2.3 Electrically-activated Self-folding Structures

Examples of self-folding structures activated by electrical stimulus are provided in Table 1.4. The extensive research in dielectric elastomers [245, 246] and electroactive polymers [247], along with recent advancements in MEMS technologies [248], have made possible the development of such self-folding structures.

For instance, Frecker and coworkers [130, 249, 250] developed a bending actuator that consisted of three layers: an active dielectric elastomer layer, a compliant passive layer, and compliant electrodes. Self-folding structures with dielectric elastomers based on the extensional concept (Figure 1.4(a)) were developed by Roudaut and

coworkers for flexible mobile device displays (previously discussed in Section 1.2.1). Their concept considered bending of a flexible mobile device through contraction and expansion of a dielectric elastomer actuator connected to two sides of the device [178].

More complex electrically-driven folding motion was demonstrated by Okuzaki and coworkers, who created a biomorphic robot fabricated by folding a conducting polymer film [251]. The folding actuation was generated by electrically-induced changes in the stiffness of the polymer film. Those changes of stiffness were caused by the absorption and desorption of water vapor molecules driven by the imposed electrical field. Okuzaki and coworkers demonstrated the feasibility of the concept by fabricating different prototypes such as an origami robot that moves rectilinearly with caterpillar-like motion. Such a motion was achieved by repeated expansion and contraction of its accordion-like body via folding/unfolding of electrically sensitive Polypyrrole (PPy [256, 257]). At the small scale, Inganäs and Lundström utilized conducting polymers as actuators within electrically-driven polymer/gold folding bilayers [252, 253]. They used conducting PPy as the active layer.

1.2.4 Magnetically-activated Self-folding Structures

Examples of magnetically-activated self-folding structures are classified in Table 1.5. Magnetoactive elastomers (MAEs [258]) have been investigated as actuators for self-folding structures by von Lockette and coworkers [130, 131, 259, 260]. The MAEs they considered were fabricated by mixing barium ferrite particles into a silicone rubber matrix. Composites consisting of PDMS sheets with MAE patches were able to achieve locomotion under the application of a time periodic magnetic field. Additionally, von Lockette and coworkers fabricated a cross-shaped PDMS sheet with four MAE patches on its sides that was shown to fold into a box induced by a magnetic field. The four MAE patches experienced translations and rotations driven

Table 1.4: Examples of electrically-activated self-folding structures.

Fold concept	Reversible	Material system	Characteristic thickness [μm]	Application	Reference
Other	Yes	Dielectric elastomer	1000.0	Robotics	[57]
Multilayer	Yes	Dielectric elastomer	350.0	Potential multipurpose morphing structures	[130, 249, 250]
Other	Yes	Electroactive polymer	20.0	Robotics/ Locomotion	[251]
Extensional	Yes	Dielectric elastomer	2000.0	Flexible mobile devices	[178]
Multilayer	Yes	Electroactive polymer	0.5	Small scale tools	[252, 253]
Multilayer	Yes	Electroactive polymer	Not available	Bending actuators	[254]
Extensional	Yes	Dielectric elastomer	300	Robotics/ Locomotion	[255]

by the magnetic field. However, it should be noted that in this particular example, the MAE patches were used only for their ability to be magnetized rather than for any intrinsic magnetic to mechanical energy conversion. Bowen and coworkers utilized such a MAE-based self-folding approach to develop bistable origami mechanisms [261, 262, 263].

After just providing a review of origami-inspired active structures, it is evident that the complexity of self-folding origami structures is large in terms of geometry and material behavior. Consequently, theoretical modeling and design approaches for such structures are needed for engineers to provide more and larger developments in this area. The following sections present a review of previous efforts for modeling and design of origami structures that can be applied to self-folding origami structures as well as those without self-folding capabilities.

1.3 Kinematics of Origami Structures

Previously in Section 1.1, conceptual designs for individual folds as well as the material selection for active self-folding structures were reviewed. Kinematic modeling for origami structures, irrespective of the material response or externally applied loads being used to effect the folding motion, is reviewed in this section.

The study of the kinematics of origami structures is an active research topic and has been investigated by various researchers [265, 266, 267, 268, 269, 270, 271, 272]. Kinematic modeling and computational simulation of origami structures [265, 273] permits understanding of their deformation and the development of computational tools for their design [7, 274, 275]. To develop a kinematic model for origami structures, three main aspects have to be considered [13, 121, 276]: (i) The geometric definition of the sheet reference configuration and the associated fold pattern, (ii) the description of allowable deformations for the sheet, and (iii) the mapping between

Table 1.5: Example of magnetically-activated self-folding structures.

Fold concept	Reversible	Material system	Characteristic thickness [μm]	Application	Reference
Other	Yes	Magnetoactive elastomer	3000.0	Potential multi-purpose morphing structures	[130, 131, 259]
Other	Yes	Magnetoactive elastomer	1500.0	Bistable mechanisms	[261, 262, 263]
Other	Yes	Polymer and permanent magnets composite	500.0	Potential multi-purpose morphing structures	[264]

the reference and the current configurations of the sheet. These aspects of kinematic modeling for origami structures are rigorously addressed in Section 2 while a literature review is presented in this section.

Two main assumptions have been made in the development of mathematical models for the kinematics of origami structures to date [121, 265, 266, 276, 277, 278, 279, 280]: that folds are straight creases having zeroth-order geometric continuity (termed as *creased folds*), and that planar faces bounded by the folds and the sheet boundary are rigid (i.e. these faces are neither bent nor stretched, refer to Figure 1.3). Models having these assumptions have been utilized for the analysis and design of deployable structures [266, 281, 282, 283, 284, 285, 286, 287, 288] and mechanisms [289, 290, 291, 292, 293, 294, 295, 296, 297, 298, 299, 300, 301, 302].

Many researchers have given significant attention to flat foldable origami [303, 304, 305, 306, 307]. Allowable configurations for flat foldable origami structures are those in which all the planar faces have parallel normal directions [13, 308, 309, 310]. The imposition of flat foldability constraints in origami structures ensures that these structures can be fabricated from a planar sheet or, conversely, be deployed towards a planar configuration. Computational simulation of flat-foldable origami structures has been explored by Mitani [311, 312]. In the framework provided by Mitani, the fold pattern is interactively designed by the user and the final flat-folded configuration and stacking order of the faces is the output. One limitation of such a framework is that it does not provide intermediate configurations between the reference configuration and the determined flat-folded configurations.

Flat-foldability highly limits the shapes that can be obtained using origami. Consequently, multiple researchers have developed origami models for which flat foldability constraints are not imposed. For example, Belcastro and Hull [121, 276] presented a model for origami derived by representing the deformation associated with folding

a crease using affine transformations. Their model provides constraints on the fold angles allowing for valid configurations as well as mappings between unfolded and folded configurations. Tachi developed the *Rigid Origami Simulator* [265, 313] for the simulation of origami that also considered a set of constraints on the fold angles analogous to those presented in [121, 276]. Using a similar approach, Tachi also developed *Freeform Origami* [314] for the simulation and design of freeform origami structures represented as triangulated meshes [315]. Also utilizing a kinematic model based on affine transformations, Ida and coworkers developed a software for interactive origami simulation called *Eos* [267, 316, 317, 318]. Such a software allows for visualization and interactive manipulation of origami structures.

Alternatively, structural truss representations [319, 320, 321] have been used for kinematic modeling of origami wherein the faces of the sheet are triangulated, each fold and boundary edge end-point is represented by a truss joint, and each fold and boundary edge is represented by a truss member. The configurations for which the displacements of the truss joints do not cause elongations of the truss members represent valid configurations. Such configurations are determined through the null space of the truss compatibility matrix [322] (i.e. those sets of truss joint displacements for which the truss member elongations are zero). Additional constraints that allow the triangulated faces to remain planar are also considered for these models.

As previously mentioned, the majority of origami modeling approaches to date are based on the assumption of creased folds (see Figure 1.8(a) for an example) that are straight line segments in the sheet that, upon folding deformation, the sheet has zeroth-order geometric continuity (G^0) at such line segments (i.e. the sheet tangent plane may be discontinuous at these folds). Curved creased folds are also feasible in origami (see [323, 324, 325, 326, 327, 328, 329, 330]); nevertheless, the focus of this work is on origami structures for which curved folds are not allowed because their

folding deformation induces bending of the faces joined to such folds [324, 331].

The idealization of physically folded structures as sheets having creased folds has been useful in the modeling and design of several origami-inspired structures in the past [94, 95, 281, 332, 333]. However, such a simplification may not be appropriate for structures having non-negligible fold thickness or constructed from materials that do not provide sufficient strain magnitudes to generate the high curvatures required for a creased idealization. For these structures, the obtained folded regions may not be accurately represented as creases but rather as *bent* sheet regions having higher-order geometric continuity. These folded regions are termed in this work as *smooth folds*. An example of a sheet with smooth folds is shown in Figure 1.8(b). The geometry of the newly introduced smooth folds is addressed later in Section 2.2.1.

There have been past efforts to model and analyze surfaces that contain bent and creased folds. Bent and creased surfaces have been modeled using collections of developable surface subdomains [334, 335, 336, 337, 338, 339]. For instance, Hwang and Yoon modeled foldable surfaces through bending operations analogous to wrapping regions of an initially planar surface onto cylindrical and conical sections [336]. Such advancements allow for the realistic animation and rendering of combinations of creases and bent regions. However, none of the aforementioned works [334, 335, 336, 337, 338, 339] has considered constraints on the geometry and deformation of the bent folded regions that are required to preserve rigid faces as in analogous origami models, which are essential when fold intersections or holes are present in the sheet. Such constraints represent one of the main contributions of the work presented in Section 2.

Modeling the kinematics of origami structures represents the first step towards fully physical modeling and design of such structures. Previous efforts for modeling the structural mechanics of origami bodies are reviewed in the following section.

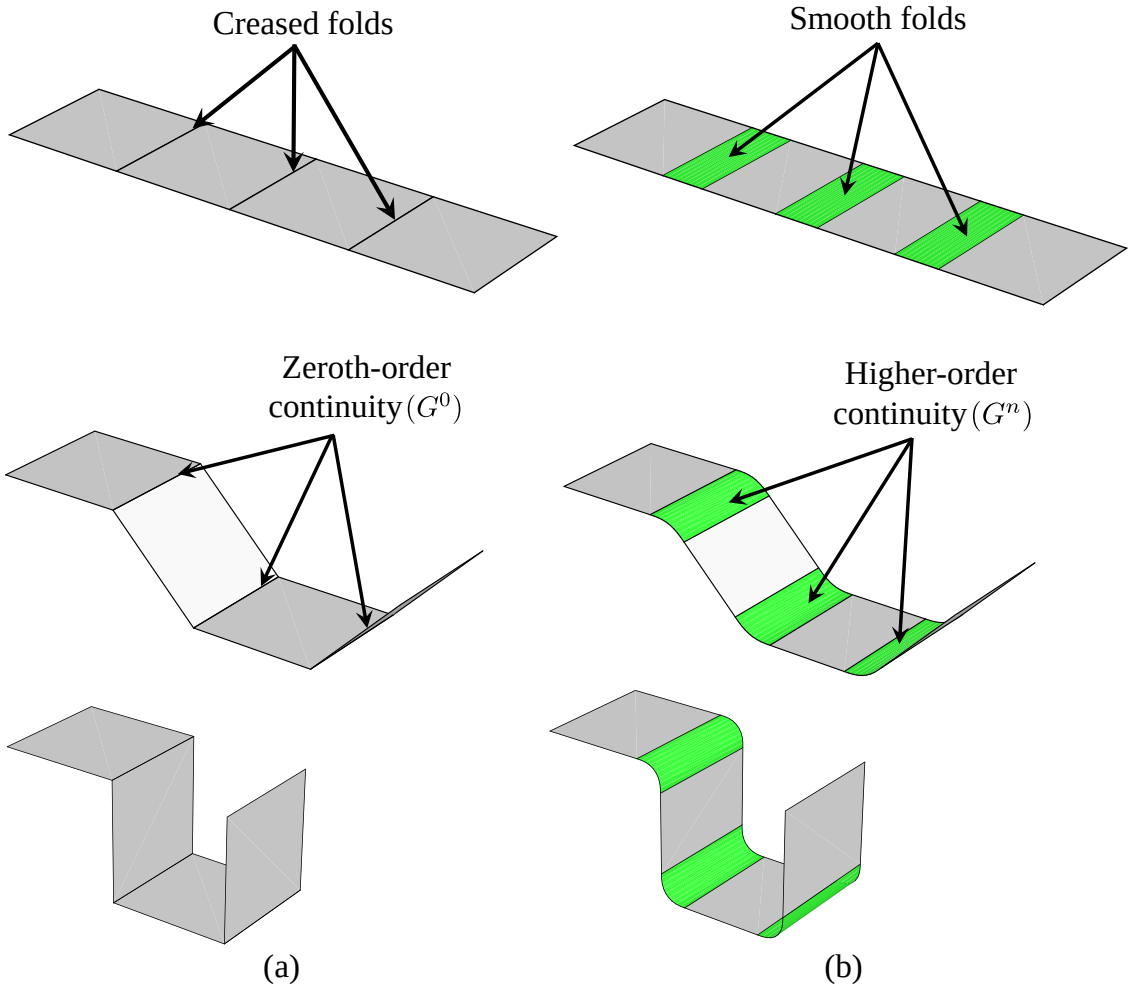

Figure 1.8: (a) A conventional origami sheet having creased folds of zeroth-order geometric continuity (G^0). (b) A sheet having *smooth folds* of non-zero surface area and higher-order geometric continuity (G^n). This figure is adapted from Figure 1 of [7]. Copyright © 2016 by ASME. Reproduced with permission.

1.4 Structural Mechanics of Origami Bodies

Modeling the structural mechanics of origami bodies is of special interest in the engineering community. It allows for the simulation and design of origami structures taking into account the constitutive behavior of their comprising materials and the influence of the external environment on the resulting folding response. Furthermore, such a modeling is needed the development of origami-based applications ranging from those of structures comprised of passive materials [85, 96, 340, 341, 342, 343, 344, 345] to the more complex structures having active material actuation (reviewed in Section 1.2).

Schenk and Guest [319] proposed a model for origami structures with elastic creased folds based on structural truss representations where each fold or boundary edge end-point is represented by a truss joint, and each fold and boundary edge is represented by a truss member. Their model introduces torsional spring behavior for the creased folds to represent their resistance against folding deformation. Qiu and coworkers adopted such a modeling approach for the analysis of origami carton-type packages [346, 347]. They numerically explored issues of origami-based packaging and their model was validated against experimental data. A structural truss approach was also utilized to simulate the behavior of tessellated origami structures [321] and structures having fold patterns inspired by tree leaves [348]. Tachi also used a structural truss model to simulate the elastic behavior of sheets with creased folds by also idealizing the folds as torsional springs and solving equations of mechanical equilibrium under constraints assuring that no fold line or boundary edge is elongated [349]. Nevertheless, representing folds as creases having torsional spring behavior may not be suitable for structures of significant fold thickness or comprised of materials that do not exhibit large enough strains to approximate creases (e.g. metal or active

material-based sheets). In these cases, the folds are properly modeled using plate or shell representations.

Wheeler and Culpepper [350] recently studied origami structures where the elastic behavior of bent folds is modeled using Euler-Bernoulli beam theory [351]. Their work provides a way to assess the failure criteria of such folds, including both failure stress and buckling criteria. However, in their work the folds are represented as beams having uniform curvature and comprised of homogeneous linear elastic materials, which limits the spectrum of origami structures for which the model can be utilized.

Existing finite element analysis (FEA) modeling approaches [352, 353] can be used directly or be extended for high-fidelity simulation of origami structures. There are various advantages provided by FEA approaches such as the capability of modeling structures having arbitrary geometry, materials, and boundary conditions. Structural finite elements developed on the basis of plate and shell theories [354, 355, 356] provide a strong option for modeling origami structures which in general have surface-like geometry. Furthermore, available FEA software packages readily allow for multi-physical simulation which is needed when considering active self-folding structures that have couplings among various physical fields (refer to Section 1.1.2).

Origami structures composed of passive materials exhibiting elastic and elasto-plastic behavior have been previously studied using FEA. Examples include boxes [82, 83, 357] and beams [343, 345, 358, 359] with pre-engineered fold patterns for energy absorption in transportation systems, and foldcore composites for applications in the aerospace field [342, 360].

Finite element analysis has also been used as the modeling approach for self-folding origami structures comprised of diverse active materials. For example, the folding response of SMA-elastomer composite sheets has been explored using both continuum finite elements [8, 361] and shell structural elements [362]. A simulation

example of such a work is provided in Figure 1.9. Ahmed and coworkers performed multi-physics simulation of origami structures actuated using dielectric elastomers and MAEs [130]. The aforementioned examples demonstrate the capabilities of FEA approaches to provide high-fidelity simulation of active origami structures considering couplings among various physical fields (mechanical-thermal in [8, 361] and mechanical-electrical-magnetic in [130]).

Although FEA approaches provide significant advantages as previously stated, they also have drawbacks when applied to the modeling of origami structures. First, the mathematical insights provided in the classical approaches of origami (e.g. geometric constructions [270]) are lost in the complexity and generality of FEA. The kinematic variables associated with FEA models (e.g. displacements and/or virtual rotations at nodes in displacement-driven FEA) are not generally compatible with those of conventional origami (e.g. fold angles). Moreover, FEA is generally not computationally efficient which could make it a non-feasible option for modeling origami structures having high complexity in terms of number of folds and folding sequence.

1.5 Design of Origami Structures

To realize a useful origami structure, designers must consider several issues beyond the choice of fold concept (Section 1.1.1) and material (Sections 1.1.2 and 1.1.3). The motivation for a design problem is to fulfill one or more desired functions. For example, designers might achieve a storage/deployment functionality for satellite solar panels using an origami structure. Important considerations are to determine what is the final folded shape (or shapes, in the case of a reconfigurable structure), to identify a fold pattern that can achieve the desired shape(s), and a folding sequence that results in the desired shape(s). Designers must achieve all of this subject to material failure constraints, system-level failure criteria, and requirements for inter-

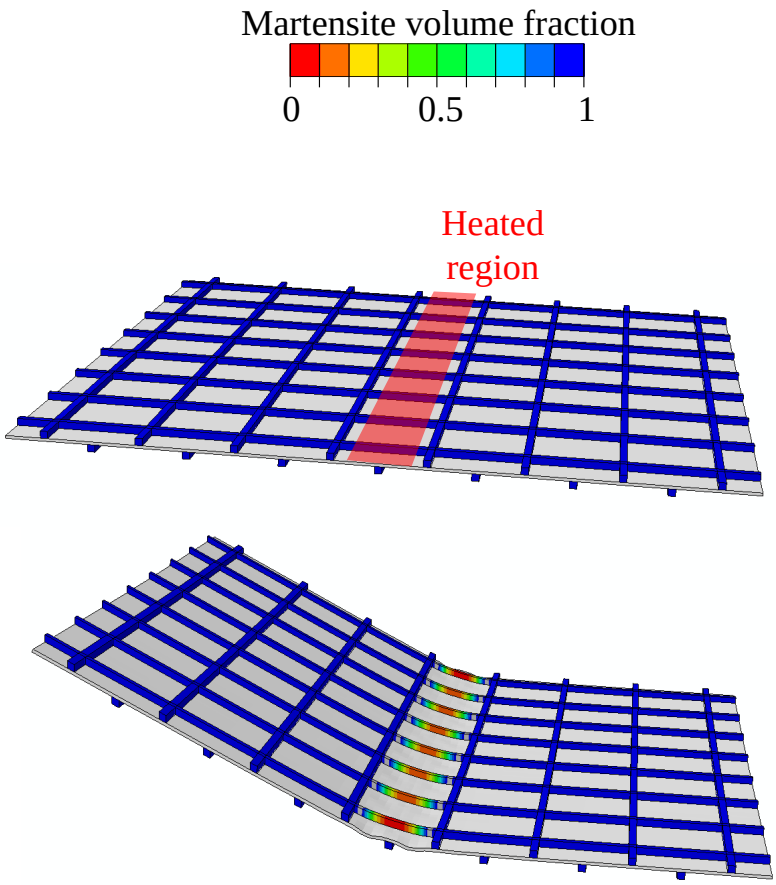

Figure 1.9: Finite element analysis of an SMA mesh-elastomer laminated composite sheet [8]. The sheet is folded through localized SMA transformation. The contour shows martensite volume fraction (0: 100% austenite, 1: 100% martensite).

facing the structure with other parts of the system (e.g. mating points). A summary of such a general design problem is provided in Table 1.6.

Designers need methodologies and tools tailored to each part of the design problem of origami structures (Table 1.6). The previous sections of this section have focused primarily on domain knowledge about single fold concepts and the various active materials available for achieving self-folding behavior. Existing computer-aided design (CAD) and FEA tools can be used directly or be extended for use in

Table 1.6: High-level definition of the general design problem for origami structures.

Given	Desired design functionality
Find	1. Folded shape(s) that achieve desired functionality 2. Sheet geometry and fold pattern that can produce such shape(s) 3. Folding sequence in which to execute folds 4. Appropriate fold concept(s) (Section 1.1.1) and detailed geometry 5. Appropriate material(s) including passive materials and active material(s) if self-folding capabilities are required (Sections 1.1.2 and 1.1.3)
Subject to	Failure criteria and interface requirements

the analysis and design of single active or passive folds. However, the challenges of identifying fold patterns and folding sequences require unique tools and methods. A review of the prior work on origami design methods in support of these design activities is provided in this section.

Creating an origami structure having desired characteristics, particularly a desired shape, is known as *origami design* [9]. Origami design is a challenge encountered not only by origami artists but also by designers and engineers who apply origami in various fields. Before obtaining extensive interest from the mathematics, science, and engineering communities, most origami design was performed through trial and error or other heuristic approaches based on the intuition of an artist or designer [363]. With the increase in complexity of origami shapes that provide engineering utility, theoretical and computational approaches for origami design have become essential for developments in this area of study [3, 13, 363]. As in most kinematic models for origami structures, current methods for origami design generally consider rigid faces and creased folds [20, 266]. Although many origami design methods have such

limitations, they provide useful start-points for addressing the design of more general origami structures.

Origami design has been studied in the past and it remains an active research subject [20, 266, 364]. One of the most well-known approaches for origami design is the *tree method* [363, 365, 366, 367]. This method has been implemented in a software package named TreeMaker [368]. The tree method generates a pattern of creased folds on a squared sheet that allows for the folding of the sheet into a *base*, a folded shape whose projection to a plane is the tree line graph of the goal shape. This planar tree line graph may have arbitrary edge lengths and topology. After the base is folded, it is left to the designer to execute additional folds in order to closely approximate the goal shape.

Demaine and coworkers proposed an origami design method for goal shapes represented as polygons or three-dimensional polyhedral surfaces [13, 369]. The approach is based on folding a sheet into a thin strip and then *wrapping* the strip around the goal shape using creased folds. Various algorithms for wrapping the goal shape were proposed [370]; these include one that uses any sheet area arbitrarily close to the goal shape surface area and another that maximizes the width of the strip subject to certain constraints.

A method for determining the geometry and pattern of creased folds associated with a planar sheet that can fold towards a goal polyhedral surface is termed as *unfolding polyhedra* [13, 371, 372, 373]. The objective in this method is to determine an *unfolding* of the goal polyhedral surface [13]. An unfolding is defined as the flattening of the goal polyhedral surface to a plane such that the surface becomes a planar polygon having boundary segments that correspond to cuts made on the polyhedral surface [13]. Generally, the unfolding must be a single simply connected polygon having no overlaps and the cuts must correspond to edges of the goal

polyhedral surface. A drawback of this approach is that it has been demonstrated that there are non-convex polyhedra which do not have unfoldings with the aforementioned characteristics [13]. It also remains an open question as to whether the method of unfolding polyhedra works for any goal convex polyhedral surface [13]. There is ongoing research on more general unfoldings comprised of multiple disconnected polygons or having cuts not limited to the edges of the goal polyhedral surface [13, 374, 375, 376, 377].

With several examples in nature of origami-like processes [378, 379, 380, 381, 382, 383, 384, 385], bioinspiration has also provided ideas for origami design methods [386]. For instance, De Focatiis and Guest [387] presented a fold pattern design approach for deployable structures inspired by a model of deploying tree leaves. They investigated the effects of combining several corrugated leaf patterns to produce deployable structures such as solar sails, solar panels, and antennas. Nature-inspired approaches for fold pattern design have also been proposed by Li and McAdams [388, 389, 390] where multiple analogies between origami and nature processes are utilized.

The currently available computational method for origami design applicable to the widest range of goal shapes was introduced by Tachi in [9, 391]. In such work, Tachi presented a method for obtaining a pattern of creased folds in a convex planar sheet that folds into an arbitrary three-dimensional goal shape represented as a polygonal mesh [9, 391] (see Figure 1.10). The method is based on the introduction of regions having two rigid faces and three creased folds placed between any two faces of the polygonal mesh connected by an interior edge. The creased folds are used to tuck fold such introduced regions to form the three-dimensional polygonal mesh starting from a planar configuration [391]. This method is shown to successfully work on goal polygonal meshes (convex and non-convex) of various complexities in

terms of number of faces and non-regular connectivity. It is noted that a process for determining a folding sequence allowing for folding motion from the determined planar sheet to the goal polygonal mesh was not addressed in [9, 391].

Although the preceding design methods for origami structures and other more recent ones (see [20, 392, 393, 389, 394, 395, 396, 397]) allow for the design of fold patterns for goal shapes of various complexities, everyone assumes that the sheet only contains creased folds. Such a simplification may not be appropriate for structures having non-negligible thickness or constructed from materials that do not provide sufficient strain magnitudes for a creased idealization (e.g. metals, glassy polymers, active materials).

There are a number of works addressing the design of origami structures considering faces of non-zero thickness but still assuming creased folds [398]. For example, Tachi proposed a method for designing three-dimensional origami structures comprised of non-zero thickness faces connected to one another by creased folds [281, 399]. Zirbel and coworkers [400, 401, 402] addressed the accommodation of thickness in origami-based deployable arrays, motivated by the need to fold thick panels that cannot bend during stowing or deployment (e.g. solar panels comprised of brittle materials). In their work, they propose a method for the modification of fold patterns originally intended for zero-thickness origami structures to accommodate thick faces in the context of a deployable space structure. They demonstrate the applicability of their model using a $1/20^{\text{th}}$ scale prototype of a deployable solar array for space applications. In another work, Ku and Demaine presented an algorithm to transform certain flat-foldable fold patterns that assume zero-thickness faces into fold patterns with similar folded configurations but considering non-zero thickness faces [403, 404]. Requirements on the input flat-foldable fold pattern for the algorithm to generate a pattern for thick faces are provided in their work.

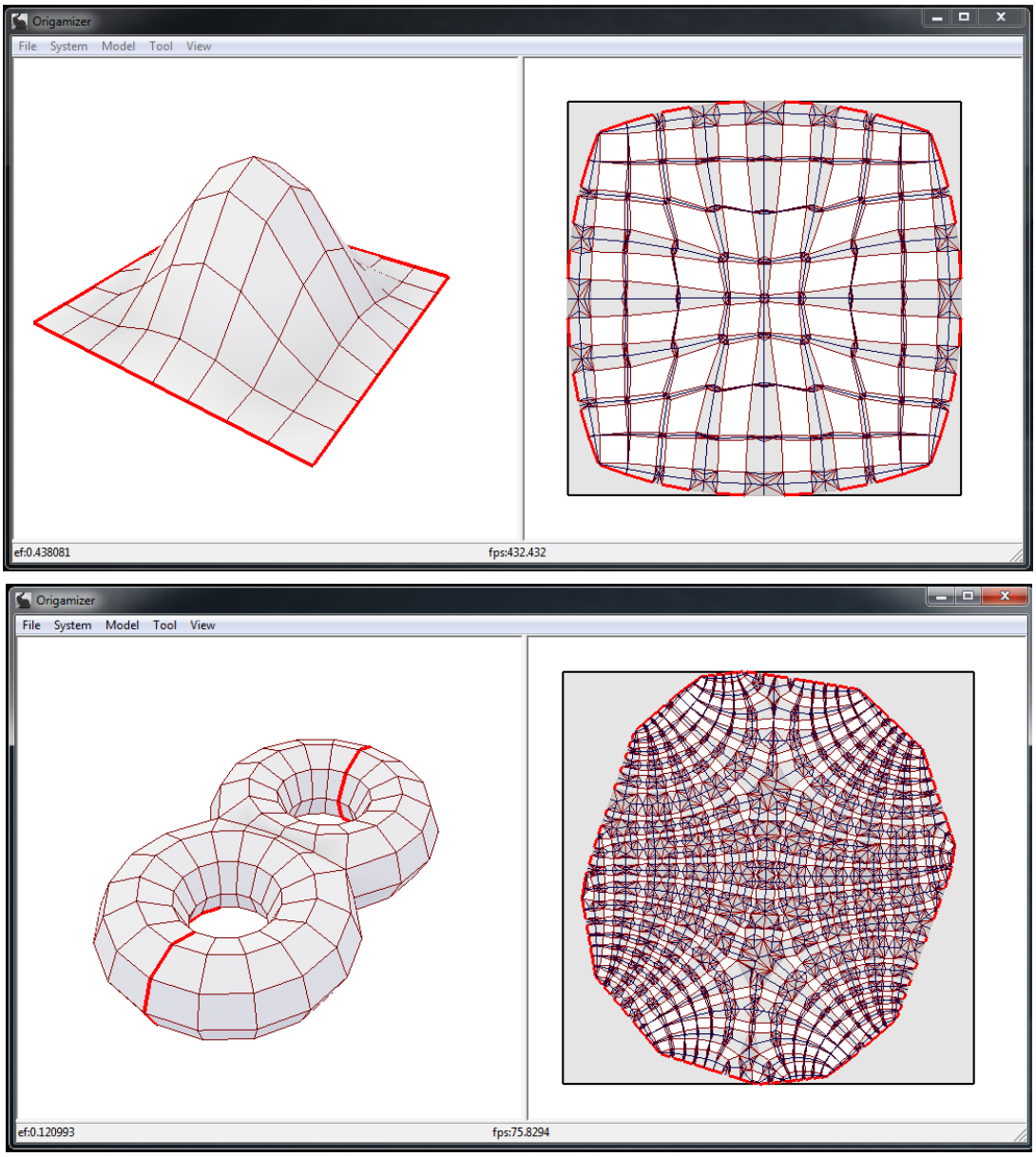

Figure 1.10: Screenshots of the graphical user interface of Origamizer showing patterns of creased folds generated for two different goal shapes (left: goal shape, right: planar sheet with fold pattern). The Origamizer [9] software by Tomohiro Tachi was obtained from `http://www.tsg.ne.jp/TT/software/`.

Akleman and coworkers [169] proposed an extension of the previously described unfolding polyhedra approach for the consideration of smooth folds (see Figure 1.8(b)). The main contribution of such a work is the process for in-surface thickening of the folds, which are creased line folds in conventional unfolding polyhedra, to smooth folds having non-zero surface area. An algorithm to subdivide each obtained unfolding into smaller quadrilaterals and triangles to generate a finite element mesh that allows for high-fidelity analysis of the folding (or self-folding) process was also presented. The feasibility of such an origami design method was tested through simulation of the SMA actuation-driven self-folding behavior of the generated unfoldings towards their associated polyhedral goal shapes [169].

1.6 Motivation and Research Objectives

After reviewing the existing and prospective applications origami structures (with and without self-folding capabilities) in Sections 1.1 and 1.2, it is clear that origami has the potential to enable new advancements in various fields such as aerospace, manufacturing, robotics, architecture, etc. To allow or facilitate such advancements, modeling and design approaches for origami structures are needed and thus there is ongoing research on the subject. From the literature review on modeling and design of origami structures presented in Sections 1.3–1.5, it is evident that there is a gap between realistic folding behavior and existing models and design methods that mostly focus on conventional origami with creased folds (refer to Figure 1.8(a)). Therefore, new approaches for origami modeling and design are needed.

The work presented in this dissertation aims to create new models and design methods for origami structures inspired from those established but allowing for the consideration of realistic smooth folds. The first objective is to develop a kinematic model for realistic folding response while retaining the important features that enrich

conventional origami. To achieve this objective, the concept of *origami structures with smooth folds* is introduced. In this concept, the folds are not limited to G^0 creases but instead may have non-zero surface area and an arbitrary order of geometric continuity G^n as in the example shown in Figure 1.8(b) (hence named *smooth folds*). By considering G^n continuity at the folds, the realistic response of origami structures based on the bending concepts (Figures 1.4(d) and (e)) can be properly captured. Important features of conventional origami with creased folds are preserved in the newly introduced concept such as having the fold angles as kinematic variables and the inclusion of rigid faces as in existing origami models.

Another objective is to develop a design method for the newly proposed origami structures with smooth folds. Specifically, a method for solving the following origami design problem is desired: given a goal shape represented as a polygonal mesh, find the geometry of a single planar sheet, its pattern of smooth folds, and a folding sequence allowing the initially planar sheet to approximate the goal mesh. To achieve this objective, one of the most general design methods for conventional origami with creased folds [9] is adapted and extended for the consideration of smooth folds. The determination of a folding sequence was not addressed in related works such as [9, 391] and therefore represents another contribution of this dissertation. It is remarked that G^0 creased folds represent a special case of the G^n smooth folds and are captured as well in the kinematic model and the design method presented in this dissertation.

A further objective is to develop a model for the structural mechanics of origami bodies with smooth folds. Such a model allows for the physics-based simulation of origami structures having folds comprised of arbitrary materials, including active materials. This objective entails the integration of the presented kinematic model for origami structures with smooth folds and existing plate theories in order to obtain a

structural representation for folds having non-zero thickness.

The last objective involves the design and analysis of active material-based self-folding structures that morph towards arbitrary three-dimensional goal shapes starting from a planar configuration. The developed kinematics, structural analysis, and design approaches for origami structures with smooth folds presented in this work are all integrated for the fulfillment of this former objective. Examples including SMA-based self-folding structures are considered although it is remarked that the developed design method and its implementation are applicable to self-folding structures actuated with other active materials.

The outline of this dissertation is presented in the following section. The work performed to accomplish the aforementioned research objectives is organized in the sections listed therein.

1.7 Outline of the Dissertation

This dissertation is organized as follows:

- A model for the kinematics of origami structures with smooth folds is presented in Section 2. The section begins with a summary of the model for conventional origami with creased folds that is adopted and extended herein for the consideration of smooth folds. Subsequently, the description of the proposed model for the kinematics of origami structures with smooth folds is provided. The section continues with the presentation of an algorithm for the kinematic simulation of origami structures with smooth folds that is applicable to sheets having arbitrary fold patterns and subject to arbitrary folding sequences. Lastly, kinematic simulation results highlighting the capabilities of the present model and its associated numerical implementation are provided.

- In Section 3, the design of origami structures with smooth folds is addressed.

Specifically, this section presents a method for solving the following origami design problem: given a goal shape represented as a polygonal mesh (termed as the goal mesh), find the geometry of a single planar sheet, its pattern of smooth folds, and a folding sequence allowing the sheet to approximate the goal mesh. First, a description of such an origami design problem is provided. The section continues with the design parameterization of the planar sheet and the constraints that allow for a valid pattern of smooth folds and approximation of the goal shape in a known folded configuration. An algorithm to determine a folding sequence allowing for the motion between the designed planar sheet and the configuration that approximates the goal shape is then outlined. Implementation results considering goal shapes of diverse geometries are presented at the end of the section.

- In Section 4, the structural mechanics of origami bodies with smooth folds are addressed. A modeling approach for origami structures comprised of arbitrary materials is developed on the basis of the kinematics presented in Section 2. First, a structural representation based on a plate theory utilized to model smooth folds having non-zero thickness is presented. A model for the structural mechanics of origami bodies comprised of arbitrary materials is then developed using such a plate representation. Numerical validation results for such a model against FEA are provided. The design method presented in Section 3 is then revisited and extended for the design of active self-folding structures that morph towards arbitrary three-dimensional goal shapes via simultaneous folding starting from a planar reference configuration.

- Finally, summarizing remarks and suggestions for future work are provided in Section 5.

2. KINEMATICS OF ORIGAMI STRUCTURES WITH SMOOTH FOLDS

[1]Origami provides novel approaches to the fabrication, assembly, and functionality of various structures and devices as reviewed in Section 1. Kinematic modeling of origami-based objects is essential to their analysis and design. A review of available kinematic models for origami structures is presented in Section 1.3. As stated in Section 1.3, two main assumptions have been made in the development of mathematical models for the kinematics of origami structures to date [121, 265, 266, 276, 277, 278, 279, 280]: that folds are straight creases having G^0 continuity (termed as *creased folds*, refer to Figure 1.8(a) for an example), and that planar faces bounded by the folds and the sheet boundary are rigid (i.e. these faces are neither bent nor stretched, refer to Figure 1.3). However, these previous models are not intended for structures having non-negligible fold thickness or maximum curvature at the folds restricted by material or structural limitations. Thus, for general structures, creased folds of merely zeroth-order geometric continuity are not appropriate idealizations of structural response and a new approach is needed.

In the model for origami kinematics presented in this section, the previously mentioned assumption of rigid faces is maintained while the assumption of creased folds is replaced by the introduction of *smooth folds*. Smooth folds have non-zero surface area and exhibit higher-order geometric continuity G^n (refer to Figure 1.8(b) for an example). The geometry of smooth folds and the constraints on their associated shape variables are presented. It is noted that the proposed model for origami with smooth folds includes origami with creased folds as a special case, hence being more

[1]Portions of this section are reprinted or adapted from [7] E. A. Peraza Hernandez, D. J. Hartl, and D. C. Lagoudas. Kinematics of origami structures with smooth folds. Journal of Mechanisms and Robotics, 8(6):061019, 2016. Copyright © 2016 by ASME. Reproduced with permission. http://dx.doi.org/10.1115/1.4034299

general. Important features of conventional origami with creased folds are preserved in the newly introduced origami with smooth folds including having the fold angles as kinematic variables. A numerical implementation of the model allowing for kinematic simulation of sheets having arbitrary fold patterns and subject to arbitrary folding sequences is also described. Simulation results are provided showing the capability of the model to capture realistic kinematic response of origami sheets with diverse fold patterns.

The outline of this section is as follows: Basic concepts of origami and a review of the model for origami with creased folds extended in this work are presented in Section 2.1. Section 2.2 presents the newly proposed model for origami with smooth folds. It includes the geometric description of smooth folds and the fold pattern, constraints required for valid configurations, and the numerical implementation of the model allowing for kinematic simulation of sheets having arbitrary patterns of smooth folds. Section 2.3 presents simulation results of sheets having diverse fold patterns that demonstrate the model capabilities and the resulting realistic kinematic structural response captured by the model. Finally, a summarizing discussion of the section is provided in Section 2.4.

2.1 Concepts and Review of Origami with Creased Folds

Various concepts of origami and a review of a model for origami with creased folds are presented in this section for the purposes of developing the novel extensions proposed in this section.

The modeling approach for origami adopted and extended herein is largely based on the one presented by Belcastro and Hull in [121, 276]. Firstly, the studied continuum body termed as the *sheet* and the shape variables associated with the creased folds in the sheet (e.g. *fold angles*) are defined. The layout of the folds in the sheet

(i.e. the *fold pattern*) is then determined by *vertices* (start-points and end-points of the line segments coincident with the creased folds in a planar reference configuration) and their connectivity. After the geometric parameters of the fold pattern are defined, *constraints* on the fold shape variables required for valid configurations are described. The configurations that satisfy the stated constraints comprise the constrained configuration space. *Continuous motion* of the sheet is achieved by continuously altering the fold shape variables such that any attained configuration is contained in the constrained configuration space.

In the present kinematic modeling approach, the required fold pattern data (e.g. vertex coordinates and fold connectivity) are provided as inputs. Methods for the design of fold patterns for specific applications are provided in [9, 13, 20, 205, 333, 362, 363, 369, 392, 405]. Additional information on the design of origami structures and a proposed design method for origami with smooth folds are presented in Section 3.

The simulation of the continuous motion of the sheet is performed sequentially by updating the values of the fold shape variables using input guess increments and subsequently apply corrections such that the resulting set of fold shape variables satisfies the proposed constraints. In this section, input guess increments for the fold shape variables are arbitrary and not obtained through any specific method. The determination of folding sequences for designed origami structures with smooth folds is addressed in Section 3 (refer to Section 3.6). Motion planning in origami for various other applications is also being addressed by multiple researchers and the reader is referred to [406, 407, 408, 409, 410] for such works.

To begin, the various concepts of origami previously introduced in Section 1.1 must be formalized. The considered continuum body termed as the *sheet* is a three-dimensional, orientable, path-connected surface with boundary. A detailed description of a sheet for origami with creased folds is provided in [13]. For origami with

creased folds, the sheet is divided into various *faces* that are connected by straight edges corresponding to the *creased folds*. Each face comprising the sheet has the same aforementioned characteristics of the sheet (i.e. they are three-dimensional, orientable, path-connected surfaces with boundary).

The orthonormal vectors $\mathbf{e}_i \in \mathbb{R}^3$, $i = 1, 2, 3$, with $\mathbf{e}_3 := \mathbf{e}_1 \times \mathbf{e}_2$ form the basis $\{\mathbf{e}_1, \mathbf{e}_2, \mathbf{e}_3\}$ that defines the fixed global coordinate system. The *reference configuration* of the sheet, denoted $\mathcal{S}_0$, is defined such that it is contained in the plane spanned by $\mathbf{e}_1$ and $\mathbf{e}_2$ with its faces not overlapping each other, except at their shared boundary edges. Although several applications that utilize origami concepts do not consider an initially planar, non-overlapping configuration (e.g. [56, 95, 110]), the reference configuration $\mathcal{S}_0$ has such characteristics in this work to agree with conventional origami modeling approaches [121, 276] and for the sake of simplicity. The configuration of the faces comprising $\mathcal{S}_0$ is denoted $\mathcal{P}_0^i \subset \mathcal{S}_0,\ i = 1, \ldots, N_\mathcal{P}$, where $N_\mathcal{P}$ is the number of faces in the sheet (i.e. $\mathcal{S}_0 = \bigcup_{i=1}^{N_\mathcal{P}} \mathcal{P}_0^i$). The side of $\mathcal{S}_0$ with normal $\mathbf{e}_3$ is selected as the *positive side* of the sheet. An example of a sheet in its reference configuration $\mathcal{S}_0$ is provided in Figure 2.1(a).

A *current configuration* of the sheet is denoted $\mathcal{S}_t$ where the time parameter t indicates the history of deformation from the reference configuration ($t = 0$) to a current configuration ($t > 0$). Examples of a sheet in the reference configuration and a current configuration are presented in Figures 2.1(a) and 2.1(b), respectively. The configuration of the faces comprising $\mathcal{S}_t$ is denoted $\mathcal{P}_t^i \subset \mathcal{S}_t,\ i = 1, \ldots, N_\mathcal{P}$, i.e. $\mathcal{S}_t = \bigcup_{i=1}^{N_\mathcal{P}} \mathcal{P}_t^i$. The taken assumption of rigid faces imposes the following constraints for the configurations $\mathcal{S}_t$ [121, 276]:

Definition 2.1. Valid configuration: *A* valid *current configuration $\mathcal{S}_t$ has the following characteristics: (i) The faces undergo only rigid deformations (i.e. they*

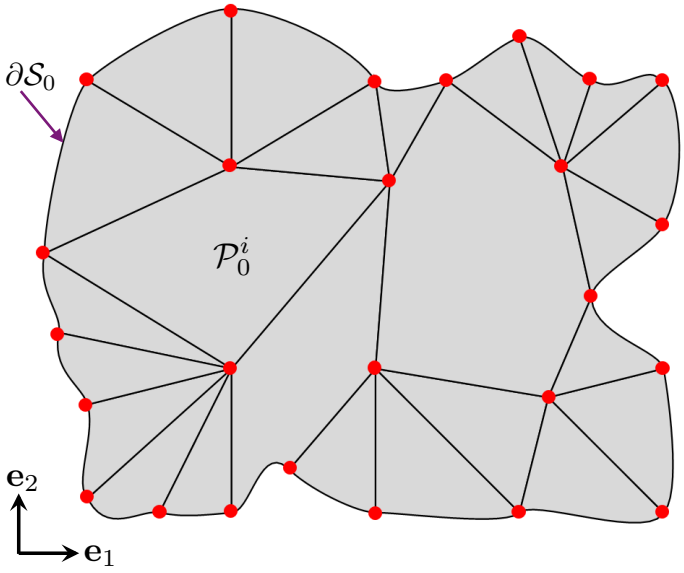

(a) Reference configuration $\mathcal{S}_0$

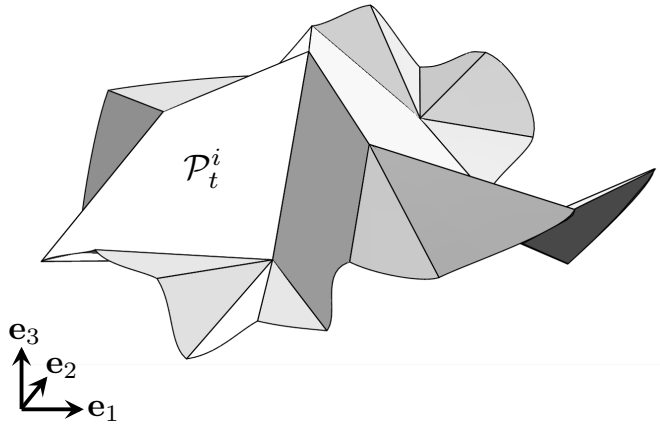

(b) Current configuration $\mathcal{S}_t$

Figure 2.1: Sheet with creased folds in its reference configuration $\mathcal{S}_0$ and a current configuration $\mathcal{S}_t$. The planar faces comprising the sheet undergo only rigid deformations.

are neither stretched nor bent), (ii) the sheet is not torn (initially joined faces remain joined) and (iii) the sheet does not self-intersect.

The only non-rigid body deformations of the sheet are thus achieved by rotating adjacent faces relative to one another along their connecting creased fold in such a manner that the sheet only attains valid configurations during such deformations. Therefore, the sheet has G^0 continuity at the creased folds.

The configuration of the sheet is fully described by the set of the *shape variables* associated with the creased folds. The only shape variable associated with a creased fold describes the relative rotation between the two faces joined by such a fold and is denoted as *fold angle*:

Definition 2.2. Fold angle: *The* fold angle $\hat{\theta}_i(t)$ *is defined as* π *radians minus the dihedral angle between the positive sides of the two faces joined by the* i^{th} *creased fold.*

Schematics showing the concept of fold angle are provided in Figure 2.2. It is noted in the previous definition that each fold angle is a function of the time parameter t. Specifically, each fold angle $\hat{\theta}_i(t)$, $i = 1, \ldots, N_{\mathcal{F}}$ (where $N_{\mathcal{F}}$ is the number of creased folds in the sheet) is a *continuous* function with respect to t since the motion of the sheet must be continuous (see [13]). For the rest of this section, the dependence of $\hat{\theta}_i$ on t is taken as implicit to simplify the notation.

To preclude self-intersection of any pair of faces joined by a creased fold, the value of the associated fold angle must be contained in the interval $[-\pi, \pi]$. The vector $\hat{\boldsymbol{\theta}} \in \mathbb{R}^{N_{\mathcal{F}}}$ is constructed by collecting the fold angles as follows:

$$\hat{\boldsymbol{\theta}} = \begin{bmatrix} \hat{\theta}_1 \\ \vdots \\ \hat{\theta}_{N_{\mathcal{F}}} \end{bmatrix}. \tag{2.1}$$

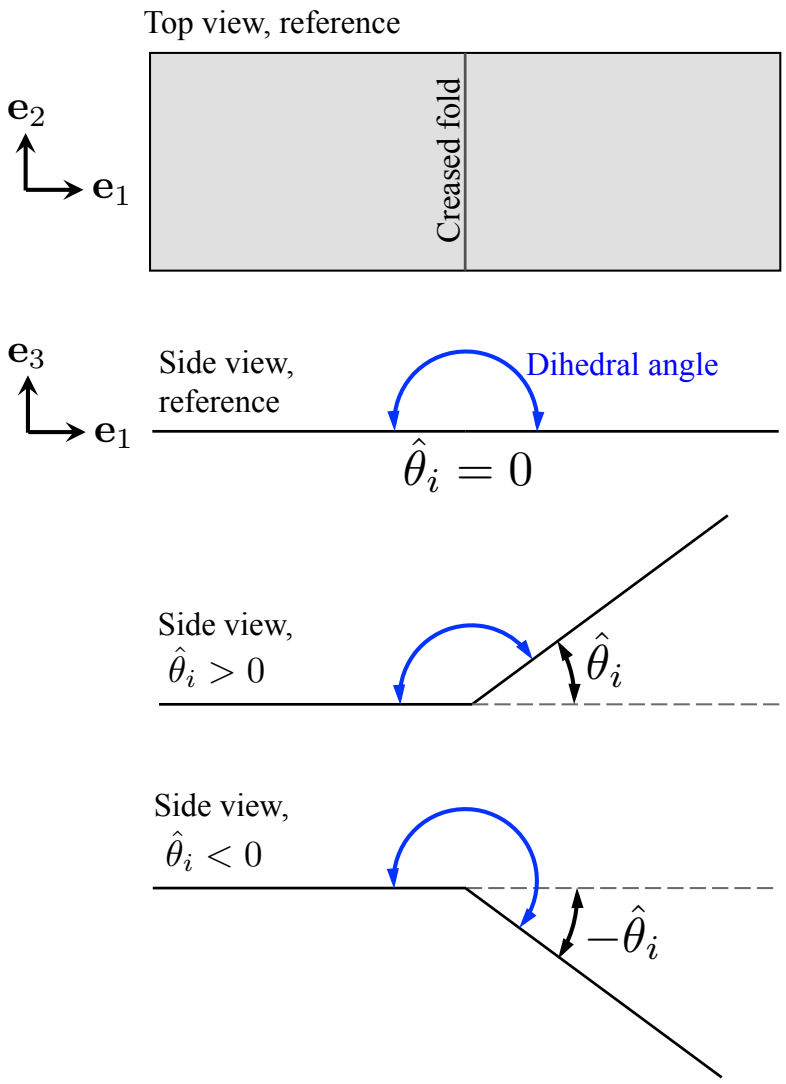

Figure 2.2: Schematics showing unfolded and folded configurations of a creased fold.

2.1.1 Fold Pattern

The location of the creased folds in $\mathcal{S}_0$ is provided in a *fold pattern*, often referred to as *crease pattern* in this context of origami with creased folds [13, 121, 276]. To describe the fold pattern, the *vertices* are introduced:

Definition 2.3. Vertices: *The* vertices *are the start-points and end-points of the line segments coincident with the creased folds in* $\mathcal{S}_0$*. Each vertex has an associated position vector denoted* $\mathbf{v}^j \in \text{span}(\mathbf{e}_1, \mathbf{e}_2)$.

The number of vertices located at the interior of $\mathcal{S}_0$ is denoted $N_{\mathcal{I}}$ and the number of vertices located at $\partial\mathcal{S}_0$ (the boundary of $\mathcal{S}_0$, see Figure 2.1(a)) is denoted $N_{\mathcal{B}}$. The vertices are enumerated starting from those located at the interior of $\mathcal{S}_0$ (with corresponding position vectors $\mathbf{v}^1, \ldots, \mathbf{v}^{N_{\mathcal{I}}}$) followed by those located at $\partial\mathcal{S}_0$ (with corresponding position vectors $\mathbf{v}^{N_{\mathcal{I}}+1}, \ldots, \mathbf{v}^{N_{\mathcal{I}}+N_{\mathcal{B}}}$). The vector $\mathbf{V} \in \mathbb{R}^{3(N_{\mathcal{I}}+N_{\mathcal{B}})}$ is formed by concatenating the vertex position vectors $\mathbf{v}^j$, $j = 1, \ldots, N_{\mathcal{I}} + N_{\mathcal{B}}$, as follows:

$$\mathbf{V} = \begin{bmatrix} \mathbf{v}^1 \\ \vdots \\ \mathbf{v}^{N_{\mathcal{I}}+N_{\mathcal{B}}} \end{bmatrix}. \tag{2.2}$$

The line segment coincident with a creased fold in $\mathcal{S}_0$, simply denoted as *fold line*, is defined by its start-point and end-point (both points corresponding to vertices by Definition 2.3). As such, to define the fold lines in $\mathcal{S}_0$, the matrix $\widehat{\mathbf{C}} \in$

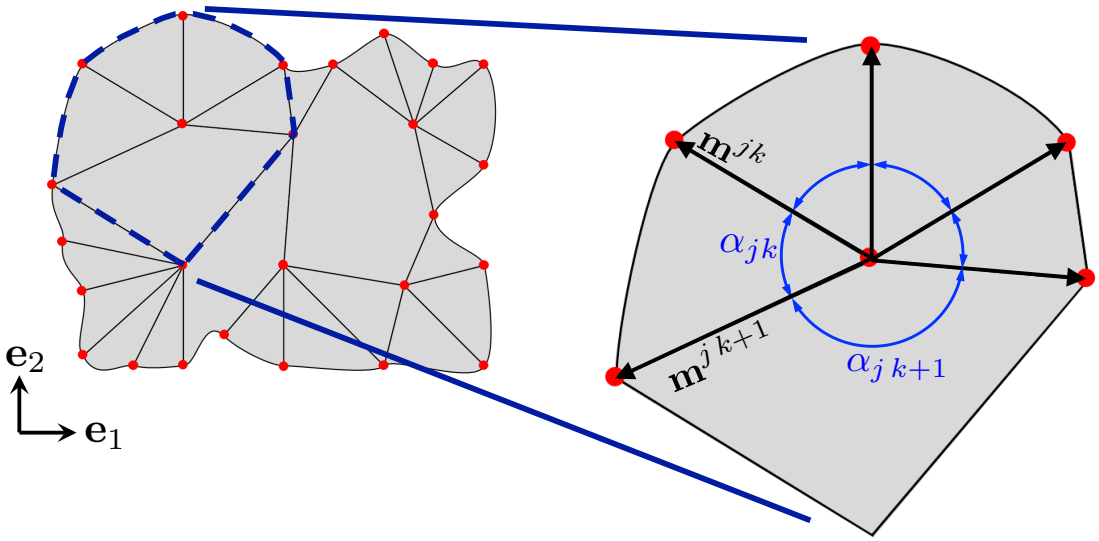

Figure 2.3: Schematic showing faces and folds connected to an interior vertex and their associated geometric parameters.

$\{-1, 0, 1\}^{N_{\mathcal{F}} \times (N_{\mathcal{I}} + N_{\mathcal{B}})}$ with elements $\widehat{C}_{ij}$ is introduced:

$$\widehat{C}_{ij} = \begin{cases} -1; & \mathbf{v}^j \text{ is the position of the } i^{\text{th}} \text{ fold line } \textit{start-point} \\ 1; & \mathbf{v}^j \text{ is the position of the } i^{\text{th}} \text{ fold line } \textit{end-point} \\ 0; & \text{otherwise, i.e. } \mathbf{v}^j \text{ is not connected to the } i^{\text{th}} \text{ fold line} \end{cases} . \tag{2.3}$$

Let n_j, $j = 1, \ldots, N_{\mathcal{I}}$, be the number of fold lines incident to each interior vertex (i.e. those vertices located at the interior of $\mathcal{S}_0$). Also let $\mathbf{m}^{jk} \in \text{span}(\mathbf{e}_1, \mathbf{e}_2)$, $j = 1, \ldots, N_{\mathcal{I}}$, $k = 1, \ldots, n_j$, be the vector along the length of the k^{th} fold line incident to the j^{th} interior vertex that emanates from such a vertex (see Figure 2.3).

Definition 2.4. *The angle between the vector* $\mathbf{y} \in \text{span}(\mathbf{e}_1, \mathbf{e}_2)$ *and* $\mathbf{e}_1$ *that starts at* $\mathbf{e}_1$ *and is measured in the counterclockwise direction, is denoted* $\varphi(\mathbf{y}) : \text{span}(\mathbf{e}_1, \mathbf{e}_2) \to$

$[0, 2\pi)$ *and is determined as follows*[2]*:*

$$\varphi(\mathbf{y}) := \begin{cases} \cos^{-1}\left(\dfrac{\mathbf{y}}{\|\mathbf{y}\|} \cdot \mathbf{e}_1\right); & \mathbf{e}_2 \cdot \mathbf{y} \geq 0 \\ \\ 2\pi - \cos^{-1}\left(\dfrac{\mathbf{y}}{\|\mathbf{y}\|} \cdot \mathbf{e}_1\right); & \mathbf{e}_2 \cdot \mathbf{y} < 0 \end{cases} . \tag{2.4}$$

For each interior vertex, its associated vectors $\mathbf{m}^{jk}$, $k = 1, \ldots, n_j$, are arranged in counterclockwise order. Let $\mathbf{M}^j \in \mathbb{R}^{3n_j}$ be the vector constructed by concatenating the vectors $\mathbf{m}^{jk}$, $k = 1, \ldots, n_j$, as follows:

$$\mathbf{M}^j = \begin{bmatrix} \mathbf{m}^{j1} \\ \vdots \\ \mathbf{m}^{jn_j} \end{bmatrix} . \tag{2.5}$$

The matrices $\mathbf{C}^j \in \{-1, 0, 1\}^{n_j \times N_{\mathcal{F}}}$, $j = 1, \ldots, N_{\mathcal{I}}$, with components C^j_{ki} are used for the identification and ordering of the folds incident to the j^{th} interior vertex and is defined as follows:

$$C^j_{ki} = \begin{cases} 1; & \mathbf{m}^{jk} \text{ is a vector along the } i^{\text{th}} \text{ fold line and emanates} \\ & \text{from the } i^{\text{th}} \text{ fold line start-point} \\ -1; & \mathbf{m}^{jk} \text{ is a vector along the } i^{\text{th}} \text{ fold line and emanates} \\ & \text{from the } i^{\text{th}} \text{ fold line end-point} \\ 0; & \text{otherwise} \end{cases} . \tag{2.6}$$

The mapping from the vertex position vectors $\mathbf{v}^j$, $j = 1, \ldots, N_{\mathcal{I}} + N_{\mathcal{B}}$, to the

[2] $\|\cdot\|$ denotes the 2-norm, i.e. $\|\mathbf{y}\| = (\mathbf{y} \cdot \mathbf{y})^{1/2}$.

vectors $\mathbf{m}^{jk}$, $k = 1, \ldots, n_j$, is then compactly given as follows[3]:

$$\mathbf{M}^j = \left(\left(\mathbf{C}^j \, \widehat{\mathbf{C}} \right) \otimes \mathbf{I}_3 \right) \mathbf{V}, \tag{2.7}$$

where $\mathbf{I}_n$ denotes the $\mathbb{R}^{n \times n}$ identity matrix.

The face corner angles surrounding each interior vertex are denoted as α_{jk}, $j = 1, \ldots, N_{\mathcal{I}}$, $k = 1, \ldots, n_j$, and are calculated as follows (see Figure 2.3):

$$\alpha_{jk} = \begin{cases} \varphi(\mathbf{m}^{j\,k+1}) - \varphi(\mathbf{m}^{jk}); & k = 1, \ldots, n_j - 1 \\ \\ 2\pi + \varphi(\mathbf{m}^{j1}) - \varphi(\mathbf{m}^{jk}); & k = n_j \end{cases} . \tag{2.8}$$

2.1.2 Constraints

Once the geometry of the fold pattern is defined, constraints on the fold shape variables (corresponding to the fold angles for creased folds) are formulated such that every current configuration is valid according to Definition 2.1[4]. In addition to constraints for valid configurations, *developability* [315] is also conventionally imposed in origami. Developability allows a surface to be flattened onto a plane without stretching or overlapping. A developable surface has zero Gaussian curvature everywhere [414]. Since valid configurations of the sheet consist of planar faces joined at straight creased folds, the only locations where the Gaussian curvature is non-trivially zero is at the interior fold intersections. The conventional differential geometry definition of Gaussian curvature as the product of the two principal curvatures is not valid at G^0 interior fold intersection [415] and therefore the *discrete Gaussian cur-*

[3]The matrix Kronecker product $\otimes$ is defined as [411, 412, 413]: $\mathbf{Y} \otimes \mathbf{Z} : \{\mathbb{R}^{m \times n}, \mathbb{R}^{p \times q}\} \to \mathbb{R}^{mp \times nq}$, where $[\mathbf{Y} \otimes \mathbf{Z}]_{ij \text{ block}} \in \mathbb{R}^{p \times q} = Y_{ij}\mathbf{Z}$.

[4]Self-intersection avoidance is an essential restriction in origami as stated in Definition 2.1. It remains an open problem to provide constraints on fold angles that would allow for three-dimensional folded configurations free of self-intersection [13, 276]. This restriction is not considered in this work.

vature, denoted K_j, is considered [415, 416, 417]. It is given as 2π radians less the sum of the face corner angles surrounding each interior fold intersection [418] and it must be zero for the fold intersection to be developable:

$$K_j = 2\pi - \sum_{k=1}^{n_j} \alpha_{jk} = 0 \qquad \forall\, j \in \{1, \ldots, N_{\mathcal{I}}\}. \tag{2.9}$$

In this work the angles α_{jk} are defined in $\mathcal{S}_0$, which is planar and free of face overlapping, and thus these angles clearly sum to 2π radians for each interior vertex. Therefore, the developability constraint in Equation (2.9) is satisfied in $\mathcal{S}_0$. No further consideration of this constraint is required since the face corner angles are constant during the deformation history of the sheet (since the faces undergo only rigid deformations for valid configurations) and thus they hold their associated values α_{jk} as defined in $\mathcal{S}_0$. As a consequence, developability is assured for any valid current configuration $\mathcal{S}_t$.

Non-trivial and important are the constraints on the fold angles that define the constrained configuration space. The set of constraints for $\hat{\theta}_i$, $i = 1, \ldots, N_{\mathcal{F}}$, required for a valid configuration can be formulated as a set of constraints for the fold angles associated with the folds incident to each interior vertex (assuming that the sheet has no holes) [281].

The fold angle associated with the k^{th} fold incident to the j^{th} interior vertex is denoted θ_{jk}. The vectors $\boldsymbol{\theta}^j \in \mathbb{R}^{n_j}$, $j = 1, \ldots, N_{\mathcal{I}}$, are formed by collecting the fold angles θ_{jk}, $k = 1, \ldots, n_j$, as follows:

$$\boldsymbol{\theta}^j = \begin{bmatrix} \theta_{j1} \\ \vdots \\ \theta_{jn_j} \end{bmatrix}, \tag{2.10}$$

and the mapping from the vector $\hat{\boldsymbol{\theta}}$ with elements corresponding to the fold angles of the sheet (defined in Equation (2.1)) to each vector $\boldsymbol{\theta}^j$ is given as follows:

$$\boldsymbol{\theta}^j = |\mathbf{C}^j|_* \, \hat{\boldsymbol{\theta}}, \tag{2.11}$$

where the elements of the matrix $\mathbf{C}^j$ are defined in Equation (2.6) and $|\cdot|_* : \mathbb{R}^{m \times n} \to \mathbb{R}^{m \times n}_{\geq 0}$ denotes the element-wise absolute value of a matrix where $[|\mathbf{Y}|_*]_{ij} = |Y_{ij}|$.

Let $\mathbf{R}_1(\phi) \in \mathbb{R}^{3\times 3}$ be the transformation matrix associated with a rotation by ϕ about an axis of rotation aligned to $\mathbf{e}_1$:

$$\mathbf{R}_1(\phi) := \begin{bmatrix} 1 & 0 & 0 \\ 0 & \cos(\phi) & -\sin(\phi) \\ 0 & \sin(\phi) & \cos(\phi) \end{bmatrix}, \tag{2.12}$$

and $\mathbf{R}_3(\phi) \in \mathbb{R}^{3\times 3}$ be the transformation matrix associated with a rotation by ϕ about an axis of rotation aligned to $\mathbf{e}_3$:

$$\mathbf{R}_3(\phi) := \begin{bmatrix} \cos(\phi) & -\sin(\phi) & 0 \\ \sin(\phi) & \cos(\phi) & 0 \\ 0 & 0 & 1 \end{bmatrix}. \tag{2.13}$$

The fold angles associated with the folds incident to each interior vertex θ_{jk}, $k = 1, \ldots, n_j$, must be constrained such that the closed strip of faces joined to every interior vertex remains closed upon folding deformation [121, 276]. For this purpose, the following constraint is proposed:

Proposition 2.1. *[13, 281] For the initially closed strip of faces joined to the j^{th} interior vertex to remain closed with each face undergoing a rigid deformation, the*

following constraint must hold:

$$\mathbf{R}^j := \prod_{k=1}^{n_j} \mathbf{R}_1(\theta_{jk})\mathbf{R}_3(\alpha_{jk}) = \mathbf{I}_3. \tag{2.14}$$

It is shown in Appendix C that this constraint for origami with creased folds is a special case of the constraints for origami with smooth folds to be presented in Section 2.2.3.

Corollary 2.1. *(i) If the j^{th} interior vertex has a single incident creased fold, it allows for a valid configuration if $\theta_{j1} = 0$.*

(ii) If the j^{th} interior vertex has two incident creased folds, it allows for a valid configuration if (ii,1) $\alpha_{j1} \neq \pi, \theta_{j1} = \theta_{j2} = 0$ or (ii,2) $\alpha_{j1} = \pi, \theta_{j1} = \theta_{j2}$.

(iii) If the j^{th} interior vertex has three incident creased folds, it allows for a valid configuration if (iii,1) $\alpha_{j1} \neq \pi, \alpha_{j2} \neq \pi, \alpha_{j3} \neq \pi, \theta_{j1} = \theta_{j2} = \theta_{j3} = 0$, or (iii,2) $\alpha_{j1} = \pi, \theta_{j1} = \theta_{j2}, \theta_{j3} = 0$, or (iii,3) $\alpha_{j2} = \pi, \theta_{j2} = \theta_{j3}, \theta_{j1} = 0$, or (iii,4) $\alpha_{j3} = \pi, \theta_{j3} = \theta_{j1}, \theta_{j2} = 0$.

Proof. Case (i): The matrix $\mathbf{R}^j$ associated with an interior vertex having one incident creased fold is $\mathbf{R}^j = \mathbf{R}_1(\theta_{j1})\mathbf{R}_3(\alpha_{j1})$. The angle α_{j1} is equal to 2π for a single fold incident to an interior vertex, thus $\mathbf{R}_3(\alpha_{j1}) = \mathbf{I}_3$. This requires $\mathbf{R}_1(\theta_{j1}) = \mathbf{I}_3$ which in the domain $\theta_{j1} \in [-\pi, \pi]$ holds true only when $\theta_{j1} = 0$. Cases (ii) and (iii) can be verified in a similar manner. □

Thus, for non-trivial folding motion, any interior vertex must have at least four incident creased folds. It can be shown that each face in the sheet undergoes a rigid deformation and no tearing occurs provided the constraint in Equation (2.14) is satisfied for each interior vertex of the sheet (see [121, 276, 419] for details). Therefore,

the constraints on the fold angles defining the constrained configuration space for a sheet with creased folds (excluding self-intersection avoidance) are as follows:

$$\mathbf{R}^j = \mathbf{I}_3 \qquad \forall\, j \in \{1, \ldots, N_{\mathcal{I}}\}. \tag{2.15}$$

For the sake of brevity, the formulation of the mapping from the reference configuration to a valid current configuration, constructed using the set of the shape variables of all the folds in the sheet, is not included here for origami creased folds and can be found in [121, 276]. It is reminded that the model for origami with creased folds reviewed in this section is a special case of the more general model for origami with smooth folds presented in Section 2.2. Thus, the mapping from reference to current configurations for origami with smooth folds provided in Section 2.2.4 covers such a mapping for origami with creased folds.

2.2 Origami with Smooth Folds

The model for origami presented in the preceding section is based on the assumption of creased folds. Such a simplification may not be appropriate for structures having folds of non-negligible fold thickness or constructed from materials that do not provide sufficient strain magnitudes to generate the high curvatures needed for a creased idealization. For such structures, the folded regions may not be accurately represented as creases but instead as *bent* sheet regions exhibiting higher-order geometric continuity (termed *smooth folds* in this work). Modeling of origami-based morphing of plate structures having significant thickness at the fold regions requires the arbitrary order of continuity of smooth folds. The present model is also useful in the kinematic analysis of sheets folded via active material actuation, where the achievable curvature at the folds is limited by the maximum strain magnitude provided by such active materials [3]. Examples of these active material-

based origami structures include liquid-crystal elastomer [199, 200], shape memory alloy [8, 128, 169, 361], dielectric elastomer [249, 250], and optically-responsive polymeric self-folding sheets [161, 188, 420], among others [3, 230, 421, 422, 423, 424, 425] (refer to Section 1.2 for a comprehensive review of active material-based origami structures). The diverse assumptions regarding strain distributions at the fold regions associated with the implementation of these various materials requires the arbitrary order of continuity considered in this work. A novel model for the kinematic response of origami structures having smooth folds is presented in this section.

The approach used to develop a model for origami with smooth folds follows that outlined at the beginning of Section 2.1. First, the *sheet* and the *shape variables* associated with the *smooth folds* in the sheet are described. The layout of the smooth folds in the sheet (i.e. the *fold pattern*) is determined by *vertices* (start-points and end-points of the smooth fold *centerlines* in a planar reference configuration), their connectivity, and the initial *width* of each smooth fold. Subsequently, *constraints* on the fold shape variables that define the constrained configuration space are derived. The *continuous motion* of the sheet represents a continuous path in such a constrained configuration space.

The studied continuum body is denoted as the *sheet* which is a three-dimensional, orientable, path-connected surface with boundary (same properties of a sheet in origami with creased folds, see Section 2.1). For origami with smooth folds, the sheet is divided into various surface subdomains denoted as *faces*, *smooth folds*, and *fold intersections*. Every surface subdomain comprising the sheet has the same aforementioned characteristics of the sheet (i.e. they are three-dimensional, orientable, path-connected surfaces with boundary). Following the notation of Section 2.1, the orthonormal vectors $\mathbf{e}_i \in \mathbb{R}^3$, $i = 1, 2, 3$, with $\mathbf{e}_3 := \mathbf{e}_1 \times \mathbf{e}_2$ form the basis $\{\mathbf{e}_1, \mathbf{e}_2, \mathbf{e}_3\}$ that defines the fixed global coordinate system.

The *reference configuration* of the sheet is denoted $\mathcal{S}_0$ and is defined such that it is contained in the plane spanned by $\mathbf{e}_1$ and $\mathbf{e}_2$ with its surface subdomains not overlapping each other, except at their shared boundary edges. The configuration of the $N_{\mathcal{P}}$ faces, $N_{\mathcal{F}}$ smooth folds, and $N_{\mathcal{I}}$ fold intersections subdomains in $\mathcal{S}_0$ are denoted $\mathcal{P}_0^i$, $i = 1, \ldots, N_{\mathcal{P}}$, $\mathcal{F}_0^i$, $i = 1, \ldots, N_{\mathcal{F}}$, and $\mathcal{I}_0^i$, $i = 1, \ldots, N_{\mathcal{I}}$, respectively. Therefore, $\mathcal{S}_0 = (\bigcup_{i=1}^{N_{\mathcal{P}}} \mathcal{P}_0^i) \cup (\bigcup_{i=1}^{N_{\mathcal{F}}} \mathcal{F}_0^i) \cup (\bigcup_{i=1}^{N_{\mathcal{I}}} \mathcal{I}_0^i)$. The side of $\mathcal{S}_0$ with normal $\mathbf{e}_3$ is selected as the positive side of the sheet. An example of a sheet with smooth folds in its reference configuration $\mathcal{S}_0$ is shown in Figure 2.4(a).

Definition 2.5. Valid configuration: *A* valid *current configuration $\mathcal{S}_t$ has the following characteristics: (i) The faces undergo only rigid deformations, (ii) the sheet is not torn (initially joined surface subdomains of the sheet remain joined), and (iii) the sheet does not self-intersect.*

The characteristics of a valid configuration provided in Definition 2.5 are the same as those of a valid configuration for a sheet with creased folds presented in Definition 2.1. However, it is noted that unlike a sheet with creased folds, a sheet with smooth folds is also comprised of other surface subdomains besides the faces (smooth folds and fold intersections) for which bending and stretching are permitted.

Definition 2.6. Smooth folds: *The* smooth folds *are ruled surfaces*[5] *of the following form:*

$$\boldsymbol{\mathcal{F}}_t^i(\zeta_1, \zeta_2) = \mathbf{c}_t^i(\zeta_1) + \zeta_2 \mathbf{h}_t^i, \qquad \frac{\mathrm{d}\mathbf{c}_t^i(\zeta_1)}{\mathrm{d}\zeta_1} \cdot \mathbf{h}_t^i = 0, \tag{2.16}$$

where $\boldsymbol{\mathcal{F}}_t^i(\zeta_1, \zeta_2) \in \mathbb{R}^3$ is a parameterization of $\mathcal{F}_t^i$. Without loss of generality, the domains for the parameters ζ_1 and ζ_2 are taken as the intervals $[-1, 1]$ and $[0, 1]$,

[5] A ruled surface is formed by the union of straight lines, called the *rulings* or generators of the surface [414].

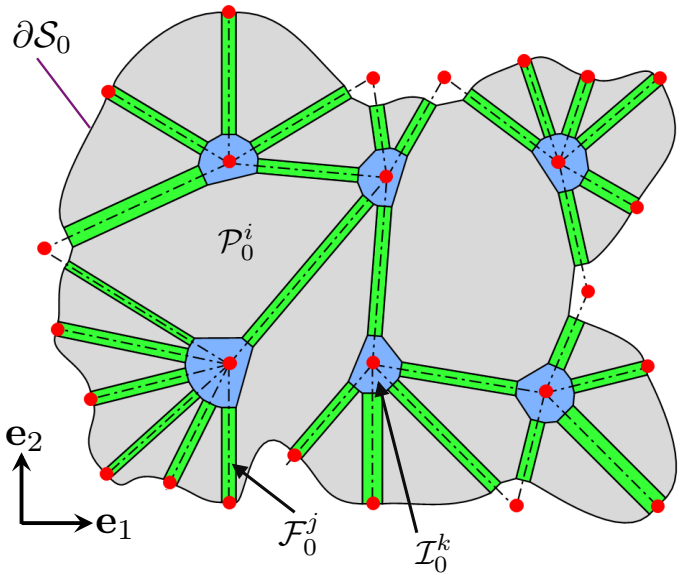

(a) Reference configuration $\mathcal{S}_0$

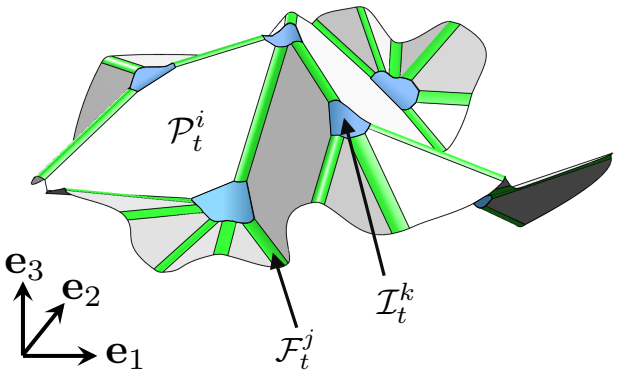

(b) Current configuration $\mathcal{S}_t$

Figure 2.4: Sheet with smooth folds in its reference configuration $\mathcal{S}_0$ and a current configuration $\mathcal{S}_t$.

respectively.

An example of a smooth fold is shown in Figure 2.5. In Definition 2.6, $\mathbf{h}_t^i \in \mathbb{R}^3$ provides the direction of the rulings comprising $\mathcal{F}_t^i$ while $\mathbf{c}_t^i(\zeta_1) \in \mathbb{R}^3$ is the parametric ruled surface directrix curve that defines the cross-section of $\mathcal{F}_t^i$. The curve parameterized by $\mathbf{c}_t^i(\zeta_1)$ is contained in a plane orthogonal to $\mathbf{h}_t^i$ as stated in Equation (2.16). It is assumed that $\|\mathbf{h}_t^i\|$ is constant for all configurations. As a consequence, the only non-rigid deformations allowed for the smooth folds are achieved through continuous bending or stretching of its cross-section defined by $\mathbf{c}_t^i(\zeta_1)$. To simplify the notation, the dependence of $\boldsymbol{\mathcal{F}}_t^i(\zeta_1, \zeta_2)$, $\mathbf{c}_t^i(\zeta_1)$, and $\mathbf{h}_t^i$ on t is taken as implicit for the remainder of the dissertation and these vectors are denoted as $\boldsymbol{\mathcal{F}}^i(\zeta_1, \zeta_2)$, $\mathbf{c}^i(\zeta_1)$, and $\mathbf{h}^i$, respectively.

The reference configuration of the smooth folds is simplified here to a rectangular shape and their deformation only includes stretching and bending of the fold cross-section. However, the model proposed in this section can be extended for the consideration of folds having a trapezoidal reference configuration (that deform into conical sections) or folds that exhibit torsional deformation. Such extensions are recommended for future studies.

Remark 2.1. *Deformation of a sheet with creased folds is the special limiting case of the more general deformation of a sheet with smooth folds. Specifically, creased folds are obtained when the curve parameterized by* $\mathbf{c}^i(\zeta_1)$ *is degenerated to a single point, thereby degenerating the smooth fold surface* $\mathcal{F}_t^i$ *to a single straight line segment.*

Each smooth fold is joined to a face at each of its two boundary rulings (i.e. $\boldsymbol{\mathcal{F}}^i(-1, \zeta_2)$ and $\boldsymbol{\mathcal{F}}^i(1, \zeta_2)$, refer to Figure 2.5). The remaining boundaries of $\mathcal{F}_t^i$ (i.e. $\boldsymbol{\mathcal{F}}^i(\zeta_1, 0)$ and $\boldsymbol{\mathcal{F}}^i(\zeta_1, 1)$) are either at the boundary of $\mathcal{S}_t$ or joined to a fold intersection. A parameterization for the fold intersections ($\mathcal{I}_t^i$, $i = 1, \ldots, N_{\mathcal{I}}$) is not

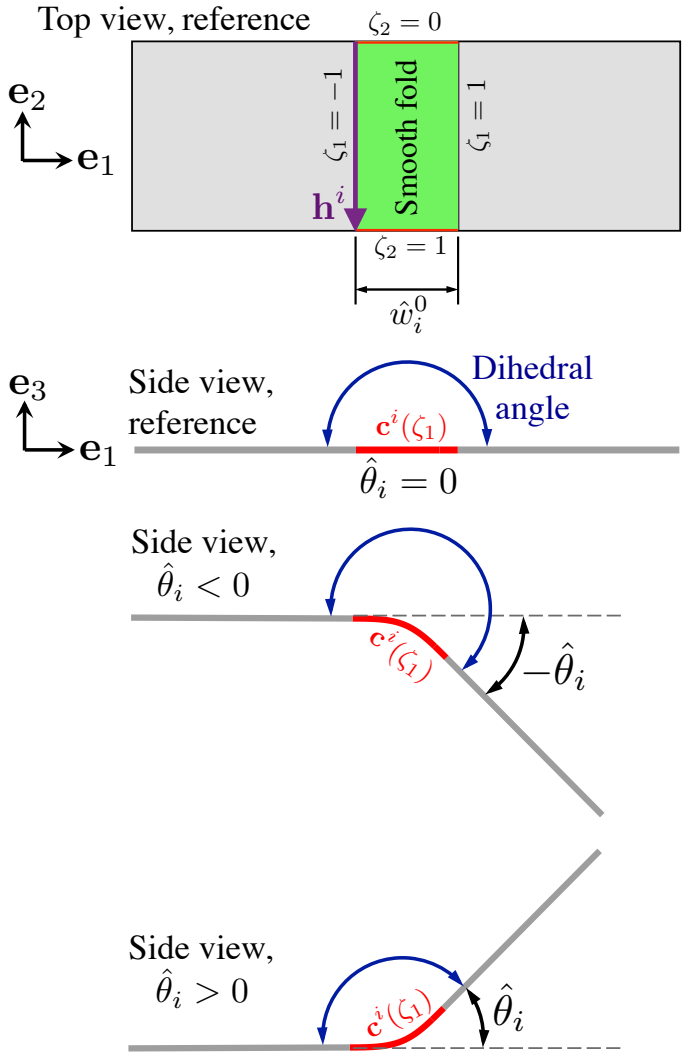

Figure 2.5: Schematics showing unfolded and folded configurations of a smooth fold, cf. Figure 2.2.

provided here. It is noted, however, that the model proposed herein is independent of the parameterization of $\mathcal{I}_t^i$.

A non-rigid body deformation of the sheet is achieved by rotating pairs of faces joined to smooth folds relative to one another in such a manner that the sheet only attains valid configurations during such a deformation. One of the *shape variables* associated with a smooth fold describes the relative rotation between the two faces joined by such a fold and is denoted as *fold angle*:

Definition 2.7. Fold angle: *The* fold angle $\hat{\theta}_i(t)$ *is defined as* π *radians minus the dihedral angle between the positive sides of the two faces joined to the* i^{th} *smooth fold.*

The dependence of the fold angles on t is left implicit for the remainder of the dissertation. The vector $\hat{\boldsymbol{\theta}} \in \mathbb{R}^{N_{\mathcal{F}}}$ constructed by collecting the fold angles $\hat{\theta}_i$, $i = 1, \ldots, N_{\mathcal{F}}$, and is defined in Equation (2.1). Schematics showing the concept of fold angle for smooth folds are provided in Figure 2.5.

2.2.1 Geometry of Smooth Folds

This section presents the detailed geometrical description of smooth folds. The conditions required for various orders of geometric continuity and particular formulations for $\mathbf{c}^i(\zeta_1)$ are also provided.

The distance between the two end-points of $\mathbf{c}^i(\zeta_1)$ with position vectors $\mathbf{c}^i(-1)$ and $\mathbf{c}^i(1)$ in any configuration is denoted $\hat{w}_i$:

$$\hat{w}_i := \|\mathbf{c}^i(1) - \mathbf{c}^i(-1)\|. \tag{2.17}$$

A schematic of a smooth fold cross-section showing $\hat{w}_i$ is provided in Figure 2.6.

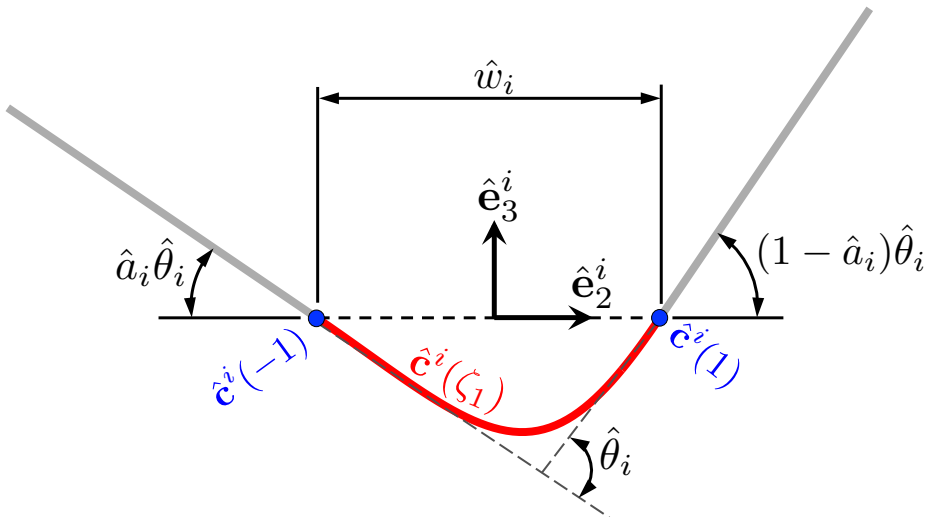

Figure 2.6: Cross-section of a smooth fold. The fold shape variables and the fold-attached coordinate system are shown.

The vector $\hat{\boldsymbol{w}} \in \mathbb{R}^{N_\mathcal{F}}$ is constructed by collecting the variables $\hat{w}_i$ as follows:

$$\hat{\boldsymbol{w}} = \begin{bmatrix} \hat{w}_1 \\ \vdots \\ \hat{w}_{N_\mathcal{F}} \end{bmatrix}. \tag{2.18}$$

The *fold width* $\hat{w}_i^0$ is the value of $\hat{w}_i$ at $t = 0$. The vector $\hat{\boldsymbol{w}}^0 \in \mathbb{R}^{N_\mathcal{F}}$ is constructed as follows:

$$\hat{\boldsymbol{w}}^0 = \begin{bmatrix} \hat{w}_1^0 \\ \vdots \\ \hat{w}_{N_\mathcal{F}}^0 \end{bmatrix}. \tag{2.19}$$

The fold-attached orthonormal vectors $\hat{\mathbf{e}}_j^i \in \mathbb{R}^3$, $i = 1, \ldots, N_\mathcal{F}$, $j = 1, 2, 3$, with $\hat{\mathbf{e}}_3^i := \hat{\mathbf{e}}_1^i \times \hat{\mathbf{e}}_2^i$ form the bases $\{\hat{\mathbf{e}}_1^i, \hat{\mathbf{e}}_2^i, \hat{\mathbf{e}}_3^i\}$ that define the local *fold coordinate system* of each smooth fold $\mathcal{F}_t^i$. The origin of this coordinate system is located at

$\frac{1}{2}\left(\mathbf{c}^i(-1) + \mathbf{c}^i(1)\right)$. The director vector $\mathbf{h}^i$ is aligned to $\hat{\mathbf{e}}_1^i$ (i.e. $\mathbf{h}^i \cdot \hat{\mathbf{e}}_1^i = \|\mathbf{h}^i\|$) and $(\mathbf{c}^i(1) - \mathbf{c}^i(-1)) \in \text{span}(\hat{\mathbf{e}}_2^i)$.

The face adjacent to a smooth fold at the boundary $\boldsymbol{\mathcal{F}}^i(-1, \zeta_2)$ makes an angle of $\hat{a}_i\hat{\theta}_i$ with $-\hat{\mathbf{e}}_2^i$ in the plane spanned by $\hat{\mathbf{e}}_2^i$ and $\hat{\mathbf{e}}_3^i$ and the face adjacent to a smooth fold at the boundary $\boldsymbol{\mathcal{F}}^i(1, \zeta_2)$ makes an angle of $(1 - \hat{a}_i)\hat{\theta}_i$ with $\hat{\mathbf{e}}_2^i$ in such a plane. This is shown schematically in Figure 2.6. The vector $\hat{\boldsymbol{a}} \in \mathbb{R}^{N_\mathcal{F}}$ is constructed by collecting the variables $\hat{a}_i$ as follows:

$$\hat{\boldsymbol{a}} = \begin{bmatrix} \hat{a}_1 \\ \vdots \\ \hat{a}_{N_\mathcal{F}} \end{bmatrix}. \tag{2.20}$$

Let $\hat{\mathbf{c}}^i(\zeta_1)$ be the parametric curve $\mathbf{c}^i(\zeta_1)$ expressed in the fold coordinate system of $\mathcal{F}_t^i$:

$$\hat{\mathbf{c}}^i(\zeta_1) = \begin{bmatrix} \hat{\mathbf{e}}_1^i & \hat{\mathbf{e}}_2^i & \hat{\mathbf{e}}_3^i \end{bmatrix}^\top \left[\mathbf{c}^i(\zeta_1) - \tfrac{1}{2}\Big(\mathbf{c}^i(-1) + \mathbf{c}^i(1)\Big)\right]. \tag{2.21}$$

If $\hat{\mathbf{c}}^i(\zeta_1)$ is at least first-order differentiable for $\zeta_1 \in [-1, 1]$, the total arc-length of the fold cross-section, denoted $\hat{s}_i$, is determined as follows:

$$\hat{s}_i = \int_{-1}^{1} \left\| \frac{\mathrm{d}\hat{\mathbf{c}}^i(\zeta_1)}{\mathrm{d}\zeta_1} \right\| \mathrm{d}\zeta_1, \tag{2.22}$$

and the arc-length coordinate $s(\zeta_1) \in \left[-\frac{\hat{s}_i}{2}, \frac{\hat{s}_i}{2}\right]$ is determined as follows:

$$s(\zeta_1) = -\frac{\hat{s}_i}{2} + \int_{-1}^{\zeta_1} \left\| \frac{\mathrm{d}\hat{\mathbf{c}}^i(\zeta)}{\mathrm{d}\zeta} \right\| \mathrm{d}\zeta. \tag{2.23}$$

The tangent direction of the parametric curve $\hat{\mathbf{c}}^i(\zeta_1)$ is determined by the unit tangent vector $\mathbf{t}^i(\zeta_1) \in \text{span}(\hat{\mathbf{e}}_2^i, \hat{\mathbf{e}}_3^i)$ and is defined at the points where $\hat{\mathbf{c}}^i(\zeta_1)$ is at

least first-order differentiable:

$$\mathbf{t}^i(\zeta_1) = \frac{\dfrac{\mathrm{d}\hat{\mathbf{c}}^i(\zeta_1)}{\mathrm{d}\zeta_1}}{\left\| \dfrac{\mathrm{d}\hat{\mathbf{c}}^i(\zeta_1)}{\mathrm{d}\zeta_1} \right\|}. \tag{2.24}$$

The curvature $\hat{\kappa}(\zeta_1)$ is defined at the points where $\hat{\mathbf{c}}^i(\zeta_1)$ is at least second-order differentiable:

$$\hat{\kappa}(\zeta_1) = \frac{\left\| \dfrac{\mathrm{d}\hat{\mathbf{c}}^i(\zeta_1)}{\mathrm{d}\zeta_1} \times \dfrac{\mathrm{d}^2\hat{\mathbf{c}}^i(\zeta_1)}{\mathrm{d}\zeta_1^2} \right\|}{\left\| \dfrac{\mathrm{d}\hat{\mathbf{c}}^i(\zeta_1)}{\mathrm{d}\zeta_1} \right\|^3}, \tag{2.25}$$

and the signed curvature $\kappa(\zeta_1)$ is given as follows[6]:

$$\kappa(\zeta_1) = \hat{\kappa}(\zeta_1)\,\mathrm{sgn}\left(\left(\frac{\mathrm{d}\hat{\mathbf{c}}^i(\zeta_1)}{\mathrm{d}\zeta_1} \times \frac{\mathrm{d}^2\hat{\mathbf{c}}^i(\zeta_1)}{\mathrm{d}\zeta_1^2} \right) \cdot \hat{\mathbf{e}}_1^i \right). \tag{2.26}$$

The order of geometric continuity of $\mathcal{S}_t$ at the interior rulings of $\mathcal{F}_t^i$ is determined by the order of geometric continuity of $\hat{\mathbf{c}}^i(\zeta_1)$, $\zeta_1 \in (-1, 1)$, while that at the joints with the planar faces adjacent to $\mathcal{F}_t^i$ depends on the particular values of $\hat{\mathbf{c}}^i(\zeta_1)$ and its derivatives at $\zeta_1 = \pm 1$. For instance, G^0 continuous joints with the faces adjacent to $\mathcal{F}_t^i$ require the following conditions on $\hat{\mathbf{c}}^i(\zeta_1)$ at $\zeta_1 = \pm 1$ (refer to Figure 2.6):

$$\hat{\mathbf{c}}^i(-1) = \begin{bmatrix} 0 \\ -\frac{\hat{w}_i}{2} \\ 0 \end{bmatrix} =: \hat{\mathbf{c}}^i_{L_0}, \tag{2.27}$$

[6]The sign function is defined as follows: $\mathrm{sgn}(y) := \begin{cases} -1; & y < 0 \\ 1; & y > 0 \\ 0; & y = 0 \end{cases}$.

$$\hat{\mathbf{c}}^i(1) = \begin{bmatrix} 0 \\ \frac{\hat{w}_i}{2} \\ 0 \end{bmatrix} =: \hat{\mathbf{c}}^i_{R_0}. \tag{2.28}$$

Continuity of the unit tangent vector $\mathbf{t}^i(\zeta_1)$ at $\zeta_1 = \pm 1$ is required for G^1 continuous joints with the planar faces adjacent to $\mathcal{F}^i_t$ in addition to G^0 continuity [426, 427]. The following values of $\mathbf{t}^i(\zeta_1)$ at $\zeta_1 = \pm 1$ are then required for G^1 continuity in addition to those conditions of Equations (2.27) and (2.28):

$$\mathbf{t}^i(-1) = \begin{bmatrix} 0 \\ \cos\left(\hat{a}_i\hat{\theta}_i\right) \\ -\sin\left(\hat{a}_i\hat{\theta}_i\right) \end{bmatrix}, \tag{2.29}$$

$$\mathbf{t}^i(1) = \begin{bmatrix} 0 \\ \cos\left((1-\hat{a}_i)\hat{\theta}_i\right) \\ \sin\left((1-\hat{a}_i)\hat{\theta}_i\right) \end{bmatrix}. \tag{2.30}$$

Therefore, the following conditions on the first derivatives of $\hat{\mathbf{c}}^i(\zeta_1)$ at $\zeta_1 = \pm 1$ are required for G^1 continuity at the joints with the planar faces adjacent to $\mathcal{F}^i_t$:

$$\left.\frac{\mathrm{d}\hat{\mathbf{c}}^i(\zeta_1)}{\mathrm{d}\zeta_1}\right|_{\zeta_1=-1} = \beta^i_{L_1} \begin{bmatrix} 0 \\ \cos\left(\hat{a}_i\hat{\theta}_i\right) \\ -\sin\left(\hat{a}_i\hat{\theta}_i\right) \end{bmatrix} =: \hat{\mathbf{c}}^i_{L_1}, \tag{2.31}$$

$$\left.\frac{\mathrm{d}\hat{\mathbf{c}}^i(\zeta_1)}{\mathrm{d}\zeta_1}\right|_{\zeta_1=1} = \beta^i_{R_1} \begin{bmatrix} 0 \\ \cos\left((1-\hat{a}_i)\hat{\theta}_i\right) \\ \sin\left((1-\hat{a}_i)\hat{\theta}_i\right) \end{bmatrix} =: \hat{\mathbf{c}}^i_{R_1}, \tag{2.32}$$

where $\beta^i_{L_1},\ \beta^i_{R_1} \in \mathbb{R}_{>0}$.

Continuity of the curvature vector (or the signed curvature) is required for G^2 continuity [427] in addition to G^1 continuity. This requires the curvature of $\hat{\mathbf{c}}^i(\zeta_1)$ at $\zeta_1 = \pm 1$ to be zero since $\mathcal{F}^i_t$ is connected to planar faces at its boundary rulings. Zero curvature at the boundary rulings of $\mathcal{F}^i_t$ requires the following according to Equation (2.25):

$$\left(\frac{\mathrm{d}\hat{\mathbf{c}}^i(\zeta_1)}{\mathrm{d}\zeta_1} \times \frac{\mathrm{d}^2\hat{\mathbf{c}}^i(\zeta_1)}{\mathrm{d}\zeta_1^2}\right)\Bigg|_{\zeta_1=-1} = \mathbf{0}_3, \tag{2.33}$$

$$\left(\frac{\mathrm{d}\hat{\mathbf{c}}^i(\zeta_1)}{\mathrm{d}\zeta_1} \times \frac{\mathrm{d}^2\hat{\mathbf{c}}^i(\zeta_1)}{\mathrm{d}\zeta_1^2}\right)\Bigg|_{\zeta_1=1} = \mathbf{0}_3, \tag{2.34}$$

where $\mathbf{0}_n$ is the zero vector in $\mathbb{R}^n$. Considering Equations (2.31)–(2.34), the following conditions on the second derivatives of $\hat{\mathbf{c}}^i(\zeta_1)$ are needed in addition to the conditions provided in Equations (2.27)–(2.32) for G^2 continuity at the joints with the planar faces adjacent to $\mathcal{F}^i_t$:

$$\left.\frac{\mathrm{d}^2\hat{\mathbf{c}}^i(\zeta_1)}{\mathrm{d}\zeta_1^2}\right|_{\zeta_1=-1} = \beta^i_{L_2} \begin{bmatrix} 0 \\ \cos\left(\hat{a}_i\hat{\theta}_i\right) \\ -\sin\left(\hat{a}_i\hat{\theta}_i\right) \end{bmatrix} =: \hat{\mathbf{c}}^i_{L_2}, \tag{2.35}$$

$$\left.\frac{\mathrm{d}^2\hat{\mathbf{c}}^i(\zeta_1)}{\mathrm{d}\zeta_1^2}\right|_{\zeta_1=1} = \beta^i_{R_2}\begin{bmatrix} 0 \\ -\cos\left((1-\hat{a}_i)\hat{\theta}_i\right) \\ -\sin\left((1-\hat{a}_i)\hat{\theta}_i\right) \end{bmatrix} =: \hat{\mathbf{c}}^i_{R_2}, \tag{2.36}$$

where $\beta^i_{L_2},\ \beta^i_{R_2} \in \mathbb{R}$. Conditions on higher-order derivatives of $\hat{\mathbf{c}}^i(\zeta_1)$ required for higher-order geometric continuity can be provided in a similar manner [426, 427].

Figure 2.7 shows schematics of folds having various orders of geometric continuity and their associated signed curvature fields as functions of arc-length (i.e. $\kappa(s)$). If the curve $\mathbf{c}^i(\zeta_1)$ is reparameterized by arc-length s, the following relation between fold angle $\hat{\theta}_i$ and the signed curvature field of the fold cross-section holds:

$$\hat{\theta}_i = \int_{-\frac{\hat{s}_i}{2}-\epsilon}^{\frac{\hat{s}_i}{2}+\epsilon} \kappa(s)\,\mathrm{d}s, \tag{2.37}$$

where $\epsilon > 0$.

2.2.1.1 Fold Shape Examples

Polynomials of the minimum order required to satisfy the previous conditions for continuity of $\hat{\mathbf{c}}^i(\zeta_1)$ and its derivatives at $\zeta_1 = \pm 1$ are used to define this parametric curve. Hermite interpolation polynomials [428] are used to represent $\hat{\mathbf{c}}^i(\zeta_1)$ in this work. Alternative representations (e.g. Bezier curves) are also applicable as long as they satisfy the conditions required for the considered order of geometric continuity. For G^1 continuity at the boundary rulings of $\mathcal{F}^i_t$, $\hat{\mathbf{c}}^i(\zeta_1)$ is expressed as follows:

$$\hat{\mathbf{c}}^i(\zeta_1) = h_{30}(\zeta_1)\hat{\mathbf{c}}^i_{L_0} + h_{31}(\zeta_1)\hat{\mathbf{c}}^i_{R_0} + h_{32}(\zeta_1)\hat{\mathbf{c}}^i_{L_1} + h_{33}(\zeta_1)\hat{\mathbf{c}}^i_{R_1}, \tag{2.38}$$

where the utilized cubic Hermite interpolation polynomials $h_{3i}(\zeta_1),\ i = 0, \ldots, 3$, are

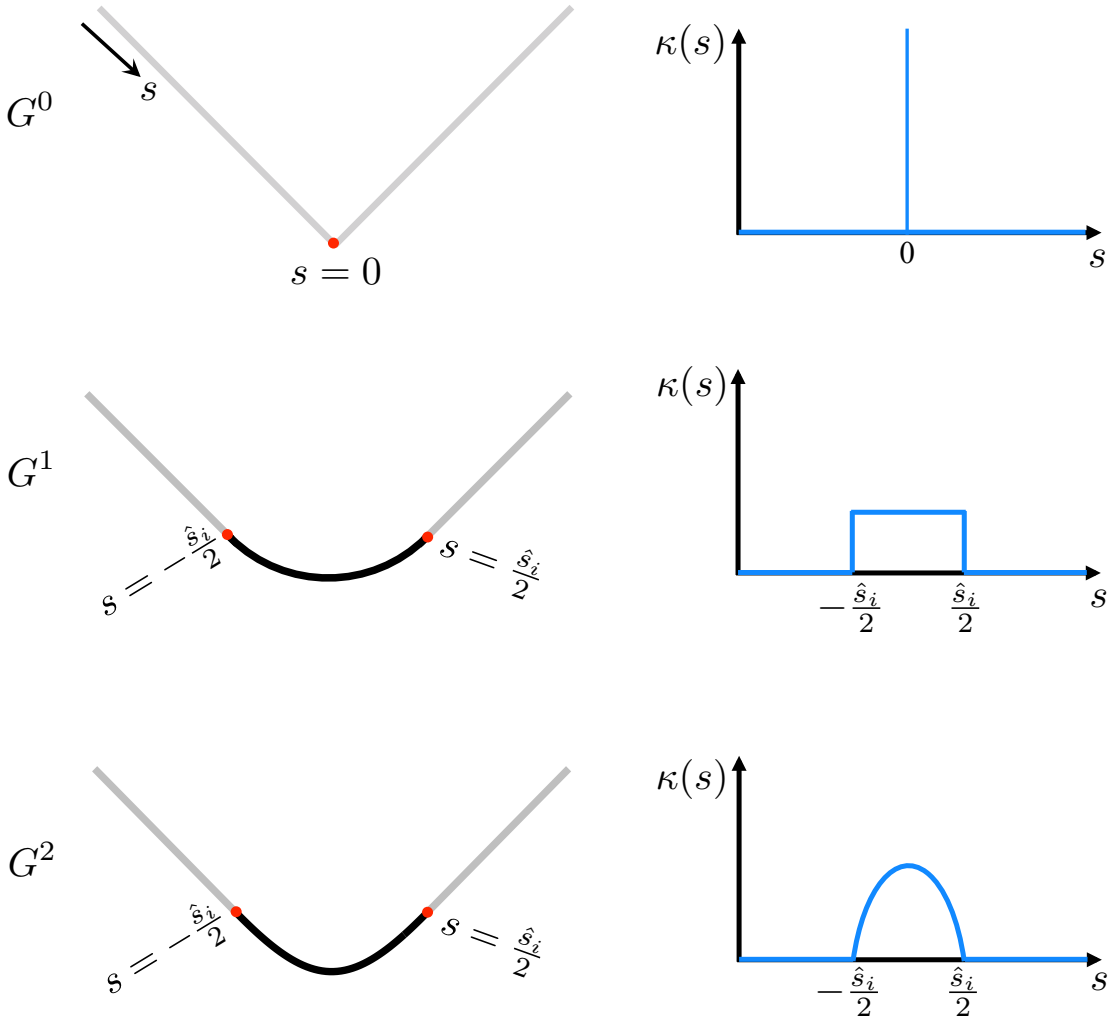

Figure 2.7: Schematics showing folds of various orders of geometric continuity and their associated curvature fields.

given as follows:

$$h_{30}(\zeta_1) = \tfrac{1}{4}\zeta_1^3 - \tfrac{3}{4}\zeta_1 + \tfrac{1}{2}, \tag{2.39}$$

$$h_{31}(\zeta_1) = -\tfrac{1}{4}\zeta_1^3 + \tfrac{3}{4}\zeta_1 + \tfrac{1}{2}, \tag{2.40}$$

$$h_{32}(\zeta_1) = \tfrac{1}{4}\zeta_1^3 - \tfrac{1}{4}\zeta_1^2 - \tfrac{1}{4}\zeta_1 + \tfrac{1}{4}, \tag{2.41}$$

$$h_{33}(\zeta_1) = \tfrac{1}{4}\zeta_1^3 + \tfrac{1}{4}\zeta_1^2 - \tfrac{1}{4}\zeta_1 - \tfrac{1}{4}. \tag{2.42}$$

For G^2 continuity at the boundary rulings of $\mathcal{F}_t^i$, $\hat{\mathbf{c}}^i(\zeta_1)$ is expressed as follows:

$$\begin{aligned} \hat{\mathbf{c}}^i(\zeta_1) = \;& h_{50}(\zeta_1)\hat{\mathbf{c}}^i_{L_0} + h_{51}(\zeta_1)\hat{\mathbf{c}}^i_{R_0} + h_{52}(\zeta_1)\hat{\mathbf{c}}^i_{L_1} \\ & + h_{53}(\zeta_1)\hat{\mathbf{c}}^i_{R_1} + h_{54}(\zeta_1)\hat{\mathbf{c}}^i_{L_2} + h_{55}(\zeta_1)\hat{\mathbf{c}}^i_{R_2}, \end{aligned} \tag{2.43}$$

where the utilized quintic Hermite interpolation polynomials $h_{5i}(\zeta_1)$, $i = 0, \ldots, 5$, are given as follows:

$$h_{50}(\zeta_1) = -\tfrac{3}{16}\zeta_1^5 + \tfrac{5}{8}\zeta_1^3 - \tfrac{15}{16}\zeta_1 + \tfrac{1}{2}, \tag{2.44}$$

$$h_{51}(\zeta_1) = \tfrac{3}{16}\zeta_1^5 - \tfrac{5}{8}\zeta_1^3 + \tfrac{15}{16}\zeta_1 + \tfrac{1}{2}, \tag{2.45}$$

$$h_{52}(\zeta_1) = -\tfrac{3}{16}\zeta_1^5 + \tfrac{1}{16}\zeta_1^4 + \tfrac{5}{8}\zeta_1^3 - \tfrac{3}{8}\zeta_1^2 - \tfrac{7}{16}\zeta_1 + \tfrac{5}{16}, \tag{2.46}$$

$$h_{53}(\zeta_1) = -\tfrac{3}{16}\zeta_1^5 - \tfrac{1}{16}\zeta_1^4 + \tfrac{5}{8}\zeta_1^3 + \tfrac{3}{8}\zeta_1^2 - \tfrac{7}{16}\zeta_1 - \tfrac{5}{16}, \tag{2.47}$$

$$h_{54}(\zeta_1) = -\tfrac{1}{16}\zeta_1^5 + \tfrac{1}{16}\zeta_1^4 + \tfrac{1}{8}\zeta_1^3 - \tfrac{1}{8}\zeta_1^2 - \tfrac{1}{16}\zeta_1 + \tfrac{1}{16}, \tag{2.48}$$

$$h_{55}(\zeta_1) = \tfrac{1}{16}\zeta_1^5 + \tfrac{1}{16}\zeta_1^4 - \tfrac{1}{8}\zeta_1^3 - \tfrac{1}{8}\zeta_1^2 + \tfrac{1}{16}\zeta_1 + \tfrac{1}{16}. \tag{2.49}$$

2.2.2 Fold Pattern

The layout of the smooth folds in $\mathcal{S}_0$ is presented in a fold pattern. To describe the fold pattern, the *vertices* are first introduced:

Definition 2.8. Vertices: *The* vertices *are the start-points and end-points of the line segments coincident with the centerlines of the smooth folds in $\mathcal{S}_0$. Each vertex has an associated position vector denoted $\mathbf{v}^j \in \text{span}(\mathbf{e}_1, \mathbf{e}_2)$.*

As in Section 2.1.1, the number of vertices located at the interior of $\mathcal{S}_0$ is denoted $N_{\mathcal{I}}$ and the number of vertices located at $\partial\mathcal{S}_0$ or outside $\mathcal{S}_0$ is denoted $N_{\mathcal{B}}$. The vertices are enumerated starting from those located at the interior of $\mathcal{S}_0$ (with corresponding position vectors $\mathbf{v}^1, \ldots, \mathbf{v}^{N_{\mathcal{I}}}$) followed by those at the located at $\partial\mathcal{S}_0$ or outside $\mathcal{S}_0$ (with corresponding position vectors $\mathbf{v}^{N_{\mathcal{I}}+1}, \ldots, \mathbf{v}^{N_{\mathcal{I}}+N_{\mathcal{B}}}$). The vertices in origami with smooth folds are used only to indicate end-points of the fold centerlines in $\mathcal{S}_0$. The points of the sheet coincident with the vertices in $\mathcal{S}_0$ do not occupy any especial location in $\mathcal{S}_t$, $t > 0$. This is in contrast to origami with creased folds where the points of the sheet coincident with the vertices in $\mathcal{S}_0$, that correspond to fold line end-points, also correspond to fold line end-points in $\mathcal{S}_t$, $t > 0$ (see Section 2.1).

Following Section 2.1.1, the vector $\mathbf{V} \in \mathbb{R}^{3(N_{\mathcal{I}}+N_{\mathcal{B}})}$ formed by concatenating the vertex position vectors is provided in Equation (2.2). The definition of the matrix

$\widehat{\mathbf{C}} \in \{-1, 0, 1\}^{N_{\mathcal{F}} \times (N_{\mathcal{I}} + N_{\mathcal{B}})}$ that identifies which vertices are the start-points and end-points of the fold centerlines follows that provided in Equation (2.3). Let $\hat{\mathbf{v}}^{i1}, \hat{\mathbf{v}}^{i2} \in \text{span}(\mathbf{e}_1, \mathbf{e}_2)$, $i = 1, \ldots, N_{\mathcal{F}}$, be the position vectors of the vertices from which each fold centerline emanates and ends, respectively. The vectors $\hat{\mathbf{V}}^1, \hat{\mathbf{V}}^2 \in \mathbb{R}^{3N_{\mathcal{F}}}$ are constructed by concatenating the vectors $\hat{\mathbf{v}}^{i1}$, $\hat{\mathbf{v}}^{i2}$, $i = 1, \ldots, N_{\mathcal{F}}$, as follows:

$$\hat{\mathbf{V}}^1 = \begin{bmatrix} \hat{\mathbf{v}}^{11} \\ \vdots \\ \hat{\mathbf{v}}^{N_{\mathcal{F}}1} \end{bmatrix}, \tag{2.50}$$

$$\hat{\mathbf{V}}^2 = \begin{bmatrix} \hat{\mathbf{v}}^{12} \\ \vdots \\ \hat{\mathbf{v}}^{N_{\mathcal{F}}2} \end{bmatrix}. \tag{2.51}$$

The mappings from the collection of all the vertex position vectors $\mathbf{V}$ to those corresponding to the position vectors of the start-points and end-points of the fold centerlines ($\hat{\mathbf{V}}^1$ and $\hat{\mathbf{V}}^2$, respectively) are given as follows:

$$\hat{\mathbf{V}}^1 = \left(\tfrac{1}{2} \left(|\widehat{\mathbf{C}}|_* - \widehat{\mathbf{C}} \right) \otimes \mathbf{I}_3 \right) \mathbf{V}, \tag{2.52}$$

$$\hat{\mathbf{V}}^2 = \left(\tfrac{1}{2} \left(|\widehat{\mathbf{C}}|_* + \widehat{\mathbf{C}} \right) \otimes \mathbf{I}_3 \right) \mathbf{V}. \tag{2.53}$$

The four corner points of $\mathcal{F}_0^i$ having associated position vectors $\hat{\mathbf{p}}_1^i, \hat{\mathbf{p}}_2^i, \hat{\mathbf{p}}_3^i, \hat{\mathbf{p}}_4^i \in \text{span}(\mathbf{e}_1, \mathbf{e}_2)$, $i = 1, \ldots, N_{\mathcal{F}}$, are then determined as follows:

$$\hat{\mathbf{p}}_1^i = \hat{\mathbf{v}}^{i1} - \frac{\hat{w}_i^0}{2} \left(\mathbf{e}_3 \times \frac{\hat{\mathbf{v}}^{i2} - \hat{\mathbf{v}}^{i1}}{\|\hat{\mathbf{v}}^{i2} - \hat{\mathbf{v}}^{i1}\|} \right) + \hat{r}_1^i \frac{\hat{\mathbf{v}}^{i2} - \hat{\mathbf{v}}^{i1}}{\|\hat{\mathbf{v}}^{i2} - \hat{\mathbf{v}}^{i1}\|}, \tag{2.54}$$

$$\hat{\mathbf{p}}_2^i = \hat{\mathbf{v}}^{i2} - \frac{\hat{w}_i^0}{2}\left(\mathbf{e}_3 \times \frac{\hat{\mathbf{v}}^{i2} - \hat{\mathbf{v}}^{i1}}{\|\hat{\mathbf{v}}^{i2} - \hat{\mathbf{v}}^{i1}\|}\right) - \hat{r}_2^i \frac{\hat{\mathbf{v}}^{i2} - \hat{\mathbf{v}}^{i1}}{\|\hat{\mathbf{v}}^{i2} - \hat{\mathbf{v}}^{i1}\|}, \tag{2.55}$$

$$\hat{\mathbf{p}}_3^i = \hat{\mathbf{v}}^{i2} + \frac{\hat{w}_i^0}{2}\left(\mathbf{e}_3 \times \frac{\hat{\mathbf{v}}^{i2} - \hat{\mathbf{v}}^{i1}}{\|\hat{\mathbf{v}}^{i2} - \hat{\mathbf{v}}^{i1}\|}\right) - \hat{r}_2^i \frac{\hat{\mathbf{v}}^{i2} - \hat{\mathbf{v}}^{i1}}{\|\hat{\mathbf{v}}^{i2} - \hat{\mathbf{v}}^{i1}\|}, \tag{2.56}$$

$$\hat{\mathbf{p}}_4^i = \hat{\mathbf{v}}^{i1} + \frac{\hat{w}_i^0}{2}\left(\mathbf{e}_3 \times \frac{\hat{\mathbf{v}}^{i2} - \hat{\mathbf{v}}^{i1}}{\|\hat{\mathbf{v}}^{i2} - \hat{\mathbf{v}}^{i1}\|}\right) + \hat{r}_1^i \frac{\hat{\mathbf{v}}^{i2} - \hat{\mathbf{v}}^{i1}}{\|\hat{\mathbf{v}}^{i2} - \hat{\mathbf{v}}^{i1}\|}, \tag{2.57}$$

where $\hat{r}_1^i, \hat{r}_2^i \in \mathbb{R}$ and the resulting fold length orthogonal to the width direction must be positive:

$$\|\hat{\mathbf{v}}^{i2} - \hat{\mathbf{v}}^{i1}\| - \hat{r}_1^i - \hat{r}_2^i > 0 \qquad \forall i \in \{1, \ldots, N_{\mathcal{F}}\}. \tag{2.58}$$

The geometric parameters that define the corner points of $\mathcal{F}_0^i$ are shown in Figure 2.8.

The vectors $\hat{\mathbf{P}}^j \in \mathbb{R}^{3N_{\mathcal{F}}}$, $j = 1, \ldots, 4$, are constructed by concatenating the vectors $\hat{\mathbf{p}}_j^i$, $i = 1, \ldots, N_{\mathcal{F}}$, as follows:

$$\hat{\mathbf{P}}^j = \begin{bmatrix} \hat{\mathbf{p}}_j^1 \\ \vdots \\ \hat{\mathbf{p}}_j^{N_{\mathcal{F}}} \end{bmatrix}. \tag{2.59}$$

As in Section 2.1.1, let n_j, $j = 1, \ldots, N_{\mathcal{I}}$, be the number of fold centerlines incident to each interior vertex (i.e. those vertices located at the interior of $\mathcal{S}_0$). Also let $\mathbf{m}^{jk} \in \text{span}(\mathbf{e}_1, \mathbf{e}_2)$, $j = 1, \ldots, N_{\mathcal{I}}$, $k = 1, \ldots, n_j$, be the vector along the length of the k^{th} fold centerline incident to the j^{th} interior vertex that emanates from this vertex. The vectors $\mathbf{m}^{jk}$, $k = 1, \ldots, n_j$, have a counterclockwise ordering,

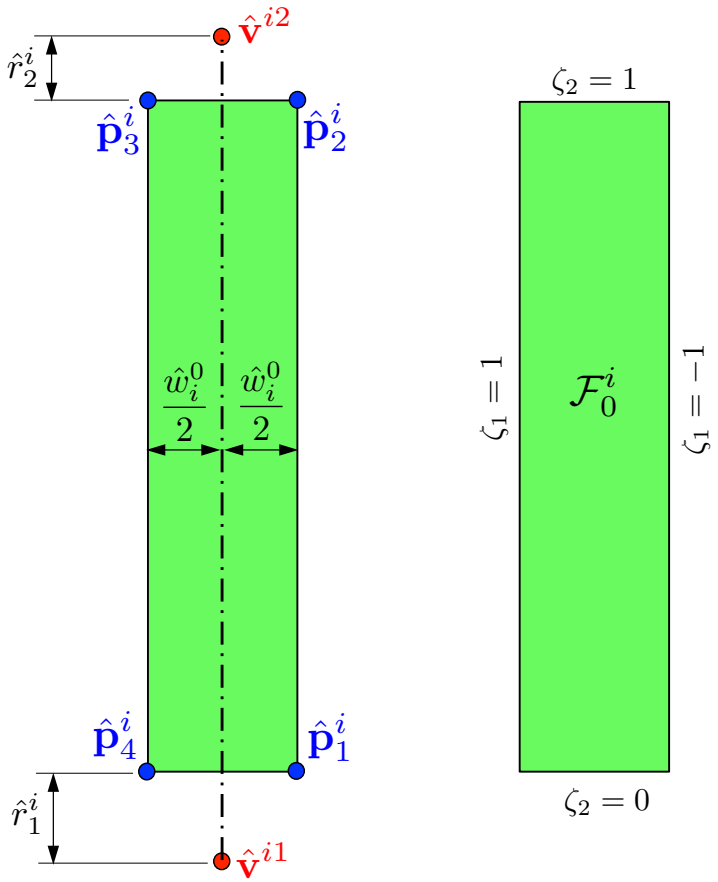

Figure 2.8: Geometric parameters defining $\mathcal{F}_0^i$.

i.e. $\varphi(\mathbf{m}^{j1}) < \varphi(\mathbf{m}^{j1}) < \cdots < \varphi(\mathbf{m}^{jn_j}) \quad \forall\, j \in \{1, \ldots, N_{\mathcal{I}}\}$ where $\varphi(\cdot)$ is defined in Equation (2.4).

The mapping from the vertex position vectors $\mathbf{v}^j$, $j = 1, \ldots, N_{\mathcal{I}} + N_{\mathcal{B}}$, to the vectors $\mathbf{m}^{jk}$, $k = 1, \ldots, n_j$, is provided in Equation (2.7). The angles between adjacent fold centerlines intersecting at a common interior vertex α_{jk}, $j = 1, \ldots, N_{\mathcal{I}}$, $k = 1, \ldots, n_j$, are calculated using Equation (2.8). A schematic showing the vectors $\mathbf{m}^{jk}$ and the angles α_{jk} is provided in Figure 2.9.

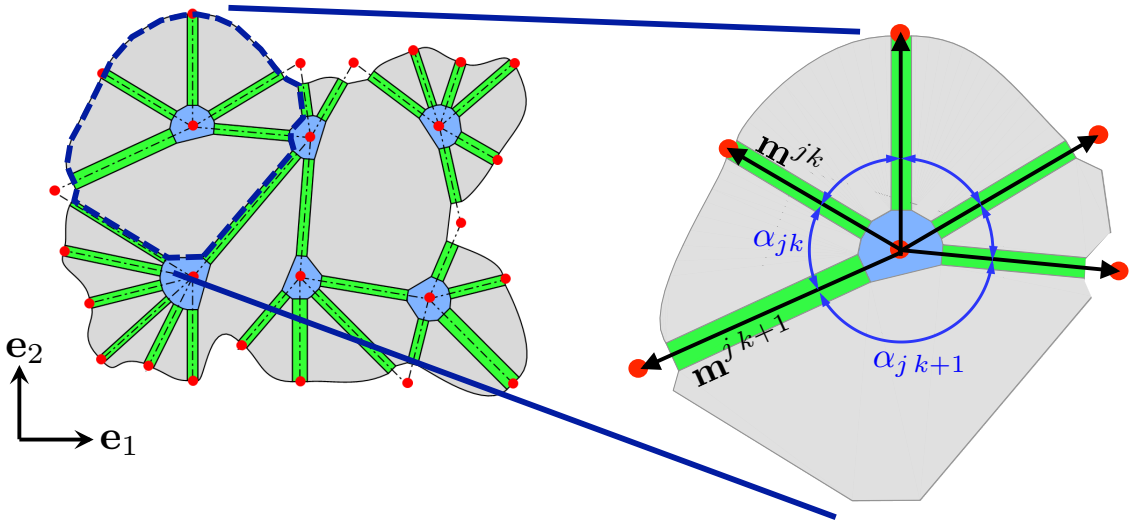

Figure 2.9: Schematic showing faces and smooth folds adjacent to an interior fold intersection and associated geometric parameters.

2.2.3 Constraints

As in conventional origami with creased folds [121, 276], constraints are required for origami with smooth folds to ensure that every current configuration $\mathcal{S}_t$ is valid[7] (according to Definition 2.5).

The angles α_{jk}, $k = 1, \ldots, n_j$, satisfy the following constraint since they are defined in $\mathcal{S}_0$:

$$K_j = 2\pi - \sum_{k=1}^{n_j} \alpha_{jk} = 0 \qquad \forall\, j \in \{1, \ldots, N_{\mathcal{I}}\}. \tag{2.60}$$

Since the faces undergo only rigid deformations, the angles α_{jk} are constant during the deformation history of the sheet, i.e. independent of t, and therefore Equation (2.60) holds at every configuration $\mathcal{S}_t$. Equation (2.60) represents the developability

[7] As stated in Section 2.1.2, self-intersection avoidance is not considered in this work.

constraint for origami with creased folds (see Equation (2.9)). However, pointwise isometric deformation is relaxed here for origami with smooth folds since stretching is permitted within the subdomains $\mathcal{F}_t^i$ and $\mathcal{I}_t^i$ and thus only $\mathcal{S}_0$ is in general pointwise developable. It is remarked that isometry is assumed for the smooth folds $\mathcal{F}_t^i$ in the direction of $\mathbf{h}^i$ (see Figure 2.5). However, the arc-length of the curve parameterized by $\hat{\mathbf{c}}^i(\zeta_1)$ may change in general during deformation and thus stretching of the smooth folds in such a direction may be allowed. Refer to Definition 2.6 and its subsequent discussion.

The variables describing the deformation associated with the folding of the smooth folds are constrained such that every configuration $\mathcal{S}_t$ is valid. These variables correspond to the fold angle $\hat{\theta}_i$, the distance $\hat{w}_i$ between the end-points of the cross-section parametric curve $\hat{\mathbf{c}}^i(\zeta_1)$, and $\hat{a}_i$, $i = 1, \ldots, N_{\mathcal{F}}$ (refer to Section 2.2.1). Following Section 2.1.2, a new set of constraints for the variables associated with the smooth folds adjacent to each interior fold intersection is now proposed.

The variables θ_{jk}, w_{jk}, and a_{jk} are those associated with the k^{th} smooth fold adjacent to $\mathcal{I}_0^j$. The vectors $\boldsymbol{\theta}^j \in \mathbb{R}^{n_j}$, $j = 1, \ldots, N_{\mathcal{I}}$, constructed by collecting the fold angles θ_{jk}, $k = 1, \ldots, n_j$, are defined in Equation (2.10). The vectors $\boldsymbol{w}^j$, $\boldsymbol{a}^j \in \mathbb{R}^{n_j}$, $j = 1, \ldots, N_{\mathcal{I}}$, are constructed by collecting the variables w_{jk} and a_{jk}, $k = 1, \ldots, n_j$, and are defined as follows:

$$\boldsymbol{w}^j = \begin{bmatrix} w_{j1} \\ \vdots \\ w_{jn_j} \end{bmatrix}, \tag{2.61}$$

$$\boldsymbol{a}^j = \begin{bmatrix} a_{j1} \\ \vdots \\ a_{jn_j} \end{bmatrix}. \tag{2.62}$$

The mapping from the vector $\hat{\boldsymbol{\theta}}$ with elements corresponding to the fold angles of the sheet to each vector $\boldsymbol{\theta}^j$ with elements corresponding to the fold angles of the smooth folds adjacent to $\mathcal{I}_0^j$ is provided in Equation (2.11). The mapping from the vector $\hat{\boldsymbol{w}}$, defined in Equation (2.18), to each vector $\boldsymbol{w}^j$ is the following:

$$\boldsymbol{w}^j = |\mathbf{C}^j|_* \, \hat{\boldsymbol{w}}, \tag{2.63}$$

where the definition of the matrix $\mathbf{C}^j$ in Equation (2.6) holds in the context of connectivity of fold centerlines. Taking into account the orientation of the adjacent smooth folds with respect to the considered fold intersection $\mathcal{I}_0^j$ (i.e. whether the interior vertex associated with $\mathcal{I}_0^j$ is the start-point or the end-point of the adjacent smooth fold centerline), the mapping from the vector $\hat{\boldsymbol{a}}$, defined in Equation (2.20), to each vector $\boldsymbol{a}^j$ is as follows:

$$\boldsymbol{a}^j = \begin{bmatrix} \mathbf{C}^j & {}^A\mathbf{C}^j \end{bmatrix} \begin{bmatrix} \hat{\boldsymbol{a}} \\ 1 \end{bmatrix}, \tag{2.64}$$

where ${}^A\mathbf{C}^j \in \mathbb{R}^{n_j}$ is a vector with elements ${}^AC_k^j$ that are determined as follows:

$${}^AC_k^j = \frac{1}{2}\left(1 - \sum_{i=1}^{N_{\mathcal{F}}} C_{ki}^j\right). \tag{2.65}$$

Note that if the vector $\mathbf{m}^{jk}$ is coincident with and has the *same* orientation as the i^{th} fold centerline, then $a_{jk} = \hat{a}_i$. Conversely, if the vector $\mathbf{m}^{jk}$ is coincident with and has the *opposite* orientation as the i^{th} fold centerline, then $a_{jk} = 1 - \hat{a}_i$. This is

obtained from the mapping provided in Equation (2.64).

The fold widths associated with the smooth folds adjacent to $\mathcal{I}_0^j$ are denoted w_{jk}^0, $k = 1, \ldots, n_j$, and are required in the subsequent derivations. Let $\boldsymbol{w}^{0,j} \in \mathbb{R}^{n_j}$ be the vector constructed by collecting the fold widths w_{jk}^0, $k = 1, \ldots, n_j$. Such a vector and its mapping from $\hat{\boldsymbol{w}}^0$ (defined in Equation (2.19)) are as follows:

$$\begin{aligned} \boldsymbol{w}^{0,j} &= \begin{bmatrix} w_{j1}^0 \\ \vdots \\ w_{jn_j}^0 \end{bmatrix} \\ &= |\mathbf{C}^j|_* \, \hat{\boldsymbol{w}}^0. \end{aligned} \tag{2.66}$$

Let $\boldsymbol{\gamma}_j(\eta) : [0, 1] \to \mathcal{S}_0$ be an arbitrary simple closed path (i.e. $\boldsymbol{\gamma}_j(0) = \boldsymbol{\gamma}_j(1)$) enclosing $\mathcal{I}_0^j$ and crossing each smooth fold adjacent to $\mathcal{I}_0^j$ once. An example of a path $\boldsymbol{\gamma}_j(\eta)$ is shown in Figure 2.10. The point having position $\boldsymbol{\gamma}_j(0) = \boldsymbol{\gamma}_j(1)$ is defined such that it is located at the face adjacent to the smooth folds with corresponding vectors $\mathbf{m}^{j1}$ and $\mathbf{m}^{jn_j}$. Also, the path $\boldsymbol{\gamma}_j(\eta)$ is defined such that it crosses the smooth folds with associated vectors $\mathbf{m}^{jk}$ in counterclockwise order (i.e. $\mathbf{m}^{j1}, \mathbf{m}^{j2}, \ldots, \mathbf{m}^{jn_j}$).

The position vectors of the points where $\boldsymbol{\gamma}_j(\eta)$ crosses each boundary ruling of the smooth folds with associated vector $\mathbf{m}^{jk}$ are denoted $\mathbf{b}_L^{jk} \in \text{span}(\mathbf{e}_1, \mathbf{e}_2)$ (point where $\boldsymbol{\gamma}_j(\eta)$ enters the smooth fold) and $\mathbf{b}_R^{jk} \in \text{span}(\mathbf{e}_1, \mathbf{e}_2)$ (point where $\boldsymbol{\gamma}_j(\eta)$ exits the smooth fold). This is shown schematically in Figure 2.10(a).

Let $\mathbf{Q}_1(\phi) \in \mathbb{R}^{4\times4}$ be the transformation matrix in homogeneous coordinates

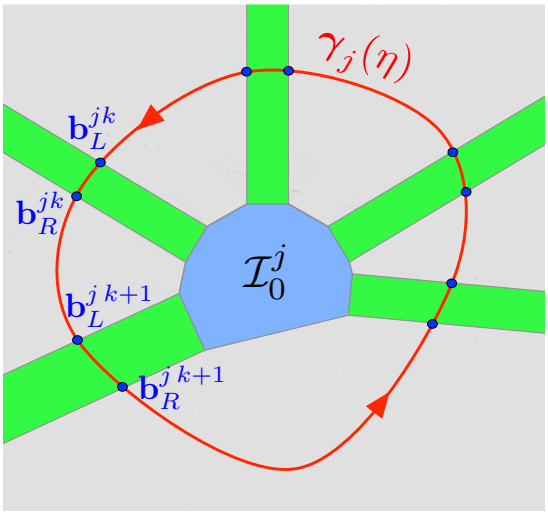

(a)

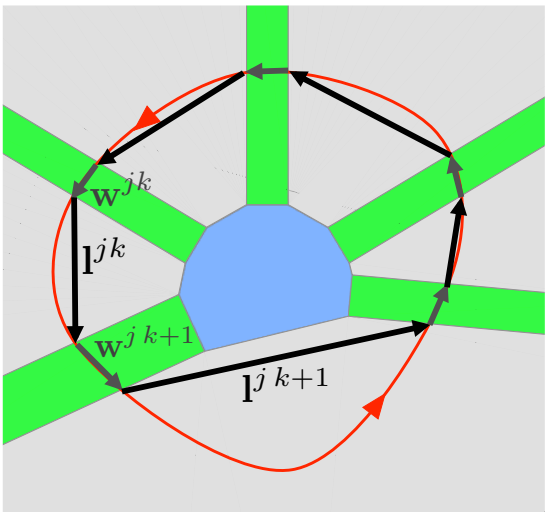

(b)

Figure 2.10: (a) Path $\boldsymbol{\gamma}_j(\eta)$ crossing the faces and smooth folds joined to $\mathcal{I}_0^j$. (b) Vectors $\mathbf{w}^{jk}$ and $\mathbf{l}^{jk}$ with start-points and end-points corresponding to the points where the path $\boldsymbol{\gamma}_j(\eta)$ crosses the boundary rulings of the smooth folds.

associated with a rotation by ϕ about an axis of rotation aligned to $\mathbf{e}_1$:

$$\mathbf{Q}_1(\phi) := \begin{bmatrix} 1 & 0 & 0 & 0 \\ 0 & \cos(\phi) & -\sin(\phi) & 0 \\ 0 & \sin(\phi) & \cos(\phi) & 0 \\ 0 & 0 & 0 & 1 \end{bmatrix} = \begin{bmatrix} \mathbf{R}_1(\phi) & \mathbf{0}_3 \\ \mathbf{0}_3^\top & 1 \end{bmatrix}, \tag{2.67}$$

and $\mathbf{Q}_3(\phi) \in \mathbb{R}^{4\times4}$ be the transformation matrix associated with a rotation by ϕ about an axis of rotation aligned to $\mathbf{e}_3$:

$$\mathbf{Q}_3(\phi) := \begin{bmatrix} \cos(\phi) & -\sin(\phi) & 0 & 0 \\ \sin(\phi) & \cos(\phi) & 0 & 0 \\ 0 & 0 & 1 & 0 \\ 0 & 0 & 0 & 1 \end{bmatrix} = \begin{bmatrix} \mathbf{R}_3(\phi) & \mathbf{0}_3 \\ \mathbf{0}_3^\top & 1 \end{bmatrix}. \tag{2.68}$$

Let $\mathbf{T}(\mathbf{b}) \in \mathbb{R}^{4\times4}$ be the matrix representing the transformation associated with a translation by vector $\mathbf{b} \in \mathbb{R}^3$ with elements b_i:

$$\mathbf{T}(\mathbf{b}) := \begin{bmatrix} 1 & 0 & 0 & b_1 \\ 0 & 1 & 0 & b_2 \\ 0 & 0 & 1 & b_3 \\ 0 & 0 & 0 & 1 \end{bmatrix} = \begin{bmatrix} \mathbf{I}_3 & \mathbf{b} \\ \mathbf{0}_3^\top & 1 \end{bmatrix}. \tag{2.69}$$

Considering an axis with direction aligned to a vector $\mathbf{y} \in \text{span}(\mathbf{e}_1, \mathbf{e}_2)$ that crosses a point with position vector $\mathbf{b} \in \text{span}(\mathbf{e}_1, \mathbf{e}_2)$, the transformation associated

with a rotation by ϕ about such an axis can be represented as follows [121, 276]:

$$\mathbf{T}(\mathbf{b})\,\mathbf{Q}_3(\varphi(\mathbf{y}))\,\mathbf{Q}_1(\phi)\,\mathbf{Q}_3^{-1}(\varphi(\mathbf{y}))\,\mathbf{T}^{-1}(\mathbf{b}). \tag{2.70}$$

Theorem 2.1. *The transformation matrix* $\mathbf{L}^{jk}$ *describing the deformation associated with the folding of the* k^{th} *smooth fold crossed by the path* $\boldsymbol{\gamma}_j(\eta)$ *is determined as follows*[8]*:*

$$\begin{aligned}\mathbf{L}^{jk} \;=\; &\Big(\mathbf{T}(\mathbf{b}_L^{jk} - \mathbf{g}^{j\,k-1})\,\mathbf{Q}_3(\varphi(\mathbf{m}^{jk}))\,\mathbf{Q}_1(a_{jk}\theta_{jk})\\ &\times \mathbf{Q}_3^{-1}(\varphi(\mathbf{m}^{jk}))\,\mathbf{T}^{-1}(\mathbf{b}_L^{jk} - \mathbf{g}^{j\,k-1})\\ &\times \mathbf{T}(\mathbf{b}_R^{jk} - \mathbf{g}^{jk})\,\mathbf{Q}_3(\varphi(\mathbf{m}^{jk}))\,\mathbf{Q}_1((1-a_{jk})\theta_{jk})\\ &\times \mathbf{Q}_3^{-1}(\varphi(\mathbf{m}^{jk}))\,\mathbf{T}^{-1}(\mathbf{b}_R^{jk} - \mathbf{g}^{jk})\Big),\end{aligned} \tag{2.71}$$

where the vectors $\mathbf{g}^{jk} \in \operatorname{span}(\mathbf{e}_1, \mathbf{e}_2)$*,* $k = 0, \ldots, n_j$*, are used to accounting for the change in the distance between the boundary rulings of the smooth folds in a current configuration and are determined recursively as follows:*

$$\begin{aligned}&\mathbf{g}^{j0} = \mathbf{0}_3,\\ &\mathbf{g}^{jk} = \mathbf{g}^{j\,k-1} + (w_{jk}^0 - w_{jk})\left(\mathbf{e}_3 \times \frac{\mathbf{m}^{jk}}{\|\mathbf{m}^{jk}\|}\right) \quad \forall\, k \in \{1, \ldots, n_j\}.\end{aligned} \tag{2.72}$$

Proof. Referring to Figures 2.11(c) and 2.11(d), the transformation associated with the folding of the k^{th} smooth fold crossed by $\boldsymbol{\gamma}_j(\eta)$ can be discretized by two consecutive rotation transformations. The first transformation corresponds to a rotation by

[8]Alternative approaches for modeling the large rotations resulting from folding include quaternions-based [273] and geometric algebra-based approaches [429]. However, such approaches are not explored in this work.

$(1-a_{jk})\theta_{jk}$ about an axis aligned to $\mathbf{m}^{jk}$ and crossing a point with position vector $\mathbf{b}_R^{jk}-\mathbf{g}^{jk}$. Using Equation (2.70), the transformation matrix associated with this rotation is the following:

$$\begin{aligned}\Big(&\mathbf{T}(\mathbf{b}_R^{jk}-\mathbf{g}^{jk})\mathbf{Q}_3(\varphi(\mathbf{m}^{jk}))\mathbf{Q}_1((1-a_{jk})\theta_{jk})\\&\times\mathbf{Q}_3^{-1}(\varphi(\mathbf{m}^{jk}))\mathbf{T}^{-1}(\mathbf{b}_R^{jk}-\mathbf{g}^{jk})\Big).\end{aligned}\tag{2.73}$$

The second transformation corresponds to a rotation by $a_{jk}\theta_{jk}$ about an axis aligned to $\mathbf{m}^{jk}$ and a crossing point with position vector $\mathbf{b}_L^{jk}-\mathbf{g}^{j\,k-1}$. The transformation matrix associated with this rotation has the form:

$$\begin{aligned}\Big(&\mathbf{T}(\mathbf{b}_L^{jk}-\mathbf{g}^{j\,k-1})\mathbf{Q}_3(\varphi(\mathbf{m}^{jk}))\mathbf{Q}_1(a_{jk}\theta_{jk})\\&\times\mathbf{Q}_3^{-1}(\varphi(\mathbf{m}^{jk}))\mathbf{T}^{-1}(\mathbf{b}_L^{jk}-\mathbf{g}^{j\,k-1})\Big).\end{aligned}\tag{2.74}$$

The composition of the transformations shown in Equations (2.73) and (2.74) results in the transformation matrix $\mathbf{L}^{jk}$ provided in Equation (2.71).

Referring to Figures 2.11(a) and 2.11(b), the change in the distance between the boundary rulings of a smooth fold in a current configuration is given by $-(w_{jk}^0-w_{jk})$. To define the position of the axes of rotation for the transformations composing $\mathbf{L}^{jk}$, the vector $\sum_{l=1}^{k-1}(w_{jl}^0-w_{jl})(\mathbf{e}_3\times\frac{\mathbf{m}^{jl}}{\|\mathbf{m}^{jl}\|})$ must be subtracted from $\mathbf{b}_L^{jk}$ while $\sum_{l=1}^{k}(w_{jl}^0-w_{jl})(\mathbf{e}_3\times\frac{\mathbf{m}^{jl}}{\|\mathbf{m}^{jl}\|})$ must be subtracted from $\mathbf{b}_R^{jk}$. The recursive definition of the vectors $\mathbf{g}^{jk}$, $k=0,\ldots,n_j$, in Equation (2.72) allows for a simplified form of these vector subtractions. □

Utilizing the block matrix expressions for the rotation and translation matrices given in Equations (2.67)–(2.69), the transformation matrices $\mathbf{L}^{jk}$ provided in Equation (2.71) can be partitioned into four blocks ($[\mathbf{L}^{jk}]_{11\,\text{block}}\in\mathbb{R}^{3\times3}$, $[\mathbf{L}^{jk}]_{12\,\text{block}}\in\mathbb{R}^{3\times1}$,

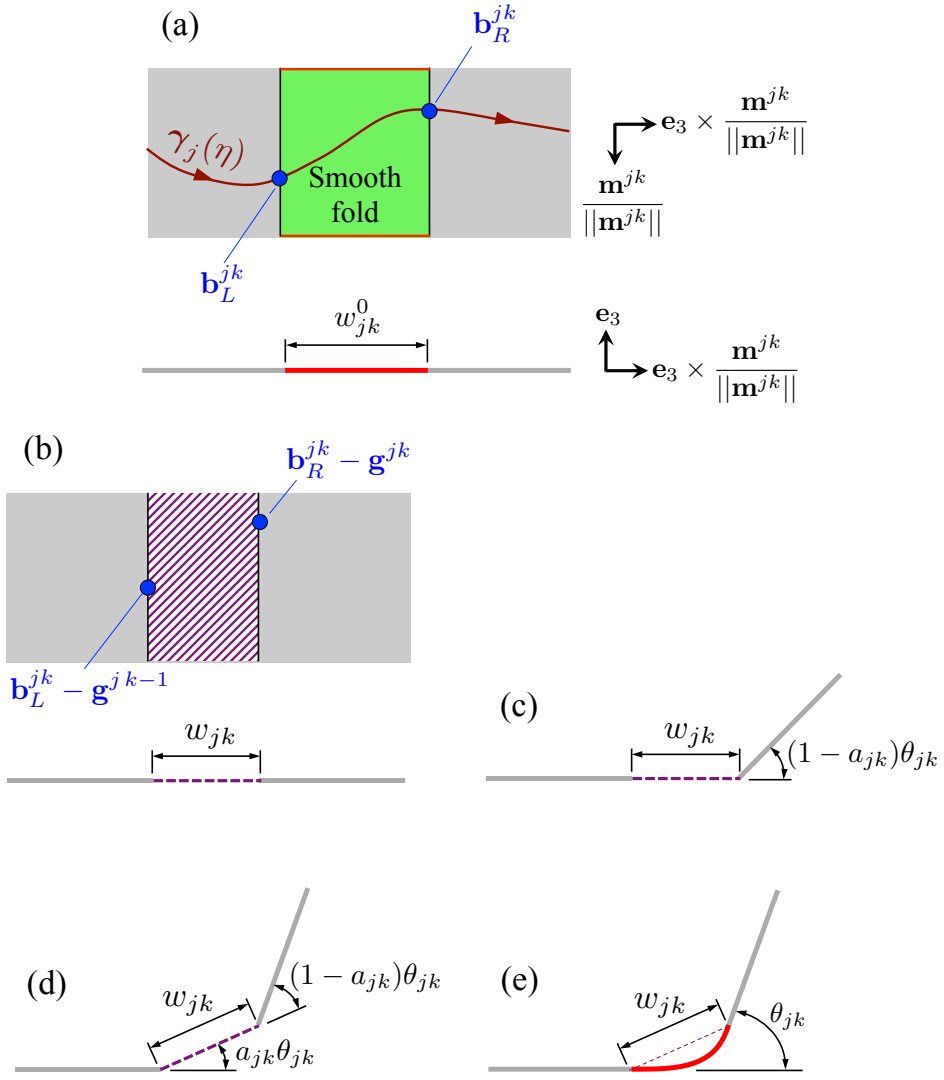

Figure 2.11: Schematics illustrating the transformation associated with folding of the k^{th} smooth fold crossed by $\boldsymbol{\gamma}_j(\eta)$. (a) Reference configuration of the fold. (b) Intermediate step to determine the location of the axes of rotation taking into account the change in the distance between the boundary rulings of the smooth fold in a current configuration. Note that the vector $\mathbf{g}^{j\,k-1}$ is subtracted from $\mathbf{b}_L^{jk}$ to account for the previous smooth folds crossed by $\boldsymbol{\gamma}_j(\eta)$. (c) Rotation by $(1-a_{jk})\theta_{jk}$ about an axis aligned to $\mathbf{m}^{jk}$ and crossing a point with position vector $\mathbf{b}_R^{jk} - \mathbf{g}^{jk}$. (d) Rotation by $a_{jk}\theta_{jk}$ about an axis aligned to $\mathbf{m}^{jk}$ and a crossing point with position vector $\mathbf{b}_L^{jk} - \mathbf{g}^{j\,k-1}$. (e) Resulting configuration of the smooth fold and its adjacent faces.

$[\mathbf{L}^{jk}]_{21\,\text{block}} \in \mathbb{R}^{1\times 3}$, $[\mathbf{L}^{jk}]_{22\,\text{block}} \in \mathbb{R}^{1\times 1}$) as follows:

$$\left[\mathbf{L}^{jk}\right]_{11\,\text{block}} = \mathbf{R}_3(\varphi(\mathbf{m}^{jk}))\mathbf{R}_1(\theta_{jk})\mathbf{R}_3^{-1}(\varphi(\mathbf{m}^{jk})), \tag{2.75}$$

$$\begin{aligned}\left[\mathbf{L}^{jk}\right]_{12\,\text{block}} \;=\; & \mathbf{b}_L^{jk} - \mathbf{g}^{j\,k-1} \\ & + \mathbf{R}_3(\varphi(\mathbf{m}^{jk}))\mathbf{R}_1(a_{jk}\theta_{jk})\mathbf{R}_3^{-1}(\varphi(\mathbf{m}^{jk})(\mathbf{b}_R^{jk} - \mathbf{g}^{jk} - \mathbf{b}_L^{jk} + \mathbf{g}^{j\,k-1}) \\ & - \mathbf{R}_3(\varphi(\mathbf{m}^{jk}))\mathbf{R}_1(\theta_{jk})\mathbf{R}_3^{-1}(\varphi(\mathbf{m}^{jk}))(\mathbf{b}_R^{jk} - \mathbf{g}^{jk}),\end{aligned} \tag{2.76}$$

$$\left[\mathbf{L}^{jk}\right]_{21\,\text{block}} = \mathbf{0}_3^\top, \tag{2.77}$$

$$\left[\mathbf{L}^{jk}\right]_{22\,\text{block}} = 1. \tag{2.78}$$

The vectors $\mathbf{w}^{jk},\ \mathbf{l}^{jk} \in \text{span}(\mathbf{e}_1, \mathbf{e}_2)$ are defined as follows:

$$\mathbf{w}^{jk} := \mathbf{b}_R^{jk} - \mathbf{g}^{jk} - \mathbf{b}_L^{jk} + \mathbf{g}^{j\,k-1}, \tag{2.79}$$

$$\mathbf{l}^{jk} := \begin{cases} \mathbf{b}_L^{j\,k+1} - \mathbf{b}_R^{jk}; & k = 1, \ldots, n_j - 1 \\ \\ \mathbf{b}_L^{j1} - \mathbf{b}_R^{jk}; & k = n_j \end{cases}. \tag{2.80}$$

The vectors $\mathbf{w}^{jk}$ and $\mathbf{l}^{jk}$ for the example in Figure 2.10(a) are shown in Figure 2.10(b). Let the vectors $\tilde{\mathbf{w}}^{jk}$ and $\tilde{\mathbf{l}}^{jk}$ be $\mathbf{w}^{jk}$ and $\mathbf{l}^{jk}$, respectively, expressed in a

coordinate system with the 1-axis aligned to $\mathbf{m}^{jk}$ and the 3-axis aligned to $\mathbf{e}_3$:

$$\tilde{\mathbf{w}}^{jk} = \mathbf{R}_3^{-1}(\varphi(\mathbf{m}^{jk}))\mathbf{w}^{jk}, \tag{2.81}$$

$$\tilde{\mathbf{l}}^{jk} = \mathbf{R}_3^{-1}(\varphi(\mathbf{m}^{jk}))\mathbf{l}^{jk}. \tag{2.82}$$

Following the process presented in [121, 276], to formulate constraints for the shape variables associated with the folds, the map from the reference to current configurations considering only the faces and smooth folds adjacent to an interior fold intersection is first constructed. The face containing the point with position $\boldsymbol{\gamma}_j(0)$ is assumed *fixed* in space (not translating or rotating) for the derivation of constraints. Let $\mathbf{X} \in \text{span}(\mathbf{e}_1, \mathbf{e}_2)$ be the position vector of a point in a face adjacent to $\mathcal{I}_0^j$ in the reference configuration and let $\mathbf{x} \in \mathbb{R}^3$ be the position vector of such a point in a current configuration. The map $\mathbf{X} \mapsto \mathbf{x}$ is constructed as the composition of transformations $\mathbf{L}^{jk}$ associated with the folds crossed by the segment of path $\boldsymbol{\gamma}_j(\eta)$ that connects $\boldsymbol{\gamma}_j(0)$ to the face containing the point with initial position $\mathbf{X}$:

$$\begin{aligned} \begin{bmatrix} \mathbf{x} \\ 1 \end{bmatrix} &= \left(\prod_{k=1}^{n_y} \mathbf{L}^{jk} \right) \mathbf{T}^{-1}(\mathbf{g}^{jn_y}) \begin{bmatrix} \mathbf{X} \\ 1 \end{bmatrix}, \\ &= \left(\prod_{k=1}^{n_y} \mathbf{H}^{jk} \right) \begin{bmatrix} \mathbf{X} \\ 1 \end{bmatrix}, \end{aligned} \tag{2.83}$$

where the *simplified fold transformation matrices* $\mathbf{H}^{jk}$, $j = 1, \ldots, N_{\mathcal{I}}$, $k = 1, \ldots, n_j$,

are expressed as follows:

$$\begin{aligned}\mathbf{H}^{jk} \;=\; & \Big(\mathbf{T}(\mathbf{b}_L^{jk})\,\mathbf{Q}_3(\varphi(\mathbf{m}^{jk}))\,\mathbf{Q}_1(a_{jk}\theta_{jk}) \\ & \times \mathbf{Q}_3^{-1}(\varphi(\mathbf{m}^{jk}))\,\mathbf{T}^{-1}(\mathbf{b}_L^{jk}) \\ & \times \mathbf{T}^{-1}\left((w_{jk}^0 - w_{jk})\left(\mathbf{e}_3 \times \tfrac{\mathbf{m}^{jk}}{\|\mathbf{m}^{jk}\|}\right)\right) \\ & \times \mathbf{T}(\mathbf{b}_R^{jk})\,\mathbf{Q}_3(\varphi(\mathbf{m}^{jk}))\,\mathbf{Q}_1((1-a_{jk})\theta_{jk}) \\ & \times \mathbf{Q}_3^{-1}(\varphi(\mathbf{m}^{jk}))\,\mathbf{T}^{-1}(\mathbf{b}_R^{jk})\Big),\end{aligned} \tag{2.84}$$

and n_y is the number of smooth folds crossed by the segment of the path $\boldsymbol{\gamma}_j(\eta)$ that connects $\boldsymbol{\gamma}_j(0)$ and the face containing the point with position vector $\mathbf{X}$. Note that $\mathbf{x}$ is the position vector of such a point in a current configuration determined by θ_{jk}, a_{jk}, and w_{jk}, $k = 1, \ldots, n_j$. Since such a mapping is a composition of translation and rotation matrices, each face undergoes a rigid deformation (required for a valid configuration). In order to prevent tearing among the surface subdomains joined to $\mathcal{I}_t^j$, the following constraints are proposed:

Theorem 2.2. *For the initially closed strip of faces and smooth folds joined to $\mathcal{I}_0^j$ to remain closed with each face undergoing a rigid deformation, two constraints must hold. These are the rotation constraint:*

$$\mathbf{R}^j := \prod_{k=1}^{n_j} \mathbf{R}_1(\theta_{jk})\mathbf{R}_3(\alpha_{jk}) = \mathbf{I}_3, \tag{2.85}$$

and the translation constraint:

$$\mathbf{d}^j := \sum_{k=1}^{n_j} \left(\left(\prod_{l=1}^{k-1} \mathbf{R}_1(\theta_{jl}) \mathbf{R}_3(\alpha_{jl}) \right) \mathbf{R}_1 \left(a_{jk} \theta_{jk} \right) \tilde{\mathbf{w}}^{jk} + \left(\prod_{l=1}^{k-1} \mathbf{R}_1(\theta_{jl}) \mathbf{R}_3(\alpha_{jl}) \right) \mathbf{R}_1 \left(\theta_{jk} \right) \tilde{\mathbf{l}}^{jk} \right) = \mathbf{0}_3. \tag{2.86}$$

Proof. The deformation map of a point in the face containing the point with position $\boldsymbol{\gamma}_j(0)$ must be the identity transformation since such a face is assumed fixed (i.e. if $n_y = n_j$ in Equation (2.83) is considered, then $\mathbf{x} = \mathbf{X}$). This requires the following:

$$\begin{aligned} \mathbf{I}_4 &= \prod_{k=1}^{n_j} \mathbf{H}^{jk} \\ &= \left(\prod_{k=1}^{n_j} \mathbf{L}^{jk} \right) \mathbf{T}^{-1}(\mathbf{g}^{jn_j}). \end{aligned} \tag{2.87}$$

Utilizing Equations (2.75)–(2.78), Equation (2.87) can be partitioned into four blocks. The 11 block is the following:

$$\begin{aligned} \mathbf{I}_3 &= \prod_{j=1}^{n_j} \mathbf{R}_3(\varphi(\mathbf{m}^{jk})) \mathbf{R}_1(\theta_{ij}) \mathbf{R}_3^{-1}(\varphi(\mathbf{m}^{jk})), \\ &= \mathbf{R}_3(\varphi(\mathbf{m}^{j1})) \left(\prod_{k=1}^{n_j - 1} \mathbf{R}_1(\theta_{jk}) \mathbf{R}_3(\alpha_{jk}) \right) \mathbf{R}_1(\theta_{jn_j}) \mathbf{R}_3^{-1}(\varphi(\mathbf{m}^{jn_j})), \end{aligned} \tag{2.88}$$

where the following equality was used:

$$\mathbf{R}_3(\alpha_{jk}) = \begin{cases} \mathbf{R}_3^{-1}(\varphi(\mathbf{m}^{jk})) \mathbf{R}_3(\varphi(\mathbf{m}^{j\,k+1})); & k = 1, \ldots, n_j - 1 \\ \\ \mathbf{R}_3^{-1}(\varphi(\mathbf{m}^{jk})) \mathbf{R}_3(\varphi(\mathbf{m}^{j1})); & k = n_j \end{cases}. \tag{2.89}$$

Multiplying the last expression in Equation (2.88) by $\mathbf{R}_3^{-1}\big(\varphi(\mathbf{m}^{j1})\big)$ from the left and by $\mathbf{R}_3\big(\varphi(\mathbf{m}^{j1})\big)$ from the right, the following is obtained:

$$\begin{aligned}
\mathbf{I}_3 &= \Bigg(\prod_{k=1}^{n_j-1}\mathbf{R}_1(\theta_{jk})\mathbf{R}_3(\alpha_{jk})\Bigg)\mathbf{R}_1(\theta_{jn_j})\mathbf{R}_3^{-1}(\varphi(\mathbf{m}^{jn_j}))\mathbf{R}_3(\varphi(\mathbf{m}^{j1})),\\
&= \Bigg(\prod_{k=1}^{n_j-1}\mathbf{R}_1(\theta_{jk})\mathbf{R}_3(\alpha_{jk})\Bigg)\mathbf{R}_1(\theta_{jn_j})\mathbf{R}_3(\alpha_{jn_j}),\\
&= \prod_{k=1}^{n_j}\mathbf{R}_1(\theta_{jk})\mathbf{R}_3(\alpha_{jk}),\\
&= \mathbf{R}^j,
\end{aligned} \tag{2.90}$$

cf. Equation (2.85). The 12 block of Equation (2.87) is the following:

$$\begin{aligned}
\mathbf{0}_3 = \sum_{k=1}^{n_j}\Bigg(&\Bigg(\prod_{l=1}^{k-1}\mathbf{R}_3(\varphi(\mathbf{m}^{jl}))\mathbf{R}_1(\theta_{jl})\mathbf{R}_3^{-1}(\varphi(\mathbf{m}^{jl}))\Bigg)\\
&\times\Bigg(\mathbf{b}_L^{jk}-\mathbf{g}^{j\,k-1}\\
&\quad+\Big(\mathbf{R}_3(\varphi(\mathbf{m}^{jk}))\mathbf{R}_1(a_{jk}\theta_{jk})\\
&\qquad\times\mathbf{R}_3^{-1}(\varphi(\mathbf{m}^{jk}))(\mathbf{b}_R^{jk}-\mathbf{g}^{jk}-\mathbf{b}_L^{jk}+\mathbf{g}^{j\,k-1})\Big)\\
&\quad-\Big(\mathbf{R}_3(\varphi(\mathbf{m}^{jk}))\mathbf{R}_1(\theta_{jk})\mathbf{R}_3^{-1}(\varphi(\mathbf{m}^{jk}))(\mathbf{b}_R^{jk}-\mathbf{g}^{jk})\Big)\Bigg)\Bigg)\\
&-\Bigg(\prod_{k=1}^{n_j}\mathbf{R}_3(\varphi(\mathbf{m}^{jk}))\mathbf{R}_1(\theta_{jk})\mathbf{R}_3^{-1}(\varphi(\mathbf{m}^{jk}))\Bigg)\mathbf{g}^{jn_j}.
\end{aligned} \tag{2.91}$$

Substituting the second expression of Equation (2.88) and Equations (2.81) and

(2.82) into Equation (2.91), the following is obtained:

$$\mathbf{0}_3 = \sum_{k=1}^{n_j} \left(\left(\prod_{l=1}^{k-1} \mathbf{R}(\varphi(\mathbf{m}^{jl})) \mathbf{R}_1(\theta_{jl}) \mathbf{R}_3^{-1}(\varphi(\mathbf{m}^{jl})) \right) \right.$$
$$\left. \left(\mathbf{R}_3(\varphi(\mathbf{m}^{jk})) \mathbf{R}_1(a_{jk}\theta_{jk}) \tilde{\mathbf{w}}^{jk} + \mathbf{R}_3(\varphi(\mathbf{m}^{jk})) \mathbf{R}_1(\theta_{jk}) \tilde{\mathbf{l}}^{jk} \right) \right). \tag{2.92}$$

Finally multiplying both sides of the previous expression by $\mathbf{R}_3^{-1}(\varphi(\mathbf{m}^{j1}))$ and simplifying using Equation (2.89), the following is obtained:

$$\begin{aligned} \mathbf{0}_3 &= \sum_{k=1}^{n_j} \left(\left(\prod_{l=1}^{k-1} \mathbf{R}_1(\theta_{jl}) \mathbf{R}_3(\alpha_{jl}) \right) \mathbf{R}_1 \left(a_{jk}\theta_{jk} \right) \tilde{\mathbf{w}}^{jk} \right. \\ &\qquad \left. + \left(\prod_{l=1}^{k-1} \mathbf{R}_1(\theta_{jl}) \mathbf{R}_3(\alpha_{jl}) \right) \mathbf{R}_1 \left(\theta_{jk} \right) \tilde{\mathbf{l}}^{jk} \right), \\ &= \mathbf{d}^j, \end{aligned} \tag{2.93}$$

cf. Equation (2.86). The 21 and the 22 blocks of the right side of Equation (2.87) are equal to $\mathbf{0}_3^\top$ and 1, respectively. □

Corollary 2.2. *(i) If $\mathcal{I}_0^j$ has a single adjacent smooth fold, it allows for a valid configuration if $\theta_{j1} = 0$.*

(ii) If $\mathcal{I}_0^j$ has two adjacent smooth folds, it allows for a valid configuration if (ii,1) $\alpha_{j1} \neq \pi, \theta_{j1} = \theta_{j2} = 0$ or (ii,2) $\alpha_{j1} = \pi, \theta_{j1} = \theta_{j2}$.

(iii) If $\mathcal{I}_0^j$ has three adjacent smooth folds, it allows for a valid configuration if (iii,1) $\alpha_{j1} \neq \pi, \alpha_{j2} \neq \pi, \alpha_{j3} \neq \pi, \theta_{j1} = \theta_{j2} = \theta_{j3} = 0$, or (iii,2) $\alpha_{j1} = \pi, \theta_{j1} = \theta_{j2}, \theta_{j3} = 0$, or (iii,3) $\alpha_{j2} = \pi, \theta_{j2} = \theta_{j3}, \theta_{j1} = 0$, or (iii,4) $\alpha_{j3} = \pi, \theta_{j3} = \theta_{j1}, \theta_{j2} = 0$.

Since the rotation constraint for smooth folds ($\mathbf{R}^j = \mathbf{I}_3$, cf. Equation (2.85)) also holds for creased folds (cf. Equation (2.14)), the proof of this corollary is the same as that provided for Corollary 2.1.

The selection of the vectors $\mathbf{b}_L^{jk}, \mathbf{b}_R^{jk}$, $k = 1, \ldots, n_j$ is not unique and depends on the particular choice of the closed path $\boldsymbol{\gamma}_j(\eta)$ (see Figure 2.10(a)). The corner points of the smooth folds defined in Equations (2.54)–(2.57) provide a simple choice for the points where $\boldsymbol{\gamma}_j(\eta)$ crosses the boundary rulings of each smooth fold adjacent to $\mathcal{I}_0^j$. Thus, they can be used to define $\mathbf{b}_L^{jk}, \mathbf{b}_R^{jk}$, $k = 1, \ldots, n_j$. First, let $\mathbf{B}_L^j, \mathbf{B}_R^j \in \mathbb{R}^{3n_j}$ be the vectors constructed by concatenating the vectors $\mathbf{b}_L^{jk}, \mathbf{b}_R^{jk}$, $k = 1, \ldots, n_j$, as follows:

$$\mathbf{B}_L^j = \begin{bmatrix} \mathbf{b}_L^{j1} \\ \vdots \\ \mathbf{b}_L^{jn_j} \end{bmatrix}, \tag{2.94}$$

$$\mathbf{B}_R^j = \begin{bmatrix} \mathbf{b}_R^{j1} \\ \vdots \\ \mathbf{b}_R^{jn_j} \end{bmatrix}. \tag{2.95}$$

Taking into account the orientation of the adjacent smooth folds with respect to the considered fold intersection $\mathcal{I}_0^j$ (i.e. whether the interior vertex associated with $\mathcal{I}_0^j$ is the start-point or the end-point of the adjacent smooth fold centerline), the mapping from the corner points of the smooth folds to $\mathbf{B}_L^j$ and $\mathbf{B}_R^j$ is compactly

given as follows:

$$\begin{bmatrix} \mathbf{B}_L^j \\ \\ \mathbf{B}_R^j \end{bmatrix} = \begin{bmatrix} \frac{1}{2}(|\mathbf{C}^j|_* + \mathbf{C}^j) \otimes \mathbf{I}_3 & \frac{1}{2}(|\mathbf{C}^j|_* - \mathbf{C}^j) \otimes \mathbf{I}_3 \\ \\ \frac{1}{2}(|\mathbf{C}^j|_* - \mathbf{C}^j) \otimes \mathbf{I}_3 & \frac{1}{2}(|\mathbf{C}^j|_* + \mathbf{C}^j) \otimes \mathbf{I}_3 \end{bmatrix} \begin{bmatrix} \hat{\mathbf{P}}^1 \\ \\ \hat{\mathbf{P}}^4 \end{bmatrix}, \tag{2.96}$$

where the vectors $\hat{\mathbf{P}}^i$ are defined in Equation (2.59). Note that the mapping provided in Equation (2.96) results in $\mathbf{b}_L^{jk} = \hat{\mathbf{p}}_1^i$, $\mathbf{b}_R^{jk} = \hat{\mathbf{p}}_4^i$ if $\mathbf{m}^{jk}$ is coincident with and has the same orientation as the i^{th} smooth fold centerline and $\mathbf{b}_L^{jk} = \hat{\mathbf{p}}_4^i$, $\mathbf{b}_R^{jk} = \hat{\mathbf{p}}_1^i$ if $\mathbf{m}^{jk}$ is coincident with and has the opposite orientation as the i^{th} smooth fold centerline.

Finally, the constraints on the fold shape variables that allow for a valid configuration (excluding self-intersection avoidance) for a sheet with smooth folds are then the following:

$$\mathbf{R}^j = \mathbf{I}_3, \quad \mathbf{d}^j = \mathbf{0}_3 \qquad \forall\, j \in \{1, \ldots, N_{\mathcal{I}}\}, \tag{2.97}$$

cf. Equation (2.15).

In general, the variables $\hat{\theta}_i$, $\hat{w}_i$, and $\hat{a}_i$ for each individual smooth fold represent its shape variables (i.e. degrees of freedom) that describe its configuration. If certain assumptions hold regarding the deformation of each individual smooth fold, the associated variables $\hat{\theta}_i$, $\hat{w}_i$, and $\hat{a}_i$ may not vary independently but rather relations among them can be derived. For simplicity in the implementation of the proposed model, assumptions on the extensibility and curvature field of the curve $\hat{\mathbf{c}}^i(\zeta_1)$ are taken such that the overall deformation of a smooth fold becomes a function of the fold angle $\hat{\theta}_i$ and the arc-length $\hat{s}_i$ (i.e. $\hat{w}_i = \hat{w}_i(\hat{\theta}_i, \hat{s}_i)$, $\hat{a}_i = \hat{a}_i(\hat{\theta}_i, \hat{s}_i)$ for each fold). Such a process involves non-dimensionalization of the parametric curve $\hat{\mathbf{c}}^i(\zeta_1)$ and is

presented in detail in Section 2.2.5 for the case of smooth folds exhibiting G^1 and G^2 continuity.

2.2.4 Folding Map

The formulation of the deformation mapping that relates the reference and current configurations (termed *folding map* here) is provided in this section. A folding map considering only the smooth folds and faces adjacent to an interior fold intersection was presented in Equation (2.83). Here such a formulation is extended for the derivation of a folding map for all the smooth folds and faces in the sheet.

First, an arbitrary face in the sheet is assumed fixed in its reference configuration[9]. Let $\breve{\boldsymbol{\gamma}}_j(\eta) : [0,1] \rightarrow \mathcal{S}_0$, $j = 1, \ldots, N_{\mathcal{P}}$, be paths connecting the fixed face to $\mathcal{P}_0^j$, $j = 1, \ldots, N_{\mathcal{P}}$, respectively (see Figure 2.12 for an example). The paths $\breve{\boldsymbol{\gamma}}_j(\eta)$, $j = 1, \ldots, N_{\mathcal{P}}$, may not cross any fold intersection (i.e. they pass only through faces and smooth folds of $\mathcal{S}_0$). Following the formulation of Equation (2.83), the map for points located in the faces is constructed as the composition of transformations associated with the smooth folds crossed by the path $\breve{\boldsymbol{\gamma}}^j(\eta)$ between $\breve{\boldsymbol{\gamma}}^j(0)$ (located at the fixed face) and $\breve{\boldsymbol{\gamma}}^j(1)$ (located at $\mathcal{P}_0^j$). Each path $\breve{\boldsymbol{\gamma}}^j(\eta)$ crosses a number of p_j smooth folds.

The path $\breve{\boldsymbol{\gamma}}^j(\eta)$ crosses a smooth fold *positively* if it enters such a fold from the ruling $\boldsymbol{\mathcal{F}}^i(-1, \zeta_2)$ and exits at the ruling $\boldsymbol{\mathcal{F}}^i(1, \zeta_2)$. Conversely, the path $\breve{\boldsymbol{\gamma}}^j(\eta)$ crosses a smooth fold *negatively* if it crosses such a fold in the opposite direction. The matrices $\breve{\mathbf{C}}^j \in \{-1, 0, 1\}^{p_j \times N_{\mathcal{F}}}$, $j = 1, \ldots, N_{\mathcal{P}}$, with elements $\breve{C}_{ki}^j$ are used for

[9] A breve ($\breve{}$) is used to distinguish the symbols related to the folding map from the symbols used in Section 2.2.3.

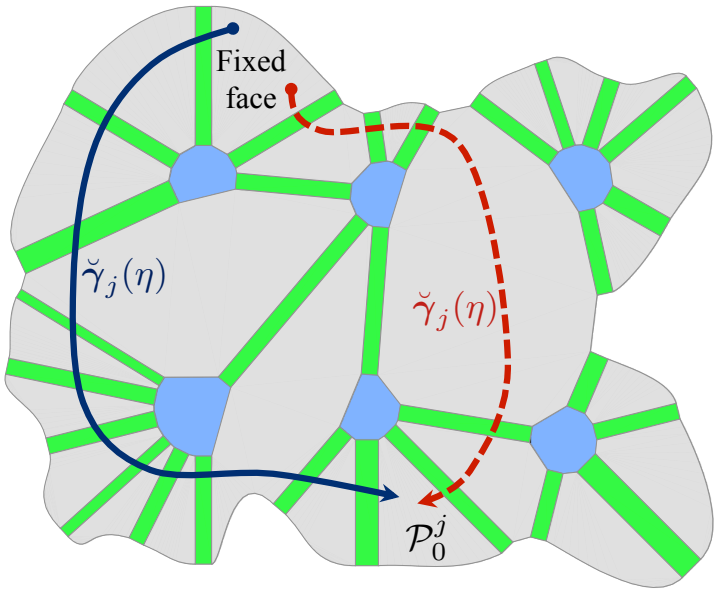

(a)

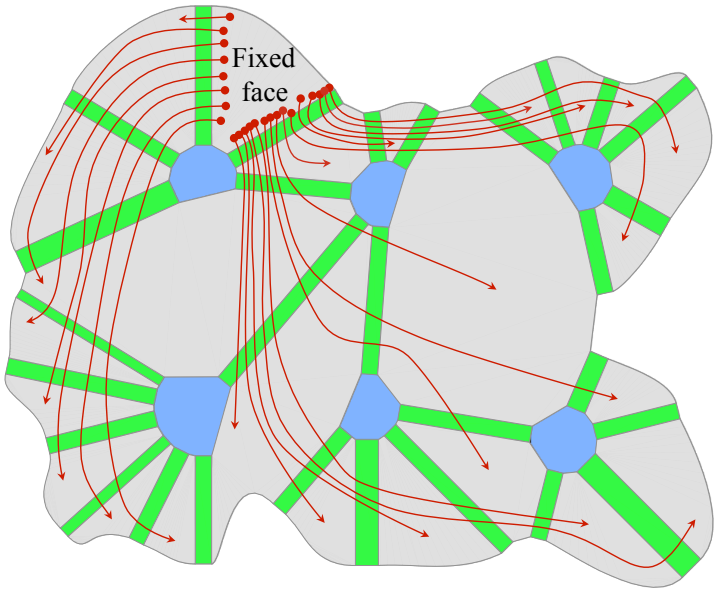

(b)

Figure 2.12: (a) Two equivalent paths $\breve{\gamma}_j(\eta)$ connecting the fixed face to $\mathcal{P}_0^j$. (b) Paths $\breve{\gamma}^j(\eta)$, $j = 1, \ldots, N_{\mathcal{P}}$, connecting the fixed face to every other face in $\mathcal{S}_0$.

the identification and ordering of the folds crossed by $\breve{\boldsymbol{\gamma}}^j(\eta)$:

$$\breve{C}^j_{ki} = \begin{cases} 1; & \mathcal{F}^i_0 \text{ is the } k^{\text{th}} \text{ fold crossed by } \breve{\boldsymbol{\gamma}}^j(\eta) \text{ and is positively crossed} \\ -1; & \mathcal{F}^i_0 \text{ is the } k^{\text{th}} \text{ fold crossed by } \breve{\boldsymbol{\gamma}}^j(\eta) \text{ and is negatively crossed} \\ 0; & \text{otherwise} \end{cases} . \tag{2.98}$$

Let $\breve{\mathbf{m}}^{jk}$ be the vector along the length of the centerline of the k^{th} smooth fold crossed by $\breve{\boldsymbol{\gamma}}_j(\eta)$. Such a vector has the same orientation as the fold centerline if $\breve{\boldsymbol{\gamma}}_j(\eta)$ crosses the fold positively and opposite orientation if $\breve{\boldsymbol{\gamma}}_j(\eta)$ crosses the fold negatively. The vector $\breve{\mathbf{M}}^j \in \mathbb{R}^{3p_j}$ is constructed by concatenating the vectors $\breve{\mathbf{m}}^{jk}$, $k = 1, \ldots, p_j$, as follows:

$$\breve{\mathbf{M}}^j = \begin{bmatrix} \breve{\mathbf{m}}^{j1} \\ \vdots \\ \breve{\mathbf{m}}^{jp_j} \end{bmatrix} . \tag{2.99}$$

The mapping from the vertex position vectors collected in the vector $\mathbf{V}$ to each vector $\breve{\mathbf{M}}^j$ is compactly given as follows:

$$\breve{\mathbf{M}}^j = \left((\breve{\mathbf{C}}^j \widehat{\mathbf{C}}) \otimes \mathbf{I}_3 \right) \mathbf{V}. \tag{2.100}$$

Let $\breve{\theta}_{jk}$, $\breve{w}_{jk}$, and $\breve{a}_{jk}$, $k = 1, \ldots, p_j$, be the shape variables associated with the ordered smooth folds crossed by $\breve{\boldsymbol{\gamma}}_j(\eta)$. The vectors $\breve{\boldsymbol{\theta}}^j, \breve{\boldsymbol{w}}^j, \breve{\boldsymbol{a}}^j \in \mathbb{R}^{p_j}$ are constructed

by collecting the variables $\breve{\theta}_{jk}$, $\breve{w}_{jk}$, and $\breve{a}_{jk}$, $k = 1, \ldots, p_j$, as follows:

$$\breve{\boldsymbol{\theta}}^j = \begin{bmatrix} \breve{\theta}_{j1} \\ \vdots \\ \breve{\theta}_{jp_j} \end{bmatrix}, \tag{2.101}$$

$$\breve{\boldsymbol{w}}^j = \begin{bmatrix} \breve{w}_{j1} \\ \vdots \\ \breve{w}_{jp_j} \end{bmatrix}, \tag{2.102}$$

$$\breve{\boldsymbol{a}}^j = \begin{bmatrix} \breve{a}_{j1} \\ \vdots \\ \breve{a}_{jp_j} \end{bmatrix}. \tag{2.103}$$

Following the formulation presented in Section 2.2.3, the vectors $\breve{\boldsymbol{\theta}}^j$, $\breve{\boldsymbol{w}}^j$, and $\breve{\boldsymbol{a}}^j$ are determined from the shape variables of the smooth folds in the sheet as follows (cf. Equations (2.11), (2.63), and (2.64)):

$$\breve{\boldsymbol{\theta}}^j = |\breve{\mathbf{C}}^j|_* \, \hat{\boldsymbol{\theta}}, \tag{2.104}$$

$$\breve{\boldsymbol{w}}^j = |\breve{\mathbf{C}}^j|_* \, \hat{\boldsymbol{w}}, \tag{2.105}$$

$$\breve{\boldsymbol{a}}^j = \begin{bmatrix} \breve{\mathbf{C}}^j & {}^A\breve{\mathbf{C}}^j \end{bmatrix} \begin{bmatrix} \hat{\boldsymbol{a}} \\ 1 \end{bmatrix}, \tag{2.106}$$

where ${}^A\breve{\mathbf{C}}^j \in \mathbb{R}^{p_j}$ is a vector with elements ${}^A\breve{C}^j_k$ determined as follows (cf. Equation

(2.65)):

$$ {}^{A}\breve{C}_k^j = \tfrac{1}{2} - \tfrac{1}{2}\sum_{i=1}^{N_{\mathcal{F}}} \breve{C}_{ki}^j. \tag{2.107} $$

The fold widths associated with the smooth folds crossed by $\breve{\boldsymbol{\gamma}}_j(\eta)$ are denoted $\breve{w}_{jk}^0$, $k = 1, \ldots, n_j$, and are required in the formulation of the folding map. As such, let $\breve{\boldsymbol{w}}^{0,j} \in \mathbb{R}^{p_j}$ be the vector constructed by collecting the fold widths $\breve{w}_{jk}^0$, $k = 1, \ldots, p_j$. Such a vector and its mapping from $\hat{\boldsymbol{w}}^0$ (defined in Equation (2.19)) are as follows:

$$ \begin{aligned} \breve{\boldsymbol{w}}^{0,j} &= \begin{bmatrix} \breve{w}_{j1}^0 \\ \vdots \\ \breve{w}_{jn_j}^0 \end{bmatrix} \\ &= |\breve{\mathbf{C}}^j|_* \, \hat{\boldsymbol{w}}^0. \end{aligned} \tag{2.108} $$

The position vectors of the points where $\breve{\boldsymbol{\gamma}}_j(\eta)$ crosses the boundary rulings of the smooth folds are denoted $\breve{\mathbf{b}}_L^{jk} \in \mathbb{R}^3$ (point where $\breve{\boldsymbol{\gamma}}_j(\eta)$ enters the smooth fold) and $\breve{\mathbf{b}}_R^{jk} \in \mathbb{R}^3$ (point where $\breve{\boldsymbol{\gamma}}_j(\eta)$ exits the smooth fold). Let $\breve{\mathbf{B}}_L^j, \breve{\mathbf{B}}_R^j \in \mathbb{R}^{3p_j}$ be the vectors constructed by concatenating the vectors $\breve{\mathbf{b}}_L^{jk}, \breve{\mathbf{b}}_R^{jk}$, $k = 1, \ldots, p_j$, respectively, as follows:

$$ \breve{\mathbf{B}}_L^j = \begin{bmatrix} \breve{\mathbf{b}}_L^{j1} \\ \vdots \\ \breve{\mathbf{b}}_L^{jp_j} \end{bmatrix}, \tag{2.109} $$

$$\breve{\mathbf{B}}_R^j = \begin{bmatrix} \breve{\mathbf{b}}_R^{j1} \\ \vdots \\ \breve{\mathbf{b}}_R^{jp_j} \end{bmatrix}. \tag{2.110}$$

The corner points of the smooth folds in $\mathcal{S}_0$ defined in Equations (2.54)–(2.57) provide a simple choice for the locations where the path $\breve{\boldsymbol{\gamma}}_j(\eta)$ crosses the boundary rulings of the smooth folds. Therefore, as in Section 2.2.3, the position vectors of such corner points are used herein to define the vectors $\breve{\mathbf{b}}_L^{jk}, \breve{\mathbf{b}}_R^{jk}$, $k = 1, \ldots, p_j$ (cf. Equation (2.96)):

$$\begin{bmatrix} \breve{\mathbf{B}}_L^j \\ \breve{\mathbf{B}}_R^j \end{bmatrix} = \begin{bmatrix} \frac{1}{2}(|\breve{\mathbf{C}}^j|_* + \breve{\mathbf{C}}^j) \otimes \mathbf{I}_3 & \frac{1}{2}(|\breve{\mathbf{C}}^j|_* - \breve{\mathbf{C}}^j) \otimes \mathbf{I}_3 \\ \frac{1}{2}(|\breve{\mathbf{C}}^j|_* - \breve{\mathbf{C}}^j) \otimes \mathbf{I}_3 & \frac{1}{2}(|\breve{\mathbf{C}}^j|_* + \breve{\mathbf{C}}^j) \otimes \mathbf{I}_3 \end{bmatrix} \begin{bmatrix} \hat{\mathbf{P}}^1 \\ \hat{\mathbf{P}}^4 \end{bmatrix}. \tag{2.111}$$

After defining all the shape variables and geometric parameters associated with the smooth folds crossed by each path $\breve{\boldsymbol{\gamma}}^j(\eta)$, $j = 1, \ldots, N_{\mathcal{P}}$, the folding map for points in the faces is obtained as the composition of transformations $\breve{\mathbf{H}}^{jk}$ associated with the smooth folds crossed by these paths (cf. Equation (2.83)):

$$\mathbf{x} = \chi(\mathbf{X}, t) \quad \text{where:} \quad \begin{bmatrix} \mathbf{x} \\ 1 \end{bmatrix} = \left(\prod_{k=1}^{p_j} \breve{\mathbf{H}}^{jk} \right) \begin{bmatrix} \mathbf{X} \\ 1 \end{bmatrix}, \tag{2.112}$$

where $\mathbf{X} \in \text{span}(\mathbf{e}_1, \mathbf{e}_2)$ is the position vector of a point in $\mathcal{P}_0^j \subset \mathcal{S}_0$ and $\mathbf{x} \in \mathbb{R}^3$ is the position vector of such a point in $\mathcal{P}_t^j \subset \mathcal{S}_t$. Since the results of Theorem 2.1 and Equations (2.83) and (2.84) are also applicable for the smooth folds crossed by the paths $\breve{\boldsymbol{\gamma}}^j(\eta)$, the simplified fold transformation matrices $\breve{\mathbf{H}}^{jk}$ follow the same

formulation presented in Equation (2.84):

$$\begin{aligned}\breve{\mathbf{H}}^{jk} \;=\; &\Big(\mathbf{T}(\breve{\mathbf{b}}_L^{jk})\,\mathbf{Q}_3(\varphi(\breve{\mathbf{m}}^{jk}))\,\mathbf{Q}_1(\breve{a}_{jk}\breve{\theta}_{jk})\\ &\times \mathbf{Q}_3^{-1}(\varphi(\breve{\mathbf{m}}^{jk}))\,\mathbf{T}^{-1}(\breve{\mathbf{b}}_L^{jk})\\ &\times \mathbf{T}^{-1}\left((\breve{w}_{jk}^0-\breve{w}_{jk})\left(\mathbf{e}_3\times\tfrac{\breve{\mathbf{m}}^{jk}}{\|\breve{\mathbf{m}}^{jk}\|}\right)\right)\\ &\times \mathbf{T}(\breve{\mathbf{b}}_R^{jk})\,\mathbf{Q}_3(\varphi(\breve{\mathbf{m}}^{jk}))\,\mathbf{Q}_1((1-\breve{a}_{jk})\breve{\theta}_{jk})\\ &\times \mathbf{Q}_3^{-1}(\varphi(\breve{\mathbf{m}}^{jk}))\,\mathbf{T}^{-1}(\breve{\mathbf{b}}_R^{jk})\Big).\end{aligned} \tag{2.113}$$

Determining the folding map for the smooth folds requires further steps since these surface subdomains undergo non-rigid deformations in addition to rotations and translations. The position vector of a point in $\mathcal{F}_t^i$ expressed in its associated fold coordinate system (with basis $\{\hat{\mathbf{e}}_1^i, \hat{\mathbf{e}}_2^i, \hat{\mathbf{e}}_3^i\}$ and origin at $\frac{1}{2}\left(\mathbf{c}^i(-1)+\mathbf{c}^i(1)\right)$, see Section 2.2.1) is denoted $\hat{\mathbf{x}} \in \mathbb{R}^3$. Since the current configuration of a smooth fold $\mathcal{F}_t^i$ is known in its associated fold coordinate system for a given set of fold shape variables, the focus here is on the formulation of the map $\mathbf{x} = \hat{\chi}(\hat{\mathbf{x}}(t), t)$. To construct this map, a transformation represented by the matrix $\hat{\mathbf{L}}^i \in \mathbb{R}^{4\times4}$ is first applied to the vector $\hat{\mathbf{x}}$. This transformation returns the position of the deformed smooth fold as joined to the reference configuration of the face adjacent to its boundary ruling $\boldsymbol{\mathcal{F}}^i(-1,\zeta_2)$ (denoted $\mathcal{P}_0^{i_\mathcal{F}}$). The transformation $\hat{\mathbf{L}}^i$ is obtained by first aligning position of the smooth fold expressed in its associated fold coordinate system with the plane spanned by $\mathbf{e}_1$ and $\mathbf{e}_2$ (performed via the transformation $\mathbf{Q}_1(\hat{a}_i\hat{\theta}_i)\mathbf{T}([0,\hat{w}_i/2,0]^\top)$) and then aligning such a resulting position to $\mathcal{P}_0^{i_\mathcal{F}}$ (performed through the transformation $\mathbf{T}(\hat{\mathbf{p}}_1^i)\mathbf{Q}_3(\varphi(\hat{\mathbf{v}}^{i2}-\hat{\mathbf{v}}^{i1}))$. Therefore, $\hat{\mathbf{L}}^i$ is given as follows:

$$\hat{\mathbf{L}}^i = \mathbf{T}(\hat{\mathbf{p}}_1^i)\,\mathbf{Q}_3(\varphi(\hat{\mathbf{v}}^{i2}-\hat{\mathbf{v}}^{i1}))\,\mathbf{Q}_1(\hat{a}_i\hat{\theta}_i)\,\mathbf{T}([0,\hat{w}_i/2,0]^\top). \tag{2.114}$$

Subsequently, the folding map associated with the face $\mathcal{P}_0^{i_\mathcal{F}}$ is applied to determine the position of the smooth fold in the current configuration expressed in the global coordinate system. Thus, the folding map for points in the smooth folds is defined as follows:

$$\mathbf{x} = \hat{\chi}(\hat{\mathbf{x}}(t), t) \quad \text{where:} \quad \begin{bmatrix} \mathbf{x} \\ 1 \end{bmatrix} = \left(\prod_{k=1}^{p_{i_\mathcal{F}}} \breve{\mathbf{H}}^{i_\mathcal{F} k} \right) \hat{\mathbf{L}}^i \begin{bmatrix} \hat{\mathbf{x}}(t) \\ 1 \end{bmatrix}, \tag{2.115}$$

where $\hat{\mathbf{x}}$ is the position vector of a point in $\mathcal{F}_t^i \subset \mathcal{S}_t$ expressed in the i^{th} fold coordinate system with basis $\{\hat{\mathbf{e}}_1^i, \hat{\mathbf{e}}_2^i, \hat{\mathbf{e}}_3^i\}$ and $\mathbf{x} \in \mathbb{R}^3$ is the position vector of such a point expressed in the global coordinate system with basis $\{\mathbf{e}_1, \mathbf{e}_2, \mathbf{e}_3\}$. Note that the position vector of a point in $\mathcal{F}_0^i \subset \mathcal{S}_0$ is obtained as $\mathbf{X} = \hat{\chi}(\hat{\mathbf{x}}(0), 0) \in \text{span}(\mathbf{e}_1, \mathbf{e}_2)$:

$$\mathbf{X} = \hat{\chi}(\hat{\mathbf{x}}(0), 0) \quad \text{where:}$$

$$\begin{aligned} \begin{bmatrix} \mathbf{X} \\ 1 \end{bmatrix} &= \mathbf{I}_4 \, \hat{\mathbf{L}}^i \Big|_{t=0} \begin{bmatrix} \hat{\mathbf{x}}(0) \\ 1 \end{bmatrix}, \\ &= \mathbf{T}(\hat{\mathbf{p}}_1^i) \, \mathbf{Q}_3(\varphi(\hat{\mathbf{v}}^{i2} - \hat{\mathbf{v}}^{i1})) \, \mathbf{T}([0, \hat{w}_i^0/2, 0]^\top) \begin{bmatrix} \hat{\mathbf{x}}(0) \\ 1 \end{bmatrix}. \end{aligned} \tag{2.116}$$

2.2.5 Determination of Fold Cross-section Shape Variables

As stated in Section 2.2.3, the full set of fold shape variables $\hat{\theta}_i$, $\hat{w}_i$, and $\hat{a}_i$, $i = 1, \ldots, N_\mathcal{F}$, is reduced for simplification to only the set of fold angles $\hat{\theta}_i$ and the arc-lengths $\hat{s}_i$, $i = 1, \ldots, N_\mathcal{F}$, by determining relations $\hat{w}_i = \hat{w}_i(\hat{\theta}_i, \hat{s}_i)$ and $\hat{a}_i = \hat{a}_i(\hat{\theta}_i, \hat{s}_i)$.

These relations are obtained by making assumptions on the form of the curvature field of the smooth folds. The process followed to determine such relations is outlined in this section.

Smooth folds having G^1 and G^2 continuous joints with their adjacent faces are considered. The formulation of the parametric curve $\hat{\mathbf{c}}^i(\zeta_1)$ describing the cross-sectional shape for these smooth folds are provided in Equations (2.38) and (2.43), respectively. In addition to $\hat{w}_i(\hat{\theta}_i, \hat{s}_i)$ and $\hat{a}_i(\hat{\theta}_i, \hat{s}_i)$, the relations $\beta^i_{L_1}(\hat{\theta}_i, \hat{s}_i)$ and $\beta^i_{R_1}(\hat{\theta}_i, \hat{s}_i)$ are also determined here because they are required to fully define the shape of smooth folds exhibiting G^1 continuity (refer to Equations (2.31) and (2.32)) even though these variables do not appear in the constraints presented in Section 2.2.3. The relations $\beta^i_{L_2}(\hat{\theta}_i, \hat{s}_i)$ and $\beta^i_{R_2}(\hat{\theta}_i, \hat{s}_i)$ are further required to fully define the shape of smooth folds exhibiting G^2 continuity (refer to Equations (2.35) and (2.36)).

To determine the fold shape variables for any value of arc-length $\hat{s}_i$, the parametric curve $\hat{\mathbf{c}}^i(\zeta_1)$ is made non-dimensional by $\hat{s}_i$ as follows:

$$\bar{\mathbf{c}}^i(\zeta_1) := \frac{\hat{\mathbf{c}}^i(\zeta_1)}{\hat{s}_i}. \tag{2.117}$$

This leads to the following non-dimensional forms of $\hat{\mathbf{c}}^i(\zeta_1)$ presented in Equations (2.38) and (2.43):

$$\bar{\mathbf{c}}^i(\zeta_1) = \quad h_{30}(\zeta_1)\bar{\mathbf{c}}^i_{L_0} + h_{31}(\zeta_1)\bar{\mathbf{c}}^i_{R_0} + h_{32}(\zeta_1)\bar{\mathbf{c}}^i_{L_1} + h_{33}(\zeta_1)\bar{\mathbf{c}}^i_{R_1}, \tag{2.118}$$

$$\begin{aligned}\bar{\mathbf{c}}^i(\zeta_1) = \quad & h_{50}(\zeta_1)\bar{\mathbf{c}}^i_{L_0} + h_{51}(\zeta_1)\bar{\mathbf{c}}^i_{R_0} + h_{52}(\zeta_1)\bar{\mathbf{c}}^i_{L_1} \\ & + h_{53}(\zeta_1)\bar{\mathbf{c}}^i_{R_1} + h_{54}(\zeta_1)\bar{\mathbf{c}}^i_{L_2} + h_{55}(\zeta_1)\bar{\mathbf{c}}^i_{R_2},\end{aligned} \tag{2.119}$$

where:

$$\begin{aligned} \bar{\mathbf{c}}^i_{L_0} &:= \frac{\hat{\mathbf{c}}^i_{L_0}}{\hat{s}_i} \\ &= \begin{bmatrix} 0 \\ -\frac{1}{2}\frac{\hat{w}_i}{\hat{s}_i} \\ 0 \end{bmatrix}, \end{aligned} \tag{2.120}$$

$$\begin{aligned} \bar{\mathbf{c}}^i_{R_0} &:= \frac{\hat{\mathbf{c}}^i_{R_0}}{\hat{s}_i} \\ &= \begin{bmatrix} 0 \\ \frac{1}{2}\frac{\hat{w}_i}{\hat{s}_i} \\ 0 \end{bmatrix}, \end{aligned} \tag{2.121}$$

$$\begin{aligned} \bar{\mathbf{c}}^i_{L_1} &:= \frac{\hat{\mathbf{c}}^i_{L_1}}{\hat{s}_i} \\ &= \frac{\beta^i_{L_1}}{\hat{s}_i} \begin{bmatrix} 0 \\ \cos\left(\hat{a}_i\hat{\theta}_i\right) \\ -\sin\left(\hat{a}_i\hat{\theta}_i\right) \end{bmatrix}, \end{aligned} \tag{2.122}$$

$$\begin{aligned} \bar{\mathbf{c}}^i_{R_1} &:= \frac{\hat{\mathbf{c}}^i_{R_1}}{\hat{s}_i} \\ &= \frac{\beta^i_{R_1}}{\hat{s}_i} \begin{bmatrix} 0 \\ \cos\left((1-\hat{a}_i)\hat{\theta}_i\right) \\ \sin\left((1-\hat{a}_i)\hat{\theta}_i\right) \end{bmatrix}, \end{aligned} \tag{2.123}$$

$$
\begin{aligned}
\bar{\mathbf{c}}^i_{L_2} &:= \frac{\hat{\mathbf{c}}^i_{L_2}}{\hat{s}_i} \\
&= \frac{\beta^i_{L_2}}{\hat{s}_i} \begin{bmatrix} 0 \\ \cos\left(\hat{a}_i\hat{\theta}_i\right) \\ -\sin\left(\hat{a}_i\hat{\theta}_i\right) \end{bmatrix},
\end{aligned}
\tag{2.124}
$$

$$
\begin{aligned}
\bar{\mathbf{c}}^i_{R_2} &:= \frac{\hat{\mathbf{c}}^i_{R_2}}{\hat{s}_i} \\
&= \frac{\beta^i_{R_2}}{\hat{s}_i} \begin{bmatrix} 0 \\ -\cos\left((1-\hat{a}_i)\hat{\theta}_i\right) \\ -\sin\left((1-\hat{a}_i)\hat{\theta}_i\right) \end{bmatrix}.
\end{aligned}
\tag{2.125}
$$

Equations (2.120)–(2.125) show that the non-dimensional fold cross-section $\bar{\mathbf{c}}^i(\zeta_1)$ is a function of the non-dimensional variables $\hat{\theta}_i$, $\hat{w}_i/\hat{s}_i$, $\hat{a}_i$, $\beta^i_{L_1}/\hat{s}_i$, $\beta^i_{R_1}/\hat{s}_i$, $\beta^i_{L_2}/\hat{s}_i$, and $\beta^i_{R_2}/\hat{s}_i$.

The non-dimensional arc-length of $\bar{\mathbf{c}}^i(\zeta_1)$, denoted $\bar{s}_i$, is given as follows:

$$
\begin{aligned}
\bar{s}_i &= \int_{-1}^{1} \left\| \frac{\mathrm{d}\bar{\mathbf{c}}^i(\zeta_1)}{\mathrm{d}\zeta_1} \right\| \mathrm{d}\zeta_1 \\
&= \frac{1}{\hat{s}_i} \int_{-1}^{1} \left\| \frac{\mathrm{d}\hat{\mathbf{c}}^i(\zeta_1)}{\mathrm{d}\zeta_1} \right\| \mathrm{d}\zeta_1 \\
&= \frac{\hat{s}_i}{\hat{s}_i} \\
&= 1,
\end{aligned}
\tag{2.126}
$$

and the non-dimensional curvature of $\bar{\mathbf{c}}^i(\zeta_1)$, denoted $\bar{\hat{\kappa}}(\zeta_1)$, is given as follows:

$$\begin{aligned} \bar{\hat{\kappa}}(\zeta_1) &:= \hat{s}_i \hat{\kappa}(\zeta_1) \\ &= \frac{\left\| \dfrac{\mathrm{d}\bar{\mathbf{c}}^i(\zeta_1)}{\mathrm{d}\zeta_1} \times \dfrac{\mathrm{d}^2\bar{\mathbf{c}}^i(\zeta_1)}{\mathrm{d}\zeta_1^2} \right\|}{\left\| \dfrac{\mathrm{d}\bar{\mathbf{c}}^i(\zeta_1)}{\mathrm{d}\zeta_1} \right\|^3}. \end{aligned} \tag{2.127}$$

The non-dimensional signed curvature of $\bar{\mathbf{c}}^i(\zeta_1)$, denoted $\bar{\kappa}(\zeta_1)$, is given as:

$$\begin{aligned} \bar{\kappa}(\zeta_1) &= \hat{s}_i \kappa(\zeta_1) \\ &= \bar{\hat{\kappa}}(\zeta_1) \operatorname{sgn}\left(\left(\frac{\mathrm{d}\bar{\mathbf{c}}^i(\zeta_1)}{\mathrm{d}\zeta_1} \times \frac{\mathrm{d}^2\bar{\mathbf{c}}^i(\zeta_1)}{\mathrm{d}\zeta_1^2} \right) \cdot \hat{\mathbf{e}}_1^i \right). \end{aligned} \tag{2.128}$$

The next step is to provide assumptions on the curvature field of the fold cross-section exhibited during folding. For smooth folds exhibiting G^1 continuity, a constant form for the goal signed curvature field $\kappa^G(\zeta_1)$ is assumed:

$$\kappa^G(\zeta_1) = \kappa^*, \tag{2.129}$$

and for smooth folds exhibiting G^2 continuity, a parabolic form for the goal signed curvature field $\kappa^G(\zeta_1)$ is assumed:

$$\kappa^G(\zeta_1) = \kappa^* \left(1 - 4\frac{s(\zeta_1)^2}{\hat{s}_i^2} \right), \tag{2.130}$$

where $s(\zeta_1)$ is defined in Equation (2.23). Note that $\kappa^G(\zeta_1) = 0$ at $s(\zeta_1) = -\frac{\hat{s}_i}{2}$ and $s(\zeta_1) = \frac{\hat{s}_i}{2}$ in Equation (2.130) to satisfy G^2 continuity.

The non-dimensional form of the goal signed curvature field in Equation (2.129),

denoted $\bar{\kappa}^G(\zeta_1)$, is the following:

$$\begin{aligned} \bar{\kappa}^G(\zeta_1) &= \hat{s}_i \kappa^G(\zeta_1) \\ &= \bar{\kappa}^*, \end{aligned} \tag{2.131}$$

while the non-dimensional form of the goal signed curvature field in Equation (2.130) is the following:

$$\begin{aligned} \bar{\kappa}^s(\zeta_1) &= \hat{s}_i \kappa^s(\zeta_1) \\ &= \bar{\kappa}^* \left(1 - 4\bar{s}(\zeta_1)^2\right), \end{aligned} \tag{2.132}$$

where:

$$\bar{\kappa}^* := \hat{s}_i \kappa^*, \tag{2.133}$$

$$\begin{aligned} \bar{s}(\zeta_1) &= \frac{s(\zeta_1)}{\hat{s}_i} \\ &= -\frac{1}{2} + \int_{-1}^{\zeta_1} \left\| \frac{\mathrm{d}\bar{\mathbf{c}}^i(\zeta)}{\mathrm{d}\zeta} \right\| \mathrm{d}\zeta. \end{aligned} \tag{2.134}$$

Once the assumptions on the curvature field are selected, the non-dimensional variables $\hat{\theta}_i$, $\hat{w}_i/\hat{s}_i$, $\hat{a}_i$, $\beta^i_{L_1}/\hat{s}_i$, $\beta^i_{R_1}/\hat{s}_i$ (and $\beta^i_{L_2}/\hat{s}_i$ and $\beta^i_{R_2}/\hat{s}_i$ if smooth folds with G^2 continuity are considered) are fitted to satisfy such assumptions. For the symmetric smooth folds resulting from the selected assumptions, the variables to fit are simplified as follows:

$$\hat{a}_i = \frac{1}{2}, \tag{2.135}$$

$$\frac{\beta^i_{L_1}}{\hat{s}^0_i} = \frac{\beta^i_{R_1}}{\hat{s}_i} =: \frac{\beta^i_1}{\hat{s}_i}, \tag{2.136}$$

$$\frac{\beta^i_{L_2}}{\hat{s}_i} = \frac{\beta^i_{R_2}}{\hat{s}_i} =: \frac{\beta^i_2}{\hat{s}_i}. \tag{2.137}$$

For a given value of $\bar{\kappa}^*_i$, the error in the non-dimensional arc-length $\bar{s}_i$ (which must be equal to 1, cf. Equation (2.126)) and the error between $\bar{\kappa}^s_i$ and $\bar{\kappa}^{sG}_i$ is minimized as follows:

$$\begin{aligned} \text{Find} \qquad & \hat{\theta}_i \in [0, \pi], \quad \frac{\hat{w}_i}{\hat{s}_i} \in (0, 1], \\ & \frac{\beta^i_1}{\hat{s}_i} \in (0, n], \quad \frac{\beta^i_2}{\hat{s}_i} \in [0, n], \\ \text{That minimize} \quad & f\left(\hat{\theta}_i, \frac{\hat{w}_i}{\hat{s}_i}, \frac{\beta^i_1}{\hat{s}_i}, \frac{\beta^i_2}{\hat{s}_i}\right), \end{aligned} \tag{2.138}$$

where:

$$f\left(\hat{\theta}_i, \frac{\hat{w}_i}{\hat{s}_i}, \frac{\beta^i_1}{\hat{s}_i}, \frac{\beta^i_2}{\hat{s}_i}\right) = (1 - \bar{s}_i)^2 + \frac{\int_{-1}^{1} \left(\bar{\kappa}^G(\zeta_1) - \bar{\kappa}(\zeta_1)\right)^2 \mathrm{d}\zeta_1}{\int_{-1}^{1} \left(\bar{\kappa}^G(\zeta_1)\right)^2 \mathrm{d}\zeta_i}. \tag{2.139}$$

It is assumed that the fold shape variables $\hat{w}_i/\hat{s}_i$, $\beta^i_1/\hat{s}_i$, and $\beta^i_2/\hat{s}_i$ are equal for folds having the same fold angle absolute value $|\hat{\theta}_i|$. Thus, the range for fold angles in the bounds of the optimization problem in Equation (2.138) only includes non-negative numbers.

The minimization problem in Equation (2.138) is repeated for a set of values of $\bar{\kappa}^*$ to obtain values of $\hat{\theta}_i, \hat{w}_i, \beta^i_1, \beta^i_2$ associated with such a maximum non-dimensional curvature that satisfy the assumptions on extensibility and curvature field. The problem is solved for each value of $\bar{\kappa}^*$ using the gradient-based optimization algorithm

in Matlab `fmincon`. The upper bound n for $\beta_1^i/\hat{s}_i$ and $\beta_2^i/\hat{s}_i$ is selected as 10, which is far from the actual values obtained for these parameters and thus it resulted in an inactive bound. Afterwards, approximations for $\hat{w}_i(\hat{\theta}_i, \hat{s}_i)$, $\beta_1^i(\hat{\theta}_i, \hat{s}_i)$, $\beta_2^i(\hat{\theta}_i, \hat{s}_i)$ and $\kappa^*(\hat{\theta}_i, \hat{s}_i)$ are interpolated from the data obtained by solving Equation (2.138) for a set of values for $\bar{\kappa}^*$.

2.2.6 Numerical Implementation

As stated in the previous sections, the *continuous motion* of the sheet is achieved by continuously altering the values of the fold shape variables ($\hat{\theta}_i$, $\hat{w}_i$, and $\hat{a}_i$, $i = 1, \ldots, N_{\mathcal{F}}$) such that any attained configuration satisfies the constraints presented in Equation (2.97) (i.e. the motion of the sheet is a continuous path in the constrained configuration space).

The simulation of the continuous motion of the sheet is executed by *incrementally* updating the values of the fold shape variables using input guess increments and then iteratively applying any required corrections such that the resulting set of fold shape variables satisfies the constraints of Equation (2.97). The iterative procedure used to perform such corrections is outlined in this section. As stated in Section 2.2.3, the full set of fold shape variables $\hat{\theta}_i$, $\hat{w}_i$, and $\hat{a}_i$, $i = 1, \ldots, N_{\mathcal{F}}$, is reduced to only the set of fold angles $\hat{\theta}_i$ and arc-lengths $\hat{s}_i$, $i = 1, \ldots, N_{\mathcal{F}}$, by establishing relations $\hat{w}_i(\hat{\theta}_i, \hat{s}_i)$ and $\hat{a}_i(\hat{\theta}_i, \hat{s}_i)$ following certain assumptions on the form of the curvature field of the smooth folds (see Section 2.2.5 for details). For kinematic simulation, here it is further assumed that the deformation exhibited by the smooth folds is inextensible:

$$\hat{s}_i = \hat{w}_i^0 \qquad \forall\, i \in \{1, \ldots, N_{\mathcal{F}}\}, \tag{2.140}$$

and as a consequence the fold angles $\hat{\theta}_i$, $i = 1, \ldots, N_{\mathcal{F}}$, are the only degrees of freedom

during kinematic simulation.

2.2.6.1 Kinematic Constraints

Given a guess set of fold angles ordered in the vector ${}^{k}_{l}\hat{\boldsymbol{\theta}} \in \mathbb{R}^{N_{\mathcal{F}}}$ where the subscript l denotes to incremental step number and the superscript k denotes to the correction iteration number, the matrices $\mathbf{R}^{j}({}^{k}_{l}\hat{\boldsymbol{\theta}})$ and the vectors $\mathbf{d}^{j}({}^{k}_{l}\hat{\boldsymbol{\theta}})$, $j = 1, \ldots, N_{\mathcal{I}}$, are calculated. If the vector of fold angles ${}^{k}_{l}\hat{\boldsymbol{\theta}}$ does not yield a configuration that satisfies Equation (2.97), $\mathbf{R}^{j}({}^{k}_{l}\hat{\boldsymbol{\theta}}) - \mathbf{I}_3$ is not equal to the zero matrix in $\mathbb{R}^{3\times3}$ and/or $\mathbf{d}^{j}({}^{k}_{l}\hat{\boldsymbol{\theta}})$ is not equal to $\mathbf{0}_3$.

Let $\mathfrak{R}({}^{k}_{l}\hat{\boldsymbol{\theta}}) \in \mathbb{R}^{6N_{\mathcal{I}}+2N_{\mathcal{F}}}$ with components $\mathfrak{R}_j({}^{k}_{l}\hat{\boldsymbol{\theta}})$ be the vector of residuals from constraints of Equation (2.97) ($6N_{\mathcal{I}}$ in total) and from constraints imposing the upper and lower fold angle bounds ($2N_{\mathcal{F}}$ in total). Since $\mathbf{R}^{j}({}^{k}_{l}\hat{\boldsymbol{\theta}})$ is an orthogonal matrix, only three of its scalar components are independent. Thus, the matrix-type constraint in Equation (2.85) provides the following three scalar constraints that contribute to the residual vector [315]:

$$\mathfrak{R}_{6j-5}({}^{k}_{l}\hat{\boldsymbol{\theta}}) = \frac{1}{2}\lambda_R \left(R^{j}_{23}({}^{k}_{l}\hat{\boldsymbol{\theta}})\right)^2, \tag{2.141}$$

$$\mathfrak{R}_{6j-4}({}^{k}_{l}\hat{\boldsymbol{\theta}}) = \frac{1}{2}\lambda_R \left(R^{j}_{31}({}^{k}_{l}\hat{\boldsymbol{\theta}})\right)^2, \tag{2.142}$$

$$\mathfrak{R}_{6j-3}({}^{k}_{l}\hat{\boldsymbol{\theta}}) = \frac{1}{2}\lambda_R \left(R^{j}_{12}({}^{k}_{l}\hat{\boldsymbol{\theta}})\right)^2, \tag{2.143}$$

where $j \in \{1, \ldots, N_{\mathcal{I}}\}$ and λ_R is the weight for residuals from Equation (2.85). This constant weight is an algorithmic parameter included in the residual vector to ensure that its components are scaled to a similar order of magnitude (i.e. the components of $\mathbf{R}^{j}({}^{k}_{l}\hat{\boldsymbol{\theta}})$ are dimensionless while those of $\mathbf{d}^{j}({}^{k}_{l}\hat{\boldsymbol{\theta}})$ have units of length). The three

components of the vector $\mathbf{d}^j({}^k_l\hat{\boldsymbol{\theta}})$, $j = 1, \ldots, N_{\mathcal{I}}$, which must be zero for the constraint in Equation (2.86) to be satisfied, provide the following components to the residual vector:

$$\mathfrak{R}_{6j-2}({}^k_l\hat{\boldsymbol{\theta}}) = \frac{1}{2}\lambda_d \left(d_1^j({}^k_l\hat{\boldsymbol{\theta}})\right)^2, \tag{2.144}$$

$$\mathfrak{R}_{6j-1}({}^k_l\hat{\boldsymbol{\theta}}) = \frac{1}{2}\lambda_d \left(d_2^j({}^k_l\hat{\boldsymbol{\theta}})\right)^2, \tag{2.145}$$

$$\mathfrak{R}_{6j}({}^k_l\hat{\boldsymbol{\theta}}) = \frac{1}{2}\lambda_d \left(d_3^j({}^k_l\hat{\boldsymbol{\theta}})\right)^2, \tag{2.146}$$

where $j \in \{1, \ldots, N_{\mathcal{I}}\}$ and λ_d is the weight for residuals from Equation (2.86).

2.2.6.2 Fold Angle Bounds

Additional components of $\mathfrak{R}({}^k_l\hat{\boldsymbol{\theta}})$ are included to ensure that the fold angles remain within prescribed upper and lower bounds during the continuous motion of the sheet. A penalty approach is used to implement the required fold angle bounds for each fold as in [315]. The lower bound for $\hat{\theta}_i$ is denoted $\hat{\theta}_i^L \in [-\pi, 0]$ and the upper bound is denoted $\hat{\theta}_i^U \in [0, \pi]$. Conventional assignments for $\hat{\theta}_i^L$ and $\hat{\theta}_i^U$ are provided in Table 2.1.

The additional components of $\mathfrak{R}({}^k_l\hat{\boldsymbol{\theta}})$ required to enforce the lower bound of ${}^k_l\hat{\theta}_i$ consist of a penalty that is zero if ${}^k_l\hat{\theta}_i \geq \hat{\theta}_i^L$ and increases proportionally to the square of the difference between ${}^k_l\hat{\theta}_i$ and $\hat{\theta}_i^L$ when ${}^k_l\hat{\theta}_i < \hat{\theta}_i^L$:

$$\mathfrak{R}_{6N_{\mathcal{I}}+2i-1}({}^k_l\hat{\boldsymbol{\theta}}) = \frac{1}{2}\lambda_B \max(0, -{}^k_l\hat{\theta}_i + \hat{\theta}_i^L)^2, \tag{2.147}$$

where $i \in \{1, \ldots, N_{\mathcal{F}}\}$ and λ_B is the weight for residuals from fold angle bound

Table 2.1: Conventional assignments for $\hat{\theta}_i^L$ and $\hat{\theta}_i^U$.

Fold type	$\hat{\theta}_i^L$	$\hat{\theta}_i^U$
No assignment	$-\pi$	π
Valley	0	π
Mountain	$-\pi$	0
Rigidized fold	0	0

constraints. Similarly, to enforce the upper bound of $\hat{\theta}_i$, a penalty that is zero if ${}_l^k\hat{\theta}_i \leq \hat{\theta}_i^U$ and increases proportionally to the square of the difference between ${}_l^k\hat{\theta}_i$ and $\hat{\theta}_i^U$ when ${}_l^k\hat{\theta}_i > \hat{\theta}_i^U$ is included in the following components of $\mathfrak{R}({}_l^k\hat{\boldsymbol{\theta}})$:

$$\mathfrak{R}_{6N_{\mathcal{I}}+2i}({}_l^k\hat{\boldsymbol{\theta}}) = \frac{1}{2}\lambda_B \max(0,\, {}_l^k\hat{\theta}_i - \hat{\theta}_i^U)^2, \tag{2.148}$$

where $i \in \{1, \ldots, N_{\mathcal{F}}\}$.

2.2.6.3 Method of Solution

Following the generalized Newton's method [315], the first-order expansion of $\mathfrak{R}(\hat{\boldsymbol{\theta}})$ is used to determine the increment in $\hat{\boldsymbol{\theta}}$ required to minimize the components of the constraint residual vector $\mathfrak{R}(\hat{\boldsymbol{\theta}})$:

$$\mathfrak{R}(\hat{\boldsymbol{\theta}} + \Delta\hat{\boldsymbol{\theta}}) \;\; = \;\; \mathfrak{R}(\hat{\boldsymbol{\theta}}) + \frac{\partial \mathfrak{R}(\hat{\boldsymbol{\theta}})}{\partial \hat{\boldsymbol{\theta}}}\Delta\hat{\boldsymbol{\theta}} + \ldots \;\; = \;\; \mathbf{0}_{6N_{\mathcal{I}}+2N_{\mathcal{F}}}. \tag{2.149}$$

The following correction increment $\Delta\hat{\boldsymbol{\theta}}$ is obtained from the previous first-order expansion:

$$\Delta\hat{\boldsymbol{\theta}} = -\left(\frac{\partial \mathfrak{R}(\hat{\boldsymbol{\theta}})}{\partial \hat{\boldsymbol{\theta}}}\right)^{\dagger} \mathfrak{R}(\hat{\boldsymbol{\theta}}), \tag{2.150}$$

where $(\cdot)^{\dagger}$ represents the Moore-Penrose pseudoinverse.

The l^{th} set of guess fold angle increments is collected in the vector ${}^{IN}_{l}\Delta\hat{\boldsymbol{\theta}} \in \mathbb{R}^{N_{\mathcal{F}}}$. First, the guess fold angle vector for the l^{th} increment (${}^{1}_{l}\hat{\boldsymbol{\theta}}$) is calculated as follows:

$$ {}^{1}_{l}\hat{\boldsymbol{\theta}} = {}_{l-1}\hat{\boldsymbol{\theta}} + {}_{l}\Delta\hat{\boldsymbol{\theta}}, \tag{2.151} $$

where the fold angles are first updated with the input fold angle increments ${}^{IN}_{l}\Delta\hat{\boldsymbol{\theta}}$ projected into the null space of the previous residual derivatives (see [315] for details):

$$ {}_{l}\Delta\hat{\boldsymbol{\theta}} = \left(\mathbf{I}_{N_{\mathcal{F}}} - \left(\frac{\partial \boldsymbol{\mathfrak{R}}({}_{l-1}\hat{\boldsymbol{\theta}})}{\partial \hat{\boldsymbol{\theta}}} \right)^{\dagger} \left(\frac{\partial \boldsymbol{\mathfrak{R}}({}_{l-1}\hat{\boldsymbol{\theta}})}{\partial \hat{\boldsymbol{\theta}}} \right) \right) {}^{IN}_{l}\Delta\hat{\boldsymbol{\theta}}. \tag{2.152} $$

If $\|\boldsymbol{\mathfrak{R}}({}^{1}_{l}\hat{\boldsymbol{\theta}})\|/(6N_{\mathcal{I}} + 2N_{\mathcal{F}}) \geq \texttt{tol1}$, the fold angles are corrected iteratively as follows:

$$ {}^{k}_{l}\Delta\hat{\boldsymbol{\theta}} = -\left(\frac{\partial \boldsymbol{\mathfrak{R}}({}^{k}_{l}\hat{\boldsymbol{\theta}})}{\partial \hat{\boldsymbol{\theta}}} \right)^{\dagger} \boldsymbol{\mathfrak{R}}({}^{k}_{l}\hat{\boldsymbol{\theta}}), \tag{2.153} $$

$$ {}^{k+1}_{l}\hat{\boldsymbol{\theta}} = {}^{k}_{l}\hat{\boldsymbol{\theta}} + {}^{k}_{l}\Delta\hat{\boldsymbol{\theta}}, \tag{2.154} $$

cf. Equation (2.150). The iterative correction process of Equations (2.153) and (2.154) is repeated until $\|\boldsymbol{\mathfrak{R}}({}^{k+1}_{l}\hat{\boldsymbol{\theta}})\|/(6N_{\mathcal{I}} + 2N_{\mathcal{F}}) < \texttt{tol1}$ or $\|{}^{k}_{l}\Delta\hat{\boldsymbol{\theta}}\|/N_{\mathcal{F}} < \texttt{tol2}$, where `tol1` and `tol2` are numerical tolerances. The numerical procedure used for the kinematic simulation of sheets with smooth folds is summarized in Table 2.2.

2.3 Implementation Examples

The numerical procedure utilized for the simulation of the motion of sheets with smooth folds presented in Section 2.2.6 is implemented in Matlab. The smooth folds $\mathcal{F}^{i}_{t}$ are plotted using the Matlab three-dimensional shaded surface plot function

Table 2.2: Numerical procedure used to simulate the motion of sheets with smooth folds followed at the l^{th} fold sequence increment.

1:	Determine ${}_{l}\Delta\hat{\boldsymbol{\theta}}$ from ${}^{IN}_{l}\Delta\hat{\boldsymbol{\theta}}$ using Equation (2.152)
2:	Calculate set of guess fold angles ${}^{1}_{l}\hat{\boldsymbol{\theta}}$ using Equation (2.151)
3:	`IF` $\|\mathfrak{R}({}^{1}_{l}\hat{\boldsymbol{\theta}})\|/N_{\mathcal{F}} <$ `tol1` `THEN` set ${}_{l}\hat{\boldsymbol{\theta}} = {}^{1}_{l}\hat{\boldsymbol{\theta}}$ and `EXIT` `ELSE CONTINUE`
4:	Determine correction of fold angles ${}^{k}_{l}\Delta\hat{\boldsymbol{\theta}}$ using Equation (2.153)
5:	Update ${}^{k+1}_{l}\hat{\boldsymbol{\theta}}$ using Equation (2.154)
6:	`IF` $\|\mathfrak{R}({}^{k+1}_{l}\hat{\boldsymbol{\theta}})\|/(6N_{\mathcal{I}} + 2N_{\mathcal{F}}) <$ `tol1` `OR` $\|{}^{k}_{l}\Delta\hat{\boldsymbol{\theta}}\|/N_{\mathcal{F}} <$ `tol2` `THEN` set ${}_{l}\hat{\boldsymbol{\theta}} = {}^{k+1}_{l}\hat{\boldsymbol{\theta}}$ and `EXIT` `ELSE` set $k \leftarrow k+1$ and `GOTO` 4

`surf` while the faces $\mathcal{P}^i_t$ are plotted through filled three-dimensional polygons using `fill3`. The complete Matlab code for the kinematic simulation of origami with smooth folds and various input examples are included in the Supplemental Material of [7] (`http://dx.doi.org/10.1115/1.4034299`).

Smooth folds having G^2 continuous joints with their adjacent faces are assumed for all the examples presented in this section. The formulation of the parametric curve $\hat{\mathbf{c}}^i(\zeta_1)$ that defines the cross-sectional shape of such smooth folds is provided in Equation (2.43). Inextensible deformation and a symmetric parabolic curvature field are assumed for $\hat{\mathbf{c}}^i(\zeta_1)$ (see Section 2.2.5 for details). Also, the range of fold angle values assumed for all the examples presented in this section is the interval $[-\pi, \pi]$. It is noted that the aforementioned assumptions are taken for simplicity and do not present a limitation of the proposed model. Other assumptions on the extensibility and curvature field of the folds are also applicable as long as such assumptions do not violate the continuity conditions for $\hat{\mathbf{c}}^i(\zeta_1)$.

A sheet having eight smooth folds meeting at one interior fold intersection is shown in Figure 2.13. The folds are enumerated in counterclockwise order. Various guess fold angle increments are considered ranging from simple to more complex. The folded configurations shown in Figure 2.13(a) are obtained through the following guess fold angle increments:

$$ {}^{IN}_{l}\Delta\hat{\boldsymbol{\theta}} = \frac{\pi}{50} \begin{bmatrix} 1 \\ 0 \\ 0 \\ 0 \\ 1 \\ 0 \\ 0 \\ 0 \end{bmatrix} \qquad \forall\, l \in \{1, \ldots, 50\}, \tag{2.155} $$

and the folded configurations shown in Figure 2.13(b) are obtained through the following guess fold angle increments:

$$ {}^{IN}_{l}\Delta\hat{\boldsymbol{\theta}} = \frac{\pi}{50} \begin{bmatrix} 0 \\ 1 \\ 0 \\ 0 \\ 0 \\ 1 \\ 0 \\ 0 \end{bmatrix} \qquad \forall\, l \in \{1, \ldots, 50\}. \tag{2.156} $$

The two previous guess fold angle increments represent simple examples and the fold angle correction procedure (refer to Table 2.2) converged prior to performing an

initial correction iteration (i.e. $\|\mathfrak{R}({}^{1}_{l}\hat{\boldsymbol{\theta}})\|/N_{\mathcal{F}} < \texttt{tol1} \quad \forall\, l \in \{1,\ldots,50\}$). Alternatively, an example of a more complex folding motion resulting from guess fold angle increments that required iterative corrections is shown in Figure 2.13(c). For this example, the guess fold angle increments are as follows:

$$ {}^{IN}_{l}\Delta\hat{\boldsymbol{\theta}} = \frac{\pi}{50}\begin{bmatrix} 1 \\ -1 \\ 1 \\ -1 \\ 1 \\ -1 \\ 1 \\ -1 \end{bmatrix} \qquad \forall\, l \in \{1,\ldots,50\}. \tag{2.157} $$

As shown in the fold angle vs. increment plot in Figure 2.13(c), the fold angles obtained from the simulation procedure differ from the simple addition of the guess fold angle increments. As observable in the configurations shown in Figure 2.13(c), all the surface subdomains comprising the sheet remain joined through the motion of the sheet. Thus, the simulation procedure presented in Section 2.2.6 successfully allows for the correction of the fold angles such that they satisfy the necessary constraints for a valid configuration presented in Equation (2.97).

More complex examples of origami sheets having two interior fold intersections are shown in Figure 2.16. The graphs of Figure 2.14 show the vertices and fold centerlines associated with such sheets. Since the two interior fold intersections for these sheets share a common adjacent fold, their associated constraint equations are coupled. For all the three sheets, the guess fold angle increments are as follows (see

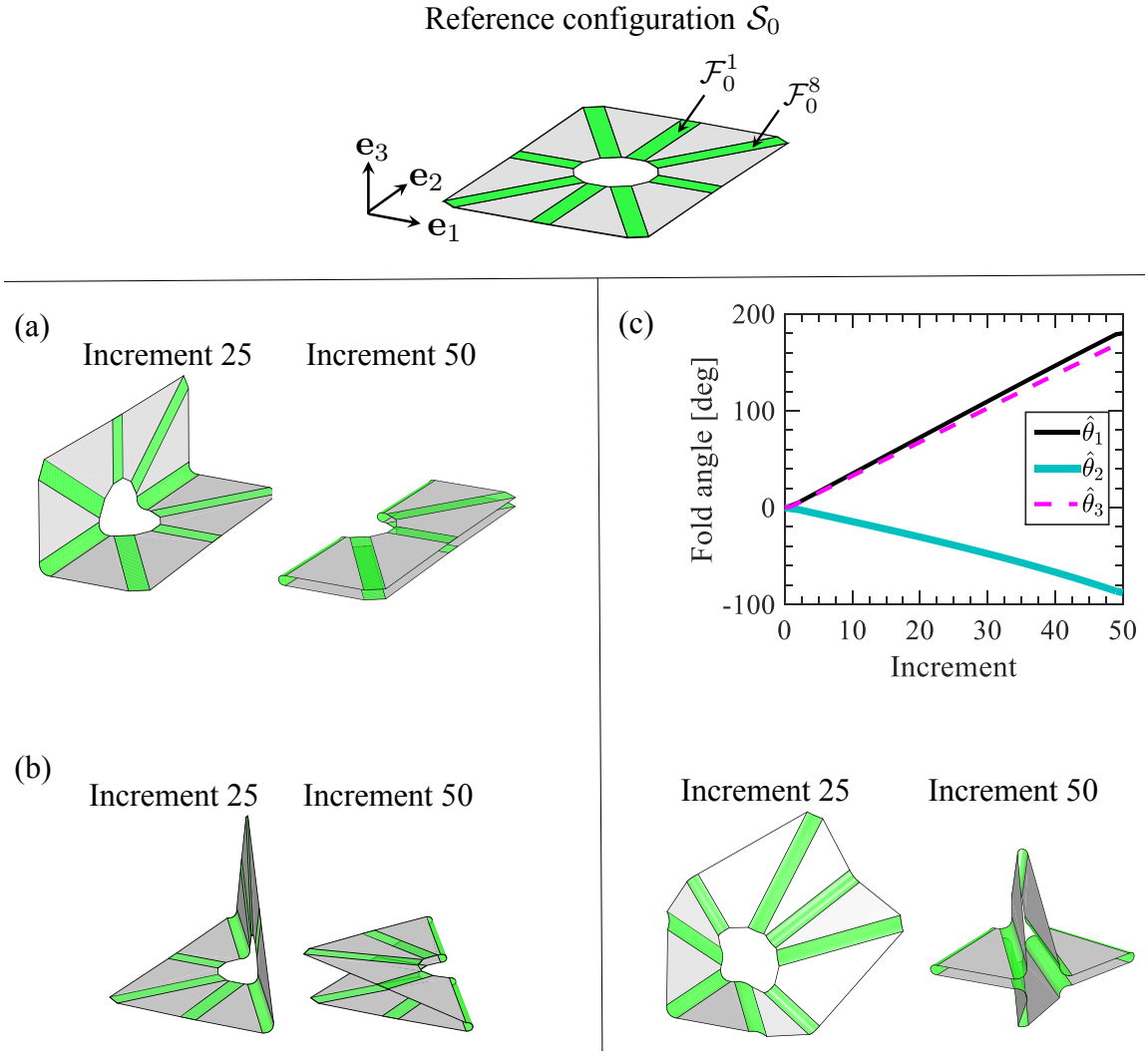

Figure 2.13: (a) and (b): Configurations of a sheet having a single interior fold intersection obtained through the guess fold angle increments provided in Equations (2.155) and (2.156), respectively. (c) Fold angles vs increment number and configurations obtained through the guess fold angle increments provided in Equation (2.157).

Figure 2.14 for the numbering of the folds):

$$ {}^{IN}_{l}\Delta\hat{\boldsymbol{\theta}} = \frac{\pi}{120} \begin{bmatrix} 1 \\ -1 \\ 1 \\ 1 \\ -1 \\ 1 \\ -1 \\ -1 \\ -1 \\ 1 \\ -1 \\ 1 \\ 1 \\ -1 \\ 1 \end{bmatrix} \qquad \forall\, l \in \{1, \ldots, 100\}. \tag{2.158} $$

The sheet with the baseline fold pattern shown in Figure 2.16(a) exhibits a symmetric behavior, which is expected from the symmetry of the fold pattern and the guess fold angle increments. Sheets having fold patterns obtained by modifying the interior vertex coordinates and the boundary vertex coordinates of the baseline fold pattern are respectively shown in Figures 2.16(b) and 2.16(c). It is observed that both sheets undergo dissimilar fold angle histories compared to the sheet having the baseline fold pattern as observed from both the folded configurations in Figure 2.16 and the fold angle vs. increment number plots in Figure 2.15. These examples show the versatility of the present model that allows for simulation of sheets having arbitrary fold patterns and boundary shapes. This permits the potential application of the model in the design of origami-based structures and mechanisms constrained by realistic material and structural constraints.

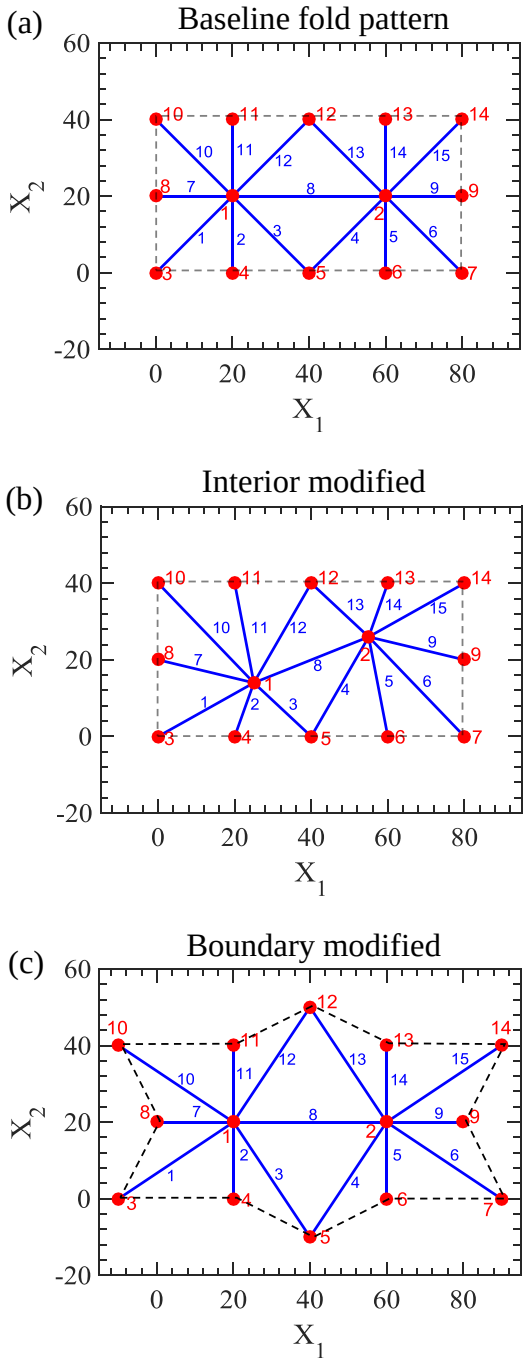

Figure 2.14: Graphs showing the vertex coordinates and fold centerlines for the sheets shown in Figure 2.16.

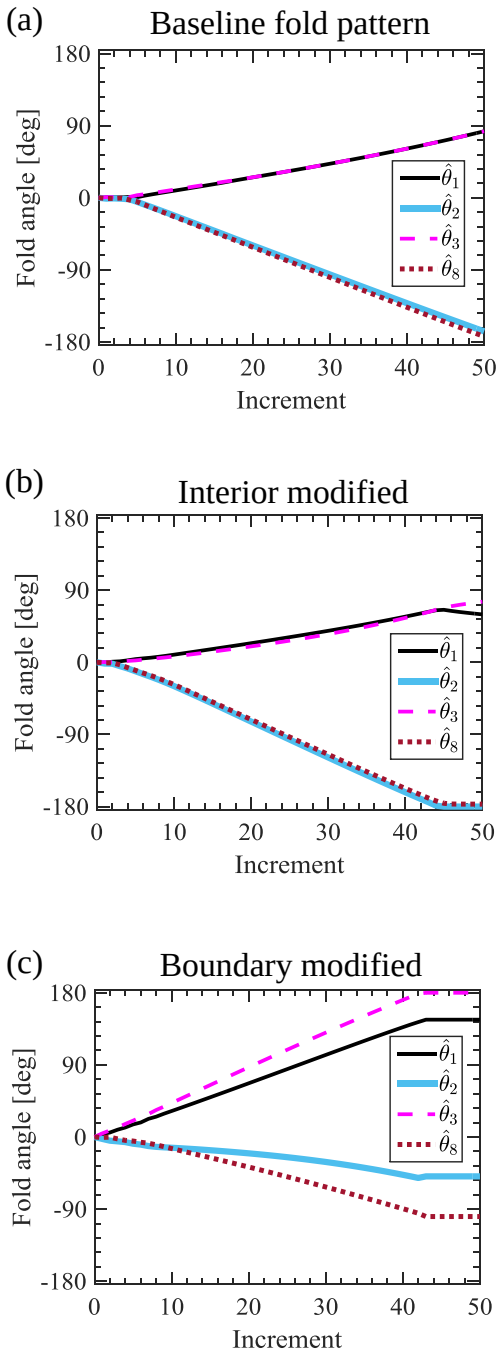

Figure 2.15: Evolution of fold angles with increment number for the sheets shown in Figure 2.16.

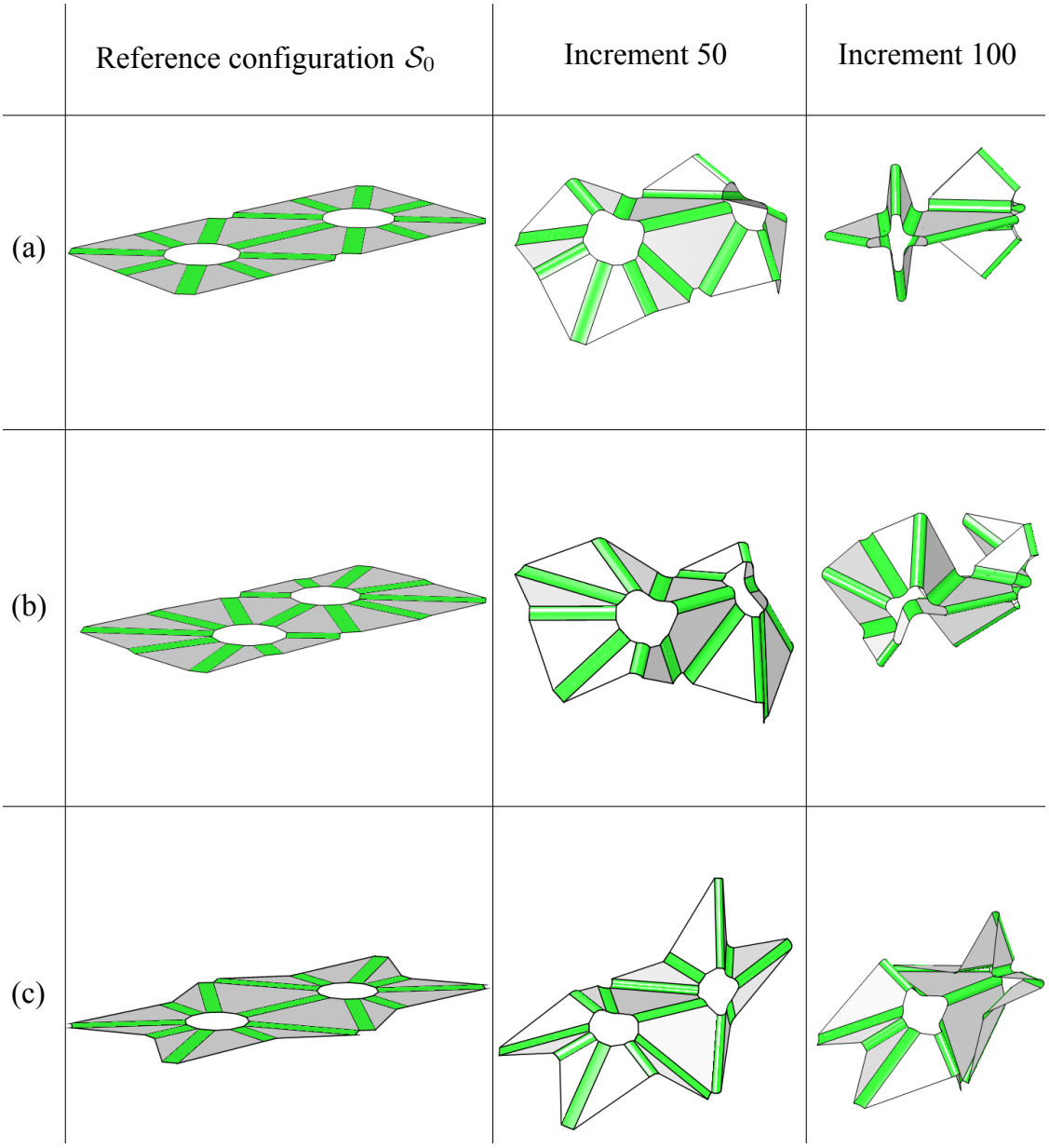

Figure 2.16: Configurations for origami sheets with vertex coordinates and fold centerlines defined in Figure 2.15: (a) Sheet with the baseline fold pattern, (b) Sheet with a fold pattern generated by modifying the interior vertex coordinates of the baseline fold pattern, and (c) Sheet with a fold pattern generated by modifying the boundary vertex coordinates of the baseline fold pattern.

The present model is also applicable for the simulation of sheets having arbitrary topology. To illustrate this, sheets having four, five, and six interior fold intersections are shown in Figure 2.17[10]. Various configurations are shown for these examples. As observed from these schematics, the present model captures well the behavior of the folded sheets during their full range of motion (fold angles vary from 0 to $\pm\pi$ for various folds in these sheets). The sheet having four interior fold intersections exhibits a desired response that the proposed model captures well, which is of configurations having all the faces located in parallel normal directions but not overlapping one another. This may aid to ongoing efforts to model and design origami structures with thick sheets (see [399, 400, 403, 430, 431, 432, 433]).

2.4 Summary and Discussion

A model for the kinematic response of origami structures with smooth folds having non-zero sheet surface area and arbitrary order of geometric continuity was presented in this section. A brief review of an established model for origami with conventional creased folds that is extended herein is provided in Section 2.1. The geometrical description of smooth folds was presented in Section 2.2.1 and parametric representations of the fold cross-sectional shape for various orders of continuity were provided in Section 2.2.1.1. The fold pattern description (Section 2.2.2), the constraints on the sheet deformation for origami with smooth folds analogous to those for origami with creased folds (Section 2.2.3), and the mapping between reference and current configurations (Section 2.2.4) were also presented. The numerical implementation of the model allowing for simulation of the motion of sheets with arbitrary fold patterns was described in Section 2.2.6 and implementation examples were provided in Section 2.3.

[10]The example shown in Figure 2.4 is also a simulation result obtained using the proposed model.

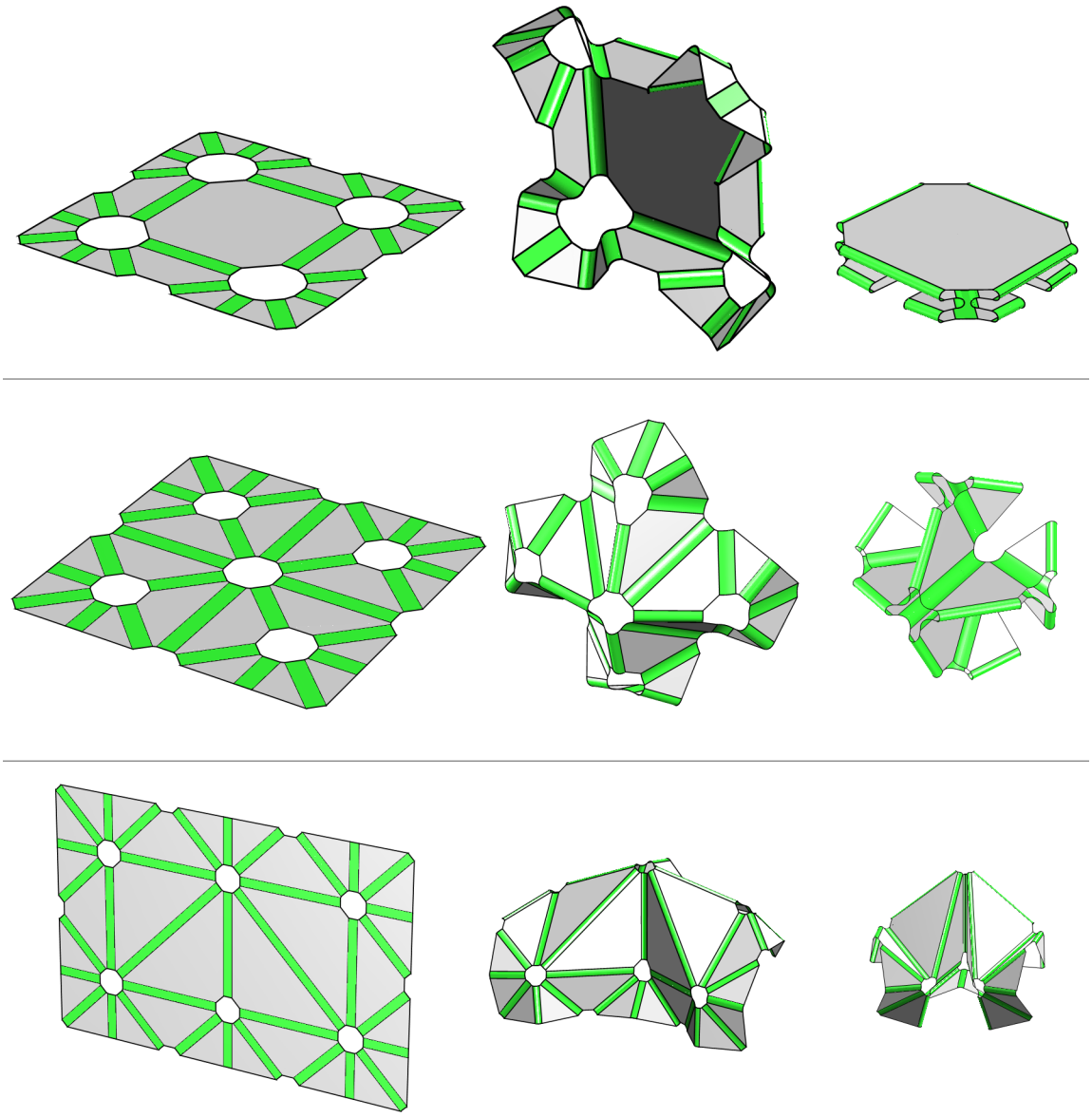

Figure 2.17: Demonstration of constrained motion associated with origami sheets having four, five, and six interior fold intersections. Note that configurations of substantial folding are captured without bending or stretching of the faces or tearing of the sheet.

From the model formulation developed and the results presented in this section, a number of concluding remarks can be stated. First, the proposed model successfully allows for the mathematical representation of origami with folds of non-zero sheet surface area and arbitrary order of geometric continuity (in terms of fold shape geometry, constraints on the fold shape variables, and mapping between reference and current configurations). The conventional origami with creased folds of G^0 continuity represents a special case of this more general model and is captured as well. Furthermore, the arbitrary order of geometric continuity in the sheet considered in this work allows for the physical modeling of origami structures having significant thickness using plate or shell representations, which is the focus in Section 4. Second, the present model and its associated numerical implementation allow for the simulation of sheets having arbitrary fold pattern geometry and boundary shape. The careful consideration of constraints ensures that only meaningful valid configurations will be predicted. The proposed modeling and simulation framework readily allows for modifications to the fold pattern and folding sequence as demonstrated in the implementation examples provided in Section 2.3. These characteristics make such a model useful in future fold pattern design and fold planning studies for origami structures and mechanisms having folds that cannot be accurately represented as creases. This is the main focus of the following section.

3. DESIGN OF ORIGAMI STRUCTURES WITH SMOOTH FOLDS

Origami has obtained the interest from researchers in various fields during the last four decades [13, 14, 45]. During this period of time, origami principles have enabled new approaches for manufacturing, assembling, and morphing of structures constructed from various materials as reviewed in Section 1. Creating an origami structure having desired characteristics, particularly a desired shape, is known as *origami design* [9]. Origami design is a challenge encountered not only by origami artists but also by designers and engineers who apply origami in various fields. Before obtaining extensive interest from the engineering and mathematics communities, most origami design was performed via trial and error or other heuristic approaches based on the intuition of an artist or designer [363]. With the increase in complexity of origami shapes that provide engineering utility, theoretical and computational approaches for the design of origami structures have become necessary for developments in this area [3, 13, 363].

Current methods for origami design are generally limited to the idealization of the folds as creases of zeroth-order geometric continuity (refer to Section 1.5 for a literature review on design methods for origami structures). Such an idealization is not proper for origami structures having non-negligible fold thickness or with maximum curvature at the folds restricted by material limitations. For such structures, the folds are not properly represented as creases but rather as bent regions of higher-order geometric continuity (i.e. *smooth folds*, see Definition 2.6).

The main contribution of this section is a novel method for origami design having its inspiration from that presented by Tachi in [9, 391] but considering smooth folds as opposed to creased folds (see Figure 1.10). The method aims to solve the fol-

lowing origami design problem: given a goal shape represented as a polygonal mesh (termed as the *goal mesh*), find the geometry of a single continuous planar sheet, its pattern of *smooth folds*, and a folding sequence allowing for folding motion from the determined planar sheet configuration to a folded configuration that approximates the goal mesh. A process for determining a folding sequence allowing for folding motion from the determined planar sheet configuration to the folded configuration that approximates the goal mesh has not been previously addressed in [9, 391]. Therefore, the determination of such a folding sequence addressed here represents another contribution of the present work and is applicable to both origami with smooth folds and conventional origami with creased folds.

The outline of this section is as follows: Section 3.1 summarizes the main aspects of kinematic simulation of origami structures presented in Section 2 for the introduction of the contributions provided in this section. The main definitions of origami design problem considered herein are presented in Section 3.2. The novel design method for origami with smooth folds proposed in this work is described in detail in Section 3.3. It includes the description of the input data, required modifications of the goal mesh, parameterization of the design, and constraints on the design variables. A numerical procedure used to determine valid designs is outlined in Section 3.4. A discussion of valid sheet designs is provided in Section 3.5. A brief description of the kinematic simulation procedure used to determine the continuous deformation of the designed sheets is provided in Section 3.6. Results illustrating the capabilities of the proposed design method are provided in Section 3.7 and a discussion of the section and concluding remarks are provided in Section 3.8.

3.1 Review of Kinematic Simulation

The problem of kinematically simulating origami structures with smooth folds, which is fully addressed in Section 2, can be summarized as follows:

- Given: the geometric parameters that describe the fold pattern in a reference configuration $\mathcal{S}_0$ (vertex position vectors and fold widths, refer to Section 2.2.2), and guess fold angle increments $\{{}^{IN}_{l}\Delta\hat{\boldsymbol{\theta}} \in \mathbb{R}^{N_{\mathcal{F}}} \,|\, l \in \{1, \ldots, n\}\}$ (i.e. the folding sequence),

- Find: the set of fold angles $\{\hat{\boldsymbol{\theta}}(t) \in \mathbb{R}^{N_{\mathcal{F}}} \mid t \in \{t_1, \ldots, t_n\}\}$ that satisfy the kinematic constraints presented in Equation (2.97) closest to those resulting from the given fold angle increments, and the set of current configurations attained by the sheet $\{\mathcal{S}_t \,|\, t \in \{t_1, \ldots, t_n\}\}$.

The numerical approach utilized to solve the aforementioned problem is presented in Section 2.2.6. Figure 3.1 illustrates the capabilities of such a kinematic simulation approach for origami structures with smooth folds. The figure shows the reference configuration $\mathcal{S}_0$ and two current configurations $\mathcal{S}_{t_k}$ and $\mathcal{S}_{t_n}$ of a sheet having an arbitrary fold pattern subject to an arbitrary folding sequence. This kinematic simulation approach is also adopted in this section as described in the subsequent section and motivates the adopted approach to origami design.

3.2 Origami Design Problem Description

As stated in Section 1.5, creating an origami structure having desired characteristics, particularly a desired shape, is known as *origami design* [9]. This section presents a novel method that aims to solve the following origami design problem:

- Given: a goal shape represented as a polygonal mesh (termed as the *goal mesh* $\mathcal{M}$),

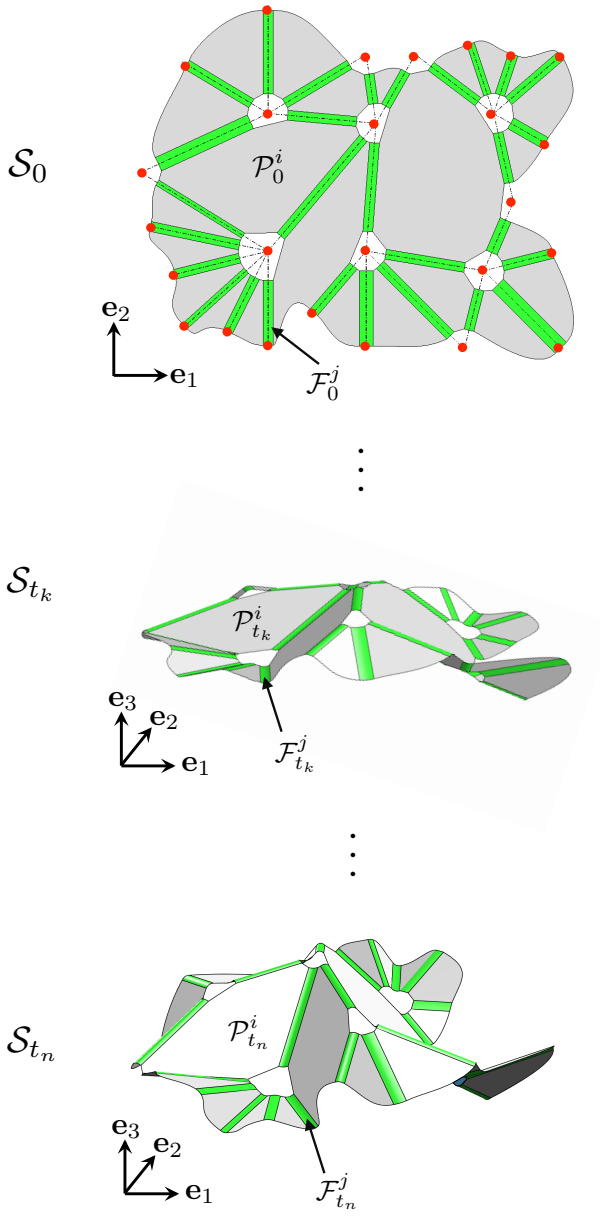

Figure 3.1: An origami sheet with smooth folds in its reference configuration $\mathcal{S}_0$, intermediate configuration $\mathcal{S}_{t_k}$, and final configuration $\mathcal{S}_{t_n}$. This result illustrates the capabilities of the kinematic simulation approach for origami structures with smooth folds presented in Section 2.

- Find: the geometry of the reference configuration $\mathcal{S}_0$ of a single planar sheet, its pattern of smooth folds, and a folding sequence allowing for folding motion from $\mathcal{S}_0$ to a folded configuration that approximates $\mathcal{M}$.

The method for origami design proposed in this section is inspired from that provided by Tachi in [9, 391] but allows for the consideration of smooth folds, as opposed to only creased folds addressed in [9, 391]. As previously noted, a process for determining a folding sequence allowing for folding motion from $\mathcal{S}_0$ to a folded configuration that approximates $\mathcal{M}$ was not addressed in [9, 391]. Therefore, the determination of such a folding sequence represents another contribution of the present work and is applicable to both origami with smooth folds and conventional origami with creased folds.

The steps in the proposed method for origami design are the following:

(i) If the given polygonal mesh is not topologically equivalent to a disk [9], edge cuts introducing an additional boundaries $\partial\mathcal{M}^C$ are applied (see Section 2.2.1 of [9] for details and additional references regarding the mesh cut procedure). Further boundary edges forming $\partial\mathcal{M}^C$ can also be introduced as long as the resulting mesh satisfies the aforementioned topological property. A goal mesh $\mathcal{M}$ with boundary $\partial\mathcal{M} = \partial\mathcal{M}^C \cup \partial\mathcal{M}^O$ and faces $\mathcal{M}^j \subset \mathcal{M}$, $j = 1, ..., N_{\mathcal{M}}$ (where $N_{\mathcal{M}}$ is the total number of faces in $\mathcal{M}$) is then obtained. The boundary $\partial\mathcal{M}^O$ is comprised of the boundary edges of the originally given mesh. The goal mesh $\mathcal{M}$ is defined by its node position vectors $\{\hat{\mathbf{y}}^i \in \mathbb{R}^3 \,|\, i \in \{1, \ldots, N_{\mathcal{N}}\}\}$ (where $N_{\mathcal{N}}$ is the number of nodes in $\mathcal{M}$) and connectivity information describing which nodes are associated with each face $\mathcal{M}^j$ (refer to Section 3.4.1 for details)

(ii) A planar sheet reference configuration $\mathcal{S}_0$ consisting of the faces $\mathcal{M}^j$, j =

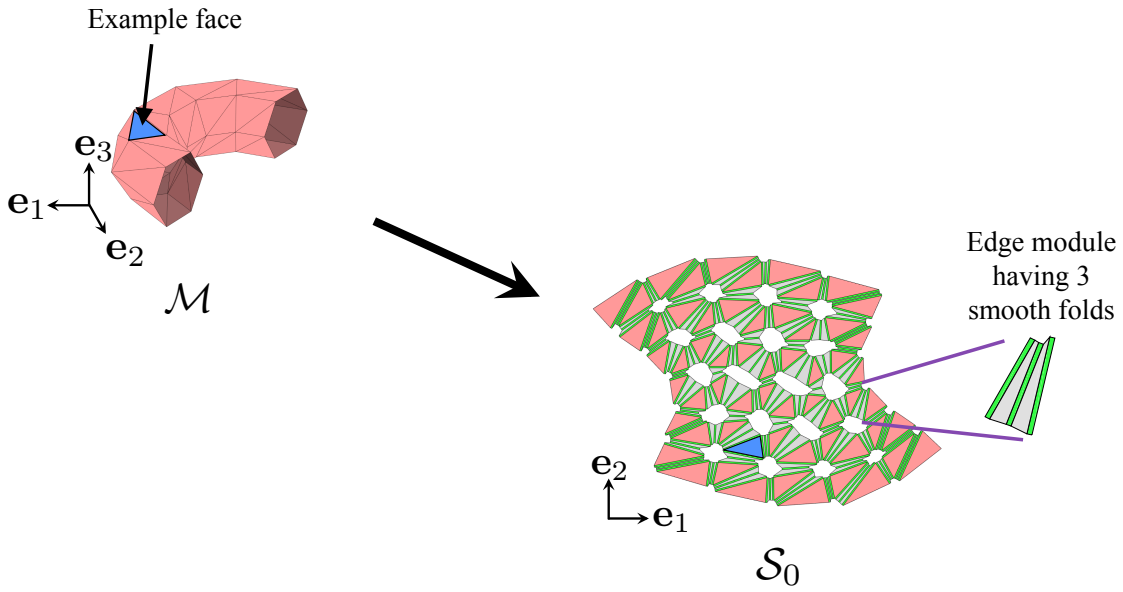

Figure 3.2: Schematic illustrating the method for origami design presented in this work: given a goal mesh $\mathcal{M}$, find the reference configuration $\mathcal{S}_0$ of a sheet that approximates $\mathcal{M}$ in a known folded configuration. The reference configuration $\mathcal{S}_0$ is comprised of the faces of $\mathcal{M}$ mapped to the plane spanned by $\mathbf{e}_1$ and $\mathbf{e}_2$ and introduced edge modules having two rigid faces and three smooth folds.

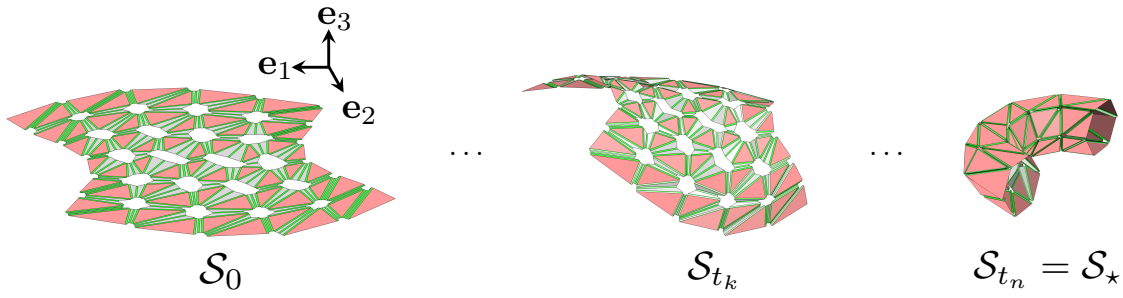

Figure 3.3: Folding motion of a determined sheet reference configuration $\mathcal{S}_0$ towards the goal configuration $\mathcal{S}_\star$ that approximates the goal mesh $\mathcal{M}$ (see Figure 3.2).

$1, ..., N_{\mathcal{M}}$, mapped to the plane spanned by $\mathbf{e}_1$ and $\mathbf{e}_2$ and $N_{\mathcal{E}}^I$ introduced *edge modules* (where $N_{\mathcal{E}}^I$ is the number of interior edges of $\mathcal{M}$) is then determined (Figure 3.2). The edge modules consist of *three smooth folds and two rigid faces* and are placed between every two faces of $\mathcal{M}$ connected by an interior edge[1], hence called edge modules. Thus, $\mathcal{S}_0$ has $3N_{\mathcal{E}}^I$ smooth folds and $2N_{\mathcal{E}}^I + N_{\mathcal{M}}$ rigid faces (refer to Section 2.2), i.e.

$$N_{\mathcal{F}} = 3N_{\mathcal{E}}^I, \tag{3.1}$$

$$N_{\mathcal{P}} = 2N_{\mathcal{E}}^I + N_{\mathcal{M}}. \tag{3.2}$$

Therefore, $\mathcal{S}_0 = (\bigcup_{i=1}^{3N_{\mathcal{E}}^I} \mathcal{F}_0^i) \cup (\bigcup_{i=1}^{2N_{\mathcal{E}}^I + N_{\mathcal{M}}} \mathcal{P}_0^i)$. The challenge in this step is to determine the geometry of the edge modules given the information of $\mathcal{M}$ and the fold widths of the smooth folds in each edge module (i.e. $\hat{w}_i^0$, $i = 1, \ldots, 3N_{\mathcal{E}}^I$) such that a valid reference configuration $\mathcal{S}_0$ is obtained (refer to Section 2.2) and such a sheet can approximate $\mathcal{M}$ in a known goal configuration $\mathcal{S}_\star$ ($\mathcal{S}_\star$ for the example shown in Figure 3.2 is shown in Figure 3.3)

(iii) The final step entails the determination of a *folding sequence* that allows for the folding motion from the reference configuration $\mathcal{S}_0$ to the goal configuration $\mathcal{S}_\star$. As described in Section 3.1, the simulation of the motion of the sheet is performed in a sequence of increments. Thus, the challenge in this step is the determination of the fold angle increments $\{{}^{IN}_{l}\Delta\hat{\boldsymbol{\theta}} \in \mathbb{R}^{3N_{\mathcal{E}}^I} \mid l \in \{1, \ldots, n\}\}$ leading to a set of fold angles $\{\hat{\boldsymbol{\theta}}(t) \in \mathbb{R}^{3N_{\mathcal{E}}^I} \mid t \in \{t_1, \ldots, t_n\}\}$ that results in

[1]The idea of introducing such modules with three folds and to *tuck* fold them in order to approximate a three-dimensional goal shape was initially introduced for conventional origami with creased folds by Tachi in [9, 391].

the set of configurations $\{\mathcal{S}_t \mid t \in \{t_1, \ldots, t_n\}, \mathcal{S}_{t_n} = \mathcal{S}_\star\}$. Figure 3.3 shows configurations attained by the sheet from the example in Figure 3.2 during a determined folding sequence allowing for folding motion from $\mathcal{S}_0$ to $\mathcal{S}_\star$.

This work addresses (ii) and (iii) of the previous list (i.e. determination of $\mathcal{S}_0$ given $\mathcal{M}$ and fold widths $\hat{w}_i^0$, $i = 1, \ldots, 3N_{\mathcal{E}}^I$, and subsequent determination of a folding sequence for deformation from $\mathcal{S}_0$ to $\mathcal{S}_\star$). Algorithms to determine a boundary that yields a surface mesh topologically equivalent to a disk are available in the literature [9, 434, 435, 436] and are not the subject of this work.

3.3 Design Method

As described in Section 3.2, the design method proposed herein aims first to determine the geometry of a planar sheet configuration $\mathcal{S}_0$ and its pattern of smooth folds that approximates a given three-dimensional surface goal shape represented as a polygonal mesh $\mathcal{M}$ in a known configuration (denoted as the *goal configuration* $\mathcal{S}_\star$). The method is based on the previously known idea of using folds to create flaps that are *tucked* in order to morph an initially planar sheet towards an arbitrary three-dimensional shape [9, 391].

The three-dimensional *goal mesh* $\mathcal{M}$ is a three-dimensional polygonal mesh topologically equivalent to a disk and having a boundary denoted as $\partial\mathcal{M}$. The polygonal faces forming $\mathcal{M}$ are denoted $\mathcal{M}^j$ such that $\mathcal{M} = \bigcup_{i=1}^{N_{\mathcal{M}}} \mathcal{M}^j$. The boundary of the originally given mesh is denoted $\partial\mathcal{M}^O$ (refer to Figure 3.4). For a given mesh that is not topologically equivalent to a disk, interior edges of such a mesh are assigned as boundary edges forming a boundary $\partial\mathcal{M}^C$ in order to obtain a goal mesh $\mathcal{M}$ that has a single continuous boundary $\partial\mathcal{M} = \partial\mathcal{M}^C \cup \partial\mathcal{M}^O$ (see the example shown in Figure 3.4). It is noted that the assignment of boundary edges forming $\partial\mathcal{M}^C$ may not only be used to generate a valid goal mesh $\mathcal{M}$ but also to obtain different sheet

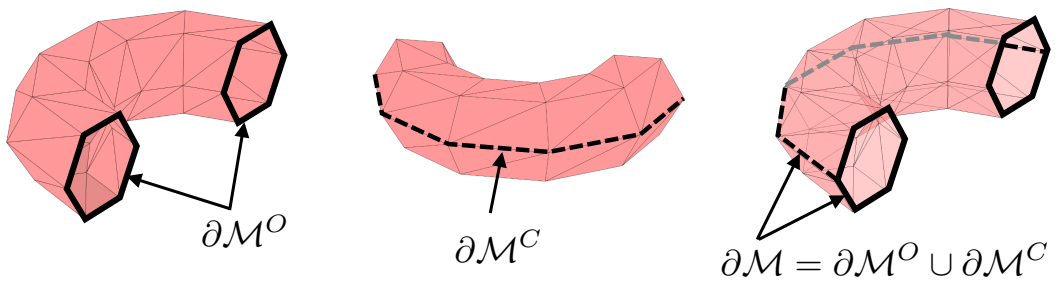

Figure 3.4: Outer edges of the given polygonal mesh forming the boundary $\partial\mathcal{M}^O$, additional boundary cut $\partial\mathcal{M}^C$, and the boundary of the *goal mesh* $\mathcal{M}$ denoted $\partial\mathcal{M} = \partial\mathcal{M}^C \cup \partial\mathcal{M}^O$. This figure is associated with the example shown in Figure 3.2.

reference configurations for the given mesh. Criteria for determining an optimal boundary $\partial\mathcal{M}$ is not currently addressed but can be found in the literature [9, 434].

An example of a simple goal mesh $\mathcal{M}$ is shown in Figure 3.5. The goal mesh has $N_{\mathcal{N}}$ nodes and $N_{\mathcal{E}}$ edges ($N_{\mathcal{N}} = 25$ and $N_{\mathcal{E}} = 56$ for the goal mesh shown in Figure 3.5). The number of interior nodes, i.e. those not contained in $\partial\mathcal{M}$, is denoted $N^I_{\mathcal{N}}$. As stated in the previous section, each node in $\mathcal{M}$ has an associated position vector $\hat{\mathbf{y}}^i \in \mathbb{R}^3$, $i = 1, \ldots, N_{\mathcal{N}}$ [2]. Each polygonal face $\mathcal{M}^j$ is defined by its ordered associated nodes. Therefore, the *input data* required to define $\mathcal{M}$ is the following: (i) The node position vectors $\hat{\mathbf{y}}^i$, $i = 1, \ldots, N_{\mathcal{N}}$, and (ii) the index list of the nodes associated with each polygonal face $\mathcal{M}^j$ (in a counterclockwise ordering which is adopted in this work). The connectivity matrices obtained from this input data and the mappings among various parameters and variables used in this work are provided in Section 3.4.1.

The steps towards determining a planar sheet having smooth folds that morphs towards the input goal mesh and its subsequent kinematic analysis are illustrated

[2] A hat ($\hat{}$) is used to distinguish the mesh-related geometric parameters and variables from those face- and node-related ones.

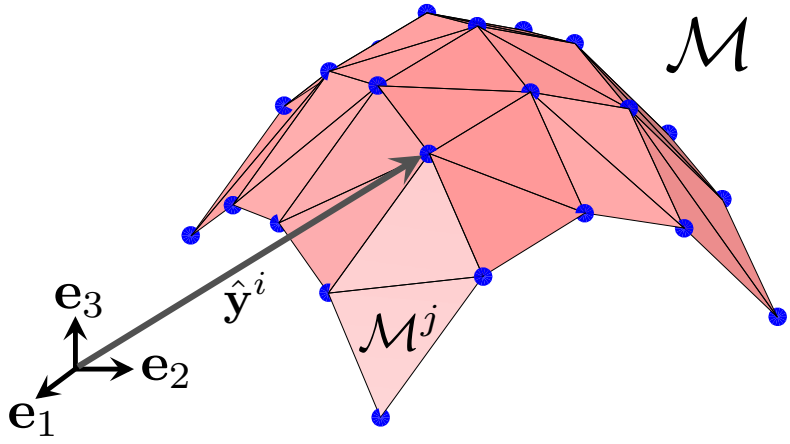

Figure 3.5: Schematic showing a goal mesh $\mathcal{M}$. A node position vector $\hat{\mathbf{y}}^i$ and a goal mesh face $\mathcal{M}^j$ are also shown.

in Figure 3.6. A simple example of a goal mesh $\mathcal{M}$ is presented in Figure 3.6(a). The faces $\mathcal{M}^j$ are initially trimmed to account for the gap that will be created by the tucked edge modules (Figure 3.6(b)). The face trimming process is described in detail in Section 3.3.1. The set of trimmed mesh faces is denoted as $\mathcal{M}_\sharp$ and its associated trimmed faces are denoted as $\mathcal{M}^j_\sharp$ such that $\mathcal{M}_\sharp = \bigcup_{i=1}^{N_\mathcal{M}} \mathcal{M}^j_\sharp$.

The method proceeds by determining the geometry of the *edge modules* (Figure 3.6(c)) that are placed between any two trimmed faces $\mathcal{M}^j_\sharp$ and $\mathcal{M}^k_\sharp$ having associated goal mesh faces $\mathcal{M}^j$ and $\mathcal{M}^k$ joined by an interior edge. The *edge modules* are comprised of three smooth folds and two rigid faces and are designed such that the faces $\mathcal{M}^j_\sharp$ together with these edge modules can be placed as a connected surface on the plane spanned by $\mathbf{e}_1$ and $\mathbf{e}_2$. Such a resulting planar surface corresponds to the sheet reference configuration $\mathcal{S}_0$ (Figure 3.6(d)).

During folding motion of the designed sheet, each edge module is tucked to morph the sheet towards its *goal configuration* $\mathcal{S}_\star$ for which the folds angles are known from the goal mesh data (Figure 3.6(d)). Note that $\mathcal{M}_\sharp \subset \mathcal{S}_\star$ under appropriate rigid

transformations. A view of the tucked edge modules, that are designed such that they do not intersect in the goal configuration, is shown in Figure 3.6(e).

Let $\mathbf{z}^{jk} \in \mathbb{R}^3$, $j = 1, \ldots, N_{\mathcal{N}}^I$, $k = 1, \ldots, n_j^{\mathcal{M}}$, be the vectors connecting the j^{th} interior node to its k^{th} adjacent node, defined in counterclockwise order, where $n_j^{\mathcal{M}}$ is the number of faces connected to the j^{th} interior node (see Figure 3.7). These vectors are readily determined from the provided input data (see Section 3.4.1.3). The parameters associated with the faces of $\mathcal{M}$ having a common interior node are the face angles ϕ_{jk} and the face unit normal vectors $\mathbf{n}^{jk} \in \mathbb{R}^3$, $j = 1, \ldots, N_{\mathcal{N}}^I$, $k = 1, \ldots, n_j^{\mathcal{M}}$. These parameters are determined respectively as follows:

$$\phi_{jk} = \cos^{-1}\left(\frac{\mathbf{z}^{jk} \cdot \mathbf{z}^{j\,k+1}}{\|\mathbf{z}^{jk}\|\,\|\mathbf{z}^{j\,k+1}\|}\right), \tag{3.3}$$

$$\mathbf{n}^{jk} = \frac{\mathbf{z}^{jk} \times \mathbf{z}^{j\,k+1}}{\|\mathbf{z}^{jk} \times \mathbf{z}^{j\,k+1}\|}. \tag{3.4}$$

3.3.1 Face Trimming

A side view of a tucked edge module is shown in Figure 3.8. It is assumed that each edge module is tucked in a symmetric manner and therefore the exterior folds for each edge module (folds 1 and 3 in Figure 3.8) have the same values for their geometric variables at $\mathcal{S}_\star$. The interior fold (fold 2 in Figure 3.8) has a fold angle of π when the edge module is tucked at $\mathcal{S}_\star$. It is observed in Figure 3.8 that due to the bending deformation of the smooth folds (as opposed to creasing), a gap results between two mesh faces connected to the edge module in the goal configuration $\mathcal{S}_\star$. To account for this gap, the faces of the goal mesh are initially recomputed to generate the *trimmed* mesh as shown in Figure 3.6(b). The removed regions compensate for the gaps and have an associated length $\hat{l}_i$, $i = 1, \ldots, N_{\mathcal{E}}^I$, as shown in Figure 3.8. To

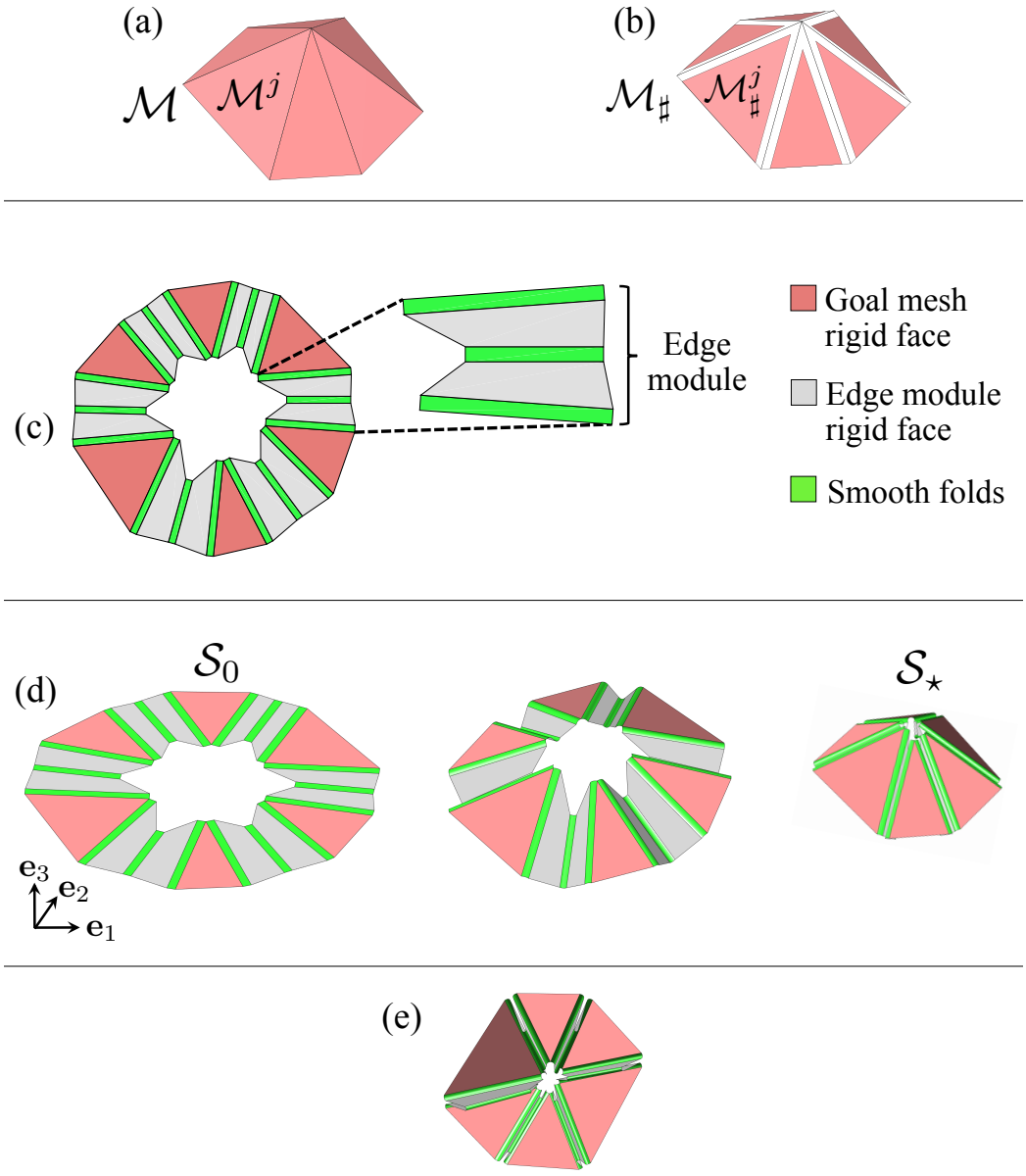

Figure 3.6: (a) Example goal mesh $\mathcal{M}$ having one interior node; (b) Set of trimmed mesh faces $\mathcal{M}_\sharp$; (c) Determined sheet geometry and fold pattern associated with the goal mesh shown in (a); (d) Folding deformation from the reference planar configuration $\mathcal{S}_0$ to the goal configuration $\mathcal{S}_\star$. Note that $\mathcal{M}_\sharp \subset \mathcal{S}_\star$ under appropriate rigid transformations; (e) View of the non-intersecting tucked edge modules in the goal configuration $\mathcal{S}_\star$.

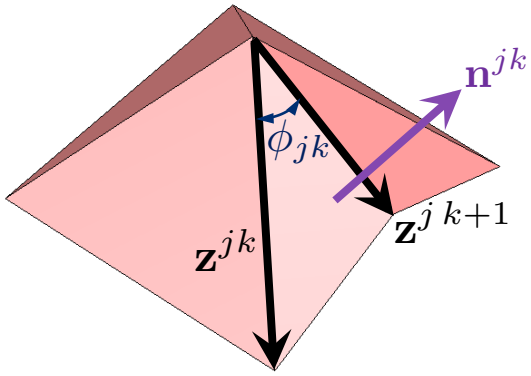

Figure 3.7: Geometric parameters associated with the faces of $\mathcal{M}$ having a common interior node.

define these removed regions, first the edge dihedral angle $\hat{\Theta}_i \in (0, 2\pi)$, $i = 1, \ldots, N_{\mathcal{E}}^I$, is calculated as follows (see Figure 3.8):

$$\hat{\Theta}_i = \begin{cases} \pi + \cos^{-1}(\hat{\mathbf{n}}^{i1} \cdot \hat{\mathbf{n}}^{i2}); & \text{for convex edges} \\ \\ \pi - \cos^{-1}(\hat{\mathbf{n}}^{i1} \cdot \hat{\mathbf{n}}^{i2}); & \text{for concave edges} \end{cases}, \tag{3.5}$$

where $\hat{\mathbf{n}}^{i1}$ and $\hat{\mathbf{n}}^{i2}$ are the unit normals of the faces adjacent to the i^{th} interior edge.

Table 3.1: Values for fold width and the shape variables of the smooth folds at the goal configuration $\mathcal{S}_\star$. Refer to Figure 3.8 for the numbering of the folds.

	Fold width	Fold angle at $\mathcal{S}_\star$	Distance between cross-section end-points at $\mathcal{S}_\star$
Fold 1	$\hat{w}_i^{\mathsf{E}0}$	$-\hat{\Theta}_i/2$	$\hat{w}_i^{\mathsf{E}\star}$
Fold 2	$\hat{w}_i^{\mathsf{I}0}$	π	$\hat{w}_i^{\mathsf{I}\star}$
Fold 3	$\hat{w}_i^{\mathsf{E}0}$	$-\hat{\Theta}_i/2$	$\hat{w}_i^{\mathsf{E}\star}$

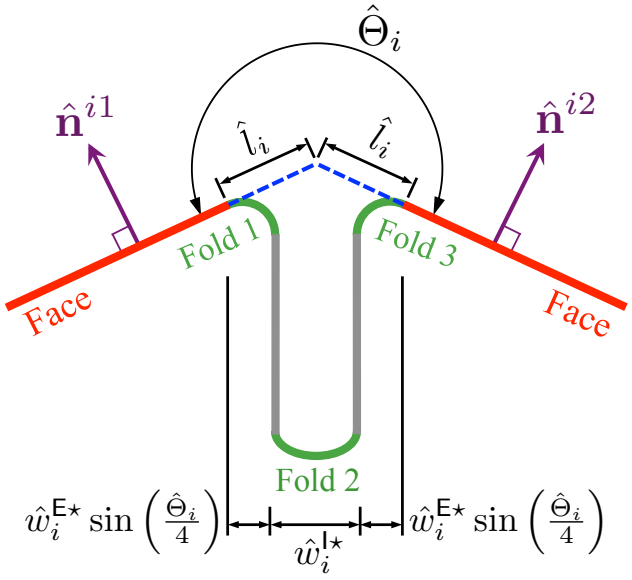

Figure 3.8: Side view of an example tucked edge module and its adjacent goal mesh faces at the goal configuration $\mathcal{S}_\star$. The geometric parameters defining the trim length $\hat{l}_i$ are shown.

Let $\hat{w}_i^{\mathsf{I}\star}$ be the distance between the cross-section end-points of the interior fold in the i^{th} edge module at $\mathcal{S}_\star$, respectively (refer to Table 3.1). Also, let $w_i^{\mathsf{E}\star}$ be the distance between the cross-section end-points of the exterior folds. The trim lengths $\hat{l}_i$ are then calculated as follows (refer to Figure 3.8):

$$\hat{l}_i = \left(\frac{\hat{w}_i^{\mathsf{I}\star}}{2} + \hat{w}_i^{\mathsf{E}\star} \sin\left(\frac{\hat{\Theta}_i}{4}\right) \right) \csc\left(\frac{\hat{\Theta}_i}{2}\right). \tag{3.6}$$

Let n_j^C be the number of corners of the goal mesh polygonal face $\mathcal{M}^j$. Also, let $\tilde{\mathbf{y}}^{jk} \in \mathbb{R}^3$, $k = 1, \ldots, n_j^C$, be the position vectors of the nodes corresponding to the corners of $\mathcal{M}^j$, ordered counterclockwise[3]. The position vectors of the corner points of the trimmed face $\mathcal{M}_\sharp^j$, denoted $\tilde{\mathbf{y}}_\sharp^{jk} \in \mathbb{R}^3$, $k = 1, \ldots, n_j^C$, are determined as follows

[3]A tilde ($\tilde{}$) is used to distinguish the face-related parameters and variables from mesh- and node-related ones.

(refer to Figure 3.9(a)):

$$\tilde{\mathbf{y}}_{\sharp}^{jk} = \tilde{\mathbf{y}}^{jk} + \tilde{l}_{j\,k-1}\csc(\tilde{\phi}_{jk})\frac{\tilde{\mathbf{y}}^{j\,k+1} - \tilde{\mathbf{y}}^{jk}}{\|\tilde{\mathbf{y}}^{j\,k+1} - \tilde{\mathbf{y}}^{jk}\|} + \tilde{l}_{jk}\csc(\tilde{\phi}_{jk})\frac{\tilde{\mathbf{y}}^{j\,k-1} - \tilde{\mathbf{y}}^{jk}}{\|\tilde{\mathbf{y}}^{j\,k-1} - \tilde{\mathbf{y}}^{jk}\|}, \tag{3.7}$$

where the interior corner angles of $\mathcal{M}^j$ denoted $\tilde{\phi}_{jk}$ are determined as follows:

$$\tilde{\phi}_{jk} = \cos^{-1}\left(\frac{(\tilde{\mathbf{y}}^{j\,k-1} - \tilde{\mathbf{y}}^{jk})\cdot(\tilde{\mathbf{y}}^{j\,k+1} - \tilde{\mathbf{y}}^{jk})}{\|\tilde{\mathbf{y}}^{j\,k-1} - \tilde{\mathbf{y}}^{jk}\|\,\|\tilde{\mathbf{y}}^{j\,k+1} - \tilde{\mathbf{y}}^{jk}\|}\right), \tag{3.8}$$

and $\tilde{l}_{jk}$, $k = 1, \ldots, n_j^C$, is the trim length associated with the k^{th} edge of $\mathcal{M}^j$. The mapping from the edge trim lengths $\hat{l}_i$, $i = 1, \ldots, N_{\mathcal{E}}^I$, to each set $\tilde{l}_{jk}$, $k = 1, \ldots, n_j^C$, is provided in Section 3.4.1.2 (see Equation (3.44)).

Only the length of the edges of $\mathcal{M}^j$ is altered by the face trimming process, while its corner angles remain unchanged under the condition stated in the following proposition:

Proposition 3.1. *The faces $\mathcal{M}^j$ and $\mathcal{M}_{\sharp}^j$ have equal corner angles if and only if $\mathcal{M}_{\sharp}^j$ is not a degenerate case of $\mathcal{M}^j$ and has the same orientation of $\mathcal{M}^j$.*

Proof. If $\mathcal{M}^j$ and $\mathcal{M}_{\sharp}^j$ have equal corner angles, then $\mathcal{M}_{\sharp}^j$ is not a degenerate case of $\mathcal{M}^j$ and both have the same orientation. To show sufficiency, it is first noted that if the vectors $\tilde{\mathbf{y}}_{\sharp}^{j\,k+1} - \tilde{\mathbf{y}}_{\sharp}^{jk}$ and $\tilde{\mathbf{y}}^{j\,k+1} - \tilde{\mathbf{y}}^{jk}$ have the same direction $\forall\, k \in \{1, \ldots, n_j^C\}$, the corner angles of $\mathcal{M}^j$ and $\mathcal{M}_{\sharp}^j$ are equal. The vector $\tilde{\mathbf{y}}_{\sharp}^{j\,k+1} - \tilde{\mathbf{y}}_{\sharp}^{jk}$ is decomposed as follows:

$$\tilde{\mathbf{y}}_{\sharp}^{j\,k+1} - \tilde{\mathbf{y}}_{\sharp}^{jk} \;=\; (\tilde{\mathbf{y}}_{\sharp}^{j\,k+1} - \tilde{\mathbf{y}}_{\sharp}^{jk})^{\parallel} \;+\; (\tilde{\mathbf{y}}_{\sharp}^{j\,k+1} - \tilde{\mathbf{y}}_{\sharp}^{jk})^{\perp}, \tag{3.9}$$

where $(\tilde{\mathbf{y}}_{\sharp}^{j\,k+1} - \tilde{\mathbf{y}}_{\sharp}^{jk})^{\parallel}$ and $(\tilde{\mathbf{y}}_{\sharp}^{j\,k+1} - \tilde{\mathbf{y}}_{\sharp}^{jk})^{\perp}$ are respectively parallel and orthogonal to

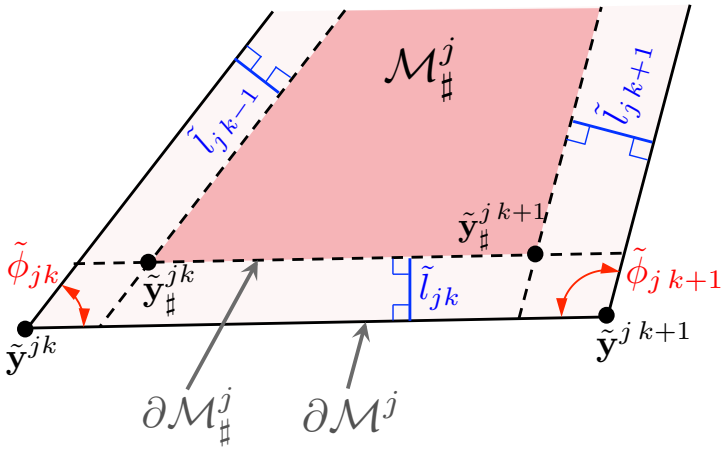

(a)

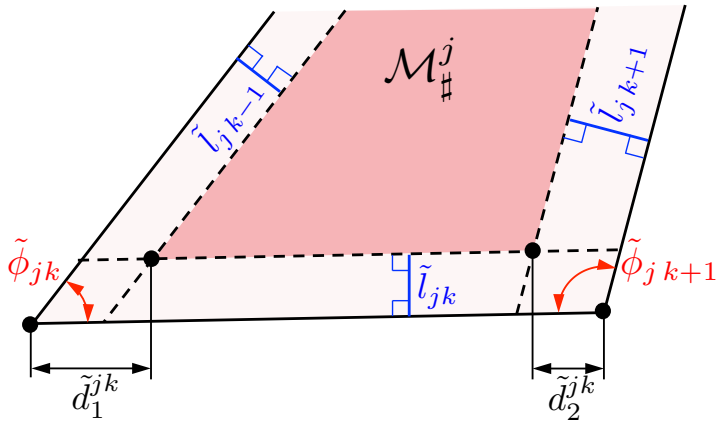

(b)

Figure 3.9: (a) Coordinates of the corner points of a face before and after trimming. The boundaries of $\mathcal{M}^j$ and $\mathcal{M}_\sharp^j$ are respectively denoted $\partial\mathcal{M}^j$ and $\partial\mathcal{M}_\sharp^j$. (b) Parameters $\tilde{d}_m^{jk}$, $m = 1, 2$, associated with the change in length of each edge of $\mathcal{M}$ due to face trimming.

$\tilde{\mathbf{y}}^{j\,k+1} - \tilde{\mathbf{y}}^{jk}$. The vector $(\tilde{\mathbf{y}}_\sharp^{j\,k+1} - \tilde{\mathbf{y}}_\sharp^{jk})^\parallel$ is given as follows:

$$\begin{aligned}
(\tilde{\mathbf{y}}_\sharp^{j\,k+1} - \tilde{\mathbf{y}}_\sharp^{jk})^\parallel &= \frac{(\tilde{\mathbf{y}}_\sharp^{j\,k+1} - \tilde{\mathbf{y}}_\sharp^{jk}) \cdot (\tilde{\mathbf{y}}^{j\,k+1} - \tilde{\mathbf{y}}^{jk})}{\|\tilde{\mathbf{y}}^{j\,k+1} - \tilde{\mathbf{y}}^{jk}\|^2}(\tilde{\mathbf{y}}^{j\,k+1} - \tilde{\mathbf{y}}^{jk}), \\
&= \left(1 - \frac{\tilde{l}_{j\,k-1}\csc(\tilde{\phi}_{jk}) + \tilde{l}_{j\,k+1}\csc(\tilde{\phi}_{j\,k+1})}{\|\tilde{\mathbf{y}}^{j\,k+1} - \tilde{\mathbf{y}}^{jk}\|}\right. \\
&\qquad \left. - \frac{\tilde{l}_{jk}(\cot(\tilde{\phi}_{jk}) + \cot(\tilde{\phi}_{j\,k+1}))}{\|\tilde{\mathbf{y}}^{j\,k+1} - \tilde{\mathbf{y}}^{jk}\|}\right)(\tilde{\mathbf{y}}^{j\,k+1} - \tilde{\mathbf{y}}^{jk}),
\end{aligned} \tag{3.10}$$

and the squared of the magnitude of the vector $(\tilde{\mathbf{y}}_\sharp^{j\,k+1} - \tilde{\mathbf{y}}_\sharp^{jk})^\perp$ is given as:

$$\begin{aligned}
\left\|(\tilde{\mathbf{y}}_\sharp^{j\,k+1} - \tilde{\mathbf{y}}_\sharp^{jk})^\perp\right\|^2 &= \left\|(\tilde{\mathbf{y}}_\sharp^{j\,k+1} - \tilde{\mathbf{y}}_\sharp^{jk}) - (\tilde{\mathbf{y}}_\sharp^{j\,k+1} - \tilde{\mathbf{y}}_\sharp^{jk})^\parallel\right\|^2, \\
&= \tilde{l}_{jk}^2\Big(\csc(\tilde{\phi}_{j\,k+1})^2 + \csc(\tilde{\phi}_{jk})^2 - (\cot(\tilde{\phi}_{jk}) + \cot(\tilde{\phi}_{j\,k+1}))^2 \\
&\qquad + 2\csc(\tilde{\phi}_{jk})\csc(\tilde{\phi}_{j\,k+1})\cos(\tilde{\phi}_{jk} + \tilde{\phi}_{j\,k+1})\Big), \\
&= 0.
\end{aligned} \tag{3.11}$$

Thus, $(\tilde{\mathbf{y}}_\sharp^{j\,k+1} - \tilde{\mathbf{y}}_\sharp^{jk}) = (\tilde{\mathbf{y}}_\sharp^{j\,k+1} - \tilde{\mathbf{y}}_\sharp^{jk})^\parallel$ which implies that $\tilde{\mathbf{y}}_\sharp^{j\,k+1} - \tilde{\mathbf{y}}_\sharp^{jk}$ is parallel to $\tilde{\mathbf{y}}^{j\,k+1} - \tilde{\mathbf{y}}^{jk}$. The coefficient of $(\tilde{\mathbf{y}}^{j\,k+1} - \tilde{\mathbf{y}}^{jk})$ in Equation (3.10) must be positive[4] for the face $\mathcal{M}_\sharp^j$ to not be a degenerate case of $\mathcal{M}^j$ and also to have the same orientation of $\mathcal{M}^j$, which then implies that the faces $\mathcal{M}^j$ and $\mathcal{M}_\sharp^j$ have equal corner angles because the vectors $\tilde{\mathbf{y}}_\sharp^{j\,k+1} - \tilde{\mathbf{y}}_\sharp^{jk}$ and $\tilde{\mathbf{y}}^{j\,k+1} - \tilde{\mathbf{y}}^{jk}$ have the same direction. □

The parameters $\tilde{d}_1^{jk}$ and $\tilde{d}_2^{jk}$ are associated with the change in length of the edges

[4]This requirement is revisited in Section 3.5.

of $\mathcal{M}^j$ due to face trimming and are determined as follows (refer to Figure 3.9(b)):

$$\tilde{d}_1^{jk} = \tilde{l}_{j\,k-1}\csc(\tilde{\phi}_{jk}) + \tilde{l}_{jk}\cot(\tilde{\phi}_{jk}), \tag{3.12}$$

$$\tilde{d}_2^{jk} = \tilde{l}_{j\,k+1}\csc(\tilde{\phi}_{j\,k+1}) + \tilde{l}_{jk}\cot(\tilde{\phi}_{j\,k+1}). \tag{3.13}$$

Since the resulting goal configuration $\mathcal{S}_\star$ contains $\mathcal{M}_\sharp$ as a subset rather than the goal mesh $\mathcal{M}$ (see Figure 3.6), the error of the approximation of $\mathcal{S}_\star$ to the goal mesh $\mathcal{M}$ must be quantified. A global measure for such an approximation error is suggested. Such a measure of approximation error is denoted as $\mathtt{E}$ and is defined as follows:

$$\mathtt{E} := 1 - \frac{\text{Area}(\mathcal{M}_\sharp)}{\text{Area}(\mathcal{M})}. \tag{3.14}$$

Since the face trimming process considered in this work only removes surface area of $\mathcal{M}$, then $\text{Area}(\mathcal{M}_\sharp)/\text{Area}(\mathcal{M}) \leq 1$. An approximation error of $\mathtt{E} = 0$ corresponds only to the case where $\mathcal{M} = \mathcal{M}_\sharp$ and for any other case $0 < \mathtt{E} < 1$. For instance, $\mathtt{E} = 0.30$ for the example shown in Figure 3.6.

3.3.2 Design Parameterization and Constraints

Since all fold widths are assumed given (refer to Section 3.2), the fold widths of the interior and exterior folds of each edge module in the planar reference configuration $\mathcal{S}_0$, respectively denoted as $\hat{w}_i^{\mathsf{I}0}$ and $\hat{w}_i^{\mathsf{E}0}$, are inputs to the design problem (see Figure 3.10(a)). In practice, the fold widths $\hat{w}_i^{\mathsf{I}0}$ and $\hat{w}_i^{\mathsf{E}0}$, $i = 1, \ldots, N_{\mathcal{E}}^I$, are determined such that the smooth folds comprised of a specific material are able to achieve their required fold angles at $\mathcal{S}_\star$ (see Figure 3.8). Such a physically-based determination of the fold widths is addressed in Section 4.

In addition to the information regarding fold widths, the geometry of edge module in the designed sheet is defined by two variables corresponding to $\hat{W}_i$ and $\hat{\psi}_i$. These variables are schematically shown in Figure 3.10(a). The modified edge module accounting for the change in edge lengths due to face trimming (refer to Section 3.3.1) is presented in Figure 3.10(b). The parameters $\hat{d}^i_{nm}$, $n, m \in \{1, 2\}$, showed therein correspond to those parameters $\tilde{d}^{jk}_m$, $m \in \{1, 2\}$ (see Equations (3.12) and (3.13)), of the two faces connected to the i^{th} interior edge (refer to Equations (3.53) and (3.54) in Section 3.4.1.3 for the mapping among such sets of variables).

Let W_{jk} and ψ_{jk}, $j = 1, \ldots, N^I_{\mathcal{N}}$, $k = 1, \ldots, n^{\mathcal{M}}_j$, be the variables that define the geometry of the edge module associated with the k^{th} interior edge adjacent to the j^{th} interior node of $\mathcal{M}$. The map from the sets of all the edge module variables $\hat{W}_i$ and $\hat{\psi}_i$, $i = 1, \ldots, N^I_{\mathcal{E}}$, to the sets W_{jk} and ψ_{jk}, $j = 1, \ldots, N^I_{\mathcal{N}}$, $k = 1, \ldots, n^{\mathcal{M}}_j$, is provided in Section 3.4.1.3 (see Equations (3.50) and (3.51)). The variables W_{jk} and ψ_{jk}, $k = 1, \ldots, n^{\mathcal{M}}_j$, must be determined such that the faces of $\mathcal{M}_\sharp$ and the edge modules associated with the j^{th} interior node of $\mathcal{M}$ form a closed strip in $\mathcal{S}_0$. If this requirement is met, where a pair of faces in $\mathcal{M}$ is connected by an interior edge, their associated faces in $\mathcal{M}_\sharp$ are connected in $\mathcal{S}_0$ by an edge module. Such a requirement is associated with the following constraints:

Proposition 3.2. *For the faces of $\mathcal{M}_\sharp$ and the edge modules associated with the j^{th} interior node of $\mathcal{M}$ to form a closed strip in $\mathcal{S}_0$, the following constraints must hold:*

$$2\pi = \sum_{k=1}^{n^{\mathcal{M}}_j} \phi_{jk} + \sum_{k=1}^{n^{\mathcal{M}}_j} \psi_{jk}, \tag{3.15}$$

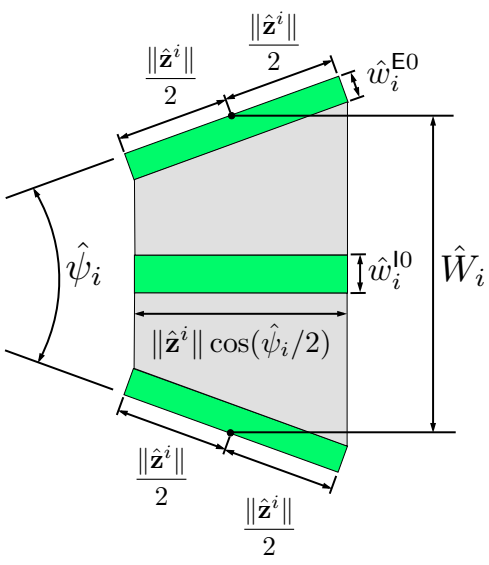

(a)

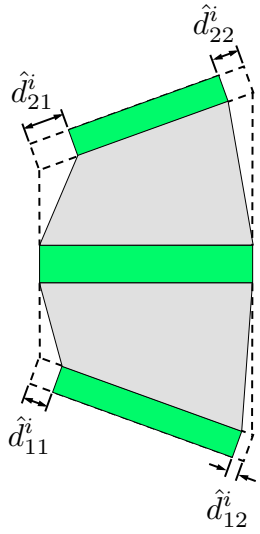

(b)

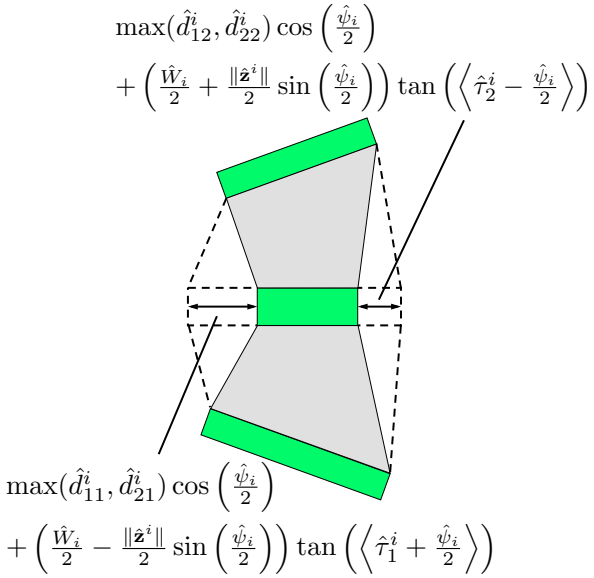

(c)

Figure 3.10: (a) Edge module and associated geometric parameters; (b) Modified edge module accounting for the change in edge lengths due to face trimming; (c) Edge module trimmed accounting for self-intersection avoidance at the goal configuration $\mathcal{S}_\star$ (addressed in Section 3.3.2.1).

and[5]*:*

$$\mathbf{0}_3 = \sum_{k=1}^{n_j^{\mathcal{M}}} \left(\mathbf{R}_3 \left(\sum_{l=1}^{k-1} \left(\frac{\psi_{jl}}{2} + \phi_{jl} + \frac{\psi_{j\,l+1}}{2} \right) \right) \times \begin{bmatrix} (d_{21}^{jk} - d_{11}^{jk}) \cos\left(\frac{\psi_{jk}}{2}\right) \\ W_{jk} + (d_{11}^{jk} + d_{21}^{jk} - \|\mathbf{z}^{jk}\|) \sin\left(\frac{\psi_{jk}}{2}\right) \\ 0 \end{bmatrix} \right). \tag{3.16}$$

Proof. Let $\mathfrak{b}^{jk} \in \text{span}(\mathbf{e}_1, \mathbf{e}_2)$, $k = 0, \ldots, n_j^{\mathcal{M}}$, be the corner position vectors of the edge modules associated with the j^{th} interior node of $\mathcal{M}$ at the reference configuration $\mathcal{S}_0$ (refer to Figure 3.11). The position vectors of two of the corners of the k^{th} edge module correspond to $\mathfrak{b}^{j\,k-1}$ and $\mathfrak{b}^{jk}$. These position vectors can be determined

[5]The matrix $\mathbf{R}_3(\phi)$ associated with a rotation by ϕ about an axis of rotation aligned to $\mathbf{e}_3$ is defined in Equation (2.12).

recursively as follows (refer to Figure 3.10(b)):

$$
\begin{aligned}
\mathfrak{b}^{jk} &= \mathfrak{b}^{j\,k-1} + \mathbf{R}_3\left(\sum_{l=1}^{k-1}\left(\tfrac{\psi_{jl}}{2} + \phi_{jl} + \tfrac{\psi_{j\,l+1}}{2}\right)\right) \\
&\qquad \times \begin{bmatrix} (d_{21}^{jk} - d_{11}^{jk})\cos\left(\tfrac{\psi_{jk}}{2}\right) \\ W_{jk} + (d_{11}^{jk} + d_{21}^{jk} - \|\mathbf{z}^{jk}\|)\sin\left(\tfrac{\psi_{jk}}{2}\right) \\ 0 \end{bmatrix}, \\
&= \sum_{l=1}^{k}\left(\mathbf{R}_3\left(\sum_{m=1}^{l-1}\left(\tfrac{\psi_{jm}}{2} + \phi_{jm} + \tfrac{\psi_{j\,m+1}}{2}\right)\right)\right. \\
&\qquad \left. \times \begin{bmatrix} (d_{21}^{jl} - d_{11}^{jl})\cos\left(\tfrac{\psi_{jl}}{2}\right) \\ W_{jl} + (d_{11}^{jl} + d_{21}^{jl} - \|\mathbf{z}^{jl}\|)\sin\left(\tfrac{\psi_{jl}}{2}\right) \\ 0 \end{bmatrix}\right) + \mathfrak{b}^{j0}.
\end{aligned}
\tag{3.17}
$$

Consider the transport of a position vector from the face with corner angle $\phi_{j\,k-1}$ to the face with corner angle ϕ_{jk}. The transformation associated with crossing the edge module located between these two faces can be decomposed into a translation by $\mathfrak{b}^{jk} - \mathfrak{b}^{j\,k-1}$ followed by a rotation of $\phi_{jk} + \psi_{jk}$ about an axis aligned to $\mathbf{e}_3$ and crossing the point with position vector $\mathfrak{b}^{jk}$. Such a transformation can be expressed

in homogeneous coordinates as follows:

$$\mathbf{T}(\mathfrak{b}^{jk})\mathbf{Q}_3(\phi_{jk}+\psi_{jk})\mathbf{T}^{-1}(\mathfrak{b}^{jk})\mathbf{T}(\mathfrak{b}^{jk}-\mathfrak{b}^{j\,k-1}) \;=\; \mathbf{T}(\mathfrak{b}^{jk})\mathbf{Q}_3(\phi_{jk}+\psi_{jk})\mathbf{T}^{-1}(\mathfrak{b}^{j\,k-1}), \tag{3.18}$$

where $\mathbf{Q}_3(\phi)$ is the transformation matrix associated with a rotation by ϕ about an axis aligned to $\mathbf{e}_3$ and $\mathbf{T}(\mathbf{b})$ is the transformation matrix associated with a translation by $\mathbf{b}$. The elements of such transformation matrices are provided explicitly in Equations (2.68) and (2.69), respectively. It follows that the composition of transformations presented in Equation (3.18) associated with crossing the edge modules with angles ψ_{jk}, $k=1,\ldots,n_j^{\mathcal{M}}$, must be identity transformation for these surfaces, along with the faces with corner angles ϕ_{jk}, $k=1,\ldots,n_j^{\mathcal{M}}$, to form a closed strip:

$$\begin{aligned}\mathbf{I}_4 &= \prod_{k=1}^{n_j^{\mathcal{M}}}\mathbf{T}(\mathfrak{b}^{jk})\mathbf{Q}_3(\phi_{jk}+\psi_{jk})\mathbf{T}^{-1}(\mathfrak{b}^{j\,k-1}),\\ &= \mathbf{T}(\mathfrak{b}^{jn_j^{\mathcal{M}}})\mathbf{Q}_3\left(\sum_{k=1}^{n_j^{\mathcal{M}}}(\phi_{jk}+\psi_{jk})\right)\mathbf{T}^{-1}(\mathfrak{b}^{j0}).\end{aligned} \tag{3.19}$$

The equation above holds if $\sum_{k=1}^{n_j^{\mathcal{M}}}(\phi_{jk}+\psi_{jk})=2\pi n$ with $n\in\mathbb{Z}$. Specifically, n must be equal to 1 for the closed strip to be developable [418] yielding the constraint of equation (3.15). In addition to such a constraint, it is required that $\mathfrak{b}^{jn_j^{\mathcal{M}}}=\mathfrak{b}^{j0}$ for Equation (3.19) to hold. Considering Equation (3.17), $\mathfrak{b}^{jn_j^{\mathcal{M}}}=\mathfrak{b}^{j0}$ implies the constraint in Equation (3.16). □

Equation (3.16) implies that the addition of the vectors shown in Figure 3.11 must be equal to $\mathbf{0}_3$. This equation provides two scalar constraints because the third component of such a vector equation is always equal to 0. Therefore, Equations

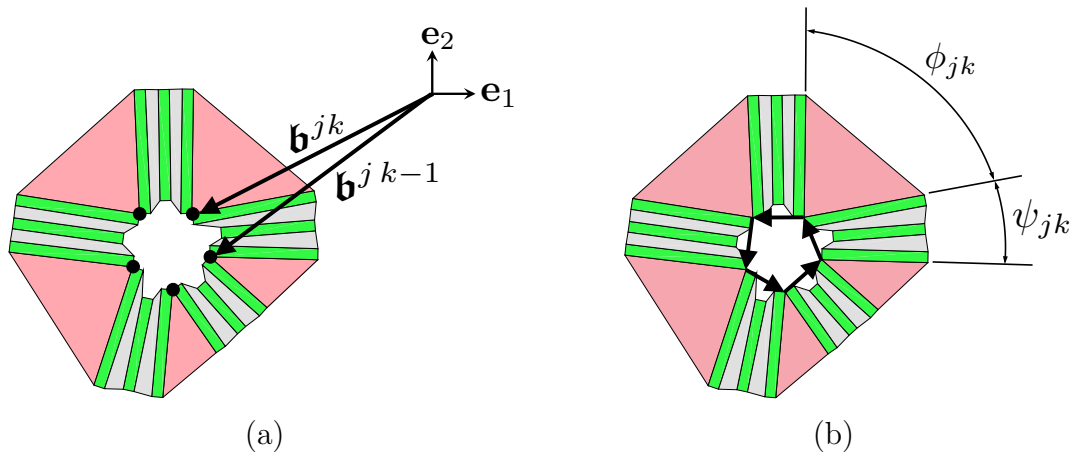

(a) (b)

Figure 3.11: Subdomain of $\mathcal{S}_0$ associated with the j^{th} interior node of $\mathcal{M}$: (a) Position vectors of the edge module corner points; (b) Face corner and edge module angles.

(3.15) and (3.16) provide a total of $3N_{\mathcal{N}}^{I}$ equality constraints.

In addition to the loop closure constraints provided in Proposition 3.2, other constraints must be imposed to ensure that the geometry of each individual edge module is valid. For instance, the interior fold (having fold width $\hat{w}_i^{\mathsf{I0}}$, see Figure 3.10(a)) and the faces of an edge module degenerate to straight line segments if $\hat{\psi}_i$ reaches $\pm\pi$ (refer to Figure 3.10(a)). Therefore, the following bounds must be imposed for this variable:

$$-\pi < \hat{\psi}_i < \pi. \tag{3.20}$$

Furthermore, the exterior folds (each having fold width $\hat{w}_i^{\mathsf{E0}}$, see Figure 3.10(a)) of an edge module must not overlap with the interior fold. This requirement yields

the following constraint (refer to Figures 3.10(a) and 3.10(b)):

$$\hat{W}_i \geq \hat{w}_i^{\mathsf{I0}} + 2\hat{w}_i^{\mathsf{E0}} \cos\left(\frac{\hat{\psi}_i}{2}\right) + \left\|\hat{\mathbf{z}}^i\right\| \sin\left(\left|\frac{\hat{\psi}_i}{2}\right|\right) - \begin{cases} (\hat{d}_{11}^i + \hat{d}_{21}^i) \sin\left(\frac{\hat{\psi}_i}{2}\right); & \hat{\psi}_i \geq 0 \\ (\hat{d}_{12}^i + \hat{d}_{22}^i) \sin\left(-\frac{\hat{\psi}_i}{2}\right); & \hat{\psi}_i < 0 \end{cases}. \tag{3.21}$$

Equation (3.21) and the upper and lower bounds of $\hat{\psi}_i$ in Equation (3.20) provide $3N_{\mathcal{E}}^I$ inequality constraints.

Intersections are not allowed in valid configurations (cf. Definition 2.5) and must be avoided when adjacent edge modules are tucked in the goal configuration $\mathcal{S}_\star$. To preclude such intersections in $\mathcal{S}_\star$, certain regions of the edge modules are removed (see Figure 3.10(c)) such that each edge module does not intersect any of its neighboring edge modules. Such a process is denoted as *edge module trimming* and is summarized in Section 3.3.2.1. Figure 3.12 shows the importance of the edge module trimming process. If the edge module trimming process is not considered and the edge module geometry is as given in Figure 3.10(b), adjacent edge modules intersect at the goal configuration $\mathcal{S}_\star$ as observed in Figure 3.12(d). However, if the edge module trimming process is considered and the geometry of the edge modules is as illustrated in Figure 3.10(c), no intersections among adjacent edge modules occur as shown in Figure 3.12(g). The angles $\hat{\tau}_1^i$ and $\hat{\tau}_2^i$, $i = 1, \ldots, N_{\mathcal{E}}^I$, are introduced to determine the trimmed regions the i^{th} edge module as shown in Figure 3.10(c). The process used to determine these angles is presented in the following section.

3.3.2.1 Edge module trimming

As previously stated, intersections among regions of the sheet are not allowed in valid configurations (cf. Definition 2.5) and therefore must be avoided when adjacent

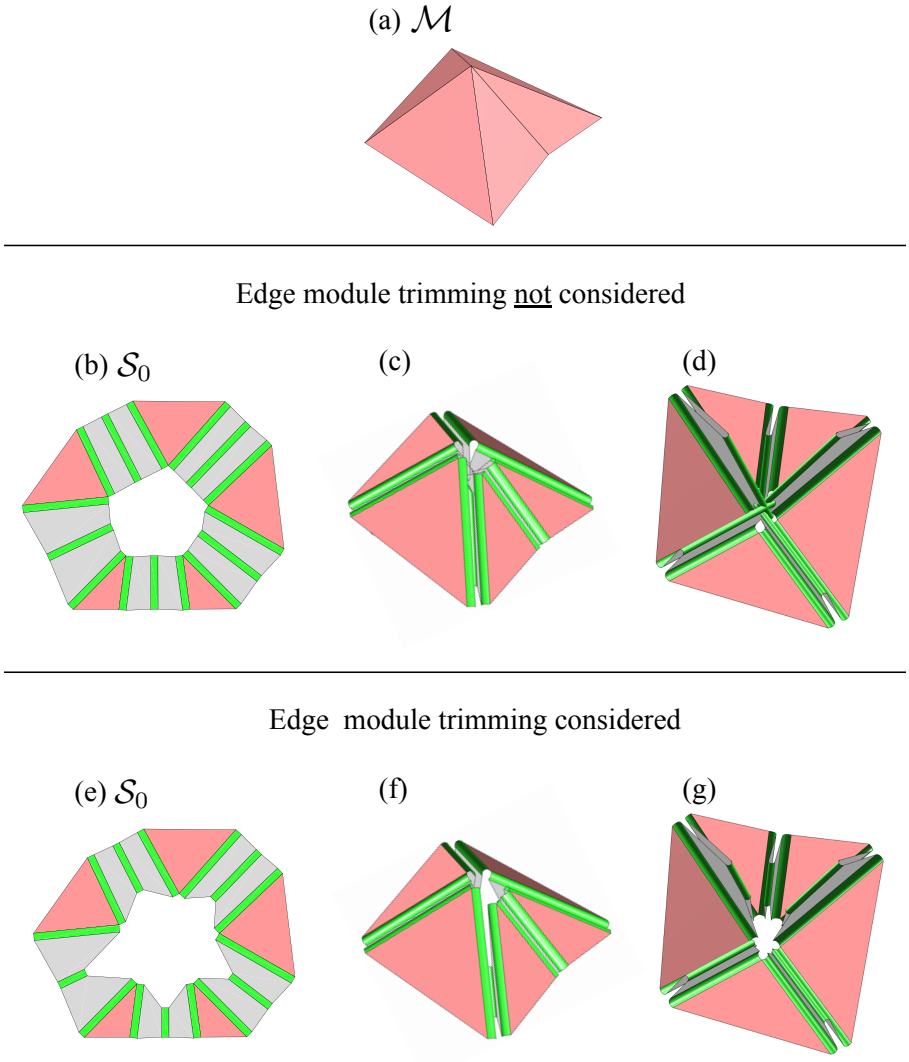

Figure 3.12: Example showing the need for *edge module trimming*. (a) A simple goal mesh $\mathcal{M}$. (b) and (e) Determined sheet designs $\mathcal{S}_0$. Edge module trimming is not considered for the sheet design shown in (b) while such a process is considered for the design in (e). (c)–(d), (f)–(g) Exterior and interior views of the goal configuration $\mathcal{S}_\star$ for both cases. It is observed in (d) that if the edge module trimming process described in Section 3.3.2.1 is not considered, the tucked edge modules intersect at $\mathcal{S}_\star$. If such a process is considered, adjacent edge modules do not intersect in $\mathcal{S}_\star$ as shown in (g).

edge modules are tucked in the goal configuration $\mathcal{S}_\star$. Thus, certain regions of the edge modules are trimmed such that each edge module does not intersect any of its neighboring edge modules. The angles $\hat{\tau}_1^i$ and $\hat{\tau}_2^i$, $i = 1, \ldots, N_{\mathcal{E}}^I$, are utilized to determine the trimmed regions the i^{th} edge module as shown in Figure 3.10(c). These angles are determined from their corresponding values in the set of angles τ_{jk}, $j \in \{1, \ldots, N_{\mathcal{N}}^I\}$, $k \in \{1, \ldots, n_j^{\mathcal{M}}\}$. The formulation for the angles τ_{jk} is summarized in this section.

Unfolded and folded configurations of an edge module are illustrated in Figure 3.13(a). First, the normal vector associated with each edge incident to an interior node of $\mathcal{M}$ that is denoted $\bar{\mathbf{n}}^{jk} \in \mathbb{R}^3$, $j = 1, \ldots, N_{\mathcal{N}}^I$, $k = 1, \ldots, n_j^{\mathcal{M}}$, is defined as follows:

$$\bar{\mathbf{n}}^{jk} := \frac{\mathbf{n}^{j\,k-1} + \mathbf{n}^{jk}}{\|\mathbf{n}^{j\,k-1} + \mathbf{n}^{jk}\|}, \tag{3.22}$$

where the face normal vectors $\mathbf{n}^{jk}$ are defined in Equation (3.4). It is noted that the rigid faces of the tucked edge modules are located in planes parallel to that spanned by $\mathbf{z}^{jk}$ and $\bar{\mathbf{n}}^{jk}$ (see Figure 3.13(a)).

The direction of the intersection axis between any two planes containing adjacent tucked edge modules is defined by the unit vector $\boldsymbol{\omega}^{jkl} \in \mathbb{R}^3$, $j = 1, \ldots, N_{\mathcal{N}}^I$, $k = 1, \ldots, n_j^{\mathcal{M}}$, $l = 1, \ldots, n_j^{\mathcal{M}}$:

$$\boldsymbol{\omega}^{jkl} = \begin{cases} \dfrac{(\bar{\mathbf{n}}^{jk} \times \mathbf{z}^{jk}) \times (\bar{\mathbf{n}}^{jl} \times \mathbf{z}^{jl})}{\|(\bar{\mathbf{n}}^{jk} \times \mathbf{z}^{jk}) \times (\bar{\mathbf{n}}^{jl} \times \mathbf{z}^{jl})\|}; & (\bar{\mathbf{n}}^{jk} \times \mathbf{z}^{jk}) \times (\bar{\mathbf{n}}^{jl} \times \mathbf{z}^{jl}) \neq 0 \\ \bar{\mathbf{n}}^{jl}; & (\bar{\mathbf{n}}^{jk} \times \mathbf{z}^{jk}) \times (\bar{\mathbf{n}}^{jl} \times \mathbf{z}^{jl}) = 0 \end{cases}. \tag{3.23}$$

As assumed in Equation (3.23), the vector $\bar{\mathbf{n}}^{jl}$ is utilized to define the vector

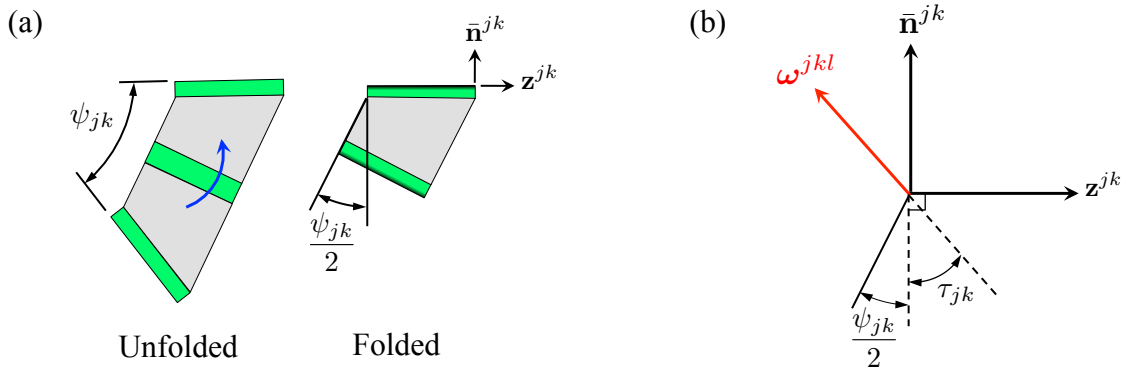

Figure 3.13: (a) Unfolded and folded configurations of an edge module. (b) View of the plane spanned by $\bar{\mathbf{n}}^{jk}$ and $\mathbf{z}^{jk}$ showing the intersection axis vector $\boldsymbol{\omega}^{jkl}$ and the trim angle τ_{jk} respectively defined in Equations (3.23) and (3.26).

$\boldsymbol{\omega}^{jkl}$ in the case where the rigid faces of the k^{th} and the l^{th} tucked edge modules are parallel.

The trim angle τ_{jk} is utilized to determine the trimmed regions of the k^{th} edge module associated with the j^{th} interior node of $\mathcal{M}$ (see Figure 3.13(b)). The angles τ_{jk} are determined through the following equations in order to prevent unnecessary trimming of the edge modules:

$$
{}^{1}\upsilon_{jkl} = \begin{cases} 0; & -\bar{\mathbf{n}}^{jk}\cdot\mathbf{z}^{jl} \le 0 \ \text{ and } \\ & -\bar{\mathbf{n}}^{jl}\cdot\mathbf{z}^{jk} \le 0 \\ -\dfrac{\pi}{2} + \begin{cases} \cos^{-1}\left(\dfrac{\mathbf{z}^{jk}}{\left\|\mathbf{z}^{jk}\right\|}\cdot\boldsymbol{\omega}^{jkl}\right); & \bar{\mathbf{n}}^{jk}\cdot\boldsymbol{\omega}^{jkl} \ge 0 \\ \cos^{-1}\left(-\dfrac{\mathbf{z}^{jk}}{\left\|\mathbf{z}^{jk}\right\|}\cdot\boldsymbol{\omega}^{jkl}\right); & \bar{\mathbf{n}}^{jk}\cdot\boldsymbol{\omega}^{jkl} < 0, \end{cases} & ; \quad \text{otherwise} \end{cases} , \tag{3.24}
$$

$$
{}^2\upsilon_{jkl} = \begin{cases} {}^1\upsilon_{jkl}; & {}^1\upsilon_{jkl} \leq {}^1\upsilon_{jlk} \\ 0; & {}^1\upsilon_{jkl} > {}^1\upsilon_{jlk} \end{cases}, \tag{3.25}
$$

$$
\tau_{jk} = \max_{l \in \{1,\ldots,n_j^{\mathcal{M}}\},\ l \neq k} ({}^2\upsilon_{jkl}). \tag{3.26}
$$

From Equation (3.24), it is noted that if $-\bar{\mathbf{n}}^{jk} \cdot \mathbf{z}^{jl} \leq 0$ and $-\bar{\mathbf{n}}^{jl} \cdot \mathbf{z}^{jk} \leq 0$, the angles ${}^1\upsilon_{jkl}$ are set to 0 as no further trimming is required in such cases. In Equation (3.25), the lower trim angle required to prevent intersections among each pair of edge modules is selected while the larger is set to zero. Finally, in Equation (3.26), the trim angle τ_{jk} required for an edge module to prevent intersections with all of its adjacent edge modules is determined.

The angles $\hat{\tau}_1^i$ and $\hat{\tau}_2^i$, $i = 1, \ldots, N_{\mathcal{E}}^I$, are introduced to determine the trimmed regions the i^{th} edge module as shown in Figure 3.10(c). These angles are obtained from their corresponding values in the set of angles τ_{jk}, $j \in \{1, \ldots, N_{\mathcal{N}}^I\}$, $k \in \{1, \ldots, n_j^{\mathcal{M}}\}$ (cf. Equation (3.26)). Each edge module must remain connected after edge trimming. This requirement is satisfied if the following inequality holds for each edge module (refer to Figure 3.10(c))[6]:

$$
\begin{aligned}
\left\|\hat{\mathbf{z}}^i\right\| \cos\left(\tfrac{\hat{\psi}_i}{2}\right) \;>\; & \left(\tfrac{\hat{W}_i}{2} - \tfrac{\|\hat{\mathbf{z}}^i\|}{2} \sin\left(\tfrac{\hat{\psi}_i}{2}\right)\right) \tan\left(\left\langle \hat{\tau}_1^i + \tfrac{\hat{\psi}_i}{2} \right\rangle\right) \\
& + \left(\tfrac{\hat{W}_i}{2} + \tfrac{\|\hat{\mathbf{z}}^i\|}{2} \sin\left(\tfrac{\hat{\psi}_i}{2}\right)\right) \tan\left(\left\langle \hat{\tau}_2^i - \tfrac{\hat{\psi}_i}{2} \right\rangle\right) \\
& + \left(\max(\hat{d}_{11}^i, \hat{d}_{21}^i) + \max(\hat{d}_{12}^i, \hat{d}_{22}^i)\right) \cos\left(\tfrac{\hat{\psi}_i}{2}\right).
\end{aligned} \tag{3.27}
$$

[6]The Macaulay brackets are denoted as $\langle \cdot \rangle$ and defined as: $\langle y \rangle = \begin{cases} y; & y \geq 0 \\ 0; & y < 0 \end{cases}$.

It is noted that if $(\hat{\tau}_1^i + \hat{\psi}_i/2) < 0$ or $(\hat{\tau}_2^i - \hat{\psi}_i/2) < 0$, these angles are set to 0 to prevent any increase in area of the edge modules during this process. Equation (3.27) yields the following constraint:

$$\begin{aligned}\hat{W}_i \;<\; & \frac{2\left(\left\|\hat{\mathbf{z}}^i\right\| - \max(\hat{d}_{11}^i, \hat{d}_{21}^i) - \max(\hat{d}_{12}^i, \hat{d}_{22}^i)\right)\cos\left(\frac{\hat{\psi}_i}{2}\right)}{\tan\left(\left\langle\hat{\tau}_1^i + \frac{\hat{\psi}_i}{2}\right\rangle\right) + \tan\left(\left\langle\hat{\tau}_2^i - \frac{\hat{\psi}_i}{2}\right\rangle\right)} \\ & + \frac{\left\|\hat{\mathbf{z}}^i\right\|\sin\left(\frac{\hat{\psi}_i}{2}\right)\left(\tan\left(\left\langle\hat{\tau}_1^i + \frac{\hat{\psi}_i}{2}\right\rangle\right) - \tan\left(\left\langle\hat{\tau}_2^i - \frac{\hat{\psi}_i}{2}\right\rangle\right)\right)}{\tan\left(\left\langle\hat{\tau}_1^i + \frac{\hat{\psi}_i}{2}\right\rangle\right) + \tan\left(\left\langle\hat{\tau}_2^i - \frac{\hat{\psi}_i}{2}\right\rangle\right)}.\end{aligned} \tag{3.28}$$

The preceding equation provides $N_{\mathcal{E}}^I$ additional inequality constraints.

In summary, the proposed design method introduces $2N_{\mathcal{E}}^I$ design variables corresponding to $\hat{W}_i$ and $\hat{\psi}_i$, $i = 1, \ldots, N_{\mathcal{E}}^I$. The loop closure constraints (Equations (3.15) and (3.16)) provide $3N_{\mathcal{N}}^I$ equality constraints. Equations (3.20), (3.21), and (3.28) allowing for valid edge module geometries and self-intersection avoidance in $\mathcal{S}_\star$ provide $4N_{\mathcal{E}}^I$ inequality constraints.

The vector of design variables $\mathbf{D} \in \mathbb{R}^{2N_{\mathcal{E}}^I}$ is defined as follows:

$$\mathbf{D} := \begin{bmatrix} \hat{W}_1 \\ \vdots \\ \hat{W}_{N_{\mathcal{E}}^I} \\ \hat{\psi}_1 \\ \vdots \\ \hat{\psi}_{N_{\mathcal{E}}^I} \end{bmatrix}. \tag{3.29}$$

The equality constraints (Equations (3.15) and (3.16)) are set to the form $\boldsymbol{h} = \mathbf{0}_{3N_{\mathcal{N}}^I}$ while the inequality constraints (Equations (3.20), (3.21), and (3.28)) are set

to the form $\boldsymbol{g} \leq \mathbf{0}_{4N_{\mathcal{E}}^I}$ [7].

The problem statement for design of origami structures with smooth folds using the present method can be stated as follows:

$$\begin{array}{ll} \text{Find} & \mathbf{D} \\ \text{That minimizes} & f(\mathbf{D}) \\ \text{Subject to} & \boldsymbol{h} = \mathbf{0}_{3N_{\mathcal{N}}^I} \\ & \boldsymbol{g} \leq \mathbf{0}_{4N_{\mathcal{E}}^I} \\ & \text{and application-dependent constraints} \end{array} \tag{3.30}$$

where $f(\mathbf{D})$ is an application-dependent function of the design variables that the user wants to minimize.

The numerical procedure to be outlined in Section 3.4.2 used to determine a valid design does not consider any function to minimize (i.e. it only iteratively corrects an initial guess solution until the presented constraints are satisfied). However, other methods can be utilized to determine a sheet design that satisfies the presented constraints while minimizing a given function $f(\mathbf{D})$.

The subsequent section describes the numerical implementation procedure used to determine a set of design variables that satisfies the aforementioned equality and inequality constraints.

3.4 Numerical Implementation

3.4.1 Mappings Among Sets of Parameters and Variables

Mappings among various sets of parameters and variables associated with the implementation of the proposed design method are described in this section, which

[7] For numerical implementation, strict inequality constraints $A < 0$ in Equations (3.20) and (3.28) are expressed as non-strict inequalities of the form $A + \epsilon \leq 0$ where $\epsilon > 0$.

only considers the most important parameters and variables used throughout the design method for the sake of brevity. It should be noted that every parameter and connectivity matrix mentioned in this section can be obtained from the position vectors of the nodes $\hat{\mathbf{y}}^i$, $i = 1, \ldots, N_{\mathcal{N}}$, and the connectivity matrix relating the nodes of $\mathcal{M}$ to the nodes associated with each face $\mathcal{M}^j$, $j = 1, \ldots, N_{\mathcal{M}}$ (formally defined afterwards in Equation (3.40)).

3.4.1.1 Mesh Parameters

Let $\hat{\mathbf{Y}} \in \mathbb{R}^{3N_{\mathcal{N}}}$ be the vector constructed by concatenating the position vectors of the nodes of $\mathcal{M}$ as follows:

$$\hat{\mathbf{Y}} := \begin{bmatrix} \hat{\mathbf{y}}^1 \\ \vdots \\ \hat{\mathbf{y}}^{N_{\mathcal{N}}} \end{bmatrix}. \tag{3.31}$$

Also, let $\hat{\mathbf{z}}^i \in \mathbb{R}^3$, $i = 1, \ldots, N_{\mathcal{E}}^I$, be a vector along the length of the i^{th} interior edge of $\mathcal{M}$. Furthermore, the vector $\hat{\mathbf{Z}} \in \mathbb{R}^{3N_{\mathcal{E}}^I}$ is constructed by concatenating the vectors $\hat{\mathbf{z}}^i$, $i = 1, \ldots, N_{\mathcal{E}}^I$, as follows:

$$\hat{\mathbf{Z}} := \begin{bmatrix} \hat{\mathbf{z}}^1 \\ \vdots \\ \hat{\mathbf{z}}^{N_{\mathcal{E}}^I} \end{bmatrix}. \tag{3.32}$$

Define the connectivity matrix $\mathbf{C}^{E_I N} \in \{-1, 0, 1\}^{N_{\mathcal{E}}^I \times N_{\mathcal{N}}}$ with elements $C_{ij}^{E_I N}$ as

follows:

$$C_{ij}^{E_I N} := \begin{cases} -1; & \hat{\mathbf{y}}^j \text{ is the position vector of the } i^{\text{th}} \text{ interior edge } \textit{start-point} \\ 1; & \hat{\mathbf{y}}^j \text{ is the position vector of the } i^{\text{th}} \text{ interior edge } \textit{end-point} \\ 0; & \text{otherwise, i.e. the point with position vector } \hat{\mathbf{y}}^j \text{ is not} \\ & \text{connected to the } i^{\text{th}} \text{ interior edge} \end{cases} . \tag{3.33}$$

The mapping from the node position vectors of $\mathcal{M}$ to the vectors along the length of the interior edges of $\mathcal{M}$ is then compactly provided as follows:

$$\hat{\mathbf{Z}} = \left(\mathbf{C}^{E_I N} \otimes \mathbf{I}_3\right) \hat{\mathbf{Y}}. \tag{3.34}$$

Let $\hat{\boldsymbol{l}} \in \mathbb{R}^{N_{\mathcal{E}}^I}$ be the vector constructed by collecting the trim lengths $\hat{l}_i$, $i = 1, \ldots, N_{\mathcal{E}}^I$ (calculated using Equation (3.6)):

$$\hat{\boldsymbol{l}} := \begin{bmatrix} \hat{l}_1 \\ \vdots \\ \hat{l}_{N_{\mathcal{E}}^I} \end{bmatrix}. \tag{3.35}$$

Also, let the vectors $\hat{\boldsymbol{W}}, \hat{\boldsymbol{\psi}} \in \mathbb{R}^{N_{\mathcal{E}}^I}$ be constructed by collecting the design variables $\hat{W}_i$ and $\hat{\psi}_i$, $i = 1, \ldots, N_{\mathcal{E}}^I$, respectively, as follows:

$$\hat{\boldsymbol{W}} := \begin{bmatrix} \hat{W}_1 \\ \vdots \\ \hat{W}_{N_{\mathcal{E}}^I} \end{bmatrix}, \tag{3.36}$$

$$\hat{\boldsymbol{\psi}} := \begin{bmatrix} \hat{\psi}_1 \\ \vdots \\ \hat{\psi}_{N_{\mathcal{E}}^I} \end{bmatrix}, \tag{3.37}$$

and let $\hat{\boldsymbol{d}}^{mn} \in \mathbb{R}^{N_{\mathcal{E}}^I}$, $m = 1, 2$, $n = 1, 2$, be the vector constructed by collecting the edge module parameters $\hat{d}^i_{mn}$ (refer to Figure 3.10(b)), $i = 1, \ldots, N_{\mathcal{E}}^I$, as follows:

$$\hat{\boldsymbol{d}}^{mn} := \begin{bmatrix} \hat{d}^1_{mn} \\ \vdots \\ \hat{d}^{N_{\mathcal{E}}^I}_{mn} \end{bmatrix}. \tag{3.38}$$

3.4.1.2 Face Parameters

Let $\tilde{\mathbf{Y}}^j \in \mathbb{R}^{3n_j^C}$, $j = 1, \ldots, N_{\mathcal{M}}$, be the vector constructed by concatenating the position vectors of the nodes corresponding to the corners of face $\mathcal{M}^j$ in counterclockwise ordering (see Figure 3.9(a)):

$$\tilde{\mathbf{Y}}^j := \begin{bmatrix} \tilde{\mathbf{y}}^{j1} \\ \vdots \\ \tilde{\mathbf{y}}^{jn_j^C} \end{bmatrix}. \tag{3.39}$$

Define the connectivity matrices ${}^j\mathbf{C}^{MN} \in \{0,1\}^{n_j^C \times N_{\mathcal{N}}}$, $j = 1, \ldots, N_{\mathcal{M}}$, with elements ${}^jC^{MN}_{ki}$, as follows:

$${}^jC^{MN}_{ki} := \begin{cases} 1; & \hat{\mathbf{y}}^i \text{ is the position vector of the } k^{\text{th}} \text{ corner (in} \\ & \text{counterclockwise order) of } \mathcal{M}^j \\ 0; & \text{otherwise} \end{cases}. \tag{3.40}$$

The mapping from the position vectors of the nodes of $\mathcal{M}$ to those associated with the corners of each face $\mathcal{M}^j$ is then given as follows:

$$\tilde{\mathbf{Y}}^j = \left({}^j\mathbf{C}^{MN} \otimes \mathbf{I}_3\right) \hat{\mathbf{Y}}. \tag{3.41}$$

Let $\tilde{\boldsymbol{l}}^j \in \mathbb{R}^{n_j^C}$, $j = 1, \ldots, N_{\mathcal{M}}$, be the vectors constructed by collecting the trim lengths $\tilde{l}_{jk}$, $k = 1, \ldots, n_j^C$ (refer to Figure 3.9), as follows:

$$\tilde{\boldsymbol{l}}^j := \begin{bmatrix} \tilde{l}_{j1} \\ \vdots \\ \tilde{l}_{jn_j^C} \end{bmatrix}. \tag{3.42}$$

Define the connectivity matrices ${}^j\mathbf{C}^{ME_I} \in \mathbb{R}^{n_j^C \times N_{\mathcal{E}}^I}$, $j = 1, \ldots, N_{\mathcal{M}}$, with elements ${}^jC_{ki}^{ME_I}$, as follows:

$${}^jC_{ki}^{ME_I} := \begin{cases} 1; & \text{the } i^{\text{th}} \text{ interior edge of } \mathcal{M} \text{ corresponds to the } k^{\text{th}} \text{ edge (in} \\ & \text{counterclockwise order) of } \mathcal{M}^j \\ 0; & \text{otherwise} \end{cases}. \tag{3.43}$$

Therefore, the mapping from the trim lengths of the interior edges of $\mathcal{M}$ to those associated with the edges of each face $\mathcal{M}^j$ is as follows:

$$\tilde{\boldsymbol{l}}^j = {}^j\mathbf{C}^{ME_I} \hat{\boldsymbol{l}}. \tag{3.44}$$

3.4.1.3 Interior Node Parameters and Variables

Let $\mathbf{Z}^j \in \mathbb{R}^{3n_j^{\mathcal{M}}}$, $j = 1, \ldots, N_{\mathcal{N}}^I$, be the vector constructed by concatenating the vectors $\mathbf{z}^{jk}$, $k = 1, \ldots, n_j^{\mathcal{M}}$ (see Figure 3.7), as follows:

$$\mathbf{Z}^j := \begin{bmatrix} \mathbf{z}^{j1} \\ \vdots \\ \mathbf{z}^{jn_j^{\mathcal{M}}} \end{bmatrix}, \tag{3.45}$$

and define the matrix ${}^j\mathbf{C}^{N_I E_I} \in \{-1, 0, 1\}^{n_j^{\mathcal{M}} \times N_{\mathcal{E}}^I}$, $j = 1, \ldots, N_{\mathcal{N}}^I$, with elements ${}^jC_{ki}^{N_I E_I}$, as follows:

$${}^jC_{ki}^{N_I E_I} := \begin{cases} 1; & \mathbf{z}^{jk} \text{ is a vector along the } i^{\text{th}} \text{ interior edge of } \mathcal{M} \text{ and emanates} \\ & \text{from the } i^{\text{th}} \text{ interior edge start-point} \\ -1; & \mathbf{z}^{jk} \text{ is a vector along the } i^{\text{th}} \text{ interior edge of } \mathcal{M} \text{ and emanates} \\ & \text{from the } i^{\text{th}} \text{ interior edge end-point} \\ 0; & \text{otherwise} \end{cases} . \tag{3.46}$$

The mapping from $\hat{\mathbf{Z}}$ and $\hat{\mathbf{Y}}$, respectively defined in Equations (3.32) and (3.31), to each vector $\mathbf{Z}^j$ is given as:

$$\begin{aligned} \mathbf{Z}^j &= \left({}^j\mathbf{C}^{N_I E_I} \otimes \mathbf{I}_3\right) \hat{\mathbf{Z}} \\ &= \left({}^j\mathbf{C}^{N_I E_I} \otimes \mathbf{I}_3\right) \left(\mathbf{C}^{E_I N} \otimes \mathbf{I}_3\right) \hat{\mathbf{Y}} \\ &= \left(\left({}^j\mathbf{C}^{N_I E_I} \mathbf{C}^{E_I N}\right) \otimes \mathbf{I}_3\right) \hat{\mathbf{Y}}. \end{aligned} \tag{3.47}$$

Let $\boldsymbol{W}^j, \boldsymbol{\psi}^j \in \mathbb{R}^{n_j^{\mathcal{M}}}$, $j = 1, \ldots, N_{\mathcal{N}}^I$, be the vectors constructed by collecting the

design variables for the edge modules associated with the j^{th} interior node of $\mathcal{M}$ (W_{jk} and ψ_{jk}, $i = 1, \ldots, n_j^{\mathcal{M}}$) as follows:

$$\boldsymbol{W}^j := \begin{bmatrix} W_{j1} \\ \vdots \\ W_{jn_j^{\mathcal{M}}} \end{bmatrix}, \tag{3.48}$$

$$\boldsymbol{\psi}^j := \begin{bmatrix} \psi_{j1} \\ \vdots \\ \psi_{jn_j^{\mathcal{M}}} \end{bmatrix}. \tag{3.49}$$

The mappings from the edge module variables of all the interior edges of $\mathcal{M}$ to those associated with the edges connected to the j^{th} interior node of $\mathcal{M}$ are given as:

$$\boldsymbol{W}^j = \left|{}^j\mathbf{C}^{N_I E_I}\right|_* \hat{\boldsymbol{W}}, \tag{3.50}$$

$$\boldsymbol{\psi}^j = {}^j\mathbf{C}^{N_I E_I} \hat{\boldsymbol{\psi}}, \tag{3.51}$$

where $|\cdot|_* : \mathbb{R}^{m \times n} \to \mathbb{R}^{m \times n}_{\geq 0}$ denotes the element-wise absolute value of a matrix (i.e. $[|\mathbf{Y}|_*]_{ij} = |Y_{ij}|$) and the vectors $\hat{\boldsymbol{W}}$ and $\hat{\boldsymbol{\psi}}$ are defined in Equations (3.36) and (3.37), respectively.

Let ${}^j\boldsymbol{d}^{mn} \in \mathbb{R}^{n_j^{\mathcal{M}}}$, $j = 1, \ldots, N_{\mathcal{N}}^I$, $m = 1, 2$, $n = 1, 2$, be the vector constructed by respectively collecting the edge module parameters d_{mn}^{jk}, $k = 1, \ldots, n_j^{\mathcal{M}}$, as follows:

$${}^j\boldsymbol{d}^{mn} = \begin{bmatrix} d_{mn}^{j1} \\ \vdots \\ d_{mn}^{jn_j^{\mathcal{M}}} \end{bmatrix}, \tag{3.52}$$

and the mapping from $\hat{\boldsymbol{d}}^{mn}$ (refer to Equation (3.38)) to each vector ${}^{j}\boldsymbol{d}^{mn}$ is given as follows:

$$\begin{bmatrix} {}^{j}\boldsymbol{d}^{11} \\ \\ {}^{j}\boldsymbol{d}^{22} \end{bmatrix} = \begin{bmatrix} \frac{1}{2}\left(\left|{}^{j}\mathbf{C}^{N_I E_I}\right|_* + {}^{j}\mathbf{C}^{N_I E_I}\right) & \frac{1}{2}\left(\left|{}^{j}\mathbf{C}^{N_I E_I}\right|_* - {}^{j}\mathbf{C}^{N_I E_I}\right) \\ \\ \frac{1}{2}\left(\left|{}^{j}\mathbf{C}^{N_I E_I}\right|_* - {}^{j}\mathbf{C}^{N_I E_I}\right) & \frac{1}{2}\left(\left|{}^{j}\mathbf{C}^{N_I E_I}\right|_* + {}^{j}\mathbf{C}^{N_I E_I}\right) \end{bmatrix} \begin{bmatrix} \hat{\boldsymbol{d}}^{11} \\ \\ \hat{\boldsymbol{d}}^{22} \end{bmatrix}, \quad (3.53)$$

$$\begin{bmatrix} {}^{j}\boldsymbol{d}^{12} \\ \\ {}^{j}\boldsymbol{d}^{21} \end{bmatrix} = \begin{bmatrix} \frac{1}{2}\left(\left|{}^{j}\mathbf{C}^{N_I E_I}\right|_* + {}^{j}\mathbf{C}^{N_I E_I}\right) & \frac{1}{2}\left(\left|{}^{j}\mathbf{C}^{N_I E_I}\right|_* - {}^{j}\mathbf{C}^{N_I E_I}\right) \\ \\ \frac{1}{2}\left(\left|{}^{j}\mathbf{C}^{N_I E_I}\right|_* - {}^{j}\mathbf{C}^{N_I E_I}\right) & \frac{1}{2}\left(\left|{}^{j}\mathbf{C}^{N_I E_I}\right|_* + {}^{j}\mathbf{C}^{N_I E_I}\right) \end{bmatrix} \begin{bmatrix} \hat{\boldsymbol{d}}^{12} \\ \\ \hat{\boldsymbol{d}}^{21} \end{bmatrix}. \quad (3.54)$$

3.4.2 Method of Solution

Given a goal mesh $\mathcal{M}$, the node coordinates of $\mathcal{M}$ and the mesh connectivity data (see Section 3.4.1) are utilized to compute all the geometric parameters presented in Section 3.3. Afterwards, an iterative numerical procedure presented in this section is used to determine a set of design variables $\hat{W}_i$ and $\hat{\psi}_i$, $i = 1, \ldots, N_{\mathcal{E}}^I$, that satisfies the proposed constraints.

Let $\boldsymbol{\mathfrak{R}} \in \mathbb{R}^{3N_{\mathcal{N}}^I + 4N_{\mathcal{E}}^I}$ be the residual vector defined as follows:

$$\boldsymbol{\mathfrak{R}}\left(\mathbf{D}\right) := \begin{bmatrix} \boldsymbol{h}\left(\mathbf{D}\right) \\ \\ \max\left(\mathbf{0}_{4N_{\mathcal{E}}^I}, \;\; \boldsymbol{g}\left(\mathbf{D}\right)\right) \end{bmatrix}, \quad (3.55)$$

where the $\max(\cdot, \cdot)$ operator in the previous equation is applied component-wise and the vector of design variables $\mathbf{D}$ is defined in Equation (3.29). The vectors of equality and inequality constraints ($\boldsymbol{h}\left(\mathbf{D}\right)$ and $\boldsymbol{g}\left(\mathbf{D}\right)$, respectively) are defined in Section 3.3.2. At the l^{th} iteration, if $\|\boldsymbol{\mathfrak{R}}({}^{l}\mathbf{D})\|/(3N_{\mathcal{N}}^I + 4N_{\mathcal{E}}^I) \geq \texttt{tol}$ (where `tol` is

Table 3.2: Numerical procedure used to determine a set of design variables that satisfies the constraints of the proposed design method. The design variables are iteratively corrected until the presented constraints are satisfied.

1:	Set $l \leftarrow 1$ and provide initial guess ${}^{1}\mathbf{D}$
2:	Determine $\|\mathfrak{R}({}^{l}\mathbf{D})\|$
3:	`IF` $\|\mathfrak{R}({}^{l}\mathbf{D})\|/(3N_{\mathcal{N}}^{I} + 4N_{\mathcal{E}}^{I}) <$ `tol THEN RETURN` ${}^{l}\mathbf{D}$ and `EXIT ELSE CONTINUE`
4:	Determine ${}^{l+1}\mathbf{D}$ using Equations (3.56) and (3.57)
5:	Set $l \leftarrow l + 1$ and `GOTO` 2

a numerical tolerance) the set of design variables is corrected using the generalized Newton's method as follows:

$$ {}^{l}\Delta\mathbf{D} = -\left(\frac{\partial\mathfrak{R}\left({}^{l}\mathbf{D}\right)}{\partial\mathbf{D}}\right)^{\dagger}\mathfrak{R}\left({}^{l}\mathbf{D}\right), \tag{3.56} $$

$$ {}^{l+1}\mathbf{D} \;=\; {}^{l}\mathbf{D} \;+\; {}^{l}\Delta\mathbf{D}, \tag{3.57} $$

where $(\cdot)^{\dagger}$ denotes the Moore-Penrose pseudoinverse. Given an initial guess for ${}^{1}\mathbf{D}$, the set of design variables is iteratively updated as indicated in Equation (3.56) and (3.57) until $\|\mathfrak{R}({}^{l}\mathbf{D})\|/(3N_{\mathcal{N}}^{I}+4N_{\mathcal{E}}^{I}) <$ `tol`. Table 3.2 summarizes the procedure used to determine a set of design variables that satisfies the constraints of the proposed design method.

3.5 Discussion

A discussion of the requirements for the existence of valid sheet designs is presented in this section. Uniqueness of valid sheet designs is also discussed.

For the present design method to be applicable, the goal mesh $\mathcal{M}$ must be an

orientable manifold mesh. The goal mesh $\mathcal{M}$ must be a manifold mesh because in the present design method each edge in $\mathcal{M}$ is assumed to be located either at $\partial\mathcal{M}$ or connecting two faces $\mathcal{M}^j$. Orientability of $\mathcal{M}$ is also required since the faces of $\mathcal{M}_\sharp$, that have the same orientation as those of $\mathcal{M}$ (see Proposition 3.1), are mapped into a common plane in $\mathcal{S}_0$. Since $\mathcal{S}_0$ is orientable, $\mathcal{M}$ must also have this property.

The face trimming process described in Section 3.3.1 must not degenerate any face of $\mathcal{M}$. This is clearly required because every face $\mathcal{M}^j$ and its associated trimmed face $\mathcal{M}^j_\sharp$ must have the same number of edges. The following corollary of Proposition 3.1 provides a practical way to check if such a requirement is met:

Corollary 3.1. *The face trimming process does not degenerate any face $\mathcal{M}^j$ if and only if the following conditions hold:*

$$\begin{aligned} &\left(\tilde{\mathbf{y}}^{j\,k+1} - \tilde{\mathbf{y}}^{jk}\right) \cdot \left(\tilde{\mathbf{y}}_\sharp^{j\,k+1} - \tilde{\mathbf{y}}_\sharp^{jk}\right) > 0 \quad \Leftrightarrow \quad \|\tilde{\mathbf{y}}^{j\,k+1} - \tilde{\mathbf{y}}^{jk}\| - \tilde{d}_1^{jk} - \tilde{d}_2^{jk} > 0 \\ &\forall\, j \in \{1, \ldots, N_{\mathcal{M}}\},\ k \in \{1, \ldots, n_j^C\}. \end{aligned} \tag{3.58}$$

The expressions for $\tilde{d}_1^{jk}$ and $\tilde{d}_2^{jk}$ are provided in Equations (3.12) and (3.13). The size of the trimmed regions increases proportionally to the width of the folds as indicated in Equation (3.6). The increase of the size of the trimmed regions with increase in fold widths is illustrated in Figure 3.14. For the special case of creased folds that have zero fold width, face trimming is not required and such a requirement is trivially satisfied (refer to the leftmost schematic in Figure 3.14). For any other case where the width of the folds is non-zero, the size of the goal mesh is subject to

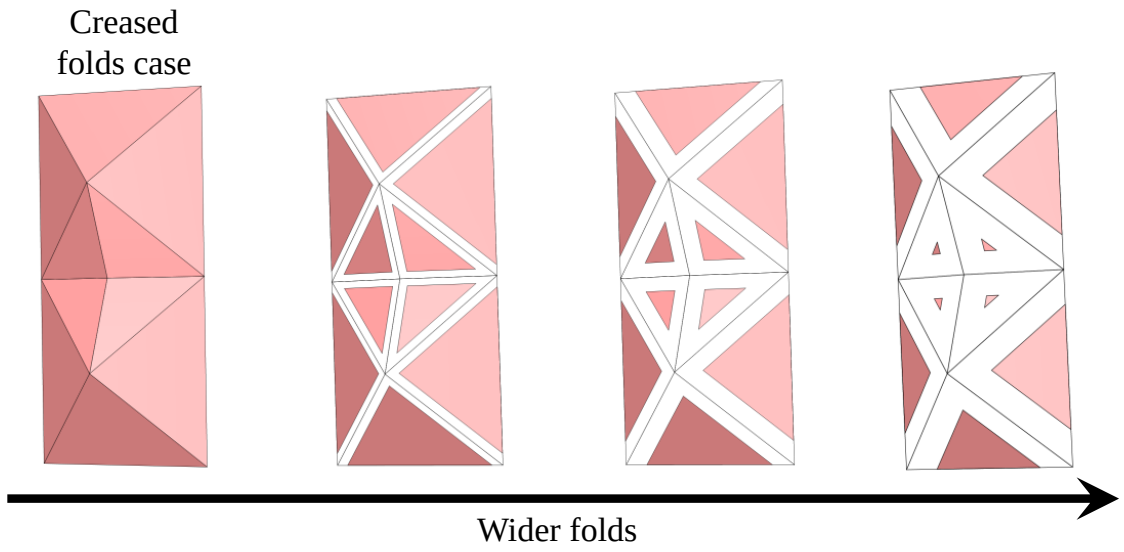

Figure 3.14: Trimmed faces associated with edge modules having smooth folds of various fold widths. The leftmost mesh corresponds to the special case of creased folds for which face trimming is not required.

the following constraint:

$$\min_{j\in\{1,\ldots,N_{\mathcal{M}}\},\, k\in\{1,\ldots,n_j^C\}} \|\tilde{\mathbf{y}}^{j\,k+1} - \tilde{\mathbf{y}}^{jk}\| - \tilde{d}_1^{jk} - \tilde{d}_2^{jk} > 0. \tag{3.59}$$

A solution to the equality constraints (Equations (3.15) and (3.16)) must be contained within the bounds of the design variables (Equations (3.20), (3.21), and (3.28)). The necessity for such a requirement is evident. The number of degrees of freedom (N_{dof}) in the design problem is given as follows:

$$N_{\text{dof}} = 2N_{\mathcal{E}}^I - 3N_{\mathcal{N}}^I, \tag{3.60}$$

where $2N_{\mathcal{E}}^I$ is the number of design variables $\hat{W}_i$, $\hat{\psi}_i$, $i = 1, \ldots, N_{\mathcal{E}}^I$, and $3N_{\mathcal{N}}^I$ is the number of equality constraints. It is assumed in Equation (3.60) that there are

no redundant equality constraints and that the inequality constraints in Equations (3.20), (3.21), and (3.28) permit solutions to the system of Equations (3.15) and (3.16). The number of interior edges $N_{\mathcal{E}}^{I}$ is additively decomposed as follows:

$$N_{\mathcal{E}}^{I} = N_{\mathcal{E}}^{I0} + N_{\mathcal{E}}^{I1} + N_{\mathcal{E}}^{I2}, \tag{3.61}$$

where $N_{\mathcal{E}}^{Im}$, $m \in \{0, 1, 2\}$, is the number of interior edges connected to m interior nodes. Also consider the following equality:

$$\bar{n}^{\mathcal{M}} N_{\mathcal{N}}^{I} = \sum_{j=1}^{N_{\mathcal{N}}^{I}} n_j^{\mathcal{M}} = 2N_{\mathcal{E}}^{I2} + N_{\mathcal{E}}^{I1}, \tag{3.62}$$

where $\bar{n}^{\mathcal{M}}$ is the average valence of the interior nodes in $\mathcal{M}$ (i.e. the average number of edges incident to the each interior node). Substituting Equations (3.61) and (3.62) into Equation (3.60), the following relation between degrees of freedom and number of interior edges is obtained:

$$N_{\text{dof}} = \left(2 - \frac{6}{\bar{n}^{\mathcal{M}}}\right) N_{\mathcal{E}}^{I2} + \left(2 - \frac{3}{\bar{n}^{\mathcal{M}}}\right) N_{\mathcal{E}}^{I1} + 2N_{\mathcal{E}}^{I0}. \tag{3.63}$$

For example, a structured triangular mesh with $\bar{n}^{\mathcal{M}} = 6$ has $N_{\text{dof}} = N_{\mathcal{E}}^{I2} + (3/2)N_{\mathcal{E}}^{I1} + 2N_{\mathcal{E}}^{I0}$ which is always greater than 0 and a structured quadrilateral mesh with $\bar{n}^{\mathcal{M}} = 4$ has $N_{\text{dof}} = (1/2)N_{\mathcal{E}}^{I2} + (5/4)N_{\mathcal{E}}^{I1} + 2N_{\mathcal{E}}^{I0}$ which is also always greater than 0. Therefore, the existence of a set of design variables $\hat{W}_i$, $\hat{\psi}_i$, $i = 1, \ldots, N_{\mathcal{E}}^{I}$, that satisfies the design constraints is generally dependent on the inequality constraints (Equations (3.20), (3.21), and (3.28)).

Another requirement is that $\mathcal{S}_0$ must not have any overlapping regions. This is needed since the reference configuration $\mathcal{S}_0$ must be planar and having no overlapping subdomains (refer to Section 2.2). The following proposition provides a requirement

on $\mathcal{M}$ that prevents overlaps of adjacent edge modules having a common interior node:

Proposition 3.3. *To prevent overlaps of adjacent edge modules in $\mathcal{S}_0$ associated with a common interior node in $\mathcal{M}$, the face angles associated with such an interior node must satisfy the following constraint:*

$$\phi_{jk} \leq \pi \qquad \forall\, j \in \{1, \ldots, N_{\mathcal{N}}^I\},\ k \in \{1, \ldots, n_j^{\mathcal{M}}\}. \tag{3.64}$$

If a face angle of an interior node in $\mathcal{M}$ is concave (i.e. if $\phi_{jk} > \pi$), the edge modules connected to such an interior node overlap in $\mathcal{S}_0$, which is not allowed. Figure 3.15 illustrates this requirement. Overlaps in $\mathcal{S}_0$ are partially precluded provided that Equation (3.64) holds for a goal mesh $\mathcal{M}$ and Equation (3.21) holds for each edge module. However, no conditions preventing overlaps of edge modules not sharing a common node, nor preventing overlaps among surface subdomains not associated with a common interior edge, are currently considered in the present design method. Nevertheless, it is shown in Section 3.7 that the considered constraints and implementation of the proposed design method successfully allow for the determination of sheet designs $\mathcal{S}_0$ free of overlapping for goal meshes of various complexities.

For a valid design, it is also required that $\mathcal{S}_\star$ must be a valid configuration (see Definition 2.5). This requirement is partially accounted for through the edge module trimming procedure (refer to Section 3.3.2.1) that prevents intersections of edge modules associated with a common interior node of $\mathcal{M}$ at $\mathcal{S}_\star$. However, no constraints are currently imposed to preclude intersections of subdomains of $\mathcal{S}_\star$ that are not associated to a common interior node in $\mathcal{M}$. Nonetheless, it is also shown in Section 3.7 that the proposed design method successfully allows for the determination of goal

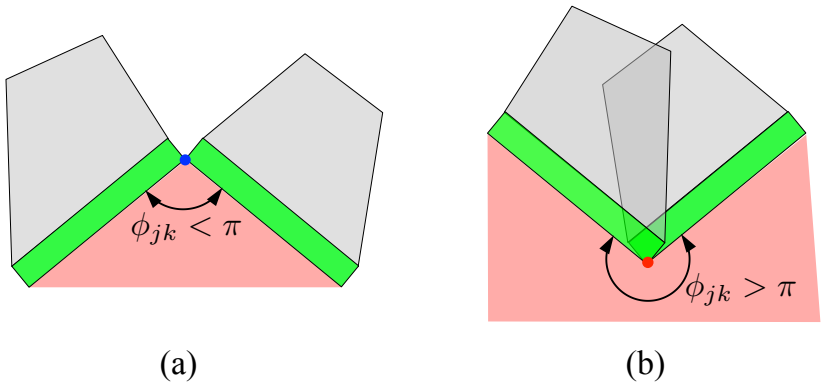

Figure 3.15: (a) Edge modules connected to a face with a convex face angle. (b) Edge modules connected to a face with a concave face angle.

configurations $\mathcal{S}_\star$ having no overlaps for goal meshes of various complexities.

Finally, for a valid design it is required that there is a *continuous* set of valid configurations from the reference configuration to the goal configuration: $\{\mathcal{S}_t,\, 0 < t < t_f \mid \mathcal{S}_{t_f} = \mathcal{S}_\star\}$. The procedure for kinematic simulation of the designed sheets to be described in Section 3.6 permits the determination of valid intermediate configurations between $\mathcal{S}_0$ and $\mathcal{S}_\star$. Although a *continuous* set of valid configurations is not obtained using such a numerical procedure, a discrete set containing an arbitrary number of intermediate configurations can be determined.

Regarding the *uniqueness* of valid designs, assuming that the inequality constraints in Equations (3.20), (3.21), and (3.28) allow for a valid design solution, such a solution is not unique because in general $N_{\text{dof}} > 0$ (refer to Equation (3.63)). One global measure to discriminate among various design solutions and drive toward a possible unique solution is referred to as the surface area efficiency E and is defined

as follows:

$$\mathsf{E} := \frac{\text{Area}(\mathcal{M})}{\text{Area}(\mathcal{S}_0)}. \tag{3.65}$$

The numerical procedure outlined in Section 3.4.2 used to determine a valid design does not consider any function to minimize or maximize (i.e. it only iteratively corrects an initial guess solution until the presented constraints are satisfied). However, other methods can be utilized to determine a sheet design that satisfies the presented constraints while optimizing a given function (e.g. maximize surface area efficiency E). Such extensions are application-dependent and are recommended for future studies. An alternative formulation of the design method utilized to maximize the value of E in Appendix D.

3.6 Determination of Folding Sequence

The determination of a folding sequence allowing for folding motion from $\mathcal{S}_0$ towards $\mathcal{S}_\star$ is considered here. The kinematic simulation approach for origami with smooth folds and its associated numerical implementation utilized herein are described in detail in Section 2. The simulation of the folding motion is executed by incrementally updating the values of the fold angles using guess increments and then iteratively applying any required corrections (see Section 2.2.6) such that the resulting folded configuration is valid (i.e. the kinematic constraints presented in Equation (2.97) are met for every fold intersection).

Let $\hat{\boldsymbol{\theta}}^\star \in \mathbb{R}^{3N_\mathcal{E}^I}$ be the vector constructed by collecting the values of the fold angles for each smooth fold at the goal configuration $\mathcal{S}_\star$. The goal fold angle for the interior fold of each edge module is equal to π while those for the exterior folds are equal to $-\hat{\Theta}_i/2$ (refer to Figure 3.8). In the reference configuration $\mathcal{S}_0$, all the fold angles are equal to 0. The simulation of the sheet folding motion uses a fold and

adjust approach and is performed in $N_{\text{fol}} + N_{\text{adj}}$ increments. The N_{fol} guess fold angle increments (${}^{IN}_{l}\Delta\hat{\boldsymbol{\theta}}$) are simply given as follows:

$$ {}^{IN}_{l}\Delta\hat{\boldsymbol{\theta}} = \frac{\hat{\boldsymbol{\theta}}^{\star}}{N_{\text{fol}}} \qquad \forall\, l \in \{1, \ldots, N_{\text{fol}}\}. \tag{3.66} $$

Since the set of fold angles at each increment is subject to iterative corrections to ensure that the kinematic constraints presented in Equation (2.97) are met, the configuration determined at the N_{fol} increment may not exactly correspond to $\mathcal{S}_{\star}$. As such, N_{adj} adjusting increments are subsequently applied. These corrective fold angle increments are calculated as follows:

$$ {}^{IN}_{l}\Delta\hat{\boldsymbol{\theta}} = \hat{\boldsymbol{\theta}}^{\star} - {}_{l-1}\hat{\boldsymbol{\theta}} \qquad \forall\, l \in \{N_{\text{fol}} + 1, \ldots, N_{\text{fol}} + N_{\text{adj}}\}. \tag{3.67} $$

Note that this framework allows for the determination of an arbitrary number $(N_{\text{fol}} + N_{\text{adj}} - 1)$ of valid intermediate configurations between $\mathcal{S}_0$ to $\mathcal{S}_{\star}$, and represents another contribution of the present work (i.e. simulation of the motion between reference and goal configurations was not addressed in related works [9, 391] and it is remarked that this work is also applicable to origami with creased folds). The simple set of fold angle increments provided in Equations (3.66) and (3.67) is effective for the determination of a folding motion from $\mathcal{S}_0$ to $\mathcal{S}_{\star}$ in all the examples presented in this work. However, it is not guaranteed to work for any arbitrary goal mesh or sheet reference configuration. For information on more complex motion planning procedures for origami the reader is referred to [406, 407, 408, 409, 410].

3.7 Implementation Results

The proposed design method for origami structures with smooth folds is now tested against various goal meshes with diverse geometries. The numerical solution

procedure for the proposed design method described in Section 3.4 and for determination of a folding sequence outlined in Section 3.6 are implemented in Matlab. The smooth folds are visualized using the Matlab three-dimensional shaded surface plot function `surf` and the rigid faces and goal meshes are visualized through filled three-dimensional polygons using `fill3`. Smooth folds having G^2 continuity are considered in all the examples presented in this section (refer to Figure 2.7).

A reference configuration $\mathcal{S}_0$ determined using the proposed design method and the corresponding goal configuration $\mathcal{S}_\star$ for a goal mesh $\mathcal{M}$ having interior nodes of positive discrete Gaussian curvature [415, 416] is presented in Figure 3.16. A goal mesh having interior nodes of negative discrete Gaussian curvature is considered in Figure 3.17.

Variations of the goal mesh shown in Figure 3.16 and their determined sheet reference configurations are shown in Figure 3.18. Using the kinematic simulation approach presented in Section 3.6, it is verified that each sheet reference configuration in Figure 3.18 folds towards their corresponding goal configuration $\mathcal{S}_\star$, although not shown here for the sake of brevity.

To illustrate the non-uniqueness of determined sheet reference configurations discussed in Section 3.5, three determined sheet reference configurations associated with a single goal mesh are presented in Figure 3.19. These different solutions are obtained by considering different initial guesses for the sheet design variables in the iterative solution procedure utilized in this work (described in Section 3.4). Values of surface area efficiency E, defined in Equation (3.65), for the determined sheet reference configurations are also included in Figure 3.19.

A more complex example of a torus goal shape is presented in Figure 3.20. Two different discretizations of the goal shape are provided in Figure 3.20(a). The design method successfully generates sheet designs for both discretizations as shown in Fig-

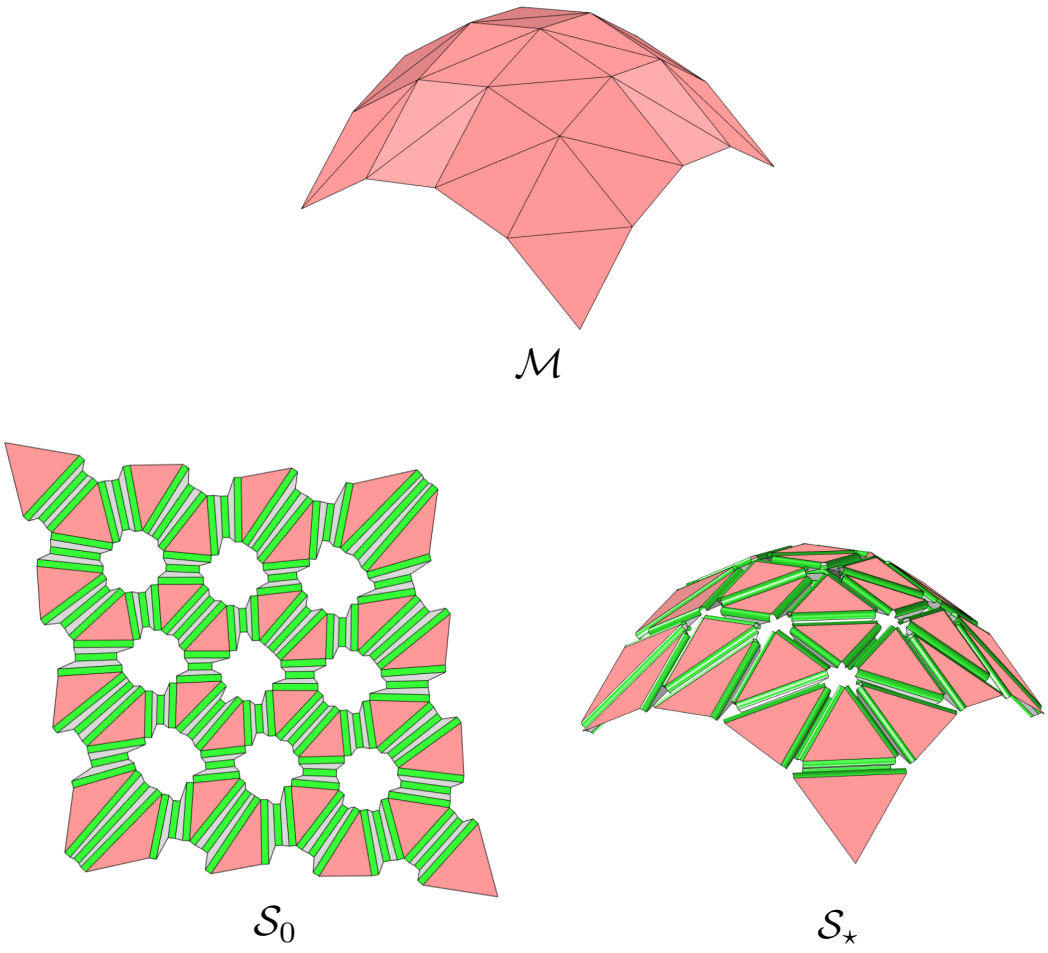

Figure 3.16: Goal mesh having nodes of positive discrete Gaussian curvature and its associated determined sheet reference configuration and folded goal configuration.

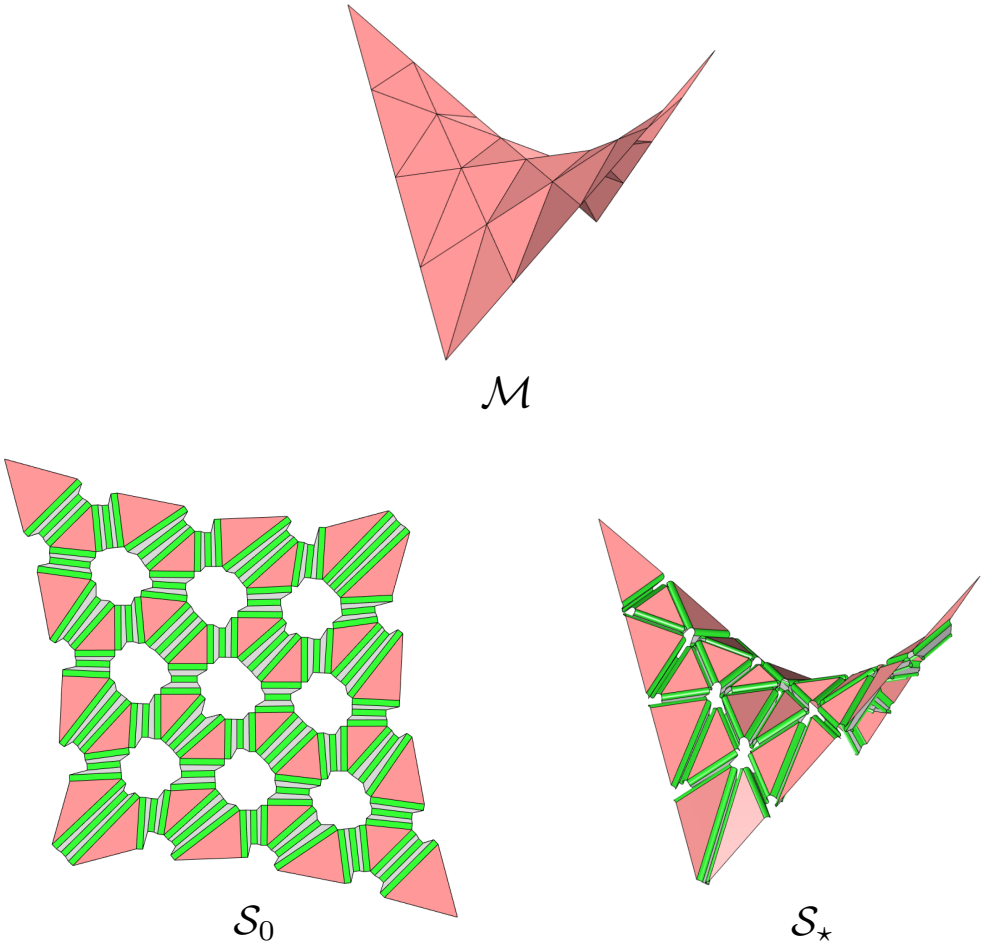

Figure 3.17: Goal mesh having nodes of negative discrete Gaussian curvature and its associated determined sheet reference configuration and folded goal configuration.

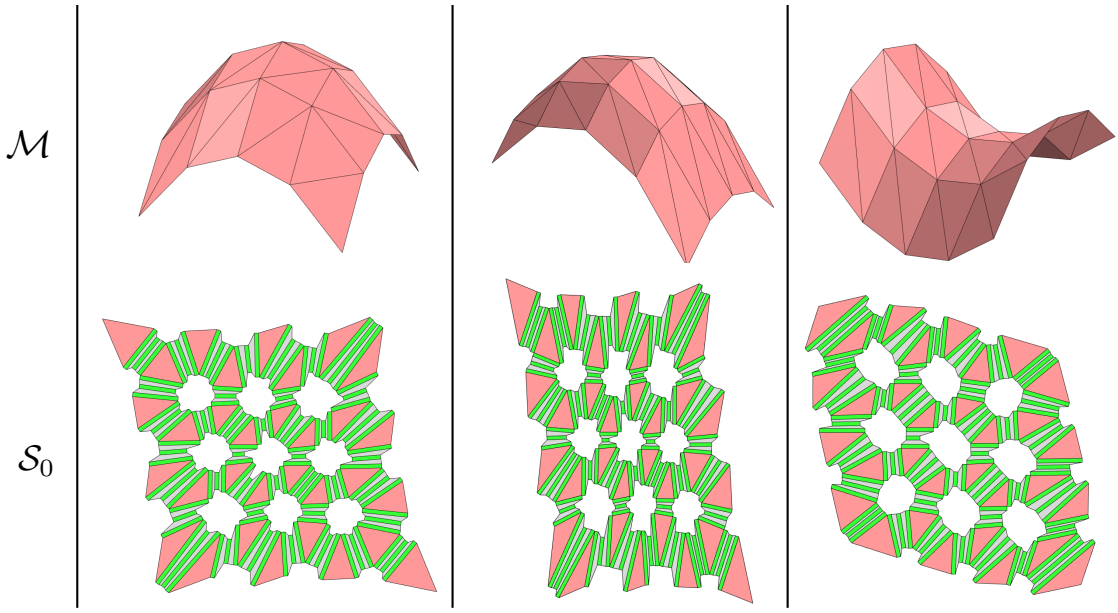

Figure 3.18: Various of a goal shapes and their corresponding goal meshes and determined sheet designs.

ure 3.20(b). The complex folding motion determined through kinematic simulation of one of the designs is shown in Figure 3.20(c). Furthermore, Figures 3.21(a)-(c) show the successful design/simulation results for a goal mesh associated with a sinusoidal tessellation.

The proposed method is not limited to triangulated meshes as the only condition on the shape of the faces in $\mathcal{M}$ is that they must be convex (see Proposition 3.3). Figure 3.22 shows an example of a reference configuration and folding deformation associated with a goal mesh comprised of quadrilaterals while Figure 3.23 shows the results for a goal mesh comprised of both octagons and triangles.

3.8 Summary and Concluding Remarks

A method for the design of origami structures with smooth folds was presented in this section. The method is based on the known idea of using folds to create flaps that

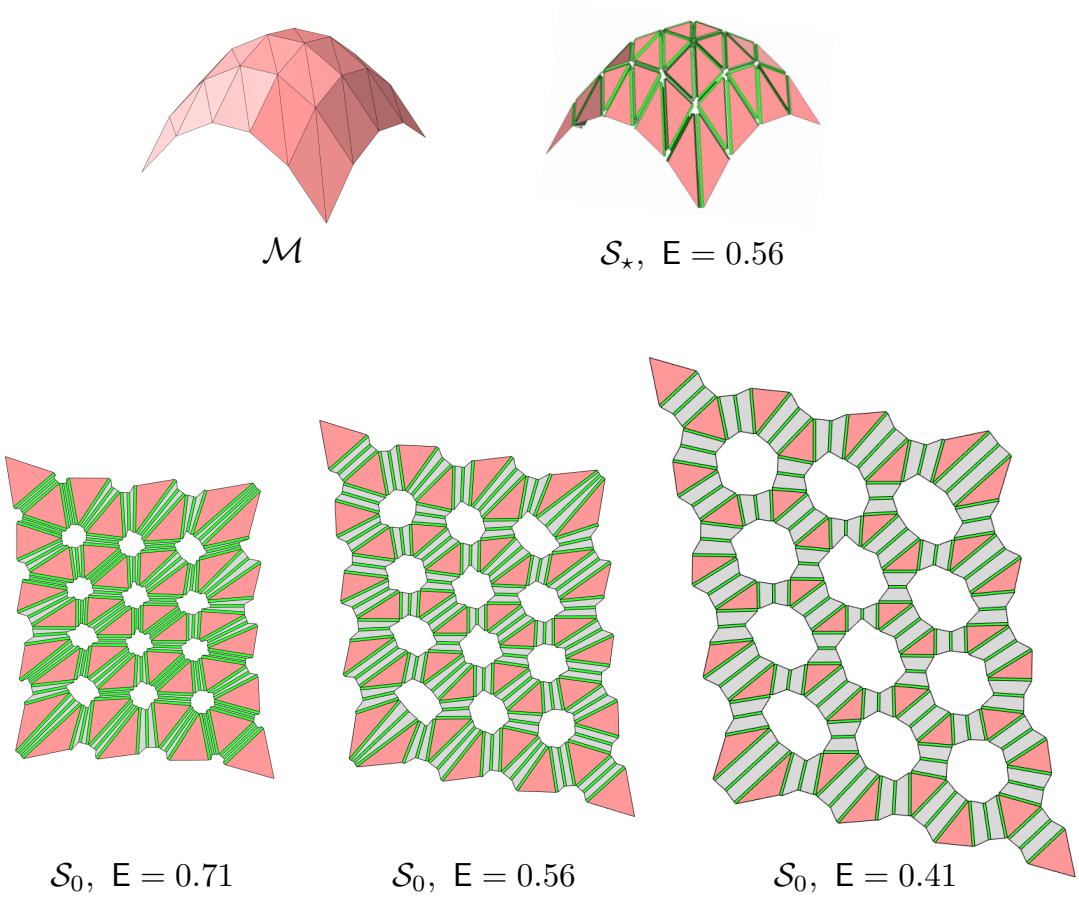

Figure 3.19: A goal mesh and three determined sheet reference configurations with different values of surface area efficiency E. The goal configuration $\mathcal{S}_\star$ associated with the sheet reference configuration having $\mathsf{E} = 0.56$ is also shown.

are tuck folded to morph an initially planar sheet into an arbitrary three-dimensional goal shape represented as a polygonal mesh. The method solves the origami design problem of determining the geometry of the planar reference configuration of a single sheet including a pattern of smooth folds that allow for the approximation of a goal mesh through such a tuck-based folding. A description of the design variables, design constraints, and a numerical solution procedure are provided. Furthermore, a folding sequence allowing for folding motion from the determined sheet reference

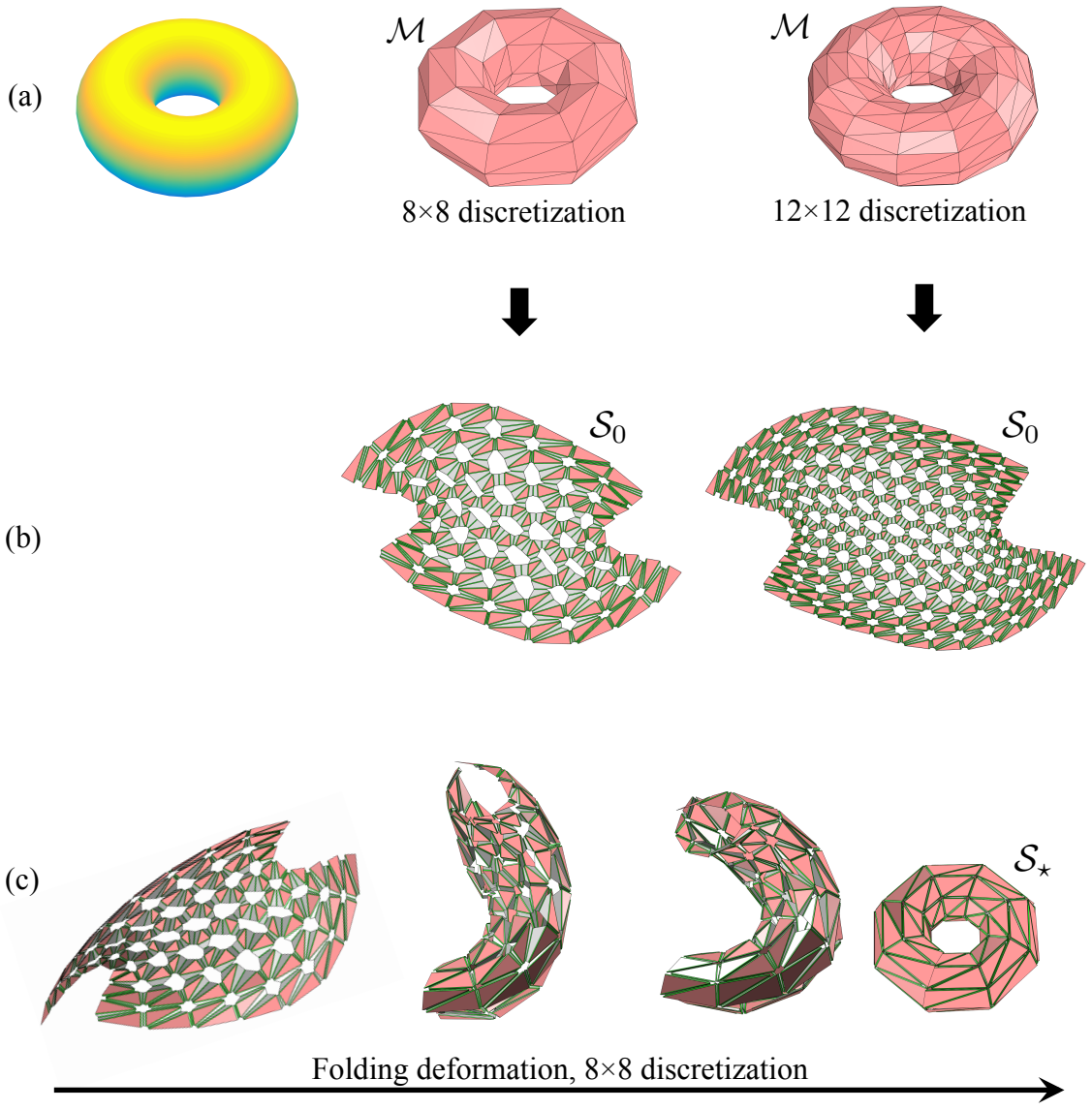

Figure 3.20: (a) Two mesh discretizations of a torus; (b) Determined sheet reference configurations for the two discretizations shown in (a); (c) Folding motion for the sheet reference configuration obtained from the 8×8 mesh discretization of the torus.

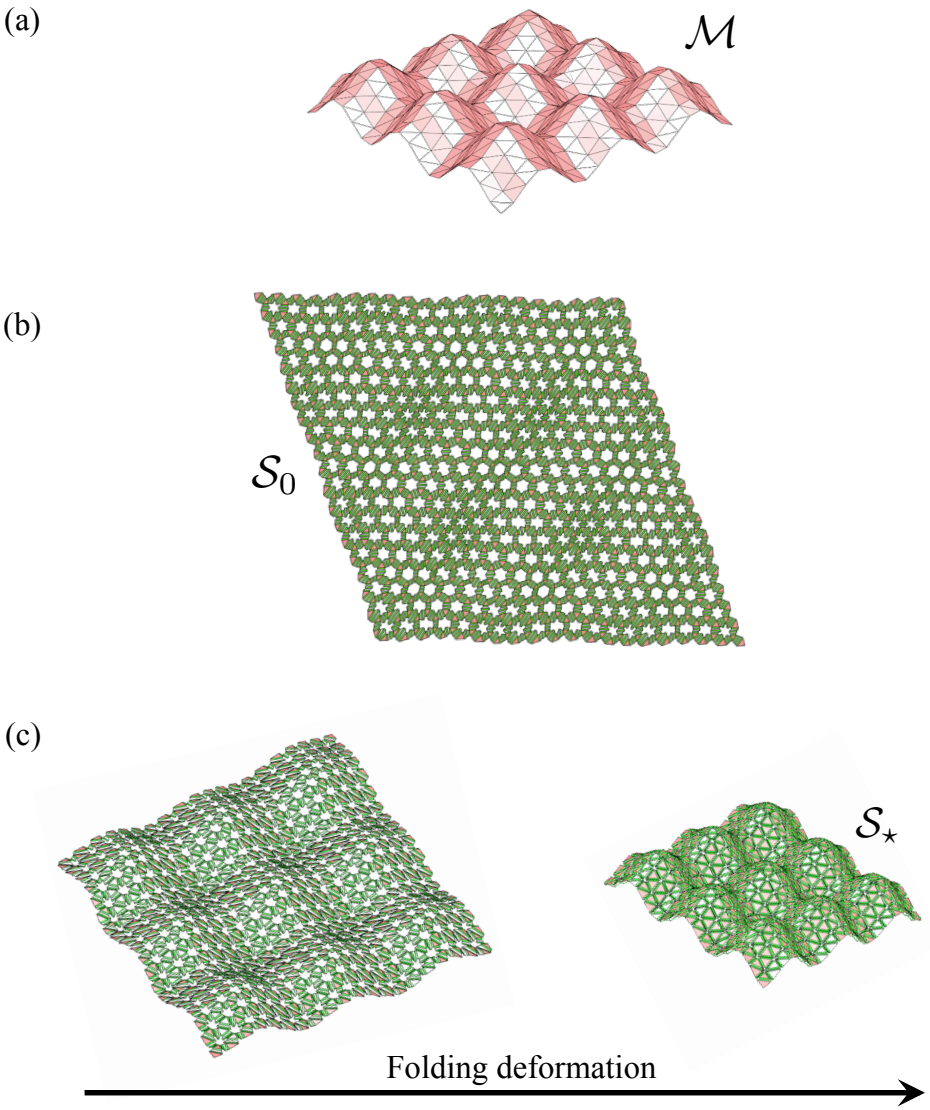

Figure 3.21: (a) Goal mesh representing a sinusoidal tessellation; (b) Determined sheet reference configuration; (c) Folding motion towards the goal configuration.

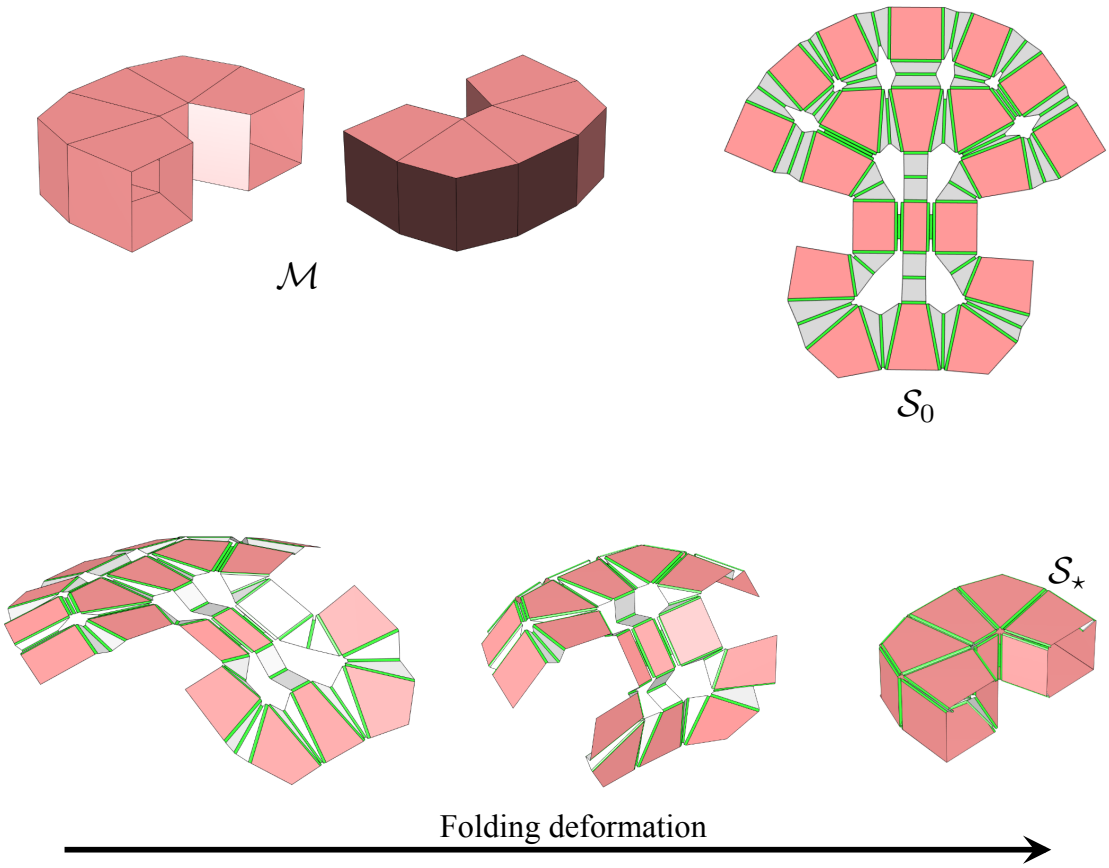

Figure 3.22: Determined sheet design and folding deformation associated with a goal mesh comprised of quadrilaterals.

configuration to a folded configuration that approximates the goal mesh is also determined. For origami design problems in which the goal shape is a not a polyhedral surface (e.g. a smooth surface), the process to determine a mesh discretization of such a surface before the utilization of the method presented in this section must be addressed. Multiple algorithms for obtaining polygonal mesh discretizations of smooth surfaces are available in the literature [437, 438].

A number of conclusions can be drawn based on the developed theory and the obtained results. First, the design method successfully provides fold patterns that can

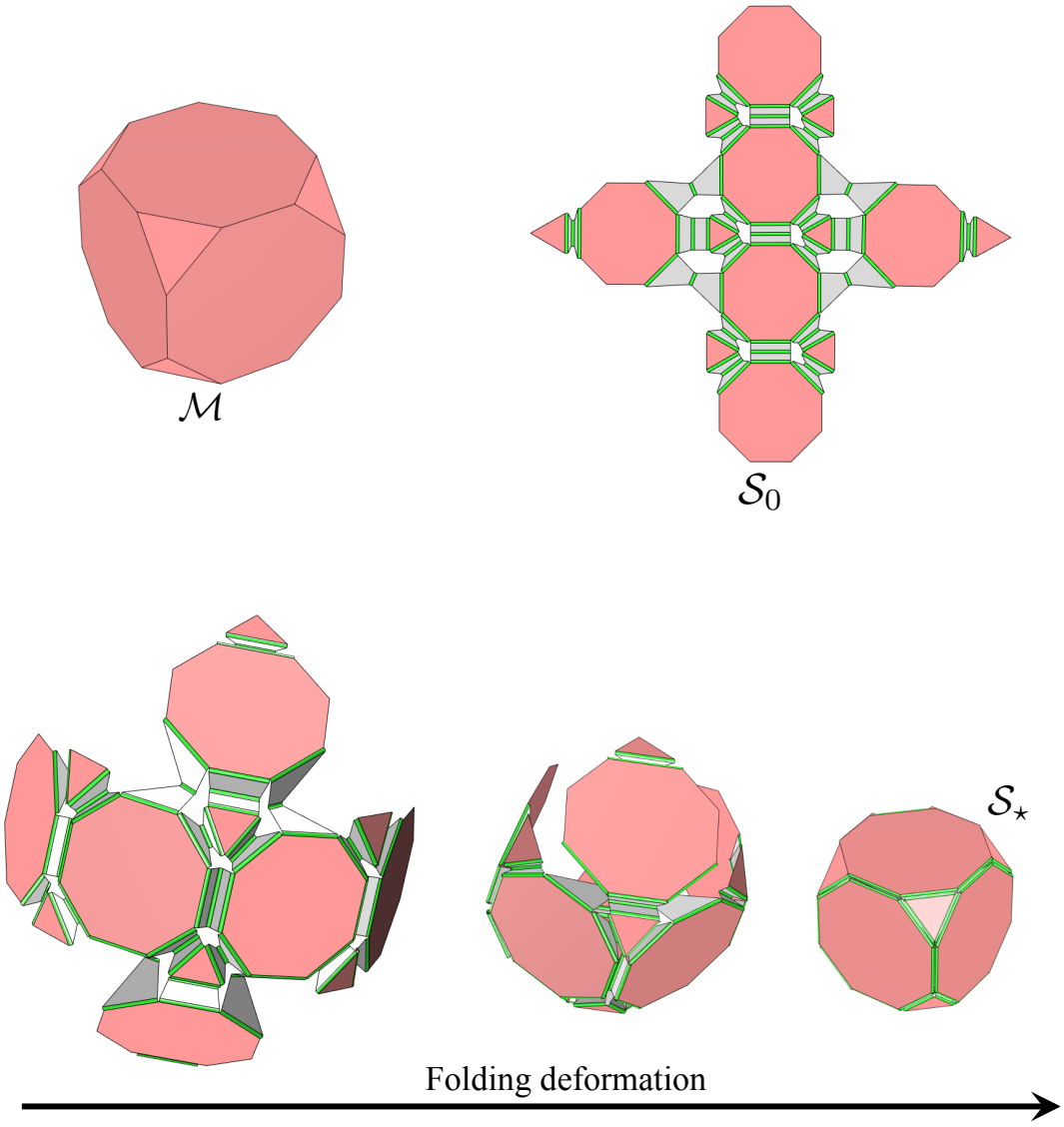

Figure 3.23: Determined sheet design and folding deformation associated with a goal mesh comprised of octagons and triangles.

be realized with diverse engineering materials (e.g. metals, glassy polymers, active materials) due to the consideration of arbitrary order of continuity G^n at the folds, as opposed to G^0 creased folds idealizations available in the literature. The method was tested on goal meshes of various geometries and complexities, yielding successful results for each. Second, comprehensive origami design/simulation is achieved using the presented framework that includes both the design method and the kinematic simulation of the determined sheet designs. This framework allows for the determination of an arbitrary number of intermediate valid configurations between reference and goal configurations. Such a comprehensive origami design/simulation framework represents another contribution of the present work and is applicable to both origami with smooth folds and conventional origami with creased folds.

4. STRUCTURAL MECHANICS OF ORIGAMI BODIES WITH SMOOTH FOLDS

As reviewed in Section 1, origami has the potential to impact numerous fields in engineering by providing new approaches to the fabrication and morphing of various structures and devices. Modeling the structural mechanics of origami bodies is of special interest in the engineering community [319, 321]. It allows for the analysis and design of origami structures taking into account the constitutive behavior of their comprising materials and the influence of the external environment on the resulting folding response.

As discussed in Section 1.4, most available models for the structural mechanics of origami bodies are limited to the idealization of folds as creases of G^0 continuity, which is not proper for origami structures having non-negligible fold thickness or with maximum curvature at the folds restricted by material limitations [350]. Structural analysis of origami bodies having creased folds requires further idealizations of the mechanical response such as the representation of the folds as torsional springs [319, 321, 348]. On the other hand, although FEA models allow for high-fidelity physical simulation of origami structures having arbitrary thickness, the mathematical insights provided in the classical approaches of origami (e.g. geometric constructions [270]) are lost in the generality of FEA. Moreover, the kinematic variables associated with FEA models such as node displacements are not generally compatible with those of conventional origami such as fold angles (refer to Section 2.1).

In view of this, a novel model for the structural mechanics of origami bodies having smooth fold domains of non-zero thickness is presented in this section. The pre-

sented structural model is developed on the basis of the kinematic model for origami structures with smooth folds described in Section 2. The arbitrary order of geometric continuity (G^n) of the smooth fold surfaces described in Section 2.2.1 allows for a proper structural analysis of smooth fold domains having non-zero thickness using plate or shell representations (in contrast to torsional spring representations used for creased folds [319, 321, 348]). Furthermore, the present model considers kinematic variables (e.g. fold angles) and constraints analogous to those of conventional origami with creased folds[1]. The present model is derived independently from the behavior of the materials comprising the origami structures; therefore, it is useful for both origami structures having regions comprised of passive materials (e.g. elastic, elastoplastic) as well as those having regions comprised of active materials. As such, the present model is useful for the analysis of active material-based self-folding structures such as those reviewed in Section 1.2.

The organization of this section is as follows: the kinematic assumptions regarding the strain field in origami bodies with smooth fold domains of non-zero thickness are presented in Section 4.1. The governing field equations and the structural modeling approach considered in this work are presented in Section 4.2. A model for the structural mechanics of origami bodies having smooth fold domains of non-zero thickness comprised of arbitrary materials is presented in Section 4.3. The design method presented in Section 3 is then revisited and extended in Section 4.4 for the design of active self-folding structures (see Section 1.1.1) that morph towards arbitrary three-dimensional goal shapes via simultaneous folding starting from a planar reference configuration. Finally, a summarizing discussion of the section is provided in Section 4.5.

[1]It is remarked that the kinematic constraints for origami with creased folds reviewed in Section 2.1.2 represent a special case of those derived for origami with smooth folds in Section 2.2.3. (refer to Appendix C).

4.1 Smooth Fold Domains and Plate Kinematics

A plate structural representation is used to model origami structures with smooth fold domains having non-zero thickness. The sheet surface $\mathcal{S}_0$ (refer to Section 2.2) is taken as the mid-surface of the plate representation for the origami structure. As stated in Section 2, the sheet surface $\mathcal{S}_0$ contains $N_{\mathcal{P}}$ faces $(\mathcal{P}_0^1, \ldots, \mathcal{P}_0^{N_{\mathcal{P}}})$ and $N_{\mathcal{F}}$ smooth folds $(\mathcal{F}_0^1, \ldots, \mathcal{F}_0^{N_{\mathcal{F}}})$ (i.e. the fold intersections surfaces introduced in Section 2.2 are not considered herein). Since the faces are assumed rigid (see Definition 2.5), the only domains that may undergo non-rigid deformations are the smooth folds and therefore the focus of this section is on these smooth fold domains.

A schematic of the plate structural representation for the smooth fold domains of non-zero thickness is provided in Figure 4.1. At the reference configuration, the i^{th} smooth fold domain in the structure has mid-surface $\mathcal{F}_0^i$ and thickness $\mathfrak{h}_i$. At a current configuration, the i^{th} smooth fold domain has mid-surface $\mathcal{F}_t^i$ and thickness $\mathfrak{h}_i$ (i.e. the thickness is assumed constant during deformation). The smooth fold domains have a parameterization $\mathfrak{F}^i(\zeta_1, \zeta_2, \zeta_3) \in \mathbb{R}^3$ of the following form:

$$\begin{aligned} \mathfrak{F}^i(\zeta_1, \zeta_2, \zeta_3) &= \hat{\mathbf{c}}^i(\zeta_1) + \zeta_2 \mathbf{h}^i + \zeta_3 \frac{\mathbf{h}^i \times \frac{\mathrm{d}\hat{\mathbf{c}}^i(\zeta_1)}{\mathrm{d}\zeta_1}}{\left\| \mathbf{h}^i \times \frac{\mathrm{d}\hat{\mathbf{c}}^i(\zeta_1)}{\mathrm{d}\zeta_1} \right\|} \\ &= \boldsymbol{\mathcal{F}}^i(\zeta_1, \zeta_2) + \zeta_3 \frac{\mathbf{h}^i \times \frac{\mathrm{d}\hat{\mathbf{c}}^i(\zeta_1)}{\mathrm{d}\zeta_1}}{\left\| \mathbf{h}^i \times \frac{\mathrm{d}\hat{\mathbf{c}}^i(\zeta_1)}{\mathrm{d}\zeta_1} \right\|}, \end{aligned} \tag{4.1}$$

where $\zeta_3 \in \left[-\frac{\mathfrak{h}_i}{2}, \frac{\mathfrak{h}_i}{2}\right]$ is the coordinate through the thickness of the i^{th} smooth fold domain, and $\boldsymbol{\mathcal{F}}^i(\zeta_1, \zeta_2) \in \mathbb{R}^3$ is a parameterization of the smooth fold surface $\mathcal{F}_t^i$ (corresponding to the mid-surface of the i^{th} smooth fold domain). Recalling Definition 2.6, the intervals for the parameters ζ_1 and ζ_2 are taken as $[-1, 1]$ and $[0, 1]$, respectively.

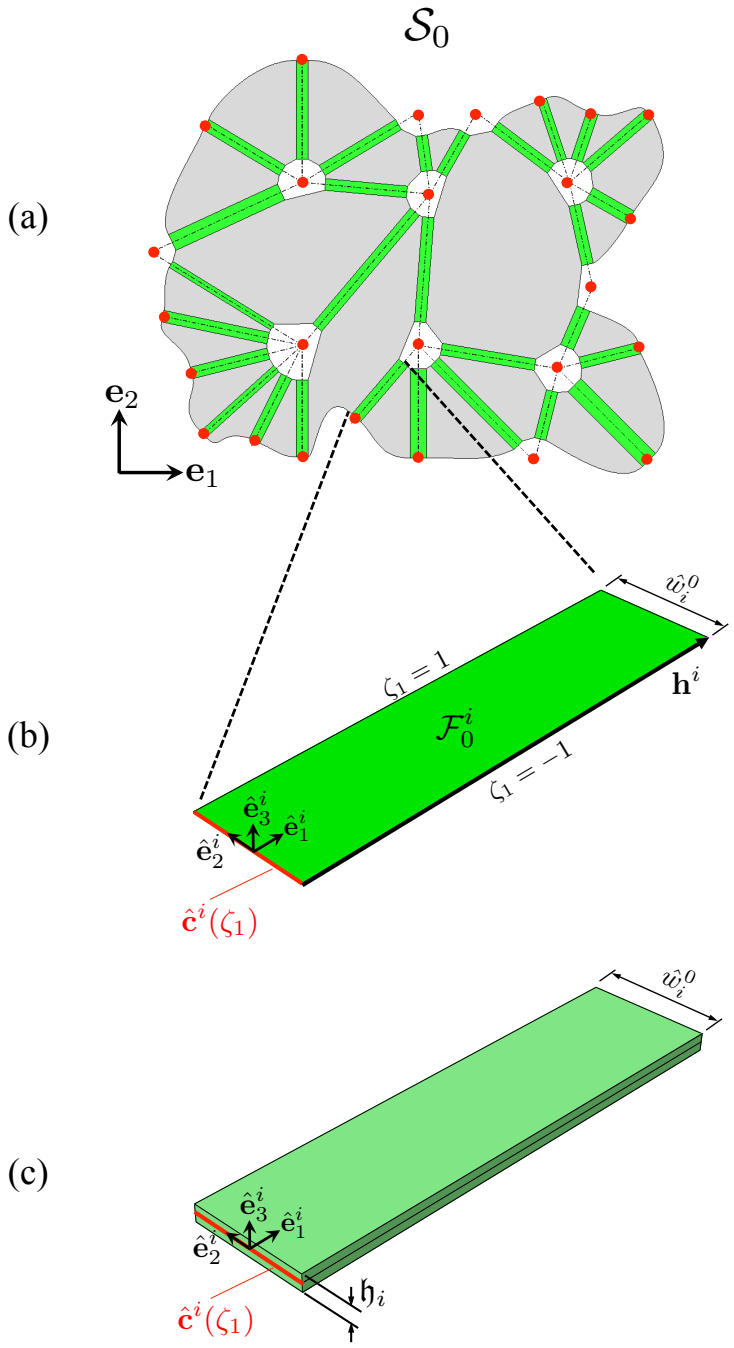

Figure 4.1: Plate structural representation of an origami structure of non-zero thickness (reference configuration shown): (a) Mid-surface of the structure corresponding to $\mathcal{S}_0$; (b) Smooth fold surface $\mathcal{F}_0^i$ corresponding to the mid-surface of the i^{th} smooth fold domain; (c) Continuum smooth fold domain having thickness $\mathfrak{h}_i$ and mid-surface $\mathcal{F}_0^i$.

In this work, only folds comprised of materials that exhibit relatively small strains ($\sim$5% or less) are considered. Therefore, the second-order linearized strain tensor $\boldsymbol{\varepsilon}$ is used as the measure for non-rigid deformation [439]. The tensorial components of any field quantity for each smooth fold domain are expressed in their associated coordinate system with basis $\{\hat{\mathbf{e}}_1^i, \hat{\mathbf{e}}_2^i, \hat{\mathbf{e}}_3^i\}$ (defined in Section 2.2.1) at the reference configuration (refer to Figures 4.1(b)–(c)). Making use of the *classical plate theory* [354], the only considered components of $\boldsymbol{\varepsilon}$ are assumed to linearly vary through the thickness of each smooth fold domain as follows [354]:

$$\begin{bmatrix} \varepsilon_{11} \\ \varepsilon_{22} \\ \varepsilon_{12} \end{bmatrix} = \begin{bmatrix} \varepsilon_{11_0} \\ \varepsilon_{22_0} \\ \varepsilon_{12_0} \end{bmatrix} - \zeta_3 \begin{bmatrix} \kappa_{11} \\ \kappa_{22} \\ \kappa_{12} \end{bmatrix}, \tag{4.2}$$

where ε_{mn_0} are the in-plane strains at the mid-surface, and κ_{mn} are the curvatures of the mid-surface. Thus, the strain field of the entire smooth fold domain of non-zero thickness depends only on the deformation of its mid-surface.

Reference and current configurations of the smooth fold surface ($\mathcal{F}_0^i$ and $\mathcal{F}_t^i$, respectively) associated with the i^{th} smooth fold domain are shown in Figure 4.2. It is stated in Section 2.2 that $\|\mathbf{h}^i\|$ is constant upon deformation and hence it is assumed that the normal strain along the 1-direction is 0. It is also noted that $\frac{\mathrm{d}\hat{\mathbf{c}}^i(\zeta_1)}{\mathrm{d}\zeta_1} \cdot \mathbf{h}^i = 0$ holds at any configuration and therefore the shear strain along the 12-plane is also assumed 0 everywhere in the smooth fold domain (refer to Definition 2.6). In summary:

$$\varepsilon_{11} = 0, \tag{4.3}$$

$$\varepsilon_{22} = \varepsilon_{22_0} - \zeta_3 \, \kappa_{22}, \tag{4.4}$$

$$\varepsilon_{12} = 0. \tag{4.5}$$

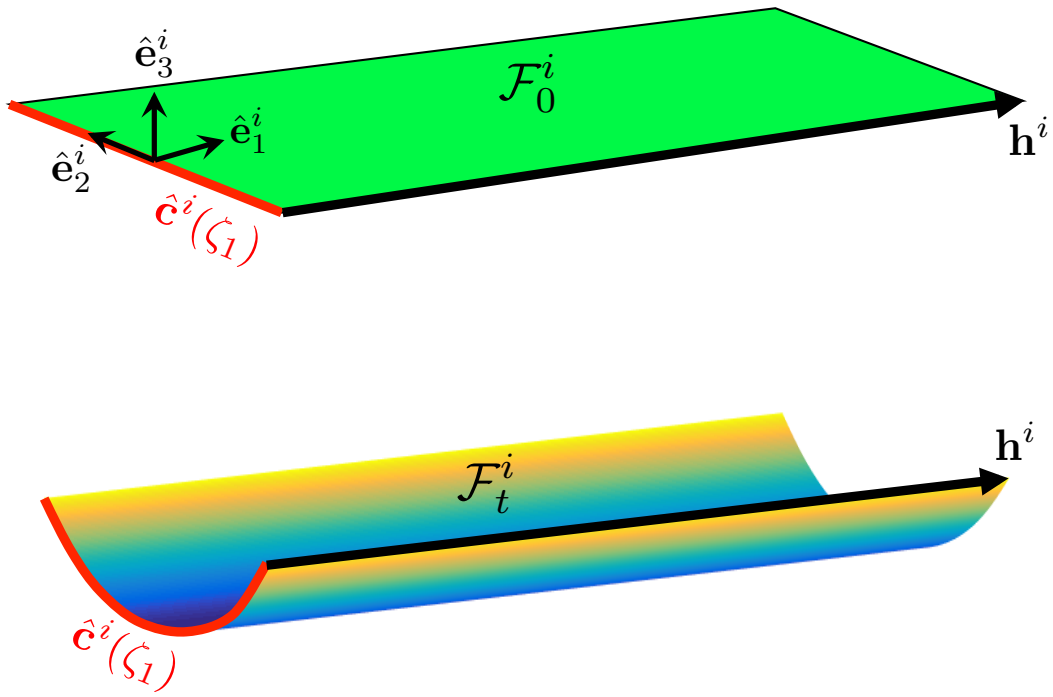

Figure 4.2: Reference and current configurations of a smooth fold surface ($\mathcal{F}_0^i$ and $\mathcal{F}_t^i$, respectively).

To simplify the notation, ε_{22}, ε_{22_0}, and κ_{22} are denoted as ε, ε_0, and κ, respectively. Following the approach presented in Section 2.2.5 to determine the shape of the smooth fold cross-section curve $\hat{\mathbf{c}}^i(\zeta_1)$, by making assumptions on the form of the extensibility field ε_0 and curvature field κ for each smooth fold, the shape of each

smooth fold is fully defined by its fold angle $\hat{\theta}_i$ and its arc-length $\hat{s}_i$. Therefore:

$$\varepsilon(\hat{\theta}_i, \hat{s}_i) = \varepsilon_0(\hat{\theta}_i, \hat{s}_i) - \zeta_3\, \kappa(\hat{\theta}_i, \hat{s}_i). \tag{4.6}$$

Thus, the strain components of every smooth fold domain expressed in their associated coordinate system with basis $\{\hat{\mathbf{e}}_1^i, \hat{\mathbf{e}}_2^i, \hat{\mathbf{e}}_3^i\}$ are given as follows:

$$\begin{aligned} \begin{bmatrix} \varepsilon_{11} \\ \varepsilon_{22} \\ \varepsilon_{12} \end{bmatrix} &= \begin{bmatrix} 0 \\ \varepsilon(\hat{\theta}_i, \hat{s}_i) \\ 0 \end{bmatrix} \\ &= \begin{bmatrix} 0 \\ \varepsilon_0(\hat{\theta}_i, \hat{s}_i) - \zeta_3\, \kappa(\hat{\theta}_i, \hat{s}_i) \\ 0 \end{bmatrix}. \end{aligned} \tag{4.7}$$

Although not explicitly stated, it is noted that ε_0 and κ are fields that in general may vary along the ζ_1 coordinate of the smooth fold. The derivatives of the strain $\varepsilon(\hat{\theta}_i, \hat{s}_i)$ with respect to $\hat{\theta}_i$ and $\hat{s}_i$ are utilized later in this section and they are simply given as follows:

$$\frac{\partial \varepsilon(\hat{\theta}_i, \hat{s}_i)}{\partial \hat{\theta}_i} = \frac{\partial \varepsilon_0(\hat{\theta}_i, \hat{s}_i)}{\partial \hat{\theta}_i} - \zeta_3\, \frac{\partial \kappa(\hat{\theta}_i, \hat{s}_i)}{\partial \hat{\theta}_i}, \tag{4.8}$$

$$\frac{\partial \varepsilon(\hat{\theta}_i, \hat{s}_i)}{\partial \hat{s}_i} = \frac{\partial \varepsilon_0(\hat{\theta}_i, \hat{s}_i)}{\partial \hat{s}_i} - \zeta_3\, \frac{\partial \kappa(\hat{\theta}_i, \hat{s}_i)}{\partial \hat{s}_i}. \tag{4.9}$$

The mid-surface strain and curvature fields $\varepsilon_0(\hat{\theta}_i, \hat{s}_i)$ and $\kappa(\hat{\theta}_i, \hat{s}_i)$ must satisfy the continuity conditions of the assumed order of geometry continuity of the smooth folds. Additionally, the following kinematic relations hold for any fields $\varepsilon_0(\hat{\theta}_i, \hat{s}_i)$ and

$\kappa(\hat{\theta}_i, \hat{s}_i)$ regardless of the order of geometry continuity:

$$\hat{s}_i - \hat{w}_i^0 = \int_{-\frac{\hat{w}_i^0}{2}}^{\frac{\hat{w}_i^0}{2}} \varepsilon_0 \, \mathrm{d}s, \tag{4.10}$$

$$\hat{\theta}_i = \int_{-\frac{\hat{w}_i^0}{2}}^{\frac{\hat{w}_i^0}{2}} \kappa \, \mathrm{d}s. \tag{4.11}$$

The continuity conditions for smooth folds exhibiting G^1 and G^2 continuity are provided in Section 2.2.1. For smooth folds exhibiting G^1 continuity, the mid-surface strain and curvature fields ($\varepsilon_0(\hat{\theta}_i, \hat{s}_i)$ and $\kappa(\hat{\theta}_i, \hat{s}_i)$, respectively) are assumed uniform throughout the fold. Also, for smooth folds exhibiting G^2 continuity, $\varepsilon_0(\hat{\theta}_i, \hat{s}_i)$ and $\kappa(\hat{\theta}_i, \hat{s}_i)$ are assumed to have a quadratic form with respect to the arc-length of $\hat{\mathbf{c}}^i(\zeta_1)$ (refer to Figure 2.7). Such a quadratic form allows for the satisfaction of the conditions for G^2 continuity (i.e. zero curvature at the ends of the curve $\hat{\mathbf{c}}^i(\zeta_1)$). Making use of the relations provided in Equations (4.10) and (4.11), the following expressions for $\varepsilon_0(\hat{\theta}_i, \hat{s}_i)$ and $\kappa(\hat{\theta}_i, \hat{s}_i)$ are obtained for smooth folds exhibiting G^1 continuity:

$$\varepsilon_0(\hat{\theta}_i, \hat{s}_i) = \frac{\hat{s}_i - \hat{w}_i^0}{\hat{w}_i^0}, \tag{4.12}$$

$$\kappa(\hat{\theta}_i, \hat{s}_i) = \frac{\hat{\theta}_i}{\hat{w}_i^0}, \tag{4.13}$$

and the following expressions for $\varepsilon_0(\hat{\theta}_i, \hat{s}_i)$ and $\kappa(\hat{\theta}_i, \hat{s}_i)$ are obtained for smooth folds exhibiting G^2 continuity:

$$\varepsilon_0(\hat{\theta}_i, \hat{s}_i) = \frac{3}{2} \frac{(\hat{s}_i - \hat{w}_i^0)((\hat{w}_i^0)^2 - 4s^2)}{(\hat{w}_i^0)^3}, \tag{4.14}$$

$$\kappa(\hat{\theta}_i, \hat{s}_i) = \frac{3}{2}\frac{\hat{\theta}_i((\hat{w}_i^0)^2 - 4s^2)}{(\hat{w}_i^0)^3}, \tag{4.15}$$

where $s \in \left[-\frac{\hat{s}_i}{2}, \frac{\hat{s}_i}{2}\right]$ is the arc-length coordinate of the curve $\hat{\mathbf{c}}^i(\zeta_1)$ defined in Equation (2.23). It is remarked that $\hat{s}_i = \hat{w}_i^0$ at the reference configuration $\mathcal{S}_0$. It is straightforward to show that the mid-surface strain and curvature fields in Equations (4.12)–(4.15) satisfy the relations provided in Equations (4.10) and (4.11).

4.2 Modeling Approach

In this section, the governing field equations used to determine the mechanical response of origami continuum bodies with smooth fold domains are briefly reviewed. Such field equations arise from the law of *conservation of linear momentum* and the law of *conservation of angular momentum* [439, 440]. Since linearized strains are assumed in this work, no specific distinction between reference and current configurations is considered in this section to simplify the notation. The boundary value problem and modeling approaches for the structural mechanics of continuum bodies considered in this work are presented afterwards. This section is intended as a review of such conservation laws and structural modeling approaches. For detailed information on these topics, the reader is referred to [351, 439, 440, 441].

4.2.1 Governing Equations

In order to model the mechanical response of origami structures with smooth fold domains, the law of conservation of linear momentum and the law of conservation of angular momentum must be considered [4]. The law of *conservation of linear momentum* states that the time rate of change of linear momentum of a continuum body is equal to the sum of the surface and body forces applied to it [4]. The integral

form of the conservation of linear momentum is given as follows [4]:

$$\frac{D}{Dt}\left(\int_{\Omega}\rho\mathbf{v}\,\mathrm{d}v\right)=\int_{\Omega}\mathbf{b}\,\mathrm{d}v\,+\int_{\partial\Omega}\mathbf{t}\,\mathrm{d}a, \tag{4.16}$$

where Ω is the region occupied by the material body, $\partial\Omega$ is the boundary of Ω, $\frac{D}{Dt}$ denotes the material time derivative, ρ is the mass density of a material point, $\mathbf{v}$ is the velocity vector of a material point, $\mathbf{b}$ is the body force vector, and $\mathbf{t}$ is the surface traction vector. The pointwise form of the conservation of linear momentum is given as follows [4]:

$$\nabla\cdot\boldsymbol{\sigma}+\mathbf{b}=\rho\dot{\mathbf{v}}, \tag{4.17}$$

where $\boldsymbol{\sigma}$ is the second-order Cauchy stress tensor and $\nabla\cdot\boldsymbol{\sigma}$ denotes the divergence of $\boldsymbol{\sigma}$ [351]. The acceleration of the material point is denoted as $\dot{\mathbf{v}}$ where $(\dot{})$ represents the material time derivative operation. *Quasi-static* deformation is assumed in this work. The pointwise form of the conservation of linear momentum provided in Equation (4.17) for the case of quasi-static deformation is given as follows:

$$\nabla\cdot\boldsymbol{\sigma}+\mathbf{b}=\mathbf{0}_3. \tag{4.18}$$

The law of *conservation of angular momentum* states that the time rate of change of angular momentum of a continuum body is equal to the sum of the moments applied by surface and body forces in addition to body couples [4]. If there are no body couples, as in all the examples considered in this work, the integral form of the conservation of angular momentum is given as follows [4]:

$$\frac{D}{Dt}\left(\int_{\Omega}\mathbf{X}\times\rho\mathbf{v}\,\mathrm{d}v\right)=\int_{\Omega}\mathbf{X}\times\mathbf{b}\,\mathrm{d}v\,+\int_{\partial\Omega}\mathbf{X}\times\mathbf{t}\,\mathrm{d}a, \tag{4.19}$$

where $\mathbf{X}$ is the position vector of a material point. The pointwise form of the conservation of angular momentum states that the second-order Cauchy stress tensor is symmetric:

$$\boldsymbol{\sigma} = \boldsymbol{\sigma}^{\top}. \tag{4.20}$$

Only governing equations arising from conservation of linear and angular momentum are taken into account in the model presented in this section. Even though structures comprised of materials exhibiting thermomechanical coupling (e.g. SMAs) are considered herein, the introduced field variables such as temperature T are taken as given and thus conservation of energy [4] is not considered within the governing equations.

4.2.2 Boundary Value Problem

In the problems addressed in this section, the objective is to determine the quasi-static deformation of origami bodies with smooth folds subject to certain boundary conditions. First, let the boundary of Ω be partitioned into the boundaries $\partial\Omega_u$ and $\partial\Omega_\sigma$ such that:

$$\partial\Omega_u \cup \partial\Omega_\sigma = \partial\Omega, \tag{4.21}$$

$$\partial\Omega_u \cap \partial\Omega_\sigma = \varnothing, \tag{4.22}$$

where $\partial\Omega_u$ is the boundary of the region occupied by the material body where displacement boundary conditions are applied, $\partial\Omega_\sigma$ is the boundary of the region occupied by the material body where traction boundary conditions are applied, and $\varnothing$ denotes an empty set.

The boundary value problem statement applicable to all the problems considered in this section is given as follows:

$$\begin{aligned}
&\text{Find} && \mathbf{u} && \forall\, \mathbf{X} \in \Omega, \quad t \geq 0 \\
&\text{Subject to} && \nabla \cdot \boldsymbol{\sigma} + \mathbf{b} = \mathbf{0}_3, && \forall\, \mathbf{X} \in \Omega, \quad t \geq 0 \\
& && \mathbf{u} = \bar{\mathbf{u}}, && \forall\, \mathbf{X} \in \partial\Omega_u, \quad t \geq 0 \\
& && \boldsymbol{\sigma}\mathbf{n} = \bar{\mathbf{t}}, && \forall\, \mathbf{X} \in \partial\Omega_\sigma, \quad t \geq 0 \\
& && \Xi = \bar{\Xi}, && \forall\, \mathbf{X} \in \Omega, \quad t \geq 0,
\end{aligned} \tag{4.23}$$

where $\bar{\mathbf{u}}$ is the vector field of applied boundary displacements, $\bar{\mathbf{t}}$ is the vector field of applied boundary tractions, $\mathbf{n}$ is the boundary unit normal vector, Ξ represents other physical fields in the material body (e.g. the absolute temperature field), and $\bar{\Xi}$ represents other physical field variables imposed in the material body (e.g. the applied absolute temperature field).

The governing field equation of the boundary value problem in Equation (4.23) arises from conservation of linear momentum (cf. Equation (4.18)). The other conditions stated in Equation (4.23) correspond to the *boundary conditions* of the problem. These boundary conditions appear in the form of applied boundary displacements $\bar{\mathbf{u}}$ or applied boundary tractions $\bar{\mathbf{t}}$, and applied field variables $\bar{\Xi}$. Although not stated explicitly in Equation (4.23), it is assumed beforehand that the second-order Cauchy stress tensor $\boldsymbol{\sigma}$ is symmetric to satisfy conservation of angular momentum (Equation (4.20)).

4.2.3 Structural Modeling Approach

Variational approaches are powerful tools for the development of exact or approximate solutions to problems in structural mechanics of continuum bodies [351, 440] (e.g. FEA). A variational approach is employed herein to determine approximate solutions for the deformation of origami structures with smooth fold domains.

The *principle of virtual work* states that a continuum body is in mechanical equilibrium (i.e. the field equation and boundary conditions in Equation (4.23) are satisfied) if and only if the virtual work of all forces, internal and external, acting on the body is zero given a virtual displacement [351]:

$$\delta W = \delta W_I - \delta W_E = 0, \tag{4.24}$$

where δW represents the virtual work of all internal and external forces given a virtual displacement, δW_I is the virtual work of all internal forces given a virtual displacement, and δW_E is the virtual work of all external forces given a virtual displacement. Their formulation is as follows[2]:

$$\delta W_I = \int_\Omega \boldsymbol{\sigma} : \delta\boldsymbol{\varepsilon} \, \mathrm{d}v, \tag{4.25}$$

$$\delta W_E = \int_\Omega \mathbf{b} \cdot \delta\mathbf{u} \, \mathrm{d}v \; + \int_{\partial\Omega} \mathbf{t} \cdot \delta\mathbf{u} \, \mathrm{d}a, \tag{4.26}$$

where $\delta\mathbf{u}$ is the *virtual displacement* and $\delta\boldsymbol{\varepsilon}$ is the virtual strain increment due to

[2] $(\cdot : \cdot)$ denotes the inner product of two second-order tensors. If such tensors are expressed in an orthonormal coordinate system, their inner product is given as $\mathbf{Y} : \mathbf{Z} = \sum_{m=1}^{3} \sum_{n=1}^{3} Y_{mn} Z_{mn}$.

the virtual displacement:

$$\delta\boldsymbol{\varepsilon} = \frac{1}{2}\Big(\nabla(\delta\mathbf{u}) + \nabla(\delta\mathbf{u})^{\top}\Big), \tag{4.27}$$

and $\nabla(\delta\mathbf{u})$ denotes the gradient of $\delta\mathbf{u}$. The virtual displacements are null on the boundary $\partial\Omega_u$ where displacements are applied through boundary conditions:

$$\delta\mathbf{u} = \mathbf{0}_3 \qquad \forall\, \mathbf{X} \in \partial\Omega_u. \tag{4.28}$$

To show that the principle of virtual work is equivalent to the boundary value problem statement in Equation (4.23), the following is first considered by taking into account Equations (4.25)–(4.28):

$$\begin{aligned} 0 &= \delta W \\ &= \delta W_I - \delta W_E \\ &= \int_\Omega \boldsymbol{\sigma} : \delta\boldsymbol{\varepsilon}\, \mathrm{d}v \; - \int_\Omega \mathbf{b}\cdot\delta\mathbf{u}\, \mathrm{d}v \; - \int_{\partial\Omega} \mathbf{t}\cdot\delta\mathbf{u}\, \mathrm{d}a \\ &= \int_\Omega \boldsymbol{\sigma} : \delta\boldsymbol{\varepsilon}\, \mathrm{d}v \; - \int_\Omega \mathbf{b}\cdot\delta\mathbf{u}\, \mathrm{d}v \; - \int_{\partial\Omega_\sigma} \bar{\mathbf{t}}\cdot\delta\mathbf{u}\, \mathrm{d}a. \end{aligned} \tag{4.29}$$

The following is then obtained by considering the relation between stress and traction vector $\mathbf{t} = \boldsymbol{\sigma}\mathbf{n}$ and the symmetry of the Cauchy stress tensor due to conser-

vation of angular momentum:

$$\begin{aligned} \bar{\mathbf{t}} \cdot \delta\mathbf{u} &= (\boldsymbol{\sigma}\mathbf{n}) \cdot \delta\mathbf{u} \\ &= (\boldsymbol{\sigma}^{\top}\delta\mathbf{u}) \cdot \mathbf{n} \\ &= (\boldsymbol{\sigma}\delta\mathbf{u}) \cdot \mathbf{n}. \end{aligned} \tag{4.30}$$

After substituting Equation (4.30) into Equation (4.29) and then using the divergence theorem, the following is obtained:

$$\begin{aligned} 0 &= \int_{\Omega} \boldsymbol{\sigma} : \delta\boldsymbol{\varepsilon} \, \mathrm{d}v - \int_{\Omega} \mathbf{b} \cdot \delta\mathbf{u} \, \mathrm{d}v - \int_{\partial\Omega_{\sigma}} (\boldsymbol{\sigma}\delta\mathbf{u}) \cdot \mathbf{n} \, \mathrm{d}a \\ &= \int_{\Omega} \boldsymbol{\sigma} : \delta\boldsymbol{\varepsilon} \, \mathrm{d}v - \int_{\Omega} \mathbf{b} \cdot \delta\mathbf{u} \, \mathrm{d}v - \int_{\Omega} \nabla \cdot (\boldsymbol{\sigma}\delta\mathbf{u}) \, \mathrm{d}v \\ &= \int_{\Omega} \Big(\boldsymbol{\sigma} : \delta\boldsymbol{\varepsilon} - \mathbf{b} \cdot \delta\mathbf{u} - \nabla \cdot (\boldsymbol{\sigma}\delta\mathbf{u}) \Big) \mathrm{d}v. \end{aligned} \tag{4.31}$$

Considering Equation (4.27) and the symmetry of $\boldsymbol{\sigma}$, the following is finally determined:

$$\begin{aligned} 0 &= \int_{\Omega} \Big(\boldsymbol{\sigma} : \delta\boldsymbol{\varepsilon} - \mathbf{b} \cdot \delta\mathbf{u} - \boldsymbol{\sigma} : \nabla(\delta\mathbf{u}) - (\nabla \cdot \boldsymbol{\sigma}) \cdot \delta\mathbf{u} \Big) \mathrm{d}v \\ &= \int_{\Omega} \Big(\boldsymbol{\sigma} : \delta\boldsymbol{\varepsilon} - \mathbf{b} \cdot \delta\mathbf{u} - \boldsymbol{\sigma} : \delta\boldsymbol{\varepsilon} - (\nabla \cdot \boldsymbol{\sigma}) \cdot \delta\mathbf{u} \Big) \mathrm{d}v \\ &= \int_{\Omega} \Big(- (\nabla \cdot \boldsymbol{\sigma} + \mathbf{b}) \cdot \delta\mathbf{u} \Big) \mathrm{d}v, \end{aligned} \tag{4.32}$$

cf. Equation (4.23). Thus, the principle of virtual work is equivalent to the boundary value problem statement presented in Equation (4.23). Such a principle is utilized in the following sections to determine approximate solutions for origami bodies having

smooth fold domains of non-zero thickness. It is noted that the principle of virtual work in Equation (4.24) does not consider any assumptions on the constitutive behavior of the material(s) comprising the continuum body. Therefore, it is applicable to any continuum body having arbitrary constitutive behavior [351] so long as strains are small enough such that the linearized strain tensor can be utilized to properly model the deformation. The principle of virtual work is utilized in the following section for the modeling of origami structures having smooth folds comprised of arbitrary materials.

4.3 Structural Mechanics Model Formulation

4.3.1 Model Development

The principle of virtual work described in the previous section is utilized here to develop a model for the structural mechanics of origami structures with smooth fold domains comprised of arbitrary materials.

The plate kinematics addressed in Section 4.1 lead to a displacement field defined by the deformation of the mid-surface of the origami body. Such a mid-surface corresponds to the origami sheet surface addressed in the kinematic model for origami with smooth folds developed in Section 2. The configuration of such an origami sheet is fully defined by the fold angles and fold arc-lengths of every smooth fold in the sheet. Therefore, the displacement field $\mathbf{u}(\mathbf{X})$ of an origami structure with smooth fold domains is a function of $\hat{\theta}_i$ and $\hat{s}_i$, $i = 1, \ldots, N_{\mathcal{F}}$. The vector $\hat{\boldsymbol{\theta}} \in \mathbb{R}^{N_{\mathcal{F}}}$ constructed by collecting the fold angles $\hat{\theta}_i$, $i = 1, \ldots, N_{\mathcal{F}}$, is defined in Equation (2.1). Likewise, the vector $\hat{\mathbf{s}} \in \mathbb{R}^{N_{\mathcal{F}}}$ is constructed by collecting the fold arc-lengths

$\hat{s}_i$, $i = 1, \ldots, N_{\mathcal{F}}$, as follows:

$$\hat{\mathbf{s}} = \begin{bmatrix} \hat{s}_1 \\ \vdots \\ \hat{s}_{N_{\mathcal{F}}} \end{bmatrix}. \tag{4.33}$$

It is assumed in the kinematic model presented in Section 2 that one face in the sheet is fixed in space (refer to Section 2.2.4). Therefore, the only displacement boundary condition considered in this work is that the displacement vector is equal to the zero vector at one face in the sheet.

The virtual displacement and the virtual strain, encountered in the formulation of the principle of virtual work (refer to Equations (4.25) and (4.26)), are related to virtual changes in fold angles and fold arc-lengths as follows:

$$\delta\mathbf{u} = \frac{\partial \mathbf{u}}{\partial \hat{\boldsymbol{\theta}}} \cdot \delta\hat{\boldsymbol{\theta}} + \frac{\partial \mathbf{u}}{\partial \hat{\mathbf{s}}} \cdot \delta\hat{\mathbf{s}}, \tag{4.34}$$

$$\delta\boldsymbol{\varepsilon} = \frac{\partial \boldsymbol{\varepsilon}}{\partial \hat{\boldsymbol{\theta}}} \cdot \delta\hat{\boldsymbol{\theta}} + \frac{\partial \boldsymbol{\varepsilon}}{\partial \hat{\mathbf{s}}} \cdot \delta\hat{\mathbf{s}}. \tag{4.35}$$

Since the configuration of an origami material body is defined by the fold angles and fold arc-lengths of each smooth fold, the kinematic constraints in Equation (2.97) allowing for valid configurations must be considered. The principle of virtual work as stated in Equation (4.24) does not take into consideration any kinematic constraints. Kinematic constraints are conventionally included through the method of Lagrange multipliers or penalty methods [351, 440]. A penalty method approach is utilized here. Consequently, let $\mathfrak{L}$ be a penalty function associated with the kinematic

constraints from Equation (2.97):

$$\begin{aligned}\mathfrak{L}(\hat{\boldsymbol{\theta}},\hat{\mathbf{s}}) = \;& \lambda_R \sum_{i=1}^{N_{\mathcal{I}}} \left(\left(R^i_{23}(\hat{\boldsymbol{\theta}}) \right)^2 + \left(R^i_{31}(\hat{\boldsymbol{\theta}}) \right)^2 + \left(R^i_{12}(\hat{\boldsymbol{\theta}}) \right)^2 \right) \\ & + \lambda_d \sum_{i=1}^{N_{\mathcal{I}}} \left(\left(d^i_1(\hat{\boldsymbol{\theta}},\hat{\mathbf{s}}) \right)^2 + \left(d^i_2(\hat{\boldsymbol{\theta}},\hat{\mathbf{s}}) \right)^2 + \left(d^i_3(\hat{\boldsymbol{\theta}},\hat{\mathbf{s}}) \right)^2 \right),\end{aligned} \tag{4.36}$$

where λ_R is the penalty scalar for rotational constraints and λ_d is the penalty scalar for translational constraints. The modified principle of virtual work statement allowing for the consideration of kinematic constraints is then given as follows:

$$\delta W_I - \delta W_E + \delta \mathfrak{L} = 0, \tag{4.37}$$

cf. Equation (4.24). By substituting Equation (4.35) into the expression for δW_I in Equation (4.25), the following is obtained:

$$\begin{aligned}\delta W_I &= \int_\Omega \boldsymbol{\sigma} : \delta\boldsymbol{\varepsilon} \, \mathrm{d}v \\ &= \int_\Omega \boldsymbol{\sigma} : \left(\frac{\partial \boldsymbol{\varepsilon}}{\partial \hat{\boldsymbol{\theta}}} \cdot \delta\hat{\boldsymbol{\theta}} + \frac{\partial \boldsymbol{\varepsilon}}{\partial \hat{\mathbf{s}}} \cdot \delta\hat{\mathbf{s}} \right) \mathrm{d}v.\end{aligned} \tag{4.38}$$

The expression for δW_I provided in Equation (4.38) can be decomposed into the contributions of each smooth fold domain in the origami body:

$$\delta W_I = \sum_{i=1}^{N_{\mathcal{F}}} \int_{\mathfrak{F}^i} \sigma \left(\frac{\partial \varepsilon}{\partial \hat{\theta}_i} \delta\hat{\theta}_i + \frac{\partial \varepsilon}{\partial \hat{s}_i} \delta\hat{s}_i \right) \mathrm{d}v, \tag{4.39}$$

where $\sigma = \sigma_{22}$ in the fold coordinate system of the i^{th} smooth fold domain and $\mathfrak{F}^i$ is the region occupied by the i^{th} smooth fold domain. Performing integration over the

thickness in the expression presented in Equation (4.39), the following is obtained:

$$\delta W_I = \sum_{i=1}^{N_{\mathcal{F}}} \int_{\mathcal{F}_i} \left(\left(N \frac{\partial \varepsilon_0}{\partial \hat{\theta}_i} - M \frac{\partial \kappa}{\partial \hat{\theta}_i} \right) \delta \hat{\theta}_i + \left(N \frac{\partial \varepsilon_0}{\partial \hat{s}_i} - M \frac{\partial \kappa}{\partial \hat{s}_i} \right) \delta \hat{s}_i \right) \mathrm{d}a, \tag{4.40}$$

where N and M are respectively the axial force and moment resultants given as follows [354]:

$$N = \int_{-\frac{\mathfrak{h}_i}{2}}^{\frac{\mathfrak{h}_i}{2}} \sigma \, \mathrm{d}\zeta_3, \tag{4.41}$$

$$M = \int_{-\frac{\mathfrak{h}_i}{2}}^{\frac{\mathfrak{h}_i}{2}} \zeta_3 \sigma \, \mathrm{d}\zeta_3. \tag{4.42}$$

By substituting Equation (4.35) into the expression for δW_E in Equation (4.26), the following is obtained:

$$\begin{aligned}
\delta W_E &= \int_\Omega \mathbf{b} \cdot \delta \mathbf{u} \, \mathrm{d}v + \int_{\partial\Omega} \mathbf{t} \cdot \delta \mathbf{u} \, \mathrm{d}a \\
&= \int_\Omega \mathbf{b} \cdot \left(\frac{\partial \mathbf{u}}{\partial \hat{\boldsymbol{\theta}}} \cdot \delta \hat{\boldsymbol{\theta}} + \frac{\partial \mathbf{u}}{\partial \hat{\mathbf{s}}} \cdot \delta \hat{\mathbf{s}} \right) \mathrm{d}v + \int_{\partial\Omega} \mathbf{t} \cdot \left(\frac{\partial \mathbf{u}}{\partial \hat{\boldsymbol{\theta}}} \cdot \delta \hat{\boldsymbol{\theta}} + \frac{\partial \mathbf{u}}{\partial \hat{\mathbf{s}}} \cdot \delta \hat{\mathbf{s}} \right) \mathrm{d}a \\
&= \int_\Omega \mathbf{b} \cdot \sum_{i=1}^{N_{\mathcal{F}}} \left(\frac{\partial \mathbf{u}}{\partial \hat{\theta}_i} \delta \hat{\theta}_i + \frac{\partial \mathbf{u}}{\partial \hat{s}_i} \delta \hat{s}_i \right) \mathrm{d}v + \int_{\partial\Omega} \mathbf{t} \cdot \sum_{i=1}^{N_{\mathcal{F}}} \left(\frac{\partial \mathbf{u}}{\partial \hat{\theta}_i} \delta \hat{\theta}_i + \frac{\partial \mathbf{u}}{\partial \hat{s}_i} \delta \hat{s}_i \right) \mathrm{d}a,
\end{aligned} \tag{4.43}$$

where the displacement $\mathbf{u}$ as a function of fold angles and fold arc-lengths can be determined using the folding map formulation provided in Section 2.2.4.

Similarly, the virtual increment in the penalty function $\mathfrak{L}$ defined in Equation

(4.36) can be expressed as follows:

$$\begin{aligned}\delta\mathfrak{L} &= \frac{\partial\mathfrak{L}}{\partial\hat{\boldsymbol{\theta}}}\cdot\delta\hat{\boldsymbol{\theta}} + \frac{\partial\mathfrak{L}}{\partial\hat{\mathbf{s}}}\cdot\delta\hat{\mathbf{s}} \\ &= \sum_{i=1}^{N_{\mathcal{F}}}\left(\frac{\partial\mathfrak{L}}{\partial\hat{\theta}_i}\delta\hat{\theta}_i + \frac{\partial\mathfrak{L}}{\partial\hat{s}_i}\delta\hat{s}_i\right).\end{aligned} \tag{4.44}$$

Substituting the expressions for δW_I, δW_E, and $\delta\mathfrak{L}$ provided in Equations (4.40), (4.43), and (4.44), respectively, into Equation (4.37), the following is obtained:

$$\begin{aligned}0 &= \delta W_I - \delta W_E + \delta\mathfrak{L} \\ &= \sum_{i=1}^{N_{\mathcal{F}}}\int_{\mathcal{F}_i}\left(\left(N\frac{\partial\varepsilon_0}{\partial\hat{\theta}_i} - M\frac{\partial\kappa}{\partial\hat{\theta}_i}\right)\delta\hat{\theta}_i + \left(N\frac{\partial\varepsilon_0}{\partial\hat{s}_i} - M\frac{\partial\kappa}{\partial\hat{s}_i}\right)\delta\hat{s}_i\right)\mathrm{d}a \\ &\quad - \int_\Omega \mathbf{b}\cdot\sum_{i=1}^{N_{\mathcal{F}}}\left(\frac{\partial\mathbf{u}}{\partial\hat{\theta}_i}\delta\hat{\theta}_i + \frac{\partial\mathbf{u}}{\partial\hat{s}_i}\delta\hat{s}_i\right)\mathrm{d}v - \int_{\partial\Omega}\mathbf{t}\cdot\sum_{i=1}^{N_{\mathcal{F}}}\left(\frac{\partial\mathbf{u}}{\partial\hat{\theta}_i}\delta\hat{\theta}_i + \frac{\partial\mathbf{u}}{\partial\hat{s}_i}\delta\hat{s}_i\right)\mathrm{d}a \\ &\quad + \sum_{i=1}^{N_{\mathcal{F}}}\left(\frac{\partial\mathfrak{L}}{\partial\hat{\theta}_i}\delta\hat{\theta}_i + \frac{\partial\mathfrak{L}}{\partial\hat{s}_i}\delta\hat{s}_i\right).\end{aligned} \tag{4.45}$$

4.3.2 Constitutive Equations

Linear elastic and SMA materials are considered in this work. For a linear elastic material, stress is related to strain via Hooke's law [439]:

$$\boldsymbol{\sigma} = \boldsymbol{C}\boldsymbol{\varepsilon}, \tag{4.46}$$

where $\boldsymbol{C}$ is the fourth-order stiffness tensor. For the plane stress assumptions made

in classical plate theory, only the following stress components are considered [354]:

$$\begin{bmatrix} \sigma_{11} \\ \sigma_{22} \\ \sigma_{12} \end{bmatrix} = \frac{E}{1-\nu^2} \begin{bmatrix} 1 & \nu & 0 \\ \nu & 1 & 0 \\ 0 & 0 & 1-\nu \end{bmatrix} \begin{bmatrix} \varepsilon_{11} \\ \varepsilon_{22} \\ \varepsilon_{12} \end{bmatrix}, \tag{4.47}$$

where E is the Young's modulus and ν is the Poisson's ratio of the linear elastic material (assumed isotropic). By substituting the expressions for strain in Equation (4.7) into Equation (4.47), the following is obtained:

$$\begin{aligned} \begin{bmatrix} \sigma_{11} \\ \sigma_{22} \\ \sigma_{12} \end{bmatrix} &= \frac{E}{1-\nu^2} \begin{bmatrix} 1 & \nu & 0 \\ \nu & 1 & 0 \\ 0 & 0 & 1-\nu \end{bmatrix} \begin{bmatrix} 0 \\ \varepsilon(\hat{\theta}_i, \hat{s}_i) \\ 0 \end{bmatrix} \\ &= \frac{E}{1-\nu^2} \begin{bmatrix} 1 & \nu & 0 \\ \nu & 1 & 0 \\ 0 & 0 & 1-\nu \end{bmatrix} \begin{bmatrix} 0 \\ \varepsilon_0(\hat{\theta}_i, \hat{s}_i) - \zeta_3 \, \kappa(\hat{\theta}_i, \hat{s}_i) \\ 0 \end{bmatrix}. \end{aligned} \tag{4.48}$$

As described in Section 1, SMAs are active materials that undergo solid-to-solid martensitic phase transformations induced by temperature and/or stress stimuli during which they can generate or recover seemingly permanent strains [4]. These characteristics allow SMAs to have multiple applications in various fields such as aerospace [125] and others [214]. Shape memory alloys exhibit the highest actuation energy density of all conventionally used active materials [4]. Therefore, SMAs can provide a significant amount of strain under large stresses, a characteristic of great utility in morphing structures for use in realistic conditions such as the origami

structures studied herein.

The detailed description of the constitutive model for monolithic SMAs used here is provided in [442]. It has been used to analyze a broad range of smart structures having SMA components [443, 444, 445, 446, 447]. The model is three-dimensional, thermodynamically consistent, and phenomenological. The internal state variables associated with the inelastic transformation process of SMAs are the martensite volume fraction ξ and the second-order transformation strain tensor $\boldsymbol{\varepsilon}^t$. Assuming a reference state in which the stress and total strain are zero but the transformation strain is not, the stress is given as follows:

$$\boldsymbol{\sigma} = \boldsymbol{C}(\xi)\left(\boldsymbol{\varepsilon} - \boldsymbol{\alpha}(T - T_0) - \boldsymbol{\varepsilon}^t + \boldsymbol{\varepsilon}^{t0}\right), \tag{4.49}$$

where $\boldsymbol{\alpha}$ is the second-order tensor of thermoelastic coefficients, T_0 is the reference temperature, and $\boldsymbol{\varepsilon}^{t0}$ is second-order tensor of pre-strains. The effective fourth-order stiffness tensor $\boldsymbol{C}(\xi)$ is determined follows:

$$\boldsymbol{C}(\xi)^{-1} = \boldsymbol{S}(\xi) = \boldsymbol{S}^A + \xi(\boldsymbol{S}^M - \boldsymbol{S}^A). \tag{4.50}$$

where $\boldsymbol{S}^A$ is the compliance tensor of austenite and $\boldsymbol{S}^M$ and is the compliance tensor of martensite. The following relation between the rates of $\boldsymbol{\varepsilon}^t$ and ξ is assumed [442]:

$$\dot{\boldsymbol{\varepsilon}}^t = \boldsymbol{\Lambda}^t \dot{\xi}, \tag{4.51}$$

where:

$$\boldsymbol{\Lambda}^t = \begin{cases} \boldsymbol{\Lambda}^t_{fwd}; & \dot{\xi} > 0 \\ \boldsymbol{\Lambda}^t_{rev}; & \dot{\xi} < 0 \end{cases}. \tag{4.52}$$

In the above relation, $\mathbf{\Lambda}^t$ is the second-order transformation direction tensor and its expression for forward transformation and reverse transformation are given as follows:

$$\mathbf{\Lambda}^t_{fwd} = \frac{3}{2} H^{cur} \frac{\boldsymbol{\sigma}'}{\bar{\sigma}}, \tag{4.53}$$

$$\mathbf{\Lambda}^t_{rev} = \frac{\boldsymbol{\varepsilon}^{t-r}}{\xi^r}, \tag{4.54}$$

where $\boldsymbol{\sigma}'$ is the second-order deviatoric stress tensor, $\bar{\sigma}$ is the von Mises stress, $\boldsymbol{\varepsilon}^{t-r}$ is the transformation strain at the cessation of forward transformation, and ξ^r is the martensite volume fraction at the cessation of forward transformation. The transformation strain magnitude for full transformation H^{cur} is given as follows [442]:

$$H^{cur}(\bar{\sigma}) = \begin{cases} H_{min}; & \bar{\sigma} \leq \bar{\sigma}_{crit} \\ H_{min} + (H_{sat} - H_{min})(1 - e^{-k(\bar{\sigma} - \bar{\sigma}_{crit})}); & \bar{\sigma} > \bar{\sigma}_{crit} \end{cases}, \tag{4.55}$$

where H_{min} corresponds to the observable two-way shape memory effect strain magnitude [442], H_{sat} is the maximum recoverable transformation strain magnitude attained by the SMA, and $\bar{\sigma}_{crit}$ denotes the critical von Mises stress below which $H^{cur} = H_{min}$. Certain constraints on the evolution of martensite volume fraction ξ must be defined [442]. To this end, the transformation function Φ^t is introduced. The constraints on the evolution of ξ are then given as follows:

$$\Phi^t \leq 0, \tag{4.56}$$

$$\dot{\xi}\Phi^t = 0, \tag{4.57}$$

$$0 \leq \xi \leq 1. \tag{4.58}$$

The following branched form of Φ^t is proposed in [442]:

$$\Phi^t = \begin{cases} \Phi^t_{fwd}; & 0 \leq \xi < 1, \quad \dot{\xi} \geq 0 \\ \Phi^t_{rev}; & 0 < \xi \leq 1, \quad \dot{\xi} \leq 0 \end{cases}, \tag{4.59}$$

where the transformation functions for forward and reverse transformation (Φ^t_{fwd} and Φ^t_{rev}, respectively), are given as follows:

$$\begin{aligned} \Phi^t_{fwd} &= (1-D)\boldsymbol{\sigma} : \boldsymbol{\Lambda}^t_{fwd} + \tfrac{1}{2}\boldsymbol{\sigma} : \Delta\boldsymbol{S}\boldsymbol{\sigma} + \rho\Delta s_0 T - \rho\Delta u_0 \\ &\quad - \left(\tfrac{1}{2}a_1(1+\xi^{n_1} - (1-\xi)^{n_2}) + a_3\right) - Y^t, \end{aligned} \tag{4.60}$$

$$\begin{aligned} \Phi^t_{rev} &= -(1+D)\boldsymbol{\sigma} : \boldsymbol{\Lambda}^t_{rev} - \tfrac{1}{2}\boldsymbol{\sigma} : \Delta\boldsymbol{S}\boldsymbol{\sigma} - \rho\Delta s_0 T + \rho\Delta u_0 \\ &\quad + \left(\tfrac{1}{2}a_2(1+\xi^{n_3} - (1-\xi)^{n_4}) - a_3\right) - Y^t, \end{aligned} \tag{4.61}$$

and $\rho\Delta s_0$, $\rho\Delta u_0$, a_1, a_2, a_3, D, and Y_t are parameters calibrated from the experimentally determined transformation temperatures at zero stress (M_s, M_f, A_s, and A_f, see Figure 4.3), the stress influence coefficients (C^A and C^M, see Figure 4.3), elastic material parameters, and parameters defining H^{cur} (see Equation (4.55)). Details on the determination of material parameters for this SMA model are provided in [442].

For the plane stress assumptions made in classical plate theory, only the following

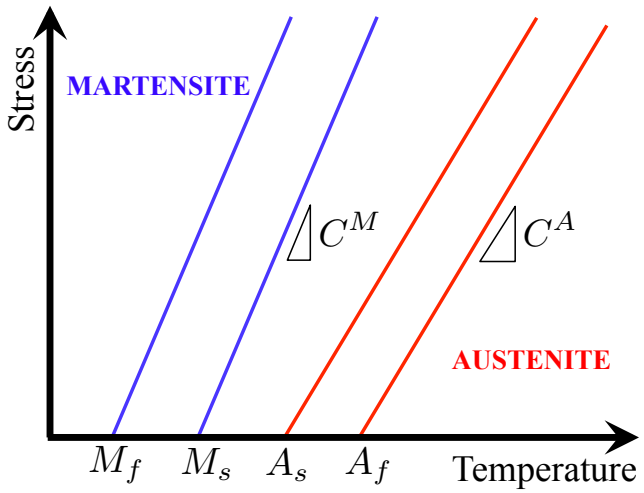

Figure 4.3: Schematic of an SMA stress-temperature phase diagram.

stress components are considered [354]:

$$\begin{bmatrix} \sigma_{11} \\ \sigma_{22} \\ \sigma_{12} \end{bmatrix} = \boldsymbol{C}^{PS}(\xi) \begin{bmatrix} \varepsilon_{11} - \alpha(T - T_0) - \varepsilon^t_{11} + \varepsilon^{t0}_{11} \\ \varepsilon_{22} - \alpha(T - T_0) - \varepsilon^t_{22} + \varepsilon^{t0}_{22} \\ \varepsilon_{12} - \varepsilon^t_{12} + \varepsilon^{t0}_{12} \end{bmatrix}, \tag{4.62}$$

where $\boldsymbol{C}^{PS}(\xi)$ is the effective plane stress stiffness matrix. By substituting the ex-

pressions for strain in Equation (4.7) into Equation (4.47), the following is obtained:

$$\begin{aligned}\begin{bmatrix}\sigma_{11}\\ \sigma_{22}\\ \sigma_{12}\end{bmatrix} &= \boldsymbol{C}^{PS}(\xi)\begin{bmatrix}-\alpha(T-T_0)-\varepsilon^t_{11}+\varepsilon^{t0}_{11}\\ \varepsilon(\hat{\theta}_i,\hat{s}_i)-\alpha(T-T_0)-\varepsilon^t_{22}+\varepsilon^{t0}_{22}\\ -\varepsilon^t_{12}+\varepsilon^{t0}_{12}\end{bmatrix} \\ &= \boldsymbol{C}^{PS}(\xi)\begin{bmatrix}-\alpha(T-T_0)-\varepsilon^t_{11}+\varepsilon^{t0}_{11}\\ \varepsilon_0(\hat{\theta}_i,\hat{s}_i)-\zeta_3\,\kappa(\hat{\theta}_i,\hat{s}_i)-\alpha(T-T_0)-\varepsilon^t_{22}+\varepsilon^{t0}_{22}\\ -\varepsilon^t_{12}+\varepsilon^{t0}_{12}\end{bmatrix}.\end{aligned} \tag{4.63}$$

For the case of regions comprised of SMA wires such as those considered in [10, 8, 448] (refer to Figure 1.9 for an example), the SMA wires are assumed to be aligned with the 2-direction of the fold domain and a one-dimensional form of the previously described three-dimensional SMA model is utilized [10]:

$$\begin{bmatrix}\sigma_{11}\\ \sigma_{22}\\ \sigma_{12}\end{bmatrix} = \begin{bmatrix}0\\ v_f E(\xi)\left(\varepsilon_0(\hat{\theta}_i,\hat{s}_i)-\zeta_3\,\kappa(\hat{\theta}_i,\hat{s}_i)-\alpha(T-T_0)-\varepsilon^t+\varepsilon^{t0}\right)\\ 0\end{bmatrix}, \tag{4.64}$$

where v_f is the volume fraction of the SMA wires and $E(\xi)$ is the effective Young's modulus dependent on the martensite volume fraction.

4.3.3 Numerical Implementation

In order to determine a configuration that satisfies mechanical equilibrium as well as the kinematic constraints in Equation (2.97), the coefficients multiplying

each virtual increment in fold angle $\delta\hat{\theta}_i$ and each virtual increment in fold arc-length $\delta\hat{s}_i$ in Equation (4.45) must be set to 0. In a numerical framework such as the one to be developed here, these coefficients are placed as components of residual vectors and iteratively minimized in magnitude using the Newton's method [353].

Let $\boldsymbol{\mathfrak{R}}^{\theta} \in \mathbb{R}^{N_{\mathcal{F}}}$ be the residual vector for which components $\mathfrak{R}_i^{\theta}$ are the coefficients of each virtual increment in fold angle $\delta\hat{\theta}_i$ in Equation (4.45):

$$\mathfrak{R}_i^{\theta} = \int_{\mathcal{F}_i} \left(N \frac{\partial \varepsilon_0}{\partial \hat{\theta}_i} - M \frac{\partial \kappa}{\partial \hat{\theta}_i} \right) \mathrm{d}a - \int_{\Omega} \mathbf{b} \cdot \frac{\partial \mathbf{u}}{\partial \hat{\theta}_i} \, \mathrm{d}v - \int_{\partial\Omega} \mathbf{t} \cdot \frac{\partial \mathbf{u}}{\partial \hat{\theta}_i} \, \mathrm{d}a + \frac{\partial \mathfrak{L}}{\partial \hat{\theta}_i}. \tag{4.65}$$

Likewise, let $\boldsymbol{\mathfrak{R}}^{s} \in \mathbb{R}^{N_{\mathcal{F}}}$ be the residual vector for which components $\mathfrak{R}_i^{s}$ are the coefficients of each virtual increment in fold arc-length $\delta\hat{s}_i$ in Equation (4.45):

$$\mathfrak{R}_i^{s} = \int_{\mathcal{F}_i} \left(N \frac{\partial \varepsilon_0}{\partial \hat{s}_i} - M \frac{\partial \kappa}{\partial \hat{s}_i} \right) \mathrm{d}a - \int_{\Omega} \mathbf{b} \cdot \frac{\partial \mathbf{u}}{\partial \hat{s}_i} \, \mathrm{d}v - \int_{\partial\Omega} \mathbf{t} \cdot \frac{\partial \mathbf{u}}{\partial \hat{s}_i} \, \mathrm{d}a + \frac{\partial \mathfrak{L}}{\partial \hat{s}_i}. \tag{4.66}$$

The applied loading to the origami structures with smooth fold domains is evolved in various loading increments. For each load increment, the configuration that satisfies Equation (4.45) must be determined. The present implementation iteratively solves for increments in fold angles and fold arc-lengths that minimize the magnitude of the components of the vectors $\boldsymbol{\mathfrak{R}}^{\theta}$ and $\boldsymbol{\mathfrak{R}}^{s}$, which must be zero (or sufficiently close to zero by introducing a numerical tolerance) for a configuration to satisfy Equation (4.45). Using the Newton's method, the fold angles and fold arc-lengths at the l^{th}

loading increment are corrected iteratively as follows:

$$\begin{bmatrix} {}^{k}_{l}\Delta\hat{\boldsymbol{\theta}} \\ \\ {}^{k}_{l}\Delta\hat{\mathbf{s}} \end{bmatrix} = - \begin{bmatrix} \dfrac{\partial \mathfrak{R}^{\theta}({}^{k}_{l}\hat{\boldsymbol{\theta}},\, {}^{k}_{l}\hat{\mathbf{s}})}{\partial \hat{\boldsymbol{\theta}}} & \dfrac{\partial \mathfrak{R}^{\theta}({}^{k}_{l}\hat{\boldsymbol{\theta}},\, {}^{k}_{l}\hat{\mathbf{s}})}{\partial \hat{\mathbf{s}}} \\ \\ \dfrac{\partial \mathfrak{R}^{s}({}^{k}_{l}\hat{\boldsymbol{\theta}},\, {}^{k}_{l}\hat{\mathbf{s}})}{\partial \hat{\boldsymbol{\theta}}} & \dfrac{\partial \mathfrak{R}^{s}({}^{k}_{l}\hat{\boldsymbol{\theta}},\, {}^{k}_{l}\hat{\mathbf{s}})}{\partial \hat{\mathbf{s}}} \end{bmatrix}^{-1} \begin{bmatrix} \mathfrak{R}^{\theta}({}^{k}_{l}\hat{\boldsymbol{\theta}},\, {}^{k}_{l}\hat{\mathbf{s}}) \\ \\ \mathfrak{R}^{s}({}^{k}_{l}\hat{\boldsymbol{\theta}},\, {}^{k}_{l}\hat{\mathbf{s}}) \end{bmatrix}, \tag{4.67}$$

$${}^{k+1}_{l}\hat{\boldsymbol{\theta}} = {}^{k}_{l}\hat{\boldsymbol{\theta}} + {}^{k}_{l}\Delta\hat{\boldsymbol{\theta}}, \tag{4.68}$$

$${}^{k+1}_{l}\hat{\mathbf{s}} = {}^{k}_{l}\hat{\mathbf{s}} + {}^{k}_{l}\Delta\hat{\mathbf{s}}, \tag{4.69}$$

where the subscripts in the previous equation refer to the load increment number and the superscripts correspond to the correction iteration number. The correction iterations in Equations (4.67)–(4.69) are repeated until $\|\mathfrak{R}^{\theta}({}^{k+1}_{l}\hat{\boldsymbol{\theta}},\, {}^{k+1}_{l}\hat{\mathbf{s}})\| < \texttt{tol1}$ and $\|\mathfrak{R}^{s}({}^{k+1}_{l}\hat{\boldsymbol{\theta}},\, {}^{k+1}_{l}\hat{\mathbf{s}})\| < \texttt{tol2}$, or alternatively until $\|{}^{k}_{l}\Delta\hat{\boldsymbol{\theta}}\| < \texttt{tol3}$ and $\|{}^{k}_{l}\Delta\hat{\mathbf{s}}\| < \texttt{tol4}$ (where `tol1`, `tol2`, `tol3`, and `tol4` are numerical tolerances). Table 4.1 summarizes the numerical procedure followed to simulate origami structures of non-zero thickness.

The components of the tangent matrices $\frac{\partial \mathfrak{R}^{\theta}}{\partial \hat{\boldsymbol{\theta}}}$, $\frac{\partial \mathfrak{R}^{\theta}}{\partial \hat{\mathbf{s}}}$, $\frac{\partial \mathfrak{R}^{s}}{\partial \hat{\boldsymbol{\theta}}}$, and $\frac{\partial \mathfrak{R}^{s}}{\partial \hat{\mathbf{s}}}$ must be calculated to determine the corrective increments in fold angles and fold arc-lengths as

Table 4.1: Numerical procedure followed at the l^{th} loading increment to determine the response of origami structures with smooth fold domains of non-zero thickness.

1:	Determine the components of the residual vectors $\mathfrak{R}^{\theta}({}^{1}_{l}\hat{\boldsymbol{\theta}}, {}^{1}_{l}\hat{\mathbf{s}})$ and $\mathfrak{R}^{s}({}^{1}_{l}\hat{\boldsymbol{\theta}}, {}^{1}_{l}\hat{\mathbf{s}})$

2:	`IF` $(\|\mathfrak{R}^{\theta}({}^{1}_{l}\hat{\boldsymbol{\theta}}, {}^{1}_{l}\hat{\mathbf{s}})\| < \texttt{tol1}$ `AND` $\|\mathfrak{R}^{s}({}^{1}_{l}\hat{\boldsymbol{\theta}}, {}^{1}_{l}\hat{\mathbf{s}})\| < \texttt{tol2})$
	`THEN` set ${}_{l}\hat{\boldsymbol{\theta}} = {}^{1}_{l}\hat{\boldsymbol{\theta}}$, ${}_{l}\hat{\mathbf{s}} = {}^{1}_{l}\hat{\mathbf{s}}$ and `EXIT`
	`ELSE CONTINUE`

3:	Determine corrections ${}^{k}_{l}\Delta\hat{\boldsymbol{\theta}}$ and ${}^{k}_{l}\Delta\hat{\mathbf{s}}$ using Equation (4.67)
4:	Update ${}^{k+1}_{l}\hat{\boldsymbol{\theta}}$ and ${}^{k+1}_{l}\hat{\mathbf{s}}$ using Equations (4.68) and (4.69)
5:	`IF` $(\|\mathfrak{R}^{\theta}({}^{k+1}_{l}\hat{\boldsymbol{\theta}}, {}^{k+1}_{l}\hat{\mathbf{s}})\| < \texttt{tol1}$ `AND` $\|\mathfrak{R}^{s}({}^{k+1}_{l}\hat{\boldsymbol{\theta}}, {}^{k+1}_{l}\hat{\mathbf{s}})\| < \texttt{tol2})$ `OR` $(\|{}^{k}_{l}\Delta\hat{\boldsymbol{\theta}}\| < \texttt{tol3}$ `AND` $\|{}^{k}_{l}\Delta\hat{\mathbf{s}}\| < \texttt{tol4})$ `THEN` set ${}_{l}\hat{\boldsymbol{\theta}} = {}^{k+1}_{l}\hat{\boldsymbol{\theta}}$, ${}_{l}\hat{\mathbf{s}} = {}^{k+1}_{l}\hat{\mathbf{s}}$ and `EXIT` `ELSE` set $k \leftarrow k+1$ and `GOTO` 3

given in Equation (4.67). These components are given as follows:

$$\begin{aligned}\frac{\partial \mathfrak{R}^{\theta}_{i}}{\partial \hat{\theta}_i} = \; & \int_{\mathcal{F}_i} \left(\frac{\partial N}{\partial \hat{\theta}_i}\frac{\partial \varepsilon_0}{\partial \hat{\theta}_i} + N\frac{\partial^2 \varepsilon_0}{\partial \hat{\theta}_i^2} - \frac{\partial M}{\partial \hat{\theta}_i}\frac{\partial \kappa}{\partial \hat{\theta}_i} - M\frac{\partial^2 \kappa}{\partial \hat{\theta}_i^2} \right) \mathrm{d}a \\ & - \int_{\Omega} \left(\frac{\partial \mathbf{b}}{\partial \hat{\theta}_i} \cdot \frac{\partial \mathbf{u}}{\partial \hat{\theta}_i} + \mathbf{b} \cdot \frac{\partial^2 \mathbf{u}}{\partial \hat{\theta}_i^2} \right) \mathrm{d}v - \int_{\partial\Omega} \left(\frac{\partial \mathbf{t}}{\partial \hat{\theta}_i} \cdot \frac{\partial \mathbf{u}}{\partial \hat{\theta}_i} + \mathbf{t} \cdot \frac{\partial^2 \mathbf{u}}{\partial \hat{\theta}_i^2} \right) \mathrm{d}a \\ & + \frac{\partial^2 \mathfrak{L}}{\partial \hat{\theta}_i^2},\end{aligned} \tag{4.70}$$

$$\begin{aligned}\frac{\partial \mathfrak{R}_i^\theta}{\partial \hat{s}_i} = & \int_{\mathcal{F}_i} \left(\frac{\partial N}{\partial \hat{s}_i} \frac{\partial \varepsilon_0}{\partial \hat{\theta}_i} + N \frac{\partial^2 \varepsilon_0}{\partial \hat{\theta}_i \partial \hat{s}_i} - \frac{\partial M}{\partial \hat{s}_i} \frac{\partial \kappa}{\partial \hat{\theta}_i} - M \frac{\partial^2 \kappa}{\partial \hat{\theta}_i \partial \hat{s}_i} \right) \mathrm{d}a \\ & - \int_\Omega \left(\frac{\partial \mathbf{b}}{\partial \hat{s}_i} \cdot \frac{\partial \mathbf{u}}{\partial \hat{\theta}_i} + \mathbf{b} \cdot \frac{\partial^2 \mathbf{u}}{\partial \hat{\theta}_i \partial \hat{s}_i} \right) \mathrm{d}v - \int_{\partial\Omega} \left(\frac{\partial \mathbf{t}}{\partial \hat{s}_i} \cdot \frac{\partial \mathbf{u}}{\partial \hat{\theta}_i} + \mathbf{t} \cdot \frac{\partial^2 \mathbf{u}}{\partial \hat{\theta}_i \partial \hat{s}_i} \right) \mathrm{d}a \\ & + \frac{\partial^2 \mathfrak{L}}{\partial \hat{\theta}_i \partial \hat{s}_i}, \end{aligned} \tag{4.71}$$

$$\begin{aligned}\left. \frac{\partial \mathfrak{R}_i^\theta}{\partial \hat{\theta}_j} \right|_{j \neq i} = & - \int_\Omega \left(\frac{\partial \mathbf{b}}{\partial \hat{\theta}_j} \cdot \frac{\partial \mathbf{u}}{\partial \hat{\theta}_i} + \mathbf{b} \cdot \frac{\partial^2 \mathbf{u}}{\partial \hat{\theta}_i \partial \hat{\theta}_j} \right) \mathrm{d}v \\ & - \int_{\partial\Omega} \left(\frac{\partial \mathbf{t}}{\partial \hat{\theta}_j} \cdot \frac{\partial \mathbf{u}}{\partial \hat{\theta}_i} + \mathbf{t} \cdot \frac{\partial^2 \mathbf{u}}{\partial \hat{\theta}_i \partial \hat{\theta}_j} \right) \mathrm{d}a + \frac{\partial^2 \mathfrak{L}}{\partial \hat{\theta}_i \partial \hat{\theta}_j}, \end{aligned} \tag{4.72}$$

$$\begin{aligned}\left. \frac{\partial \mathfrak{R}_i^\theta}{\partial \hat{s}_j} \right|_{j \neq i} = & - \int_\Omega \left(\frac{\partial \mathbf{b}}{\partial \hat{s}_j} \cdot \frac{\partial \mathbf{u}}{\partial \hat{\theta}_i} + \mathbf{b} \cdot \frac{\partial^2 \mathbf{u}}{\partial \hat{\theta}_i \partial \hat{s}_j} \right) \mathrm{d}v \\ & - \int_{\partial\Omega} \left(\frac{\partial \mathbf{t}}{\partial \hat{s}_j} \cdot \frac{\partial \mathbf{u}}{\partial \hat{\theta}_i} + \mathbf{t} \cdot \frac{\partial^2 \mathbf{u}}{\partial \hat{\theta}_i \partial \hat{s}_j} \right) \mathrm{d}a + \frac{\partial^2 \mathfrak{L}}{\partial \hat{\theta}_i \partial \hat{s}_j}, \end{aligned} \tag{4.73}$$

$$\begin{aligned}\frac{\partial \mathfrak{R}_i^s}{\partial \hat{s}_i} = & \int_{\mathcal{F}_i} \left(\frac{\partial N}{\partial \hat{s}_i} \frac{\partial \varepsilon_0}{\partial \hat{s}_i} + N \frac{\partial^2 \varepsilon_0}{\partial \hat{s}_i^2} - \frac{\partial M}{\partial \hat{s}_i} \frac{\partial \kappa}{\partial \hat{s}_i} - M \frac{\partial^2 \kappa}{\partial \hat{s}_i^2} \right) \mathrm{d}a \\ & - \int_\Omega \left(\frac{\partial \mathbf{b}}{\partial \hat{s}_i} \cdot \frac{\partial \mathbf{u}}{\partial \hat{s}_i} + \mathbf{b} \cdot \frac{\partial^2 \mathbf{u}}{\partial \hat{s}_i^2} \right) \mathrm{d}v - \int_{\partial\Omega} \left(\frac{\partial \mathbf{t}}{\partial \hat{s}_i} \cdot \frac{\partial \mathbf{u}}{\partial \hat{s}_i} + \mathbf{t} \cdot \frac{\partial^2 \mathbf{u}}{\partial \hat{s}_i^2} \right) \mathrm{d}a \\ & + \frac{\partial^2 \mathfrak{L}}{\partial \hat{s}_i^2}, \end{aligned} \tag{4.74}$$

$$
\begin{aligned}
\frac{\partial \mathfrak{R}_i^s}{\partial \hat{\theta}_i} = & \int_{\mathcal{F}_i} \left(\frac{\partial N}{\partial \hat{\theta}_i} \frac{\partial \varepsilon_0}{\partial \hat{s}_i} + N \frac{\partial^2 \varepsilon_0}{\partial \hat{\theta}_i \partial \hat{s}_i} - \frac{\partial M}{\partial \hat{\theta}_i} \frac{\partial \kappa}{\partial \hat{s}_i} - M \frac{\partial^2 \kappa}{\partial \hat{\theta}_i \partial \hat{s}_i} \right) \mathrm{d}a \\
& - \int_\Omega \left(\frac{\partial \mathbf{b}}{\partial \hat{\theta}_i} \cdot \frac{\partial \mathbf{u}}{\partial \hat{s}_i} + \mathbf{b} \cdot \frac{\partial^2 \mathbf{u}}{\partial \hat{\theta}_i \partial \hat{s}_i} \right) \mathrm{d}v - \int_{\partial\Omega} \left(\frac{\partial \mathbf{t}}{\partial \hat{\theta}_i} \cdot \frac{\partial \mathbf{u}}{\partial \hat{s}_i} + \mathbf{t} \cdot \frac{\partial^2 \mathbf{u}}{\partial \hat{\theta}_i \partial \hat{s}_i} \right) \mathrm{d}a \\
& + \frac{\partial^2 \mathfrak{L}}{\partial \hat{\theta}_i \partial \hat{s}_i},
\end{aligned}
\tag{4.75}
$$

$$
\begin{aligned}
\left. \frac{\partial \mathfrak{R}_i^s}{\partial \hat{s}_j} \right|_{j \neq i} = & - \int_\Omega \left(\frac{\partial \mathbf{b}}{\partial \hat{s}_j} \cdot \frac{\partial \mathbf{u}}{\partial \hat{s}_i} + \mathbf{b} \cdot \frac{\partial^2 \mathbf{u}}{\partial \hat{s}_i \partial \hat{s}_j} \right) \mathrm{d}v \\
& - \int_{\partial\Omega} \left(\frac{\partial \mathbf{t}}{\partial \hat{s}_j} \cdot \frac{\partial \mathbf{u}}{\partial \hat{s}_i} + \mathbf{t} \cdot \frac{\partial^2 \mathbf{u}}{\partial \hat{s}_i \partial \hat{s}_j} \right) \mathrm{d}a + \frac{\partial^2 \mathfrak{L}}{\partial \hat{s}_i \partial \hat{s}_j},
\end{aligned}
\tag{4.76}
$$

$$
\begin{aligned}
\left. \frac{\partial \mathfrak{R}_i^s}{\partial \hat{\theta}_j} \right|_{j \neq i} = & - \int_\Omega \left(\frac{\partial \mathbf{b}}{\partial \hat{\theta}_j} \cdot \frac{\partial \mathbf{u}}{\partial \hat{s}_i} + \mathbf{b} \cdot \frac{\partial^2 \mathbf{u}}{\partial \hat{s}_i \partial \hat{\theta}_j} \right) \mathrm{d}v \\
& - \int_{\partial\Omega} \left(\frac{\partial \mathbf{t}}{\partial \hat{\theta}_j} \cdot \frac{\partial \mathbf{u}}{\partial \hat{s}_i} + \mathbf{t} \cdot \frac{\partial^2 \mathbf{u}}{\partial \hat{s}_i \partial \hat{\theta}_j} \right) \mathrm{d}a + \frac{\partial^2 \mathfrak{L}}{\partial \hat{s}_i \partial \hat{\theta}_j},
\end{aligned}
\tag{4.77}
$$

where the derivatives of the axial force and moment resultants with respect to fold

angle and fold arc-length are given as follows:

$$\begin{aligned}
\frac{\partial N}{\partial \hat{\theta}_i} &= \frac{\partial}{\partial \hat{\theta}_i} \int_{-\frac{\mathfrak{h}_i}{2}}^{\frac{\mathfrak{h}_i}{2}} \sigma \, \mathrm{d}\zeta_3 \\
&= \int_{-\frac{\mathfrak{h}_i}{2}}^{\frac{\mathfrak{h}_i}{2}} \frac{\partial \sigma}{\partial \hat{\theta}_i} \, \mathrm{d}\zeta_3 \\
&= \int_{-\frac{\mathfrak{h}_i}{2}}^{\frac{\mathfrak{h}_i}{2}} \frac{\partial \sigma}{\partial \varepsilon} \frac{\partial \varepsilon}{\partial \hat{\theta}_i} \, \mathrm{d}\zeta_3 \\
&= \int_{-\frac{\mathfrak{h}_i}{2}}^{\frac{\mathfrak{h}_i}{2}} \frac{\partial \sigma}{\partial \varepsilon} \left(\frac{\partial \varepsilon_0}{\partial \hat{\theta}_i} - \zeta_3 \frac{\partial \kappa}{\partial \hat{\theta}_i} \right) \mathrm{d}\zeta_3,
\end{aligned} \tag{4.78}$$

similarly:

$$\begin{aligned}
\frac{\partial N}{\partial \hat{s}_i} &= \frac{\partial}{\partial \hat{s}_i} \int_{-\frac{\mathfrak{h}_i}{2}}^{\frac{\mathfrak{h}_i}{2}} \sigma \, \mathrm{d}\zeta_3 \\
&= \int_{-\frac{\mathfrak{h}_i}{2}}^{\frac{\mathfrak{h}_i}{2}} \frac{\partial \sigma}{\partial \hat{s}_i} \, \mathrm{d}\zeta_3 \\
&= \int_{-\frac{\mathfrak{h}_i}{2}}^{\frac{\mathfrak{h}_i}{2}} \frac{\partial \sigma}{\partial \varepsilon} \frac{\partial \varepsilon}{\partial \hat{s}_i} \, \mathrm{d}\zeta_3 \\
&= \int_{-\frac{\mathfrak{h}_i}{2}}^{\frac{\mathfrak{h}_i}{2}} \frac{\partial \sigma}{\partial \varepsilon} \left(\frac{\partial \varepsilon_0}{\partial \hat{s}_i} - \zeta_3 \frac{\partial \kappa}{\partial \hat{s}_i} \right) \mathrm{d}\zeta_3,
\end{aligned} \tag{4.79}$$

$$
\begin{aligned}
\frac{\partial M}{\partial \hat{\theta}_i} &= \frac{\partial}{\partial \hat{\theta}_i} \int_{-\frac{\mathfrak{h}_i}{2}}^{\frac{\mathfrak{h}_i}{2}} \zeta_3 \sigma \, \mathrm{d}\zeta_3 \\
&= \int_{-\frac{\mathfrak{h}_i}{2}}^{\frac{\mathfrak{h}_i}{2}} \zeta_3 \frac{\partial \sigma}{\partial \hat{\theta}_i} \, \mathrm{d}\zeta_3 \\
&= \int_{-\frac{\mathfrak{h}_i}{2}}^{\frac{\mathfrak{h}_i}{2}} \zeta_3 \frac{\partial \sigma}{\partial \varepsilon} \frac{\partial \varepsilon}{\partial \hat{\theta}_i} \, \mathrm{d}\zeta_3 \\
&= \int_{-\frac{\mathfrak{h}_i}{2}}^{\frac{\mathfrak{h}_i}{2}} \frac{\partial \sigma}{\partial \varepsilon} \left(\zeta_3 \frac{\partial \varepsilon_0}{\partial \hat{\theta}_i} - (\zeta_3)^2 \frac{\partial \kappa}{\partial \hat{\theta}_i} \right) \mathrm{d}\zeta_3,
\end{aligned}
\tag{4.80}
$$

$$
\begin{aligned}
\frac{\partial M}{\partial \hat{s}_i} &= \frac{\partial}{\partial \hat{s}_i} \int_{-\frac{\mathfrak{h}_i}{2}}^{\frac{\mathfrak{h}_i}{2}} \zeta_3 \sigma \, \mathrm{d}\zeta_3 \\
&= \int_{-\frac{\mathfrak{h}_i}{2}}^{\frac{\mathfrak{h}_i}{2}} \zeta_3 \frac{\partial \sigma}{\partial \hat{s}_i} \, \mathrm{d}\zeta_3 \\
&= \int_{-\frac{\mathfrak{h}_i}{2}}^{\frac{\mathfrak{h}_i}{2}} \zeta_3 \frac{\partial \sigma}{\partial \varepsilon} \frac{\partial \varepsilon}{\partial \hat{s}_i} \, \mathrm{d}\zeta_3 \\
&= \int_{-\frac{\mathfrak{h}_i}{2}}^{\frac{\mathfrak{h}_i}{2}} \frac{\partial \sigma}{\partial \varepsilon} \left(\zeta_3 \frac{\partial \varepsilon_0}{\partial \hat{s}_i} - (\zeta_3)^2 \frac{\partial \kappa}{\partial \hat{s}_i} \right) \mathrm{d}\zeta_3,
\end{aligned}
\tag{4.81}
$$

The evaluation of the integrals over the smooth fold surfaces and over the thickness of the smooth fold domains in the previous equations is performed through numerical integration [428, 449]. Figure 4.4 shows the location of integration points used for in-surface integration and also the location of integration points through the thickness of each layer. Integration points at only one location along the 1-direction (i.e. that aligned with $\hat{\mathbf{e}}_1^i$) are needed as strain is assumed uniform throughout this direction. Gauss-Legendre quadrature rule is used for integration along the 2-direction.

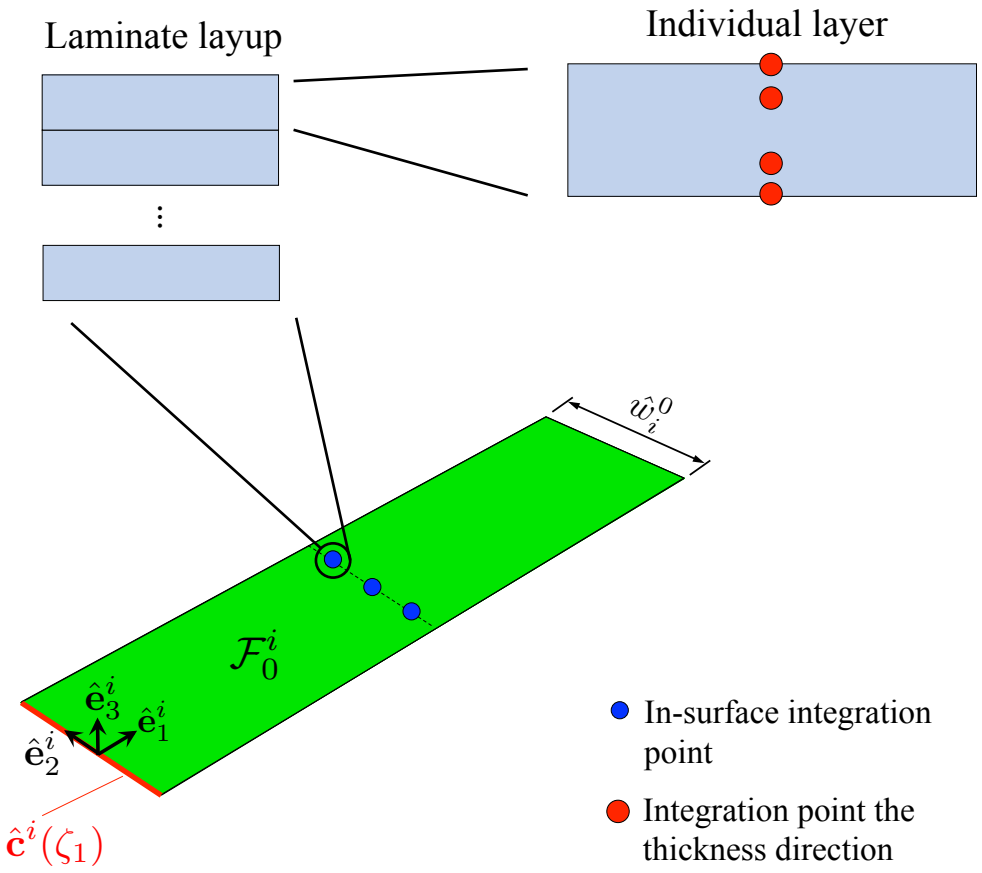

Figure 4.4: Schematic of a smooth fold surface showing the location of in-surface integration points and integration points through the thickness of each layer.

The number of integration points needed in the 2-direction is dictated by assumed in-plane strain and curvature fields in the fold domain (refer to Section 4.1). Integration through the thickness of the smooth fold domains is performed layer by layer as shown in Figure 4.4. For each individual layer, Gauss-Lobatto quadrature rule is used for integration [428, 450] because it considers integration points at the ends of the integration domain (i.e. the top and bottom of each layer) which often are the locations of maximum stress.

4.3.4 Implementation Results

In this section, implementation results of the model derived in Section 4.3 are presented. The numerical procedure used for the simulation of the response of origami structures with smooth fold domains presented in Section 4.3.3 is implemented in Matlab. Diverse patterns of smooth folds are analyzed using the proposed model. The smooth folds $\mathcal{F}_t^i$ are visualized using the Matlab three-dimensional shaded surface plot function `surf` while the faces $\mathcal{P}_t^i$ are visualized as filled three-dimensional polygons using `fill3`.

Finite element analysis is used for numerical validation of the model. In this work, FEA is performed using Abaqus finite element software. Static analysis steps considering large rotations (i.e. the `NLGEOM` option in Abaqus is active, see [10, 451]) are used. Abaqus `S4` elements (4-node doubly curved general-purpose shells, finite membrane strains) are used to discretize the sheet in all the FEA examples shown in this section. In order to capture rigid behavior for the faces which is assumed in the model derived in Section 4.3, rigid body constraints are imposed to the finite elements located at the face regions.

Implementation examples considering smooth fold domains comprised of elastic and SMA materials are considered herein. Nonetheless, it is remarked that the present model is applicable to smooth folds comprised of other passive or active materials so long as strains are small enough such that the linearized strain tensor can be utilized to properly model the deformation.

The first example considers a structure having one linear elastic smooth fold domain of 0.5 mm thickness and subject to a point load. The boundary value problem is schematically shown in Figure 4.5. The material parameters for the linear elastic smooth fold domain are provided in Table 4.2. The results for this simple example

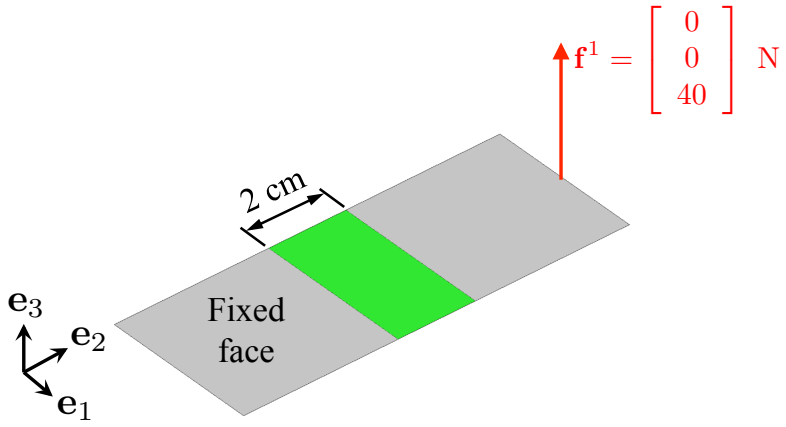

Figure 4.5: Boundary value problem considering a structure having one smooth fold domain of thickness $\mathfrak{h}_i = 0.5$ mm. The material parameters of the elastic smooth fold domain are provided in Table 4.2.

Table 4.2: Material parameters assumed for the aluminum layers.

Parameter	Value
E	70 GPa
ν	0.3

are shown in Figure 4.6. The applied load vector is parallel to the normal direction of the structure; therefore, it induces folding deformation. It is observed in Figure 4.6 that the out-of-plane displacement determined using both the smooth folds model developed here and FEA are in good agreement for the entire loading history.

The second example considers a boundary value problem with the same planar geometry as that shown in Figure 4.5 but includes SMA layers in addition to elastic layers at the smooth fold domain. The boundary value problem of this second example is shown in Figure 4.7. The laminate comprising the smooth fold domain has

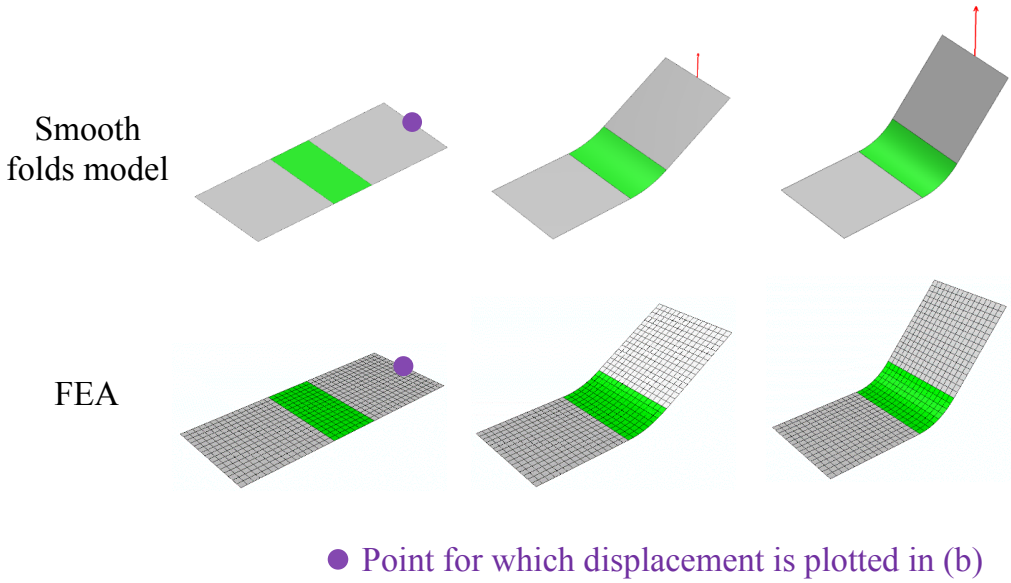

(a)

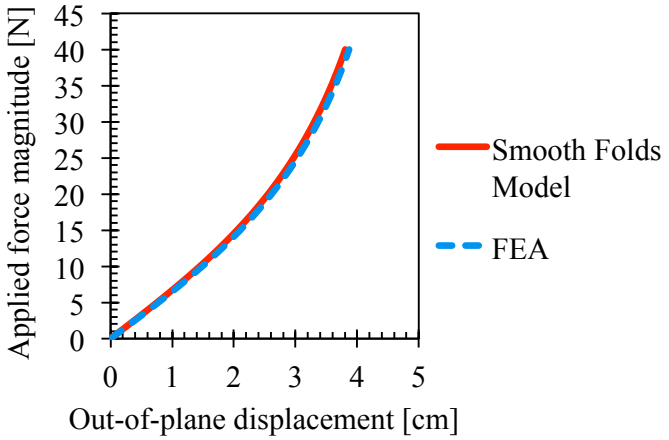

(b)

Figure 4.6: Results associated with the boundary value problem presented in Figure 4.5: (a) Configurations attained by the structure during the applied loading history (reference, intermediate, and final); (b) Magnitude of applied force vs. out-of-plane displacement at a point. Results using both the smooth folds model and FEA are shown.

three layers. The upper layer corresponds to an SMA (wire) layer having material response defined by Equation (4.64), a pre-strain of $\varepsilon^{t0} = H_{sat}$, and volume fraction $v_f = 0.05$. The material parameters of the SMA layer, the elastomer layer, and the aluminum layer are provided in Tables 4.3, 4.4, and 4.2, respectively. Initially at a temperature of 300 K, the SMA layer is in a fully pre-strained martensitic phase. By increasing the temperature from 300 K to 400 K, the SMA layer undergoes phase transformation from martensite to austenite and its transformation strain is recovered (because $A_s = 337.15$ K, refer to Table 4.3). Since the SMA layer is placed off-center relative to the thickness direction of the laminate, the recovery of transformation strain induces folding deformation of the smooth fold domain. The results for this problem are shown in Figure 4.8. It is observed from the out-of-plane displacement vs. applied temperature plot in Figure 4.8(b) that the results obtained using the present smooth folds model and those obtained from FEA are in good agreement for this example considering SMA-actuated folds.

A more complex example considers a structure having four elastic smooth fold domains meeting at a single fold intersection. The boundary value problem associated with this example is shown in Figure 4.9. Two point loads are applied to the structure as shown in Figure 4.9. Unlike the two previous examples shown in Figures 4.5 and 4.7, the kinematic constraints in Equation (2.97) must be considered since a fold intersection is present in the structure. The results for this example are shown in Figure 4.10. It is observed from the deformed configuration plots and the plot showing the components of the displacement vector at a point during the applied loading history (Figures 4.10(a) and 4.10(b), respectively) that the results between the smooth folds model and FEA are also in good agreement for this example of an structure having a fold intersection.

An example of a structure with one fold intersection that morphs via SMA actu-

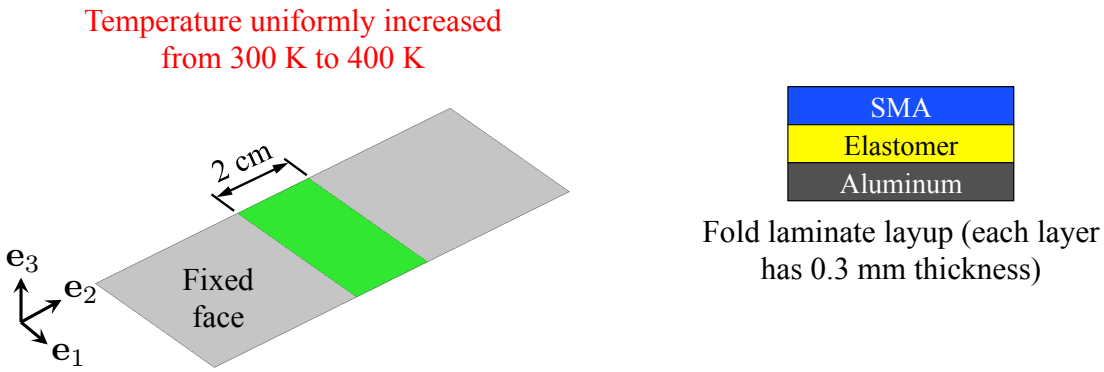

Figure 4.7: Boundary value problem considering a structure having one smooth fold domain comprised of a three-layer laminate. The material parameters of the SMA layer, the elastomer layer, and the aluminum layer are provided in Tables 4.3, 4.4, and 4.2, respectively. The material response of the SMA layer is determined using Equation (4.64) and $\varepsilon^{t0} = H_{sat}$.

ation is shown in Figure 4.11. It is noted that the location of the SMA layer (top or bottom) determines the intended direction of the resulting fold (valley or mountain, respectively). Upon increasing the temperature from 300 K to 400 K, the SMA layers in the smooth fold domains actuate and induce folding of the structure as shown in Figure 4.12. The deformed configuration plots and the plot showing components of the displacement vector at a point during the applied loading history in Figure 4.12 show that there is good agreement between the smooth folds model and FEA also for this example.

Figure 4.13 shows a boundary value problem of a structure having four fold intersections. The smooth fold domains in this example are all linear elastic having material parameters provided in Table 4.2. The central face is fixed and four point loads are applied. The direction and maximum magnitude of the four point loads are equal. The results for this example are shown in Figure 4.14. Figure 4.14(a) shows configurations attained by the structure during the applied loading history (reference

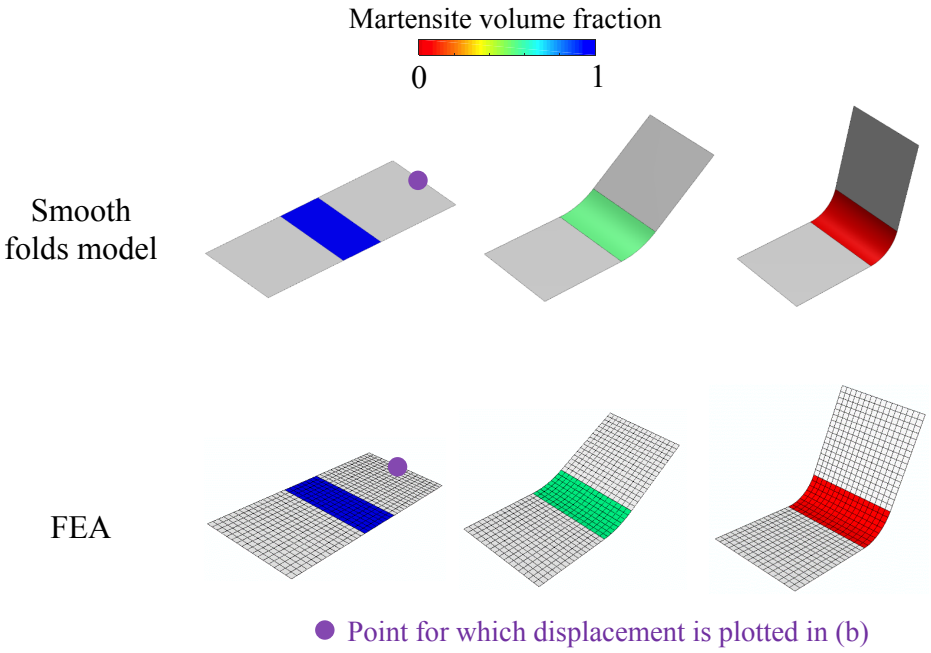

(a)

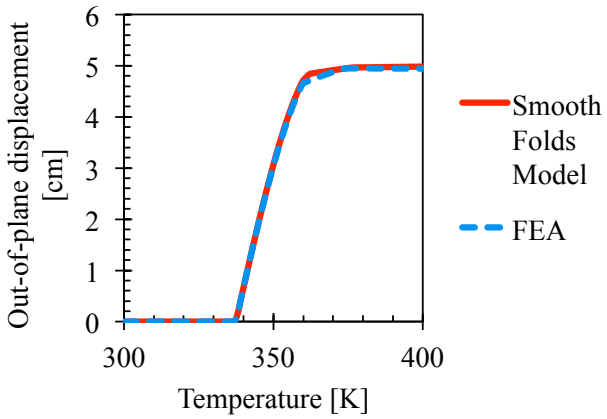

(b)

Figure 4.8: Results associated with the boundary value problem presented in Figure 4.7: (a) Configurations attained by the structure during the applied loading history (reference, intermediate, and final). The martensite volume fraction contour plot of the SMA layer is shown. (b) Out-of-plane displacement at a point vs. applied temperature. Results using both the smooth folds model and FEA are shown.

Table 4.3: Material parameters assumed for the SMA layers based on those provided in [10].

Parameter	Value
E^A	48 GPa
E^M	42.9 GPa
ν^A	0.3
ν^M	0.3
α	0 K^{-1}
M_s	332.15 K
M_f	302.15 K
A_s	337.15 K
A_f	362.15 K
C^A	9.54 MPa/K
C^M	9.00 MPa/K
H_{min}	4.4%
H_{sat}	4.4%
k	0.24 MPa^{-1}
n_1	1
n_2	1
n_3	1
n_4	1

Table 4.4: Material parameters assumed for the elastomer layers based on those provided in [11].

Parameter	Value
E	15.2 MPa
ν	0.45

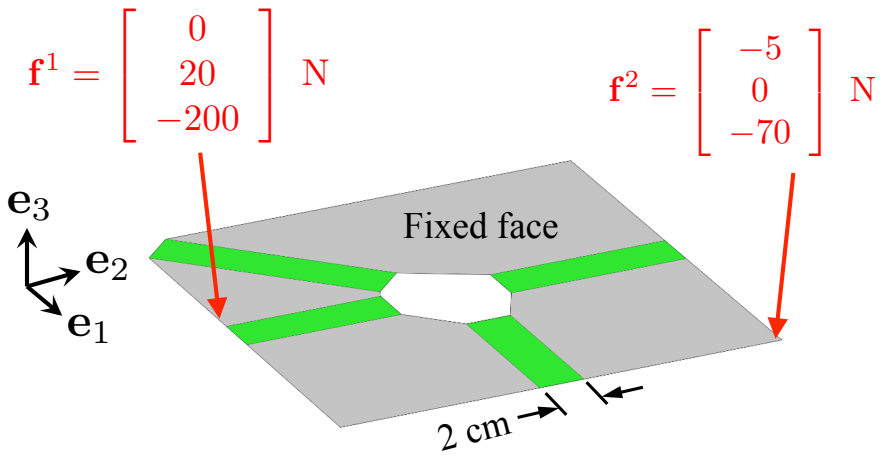

Figure 4.9: Boundary value problem considering a structure having one fold intersection. The elastic smooth fold domains have thickness $\mathfrak{h}_i = 0.5$ mm. The material parameters of the elastic smooth fold domain are provided in Table 4.2.

and final) for both the smooth folds model and FEA. Figure 4.14(b) shows a plot of two components of the displacement vector at a point exhibited during the applied loading history. It is observed from the results in Figure 4.14(a) and Figure 4.14(b) that there is good agreement between FEA and the smooth folds model for this more complicated example.

The last example considers the planar geometry as that shown in Figure 4.13 but includes smooth folds comprised of laminates having SMA layers. The boundary value problem for this example is shown in Figure 4.15. The central face of the origami structure is fixed and the temperature at four folds is increased from 300 K to 400 K to induce folding deformation of the structure. The results for this example are presented in Figure 4.16. Just as in the previous examples, the deformation determined using the proposed model is good agreement with that determined using FEA.

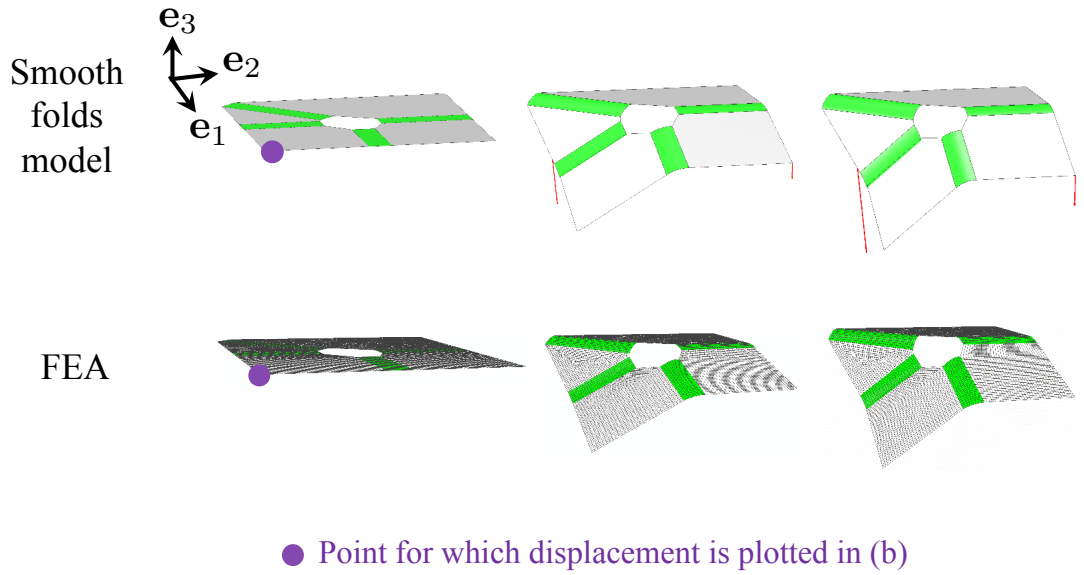

(a)

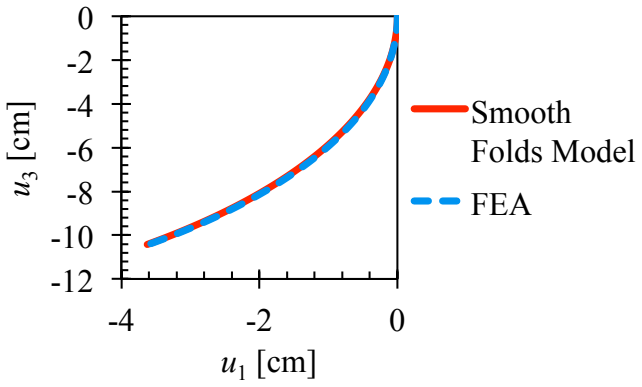

(b)

Figure 4.10: Results associated with the boundary value problem presented in Figure 4.9: (a) Configurations attained by the structure during the applied loading history (reference, intermediate, and final); (b) Two components of the displacement vector at a point exhibited during the applied loading history. Results using both the smooth folds model and FEA are shown.

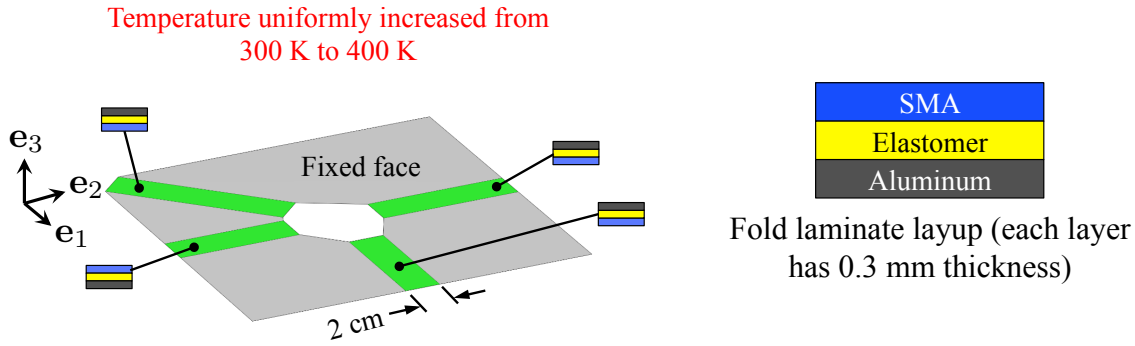

Figure 4.11: Boundary value problem considering a structure having one fold intersection and smooth fold domains comprised of a three-layer laminate. The laminate layup for each individual smooth fold domain are shown. The material parameters of the SMA layers, the elastomer layers, and the aluminum layers are provided in Tables 4.3, 4.4, and 4.2, respectively. The material response of the SMA layers is defined by Equation (4.64) and $\varepsilon^{t0} = H_{sat}$.

The computational efficiency of the proposed model for origami structures with smooth domains as compared to FEA is also explored. All the simulations presented in this work (using the smooth folds model and FEA) were performed on the same computer. Table 4.5 shows the wall-clock time in seconds required for the simulation of each boundary value problem considering SMA behavior shown in Figures 4.7, 4.11, and 4.15. The wall-clock time required for analysis using the proposed model is significantly lower than that required using FEA for all the problems (by more than 90% in all problems). Such results show that the proposed model provides accurate results as compared to higher-fidelity FEA while being significantly more computationally efficient.

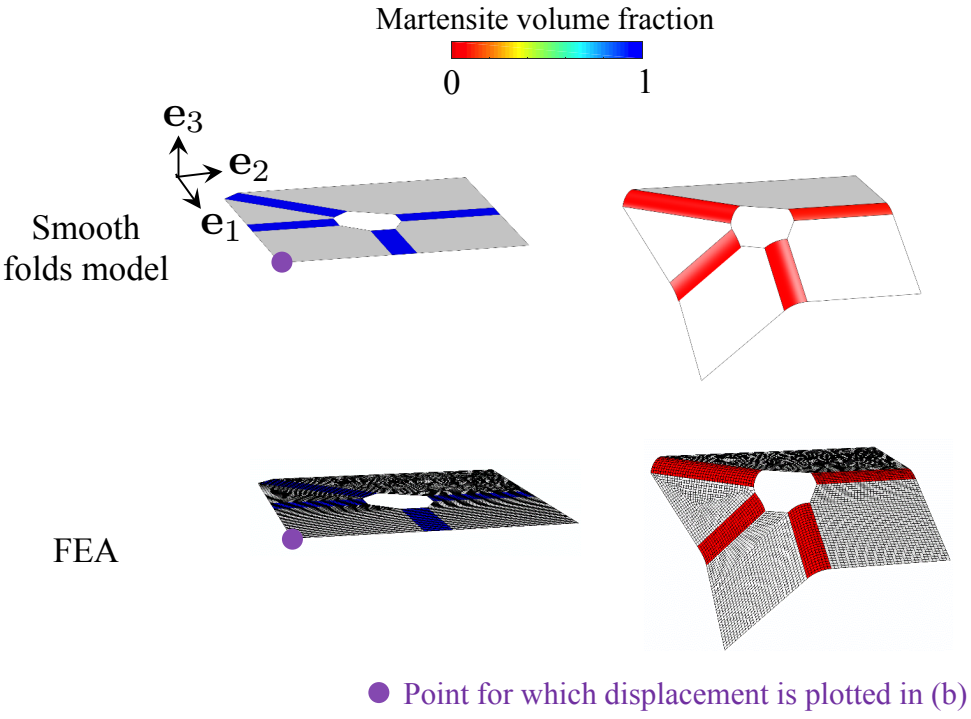

(a)

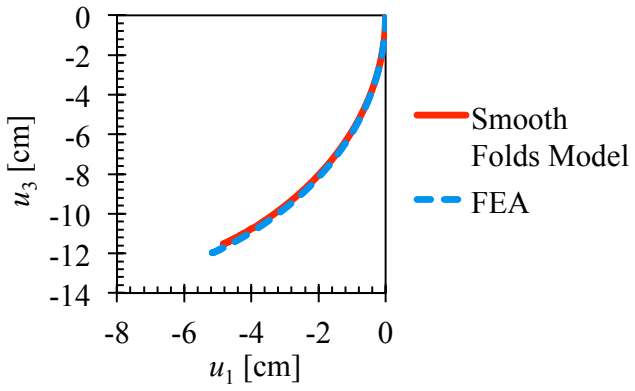

(b)

Figure 4.12: Results associated with the boundary value problem presented in Figure 4.11: (a) Configurations attained by the structure during the applied loading history (reference and final). The martensite volume fraction contour plot of the SMA layers is shown. (b) Two components of the displacement vector at a point exhibited during the applied loading history. Results using both the smooth folds model and FEA are shown.

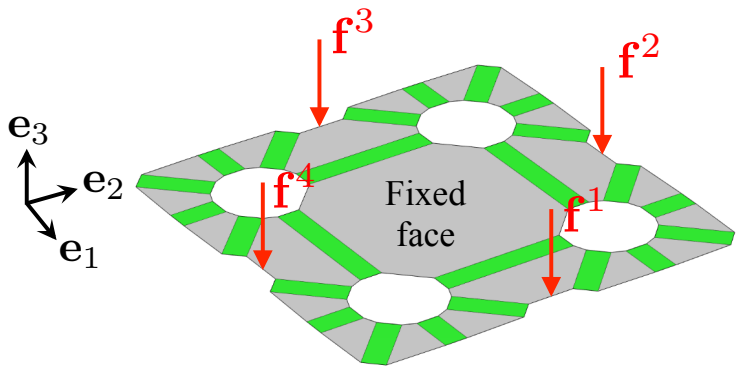

$$\mathbf{f}^1 = \mathbf{f}^2 = \mathbf{f}^3 = \mathbf{f}^4 = \begin{bmatrix} 0 \\ 0 \\ -200 \end{bmatrix} \text{ N}$$

Figure 4.13: Boundary value problem considering a structure having four fold intersections. The elastic smooth fold domains have thickness $\mathfrak{h}_i = 0.5$ mm. The material parameters of the elastic smooth fold domain are provided in Table 4.2.

Table 4.5: Wall-clock time in seconds required for each example considering SMA behavior.

Example	Smooth folds model	FEA	Difference (%)
Single fold example (Figure 4.7)	3.6	60	94.0%
Single fold intersection example (Figure 4.11)	82	2418	96.6%
Fold fold intersections example (Figure 4.15)	475	6215	92.4%

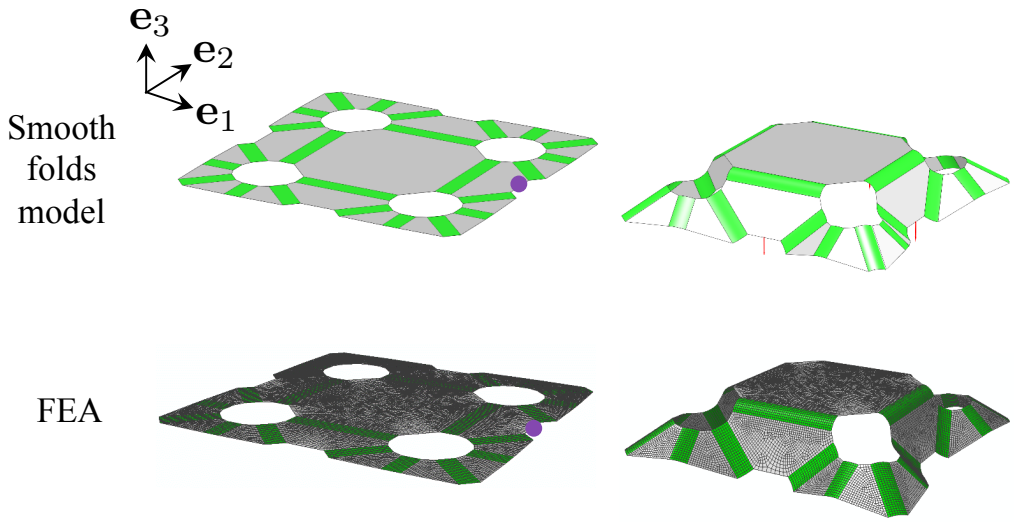

(a)

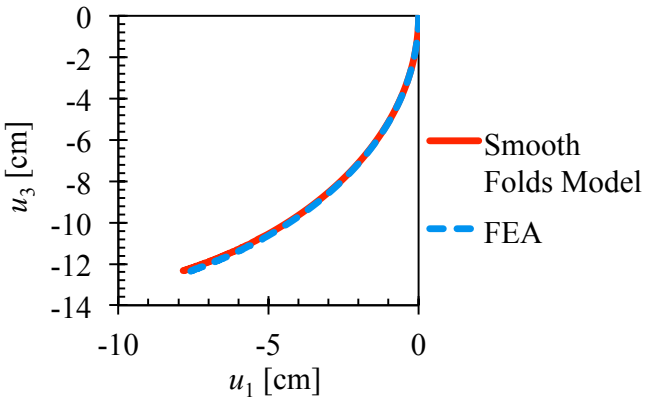

(b)

Figure 4.14: Results associated with the boundary value problem presented in Figure 4.13: (a) Configurations attained by the structure during the applied loading history (reference and final); (b) Two components of the displacement vector at a point exhibited by the origami structure during the applied loading history. Results using both the smooth folds model and FEA are shown.

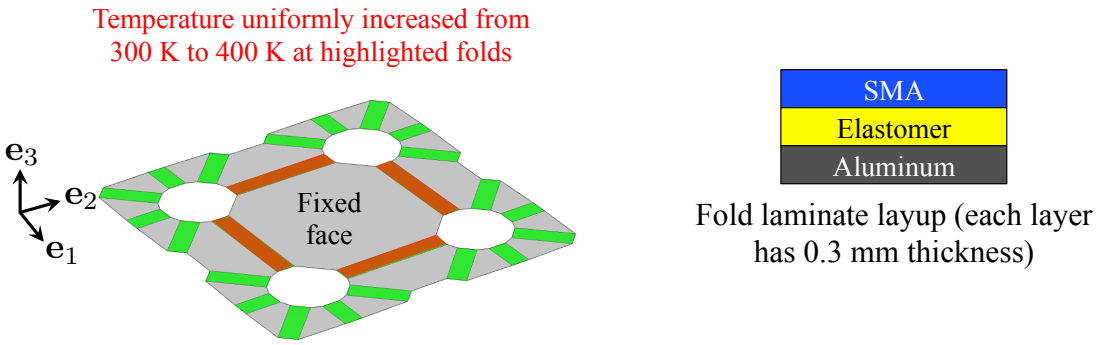

Figure 4.15: Boundary value problem considering a structure having four fold intersections and smooth fold domains comprised of a three-layer laminate. The folds at which the temperature is uniformly increased are highlighted. The material parameters of the SMA layers, the elastomer layers, and the aluminum layers are provided in Tables 4.3, 4.4, and 4.2, respectively. The material response of the SMA layers is defined by Equation (4.64) and $\varepsilon^{t0} = H_{sat}$.

4.4 Design of Self-folding Origami Structures with Smooth Folds

In this section, the design method for origami structures with smooth folds presented in Section 3 is extended for the design of self-folding structures morphed through active material actuation (unlike the purely kinematic-based approach taken in Section 3). First, it is noted that the origami design method presented in Section 3 allows for simple folding sequences for motion between the determined reference configuration $\mathcal{S}_0$ and the goal configuration $\mathcal{S}_\star$. In Section 3.6, the folding sequence is determined by simultaneously folding all the smooth folds in the origami structure. Such a characteristic is desirable and utilized here to develop a design method for self-folding origami structures with smooth folds. The method introduced here is based on simultaneous folding in structures having active smooth fold domains driven by uniform imposition of the activation field (e.g. uniform increase in temperature for SMAs). Therefore, the presented design method does not require

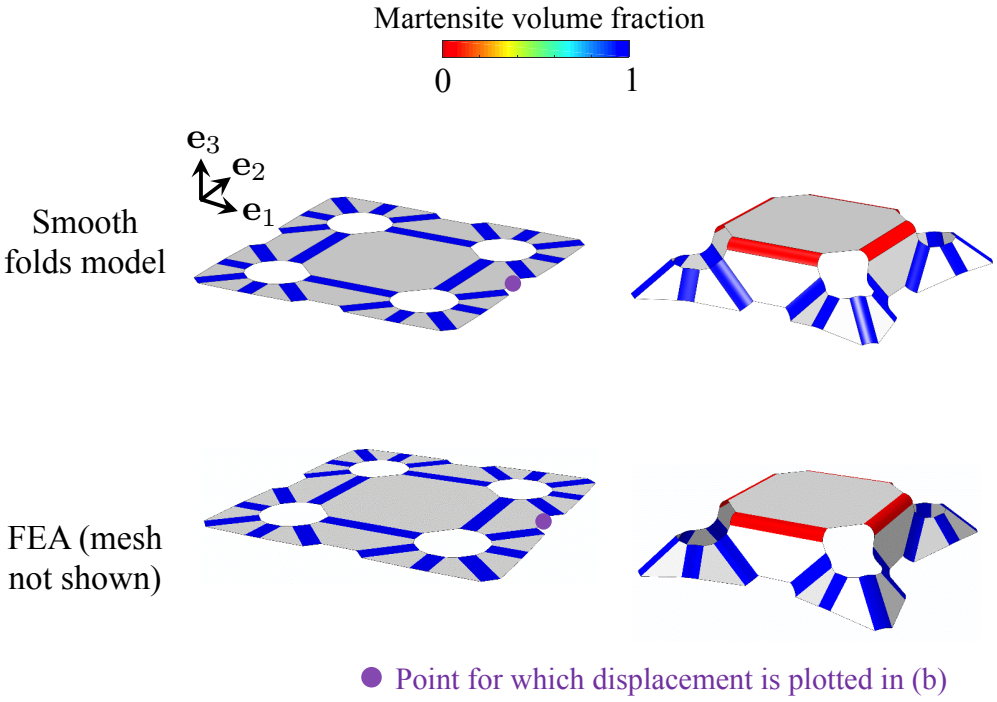

(a)

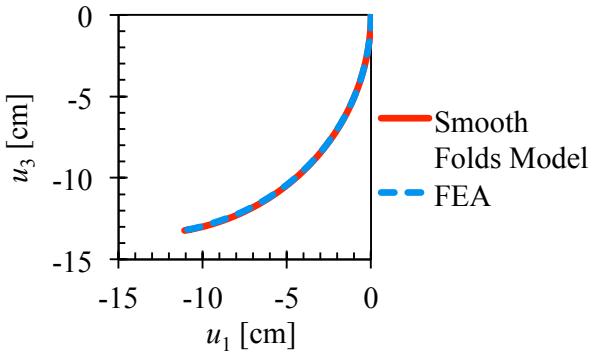

(b)

Figure 4.16: Results associated with the boundary value problem presented in Figure 4.15: (a) Configurations attained by the structure during the applied loading history (reference and final). The martensite volume fraction contour plot of the SMA layers is shown. (b) Two components of the displacement vector at a point exhibited during the applied loading history. Results using both the smooth folds model and FEA are shown.

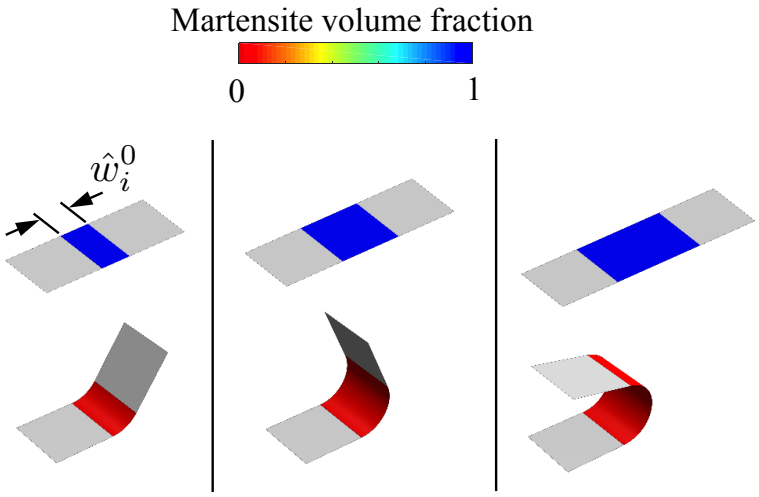

Figure 4.17: Simulation results of a sheet having a single smooth fold domain with the laminate layup shown in Figure 4.7. It is observed that by increasing the fold width $\hat{w}_i^0$, a higher fold angle magnitude can be achieved when the SMA layer is fully transformed into austenite.

any particular control over the actuation of each individual fold. The design method entails the consideration of the fold widths as design variables which dictate the fold angle achieved by the active smooth fold domain under the uniform imposition of the activation field. Figure 4.17 shows simulation results of a structure having a single smooth fold domain with the laminate layup shown in Figure 4.7. It is observed that by increasing the fold width $\hat{w}_i^0$, a higher fold angle magnitude can be achieved when the SMA layer is fully transformed from pre-strained martensite into austenite. Therefore, the fold widths $\hat{w}_i^0$, $i = 1, \ldots, N_{\mathcal{F}}$, must be considered as design variables in the present method, in contrast to the method addressed in Section 3 where the fold widths were given.

4.4.1 Problem Statement and Implementation

In the present design method, the laminate layup and material selection for each smooth fold domain are given. These can be determined prior to the application of the method by optimizing layer thicknesses and other design variables allowing for higher curvatures at the smooth folds. Such efforts are not discussed herein but were addressed previously in [8, 128, 361, 448]. The problem statement is as follows:

- Given: a goal shape represented as a polygonal mesh (termed as the *goal mesh* $\mathcal{M}$) and a laminate layup for the smooth fold domains in the structure,
- Find: the geometry of the reference configuration $\mathcal{S}_0$ of a single planar sheet that morphs towards a configuration that approximates $\mathcal{M}$ via active material-driven simultaneous folding.

Following the approach presented in Section 3, the geometry of the introduced edge modules in $\mathcal{S}_0$ (refer to Figure 3.2) is defined by the length variables $\hat{W}_i$ and the angle variables $\hat{\psi}_i$, $i = 1, \ldots, N_{\mathcal{E}}^I$ (where $N_{\mathcal{E}}^I$ is the number of interior edges in $\mathcal{M}$). Here, the fold widths $\hat{w}_i^0$, $i = 1, \ldots, N_{\mathcal{F}}$, are the newly introduced design variables. Each edge module has three smooth folds and thus $N_{\mathcal{F}} = 3N_{\mathcal{E}}^I$. Let $\mathbf{D} \in \mathbb{R}^{5N_{\mathcal{E}}^I}$ be the vector of design variables defined as follows (cf. Equation (3.29)):

$$\mathbf{D} := \begin{bmatrix} \hat{\boldsymbol{W}} \\ \hat{\boldsymbol{\psi}} \\ \hat{\boldsymbol{w}}^0 \end{bmatrix}, \tag{4.82}$$

where $\hat{\boldsymbol{W}} \in \mathbb{R}^{N_{\mathcal{E}}^I}$ is the vector having components $\hat{W}_i$, $i = 1, \ldots, N_{\mathcal{E}}^I$, and $\hat{\boldsymbol{\psi}} \in \mathbb{R}^{N_{\mathcal{E}}^I}$ is the vector having components $\hat{\psi}_i$, $i = 1, \ldots, N_{\mathcal{E}}^I$, defined in Equations (3.36) and (3.37), respectively. The vector $\hat{\boldsymbol{w}}^0 \in \mathbb{R}^{3N_{\mathcal{E}}^I}$ has components corresponding to the

fold widths $\hat{w}_i^0$, $i = 1, \ldots, 3N_{\mathcal{E}}^I$, and is defined in Equation (2.19). The optimization problem associated with this design method is stated as follows:

$$\begin{aligned} &\text{Find} && \mathbf{D} \\ &\text{That minimizes} && \|\hat{\boldsymbol{\theta}}^{t_f} - \hat{\boldsymbol{\theta}}^{\star}\| \\ &\text{Subject to} && \boldsymbol{h} = \mathbf{0}_{3N_{\mathcal{N}}^I} \\ & && \boldsymbol{g} \leq \mathbf{0}_{4N_{\mathcal{E}}^I} \\ & && \hat{\boldsymbol{w}}_L^0 \leq \hat{\boldsymbol{w}}^0 \leq \hat{\boldsymbol{w}}_U^0 \end{aligned} \tag{4.83}$$

where $\hat{\boldsymbol{\theta}}^{t_f} \in \mathbb{R}^{3N_{\mathcal{E}}^I}$ is the vector having components corresponding to the fold angles at the final configuration attained by the active origami structure (e.g. the fold angles of an SMA-based origami structure at full transformation from pre-strained martensite into austenite of the SMA layers in its folds). The vector $\hat{\boldsymbol{\theta}}^{\star} \in \mathbb{R}^{3N_{\mathcal{E}}^I}$ has components corresponding to the fold angles of the goal configuration $\mathcal{S}_{\star}$. The vectors $\boldsymbol{h} \in \mathbb{R}^{3N_{\mathcal{N}}^I}$ and $\boldsymbol{g} \in \mathbb{R}^{4N_{\mathcal{E}}^I}$ are those associated with the equality and inequality constraints of the design method presented in Section 3, respectively, allowing for a valid reference configurations $\mathcal{S}_0$ (refer to Section 3.4.2). The vectors $\hat{\boldsymbol{w}}_L^0 \in \mathbb{R}^{3N_{\mathcal{E}}^I}$ and $\hat{\boldsymbol{w}}_U^0 \in \mathbb{R}^{3N_{\mathcal{E}}^I}$ have components corresponding to the lower and upper bounds allowed for the fold widths. The optimization problem in Equation (4.83) is solved here using the gradient-based optimization algorithm in Matlab `fmincon`. Each design evaluation is performed using the model presented in Section 4.3.

4.4.2 Results

For the results presented in this section, the laminate layup shown in Figure 4.7 is adopted for all the examples. The material parameters of the SMA layer, the elastomer layer, and the aluminum layer of such a laminate layup are provided in

Tables 4.3, 4.4, and 4.2, respectively. The orientation of the laminate layup (i.e. whether the SMA layer is located on the top or the bottom of the laminate) is decided by the direction of the intended fold angle (see Figure 3.8). Figure 4.18 shows the goal mesh $\mathcal{M}$ and determined sheet design $\mathcal{S}_0$ associated with a goal shape of positive Gaussian curvature. As in the examples shown in Section 4.3.4, the temperature is raised from 300 K (where the SMA is fully in pre-strained martensite phase) to 400 K (where the SMA has completed full transformation into austenite). Configurations attained by the designed structure during its deformation history are also shown in Figure 4.18.

Figure 4.19 shows the same results as those in Figure 4.18 but considering a goal mesh associated with a shape of negative Gaussian curvature. Both examples show that the design method successfully provides the geometry of the reference configuration $\mathcal{S}_0$ of a single planar sheet that morphs towards a configuration that approximates $\mathcal{M}$ via active material-driven simultaneous folding. The examples addressed in Section 3 of goal meshes having not only triangulated faces (illustrated in Figures 3.22 and 3.23) are revisited here and their associated results are shown in Figures 4.20 and 4.21, respectively. It is observed in these figures that the present design method for self-folding structures successfully provides results for such examples. Although only examples where SMA actuation is utilized are provided here, the present design method is applicable to structures having smooth fold domains comprised of other active materials so long as strains are small enough such that the linearized strain tensor can be utilized to properly model the deformation.

4.5 Summary and Discussion

A model for the structural response of origami bodies with smooth folds was presented in this section. The description of motion and kinematic constraints for

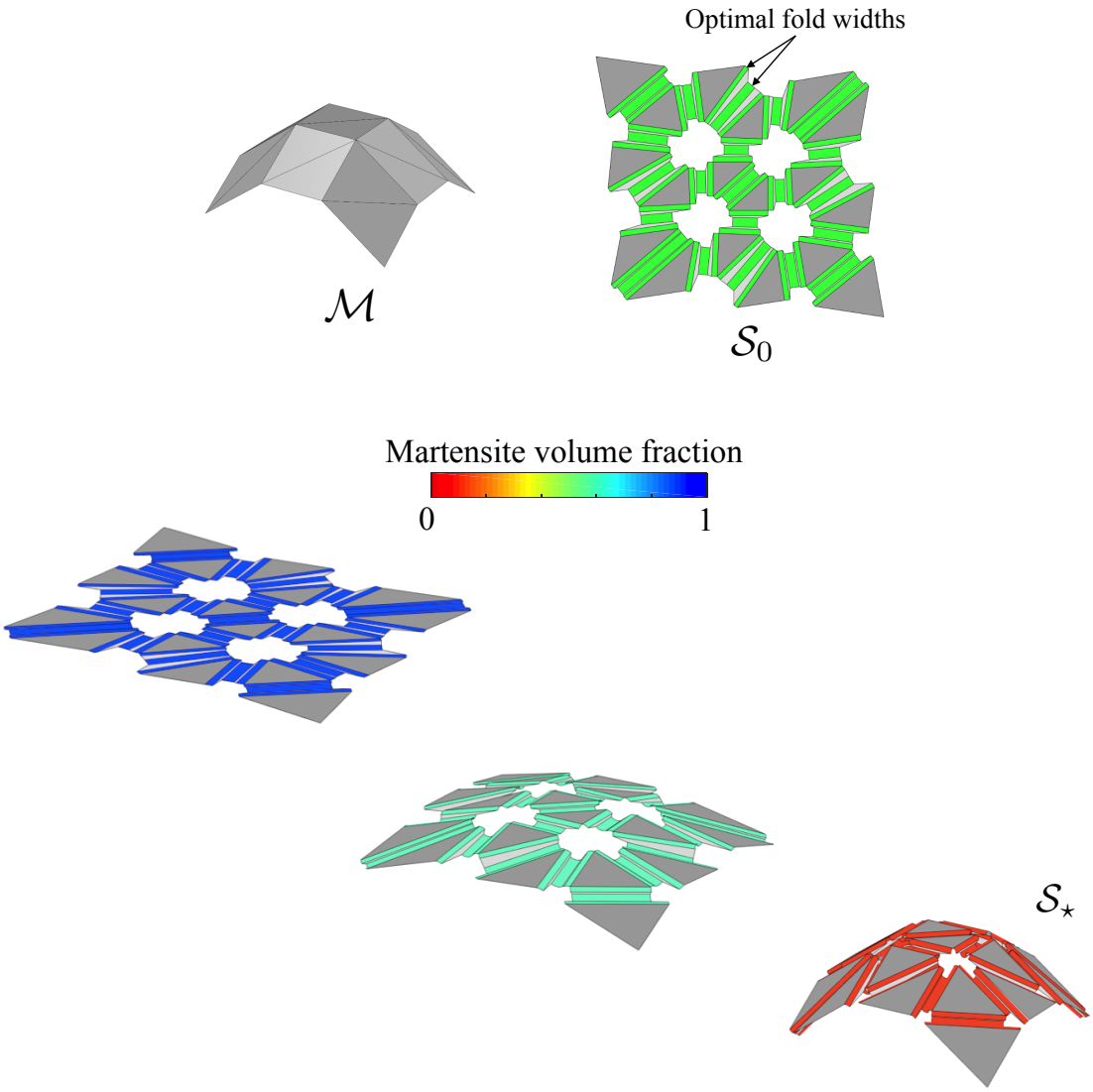

Figure 4.18: Implementation results of the design method for self-folding structures associated with a dome goal mesh. The goal mesh, its associated determined sheet design with optimal fold widths, and the configurations attained by the structure during its deformation history are shown.

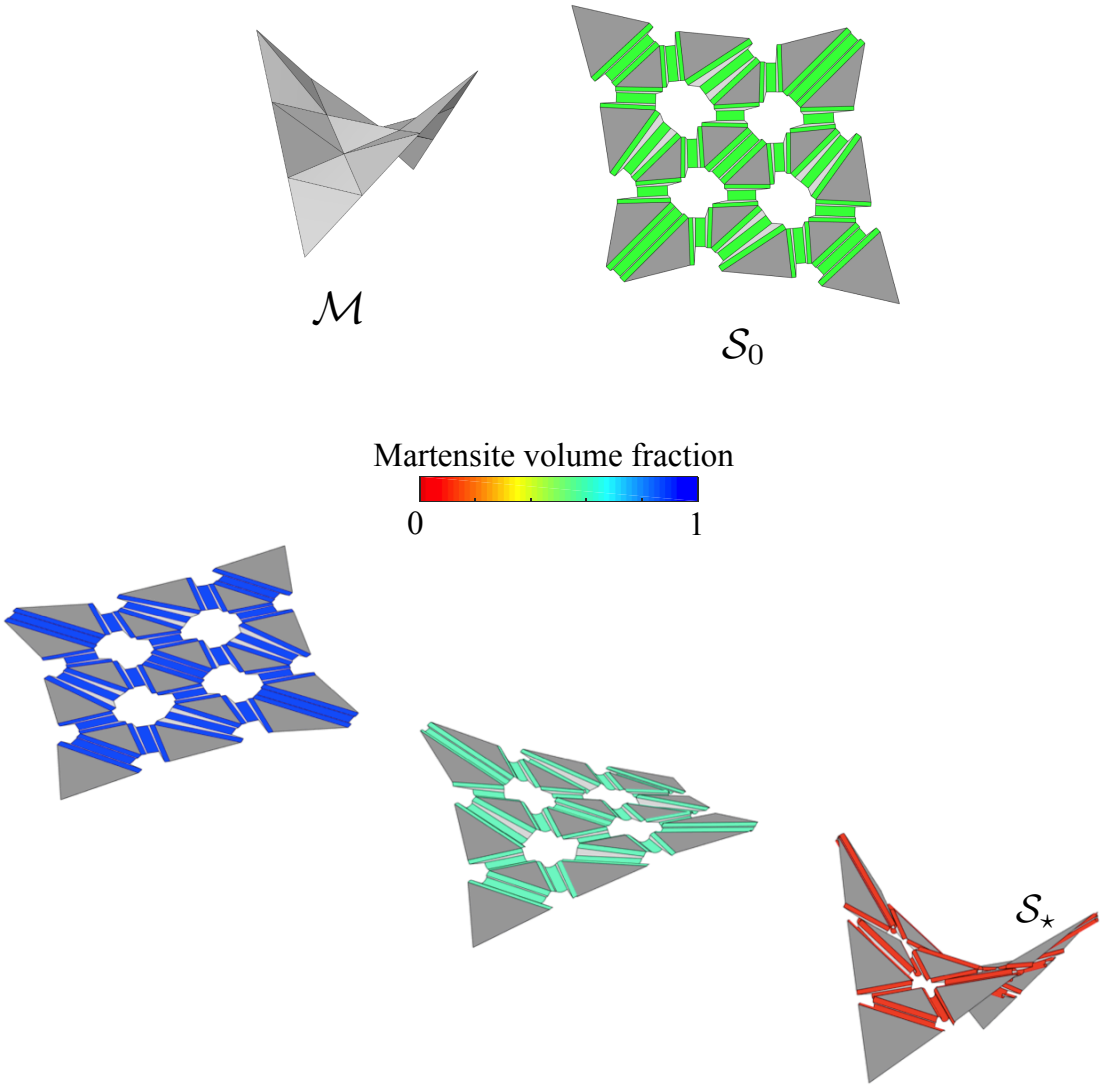

Figure 4.19: Implementation results of the design method for self-folding structures associated with a saddle goal mesh. The goal mesh, its associated determined sheet design with optimal fold widths, and the configurations attained by the structure during its deformation history are shown.

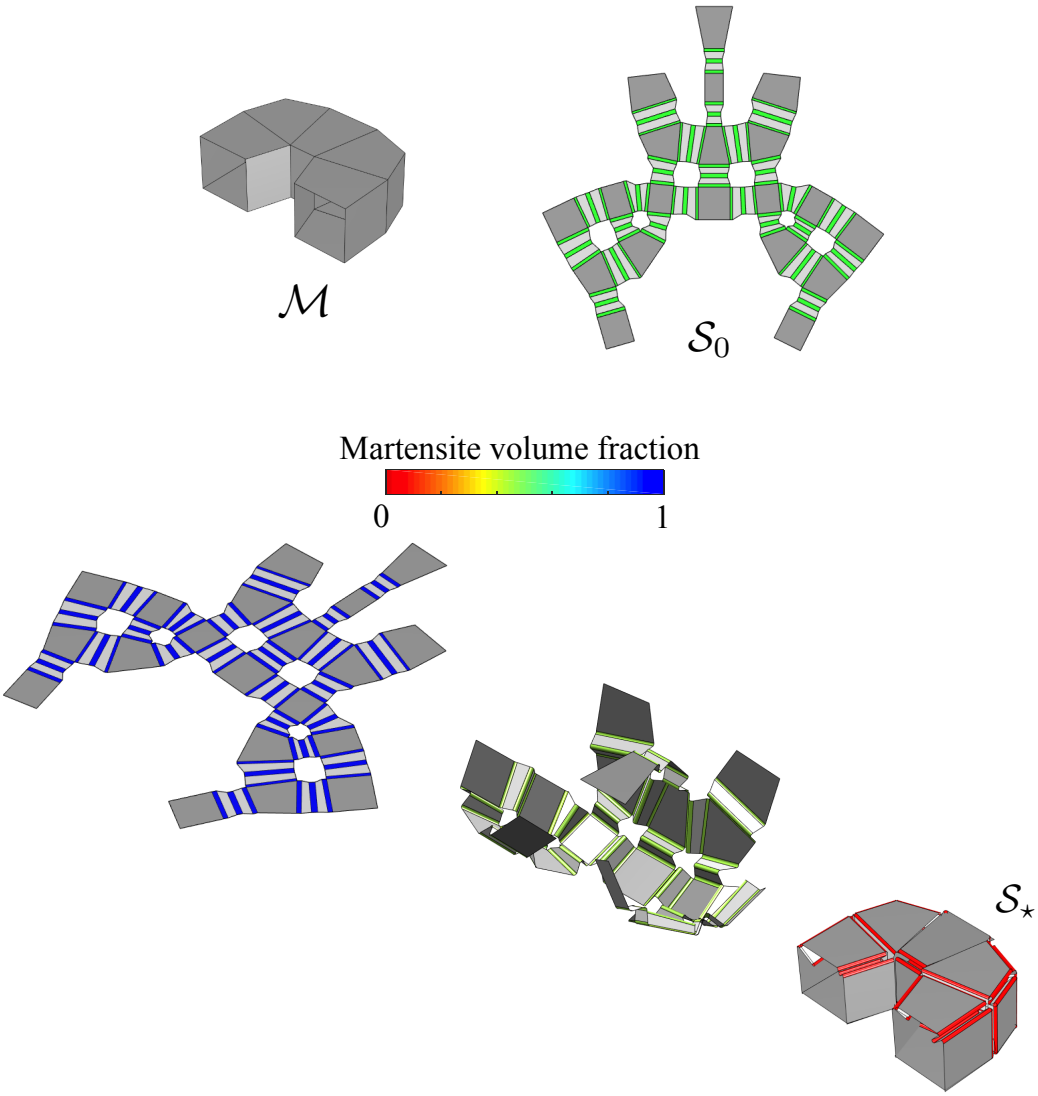

Figure 4.20: Implementation results of the design method for self-folding structures associated with a goal mesh comprised of quadrilateral faces. The goal mesh, its associated determined sheet design with optimal fold widths, and the configurations attained by the structure during its deformation history are shown.

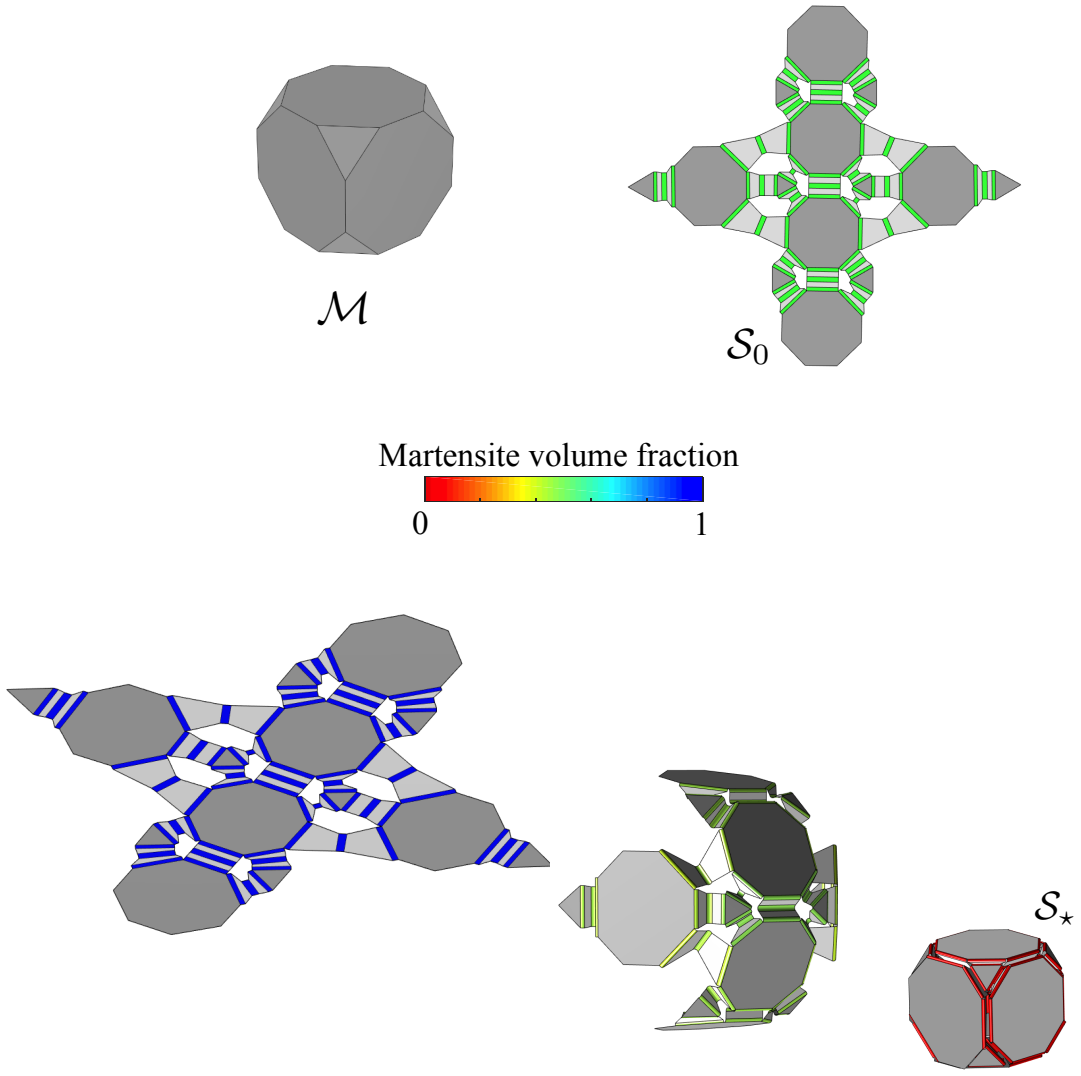

Figure 4.21: Implementation results of the design method for self-folding structures associated with a goal mesh comprised of triangular and octagonal faces. The goal mesh, its associated determined sheet design with optimal fold widths, and the configurations attained by the structure during its deformation history are shown.

the model correspond to those presented in Section 2. Relations between the strain field in each smooth fold domain of non-zero thickness and their fold angle and fold arc-length were derived. Consequently, the kinematic variables fully describing the deformation of origami structures having smooth fold domains of non-zero thickness correspond to the fold angles and fold arc-lengths of each fold in the structure. The governing field equations were presented and the principle of virtual work including the consideration of kinematic constraints was used to develop a structural mechanics model for origami bodies. The present model does not make any assumptions on the material response of the origami structures; therefore, it is applicable to a large spectrum of origami structures (ranging from those having elastic folds to those having active material actuation). The numerical implementation of the model was described and various implementation examples were presented. The results determined using the present model were numerically validated against higher-fidelity FEA and good agreement is observed for all the examples. Furthermore, it was shown that the present model is significantly more computationally efficient as compared to FEA (by more than 90% in the examples shown) while providing accurate results. Thus, it can be utilized for computationally efficient structural analysis of origami bodies having smooth fold domains such as the active material based-morphing structures described in Section 1.

The design method for origami with smooth folds presented in Section 3 was then revisited and extended for the design of self-folding structures morphed through active material actuation. The approach is based on simultaneous folding in structures having active smooth fold domains driven by uniform imposition of the activation field (e.g. uniform increase in temperature for SMAs). Therefore, the presented design method does not require any particular control over the actuation of each individual fold. The design method entails the consideration of the fold widths as design

variables which dictate the fold angle achieved by the active smooth fold domain under the uniform imposition of the activation field. The numerical implementation of the design method is presented. Results of SMA-based origami structures that morph into arbitrary three-dimensional shapes starting from a planar configuration are provided.

5. SUMMARY AND FUTURE WORK

Although the art of origami is ancient, the science and technology associated with origami engineering structures is new and developing rapidly. After reviewing the existing and prospective applications origami-inspired structures (with and without self-folding capabilities) in Sections 1.1 and 1.2, it was clear that origami has the potential to enable new advancements in various fields such as aerospace, manufacturing, robotics, architecture, etc. To allow or facilitate such advancements, modeling and design approaches for origami structures are needed and hence there is ongoing research on the subject. From the literature review on modeling and design of origami structures presented in Sections 1.3–1.5, it was evident that there is a gap between realistic folding behavior and existing models and design methods that mostly focus on conventional origami with creased folds. Consequently, new approaches for origami modeling and design are needed and were the focus of this dissertation. The work presented in the previous sections is summarized here and suggestions for future work are provided.

5.1 Kinematics of Origami Structures with Smooth Folds

A model for the kinematic response of origami structures with smooth folds having non-zero surface area and arbitrary order of geometric continuity was presented in Section 2. Therein, the folds are not limited to G^0 creases as conventionally assumed in the literature but instead may have non-zero surface area and arbitrary order of geometric continuity G^n (termed as smooth folds). By considering G^n continuity at the folds, the realistic response of origami structures based on the bending concepts (Figures 1.4(d) and (e)) can be properly captured. The section begins with a review of an established model for origami with conventional creased folds that

is adopted and extended in this work. Subsequently, the geometrical description of smooth folds was presented in Section 2.2.1 and parametric representations of the fold cross-sectional shape for various orders of geometric continuity were provided. The fold pattern description, the constraints on the sheet deformation for origami with smooth folds analogous to those for origami with creased folds, and the mapping between reference and current configurations were also presented. The numerical implementation of the model allowing for simulation of the motion of sheets having arbitrary fold patterns and subject to arbitrary folding sequences was described and implementation examples were provided.

The model for conventional origami with creased folds of zeroth-order geometric continuity reviewed in Section 2.1 represents a special case of the proposed model for origami with smooth folds and is captured as well. It is shown in Appendix C that the known kinematic constraints for origami with creased folds are a special case of those derived here for origami with smooth folds.

There are various directions for future work in the modeling of the kinematics of origami structures with smooth folds. First, fold intersections surfaces briefly introduced in Section 2.2 (refer to Figure 2.4) were not addressed in the current work. For the modeling of origami structures in which holes at the fold intersections are not desired, parametric formulations for the fold intersection surfaces and kinematic variables defining their geometry must be addressed. Another effort suggested for future work entails the consideration of contact detection algorithms to prevent self-intersections in the kinematic simulation procedure, which were not considered in this work. Also, here the reference configuration of the smooth folds is simplified to a rectangular shape and their deformation only includes stretching and bending of the fold cross-section. However, the kinematic modeling framework proposed in Section 2 can be extended for the consideration of folds having a trapezoidal refer-

ence configuration (that deform into conical sections) or folds that exhibit torsional deformation. Such extensions are also recommended for future studies.

5.2 Design of Origami Structures with Smooth Folds

Section 3 addresses a method for the design of origami structures with smooth folds. The method is developed based on the previously known idea of using modules having three folds and two rigid faces to create flaps that are tuck folded to morph an initially planar sheet into an arbitrary three-dimensional goal shape represented as a polygonal manifold mesh [9, 391]. The method solves the origami design problem of finding the geometry of a single planar sheet and its pattern of smooth folds that allow for the approximation of a goal mesh through such a tuck-based folding. The work presented in Section 3 includes parameterization of the sheet design, constraints on the design variables, and a numerical solution procedure.

A process for determining a folding sequence allowing for folding motion from the determined planar sheet configuration to the folded configuration that approximates the goal mesh is also presented. Such a process has not been previously addressed in related work (e.g. [9, 391]). Therefore, the determination of such a folding sequence addressed here represents another contribution of the present work and is applicable to both origami with smooth folds and conventional origami with creased folds. The design method is shown to successfully provide origami structures that can be physically realized with various engineering materials due to the consideration of arbitrary order of continuity G^n at the folds. The method was tested against goal meshes of various geometries and complexities and successful results were obtained for each.

For origami design problems in which the goal shape is not a polyhedral surface (e.g. a smooth surface), the process to determine a mesh discretization of such a

surface before the utilization of the method presented in Section 3 must be addressed. Multiple algorithms for obtaining polygonal mesh discretizations of smooth surfaces are available in the literature [437, 438]. Also, algorithms to determine a boundary that yields a surface mesh topologically equivalent to a disk (a necessary property for the applicability of the proposed design method) are available in the literature [9, 434, 435, 436, 452] and were not addressed in the work presented in Section 3. Thus, one direction for future work is the development of a tool for origami design that integrates in a synergistic manner the mesh determination or simplification [453, 454], determination of an optimal mesh boundary, and the design method presented in Section 3.

5.3 Structural Mechanics of Origami Bodies

As identified in Section 1, active materials can play a significant role in the realization of self-folding origami structures. Researchers have demonstrated self-folding behavior in many active material-based structures with activation fields that include thermal, chemical, electrical, and magnetic. Several combinations of materials, geometry, and inducing field are feasible, yielding a large spectrum of design options. To allow for developments of such origami structures, models for their structural mechanics must be created and were the focus of Section 4.

Section 4 presents a model for the structural response of origami bodies with smooth folds domains of non-zero thickness. The kinematic variables and constraints for the model correspond to those provided in Section 2. The kinematic variables that fully describe the configuration of origami structures having smooth fold domains of non-zero thickness corresponded to the fold angles and fold arc-lengths of each fold in the structure. The governing field equations were presented and the principle of virtual work including the consideration of kinematic constraints via a penalty method

was used to develop a structural mechanics model for continuum origami bodies. No assumptions about the material response of the origami structures were made on the derivation of the model; thus, it is applicable to a wide domain of origami structures. The numerical implementation of the model was described in detail. Implementation examples considering structures having smooth fold domains comprised of elastic and SMA materials were considered therein. Nevertheless, it is remarked that the present model is applicable to smooth folds comprised of other passive or active materials so long as strains are small enough such that the linearized strain tensor can be utilized to properly model their deformation. The results determined using the present model were numerically validated against FEA and good agreement was observed for all the examples. Moreover, the present model was shown to be significantly more computationally efficient as compared to FEA while providing comparable results.

The design method for origami structures with smooth folds developed in Section 3 was then extended for the design of self-folding structures morphed through active material actuation. The considered approach assumes simultaneous folding in structures having active smooth fold domains driven by uniform imposition of the activation field (such as a uniform increase in temperature for SMA-based structures). Therefore, the presented design method does not require any particular control over the actuation of each individual fold. The design method entails the consideration of the fold widths as design variables which determine the fold angle achieved by the active smooth fold domain under the uniform imposition of the activation field. Results of SMA-based origami structures that morph towards arbitrary three-dimensional shapes starting from a planar configuration are provided. Further examples of the design method for active self-folding structures of Section 4.4 considering other active materials (e.g. SMPs) could be considered in future work.

Regarding the design method for self-folding origami structures presented in Sec-

tion 4.4, it is recommended as future work to consider sensitivity analyses to determine the influence of the various material and geometric parameters on the resulting folding response (i.e. whether variations in such parameters could considerably affect the final fold angles and thus result in a configuration significantly different from the goal configuration). In the model developed in Section 4, classical plate theory assumptions are made for the kinematics of the plate representation for each smooth fold domain. For future work, higher-order plate theories [355, 455, 456] or layerwise theories [354, 457] may be considered to improve the current model.

REFERENCES

[1] S. Miyashita, S. Guitron, M. Ludersdorfer, C. R. Sung, and D. Rus. An untethered miniature origami robot that self-folds, walks, swims, and degrades. In *Proceedings of the 2015 IEEE International Conference on Robotics and Automation (ICRA)*, pages 1490–1496. IEEE, 2015.

[2] N. Bassik, G. M. Stern, and D. H. Gracias. Microassembly based on hands free origami with bidirectional curvature. *Applied Physics Letters*, 95(9):091901, 2009.

[3] E. A. Peraza-Hernandez, D. J. Hartl, R. J. Malak Jr, and D. C. Lagoudas. Origami-inspired active structures: a synthesis and review. *Smart Materials and Structures*, 23(9):094001, 2014.

[4] D. C. Lagoudas (editor). *Shape Memory Alloys: Modeling and Engineering Applications*. Springer Science + Business Media, LLC, New York, NY, 2008.

[5] E. Hawkes, B. An, N. M. Benbernou, H. Tanaka, S. Kim, E. D. Demaine, D. Rus, and R. J. Wood. Programmable matter by folding. *Proceedings of the National Academy of Sciences*, 107(28):12441–12445, 2010.

[6] E. Peraza-Hernandez, D. Hartl, and D. Lagoudas. Shape memory alloy laminate for design of self-folding reconfigurable structures. In *The 19th International Conference on Composite Materials*, Montreal, Canada, 2013.

[7] E. A. Peraza Hernandez, D. J. Hartl, and D. C. Lagoudas. Kinematics of origami structures with smooth folds. *Journal of Mechanisms and Robotics*, 8(6):061019, 2016.

[8] E. A. Peraza-Hernandez, D. J. Hartl, and R. J. Malak Jr. Design and numerical analysis of an SMA mesh-based self-folding sheet. *Smart Materials and Structures*, 22(9):094008, 2013.

[9] T. Tachi. Origamizing polyhedral surfaces. *IEEE Transactions on Visualization and Computer Graphics*, 16(2):298–311, 2010.

[10] E. A. Peraza Hernandez, B. Kiefer, D. J. Hartl, A. Menzel, and D. C. Lagoudas. Analytical investigation of structurally stable configurations in shape memory alloy-actuated plates. *International Journal of Solids and Structures*, 69:442–458, 2015.

[11] E. Peraza Hernandez, D. Hartl, E. Akleman, and D. Lagoudas. Modeling and analysis of origami structures with smooth folds. *Computer-Aided Design*, 78:93 – 106, 2016.

[12] L. Ionov. Soft microorigami: self-folding polymer films. *Soft Matter*, 7(15):6786–6791, 2011.

[13] E. D. Demaine and J. O'Rourke. *Geometric Folding Algorithms*. Cambridge University Press, Cambridge, 2007.

[14] R. J. Lang. The science of origami. *Physics World*, 20(2):30–31, 2007.

[15] R. J. Lang. Origami: Complexity in creases (again). *Engineering and Science*, 67(1):5–19, 2004.

[16] E. D. Demaine. Folding and unfolding linkages, paper, and polyhedra. In *Discrete and Computational Geometry*, pages 113–124. Springer, 2001.

[17] L. J. Fei and D. Sujan. Origami theory and its applications: A literature review. *International Journal of Social, Human Science and Engineering*, 7(1):113 – 117, 2013.

[18] B. A. Cipra. In the fold: Origami meets mathematics. *SIAM News*, 34(8):1–4, 2001.

[19] T. Tarnai. Origami in structural engineering. In *Proceedings of the IASS Symposium 2001: International Symposium on Theory, Design and Realization of Shell and Spatial Structures, Nagoya, Japan, 9-13 Oct. 2001*, pages 298–299, 2001.

[20] X. Zhou, H. Wang, and Z. You. Design of three-dimensional origami structures based on a vertex approach. *Proceedings of the Royal Society of London A: Mathematical, Physical and Engineering Sciences*, 471(2181):20150407, 2015.

[21] D. Dureisseix. An overview of mechanisms and patterns with origami. *International Journal of Space Structures*, 27(1):1–14, 2012.

[22] E. D. Demaine, M. L. Demaine, V. Hart, G. N. Price, and T. Tachi. (Non)existence of pleated folds: How paper folds between creases. *Graphs and Combinatorics*, 27(3):377–397, 2011.

[23] C. Cromvik and K. Eriksson. Airbag folding based on origami mathematics. In *Origami 4: Fourth International Meeting of Origami Science, Mathematics, and Education*, pages 129–139, 2006.

[24] R. Hoffman. Airbag folding: Origami design applied to an engineering problem. In *Third International Meeting of Origami Science Math and Education, Asilomar, CA*, 2001.

[25] S. Gray, N. Zeichner, V. Kumar, and M. Yim. A simulator for origami-inspired self-reconfigurable robots. In *Origami 5: Fifth International Meeting of Origami Science, Mathematics, and Education*, pages 323–333. CRC Press, 2011.

[26] W. Gao, K. Ramani, R. J. Cipra, and T. Siegmund. Kinetogami: A reconfigurable, combinatorial, and printable sheet folding. *Journal of Mechanical Design*, 135(11):111009, 2013.

[27] S. Pandey, E. Gultepe, and D. H. Gracias. Origami inspired self-assembly of patterned and reconfigurable particles. *Journal of Visualized Experiments: JoVE*, (72):e50022, 2013.

[28] N. S. Shaar, G. Barbastathis, and C. Livermore. Integrated folding, alignment, and latching for reconfigurable origami microelectromechanical systems. *Journal of Microelectromechanical Systems*, 24(4):1043–1051, 2015.

[29] E. T. Filipov, G. H. Paulino, and T. Tachi. Origami tubes with reconfigurable polygonal cross-sections. *Proceedings of the Royal Society A: Mathematical, Physical and Engineering Sciences*, 472(2185):20150607, 2016.

[30] S. Yao, S. V. Georgakopoulos, B. Cook, and M. Tentzeris. A novel reconfigurable origami accordion antenna. In *Proceedings of the IEEE/RSJ International Conference on Intelligent Robots and Systems, Chicago, IL, USA*, pages 14–18, 2014.

[31] Z. You. Folding structures out of flat materials. *Science*, 345(6197):623–624, 2014.

[32] C. D. Saintsing, B. S. Cook, and M. M. Tentzeris. An origami inspired reconfigurable spiral antenna. In *Proceedings of the ASME 2014 International Design Engineering Technical Conferences and Computers and Information in Engineering Conference IDETC/CIE*, pages Paper No. DETC2014–35353, pp. V05BT08A050. American Society of Mechanical Engineers, 2014.

[33] S. Mueller, B. Kruck, and P. Baudisch. Laser Origami: laser-cutting 3D objects. In *Proceedings of the SIGCHI Conference on Human Factors in Computing Systems*, pages 2585–2592. ACM, 2013.

[34] B. Shin, S. M. Felton, M. T. Tolley, and R. J. Wood. Self-assembling sensors for printable machines. In *Proceedings of the 2014 IEEE International Conference on Robotics and Automation (ICRA)*, pages 4417–4422. IEEE, 2014.

[35] J. Morgan, S. P. Magleby, R. J. Lang, and L. L. Howell. A preliminary process for understanding origami-adapted design. In *Proceedings of the ASME 2015 International Design Engineering Technical Conferences and Computers and Information in Engineering Conference IDETC/CIE*, pages No. DETC2015–47559, pp. V05BT08A053. American Society of Mechanical Engineers, 2015.

[36] B. An, S. Miyashita, M. T. Tolley, D. M. Aukes, L. Meeker, E. D. Demaine, M. L. Demaine, R. J. Wood, and D. Rus. An end-to-end approach to making self-folded 3D surface shapes by uniform heating. In *Proceedings of the 2014 IEEE International Conference on Robotics and Automation (ICRA)*, pages 1466–1473. IEEE, 2014.

[37] A. Piqué, S. A. Mathews, N. A. Charipar, and A. J. Birnbaum. Laser origami: a new technique for assembling 3D microstructures. In *Proceedings of SPIE*, volume 8244, pages 82440B–82440B–7. International Society for Optics and Photonics, 2012.

[38] P. W. K. Rothemund. Folding DNA to create nanoscale shapes and patterns. *Nature*, 440(7082):297–302, 2006.

[39] T. Tørring, N. V. Voigt, J. Nangreave, H. Yan, and K. V. Gothelf. DNA origami: a quantum leap for self-assembly of complex structures. *Chemical Society Reviews*, 40(12):5636–5646, 2011.

[40] J. Nangreave, D. Han, Y. Liu, and H. Yan. DNA origami: a history and current perspective. *Current Opinion in Chemical Biology*, 14(5):608–615, 2010.

[41] A. Edwards and H. Yan. DNA origami. In *Nucleic Acid Nanotechnology*, pages 93–133. Springer, 2014.

[42] A. E. Marras, L. Zhou, H.-J. Su, and C. E. Castro. Programmable motion of DNA origami mechanisms. *Proceedings of the National Academy of Sciences*, 112(3):713–718, 2015.

[43] C. Cao, Y. Feng, J. Zang, G. P. López, and X. Zhao. Tunable lotus-leaf and rose-petal effects via graphene paper origami. *Extreme Mechanics Letters*, 4:18–25, 2015.

[44] K. Miura. Map fold a la Miura style, its physical characteristics and application to the space science. *Research of Pattern Formation, ktk scientific publishers Edition. R. Takaki*, pages 77–90, 1994.

[45] R. J. Lang. Computational origami: from flapping birds to space telescopes. In *Proceedings of the Twenty-fifth Annual Symposium on Computational Geometry*, pages 159–162. ACM, 2009.

[46] L. Wilson, S. Pellegrino, and R. Danner. Origami sunshield concepts for space telescopes. In *Proceedings of the 54th AIAA/ASME/ASCE/AHS/ASC Structures, Structural Dynamics, and Materials Conference*, pages 2013–1594, 2013.

[47] D. Pohl and W. D. Wolpert. Engineered spacecraft deployables influenced by nature. In *Proceedings of SPIE*, volume 7424, pages 742408–742408–9, 2009.

[48] J. T. Early, R. Hyde, and R. L. Baron. Twenty-meter space telescope based on diffractive Fresnel lens. In *Proceedings of the SPIE's 48th Annual Meet-*

ing, Optical Science and Technology, pages 148–156. International Society for Optics and Photonics, 2004.

[49] J. M. Zanardi Ocampo, P. O. Vaccaro, K. Kubota, T. Fleischmann, T.-S. Wang, T. Aida, T. Ohnishi, A. Sugimura, R. Izumoto, M. Hosoda, et al. Characterization of GaAs-based micro-origami mirrors by optical actuation. *Microelectronic Engineering*, 73:429–434, 2004.

[50] Q. Cheng, Z. Song, T. Ma, B. B. Smith, R. Tang, H. Yu, H. Jiang, and C. K. Chan. Folding paper-based lithium-ion batteries for higher areal energy densities. *Nano Letters*, 13(10):4969–4974, 2013.

[51] Z. Song, T. Ma, R. Tang, Q. Cheng, X. Wang, D. Krishnaraju, R. Panat, C. K. Chan, H. Yu, and H. Jiang. Origami lithium-ion batteries. *Nature Communications*, 5:No. 3140, 2014.

[52] I. Nam, G.-P. Kim, S. Park, J. W. Han, and J. Yi. All-solid-state, origami-type foldable supercapacitor chips with integrated series circuit analogues. *Energy & Environmental Science*, 7(3):1095–1102, 2014.

[53] S. Miyashita, L. Meeker, M. T. Tolley, R. J. Wood, and D. Rus. Self-folding miniature elastic electric devices. *Smart Materials and Structures*, 23(9):094005, 2014.

[54] R. Tang, H. Huang, H. Tu, H. Liang, M. Liang, Z. Song, Y. Xu, H. Jiang, and H. Yu. Origami-enabled deformable silicon solar cells. *Applied Physics Letters*, 104(8):083501, 2014.

[55] J. W. Hu, Z. P. Wu, S. W. Zhong, W. B. Zhang, S. Suresh, A. Mehta, and N. Koratkar. Folding insensitive, high energy density lithium-ion battery featuring carbon nanotube current collectors. *Carbon*, 87:292–298, 2015.

[56] D.-Y. Lee, J.-S. Kim, S.-R. Kim, J.-S. Koh, and K.-J. Cho. The deformable wheel robot using magic-ball origami structure. In *Proceedings of the ASME 2013 International Design Engineering Technical Conferences and Computers and Information in Engineering Conference IDETC/CIE*, pages Paper DETC2013–13016, pp. V06BT07A040. American Society of Mechanical Engineers, 2013.

[57] P. J. White, S. Latscha, S. Schlaefer, and M. Yim. Dielectric elastomer bender actuator applied to modular robotics. In *Proceedings of the 2011 IEEE/RSJ International Conference on Intelligent Robots and Systems (IROS)*, pages 408–413. IEEE, 2011.

[58] A. M. Hoover and R. S. Fearing. Fast scale prototyping for folded millirobots. In *Proceedings of the 2008 IEEE International Conference on Robotics and Automation ICRA 2008*, pages 886–892. IEEE, 2008.

[59] E. Vander Hoff, D. Jeong, and K. Lee. OrigamiBot-I: A thread-actuated origami robot for manipulation and locomotion. In *Proceedings of the 2014 IEEE/RSJ International Conference on Intelligent Robots and Systems*, pages 1421–1426. IEEE, 2014.

[60] Z. Zhakypov, M. Falahi, M. Shah, and J. Paik. The design and control of the multi-modal locomotion origami robot, Tribot. In *Proceedings of the 2015 IEEE/RSJ International Conference on Intelligent Robots and Systems (IROS)*, pages 4349–4355. IEEE, 2015.

[61] C. D. Onal, M. T. Tolley, R. J. Wood, and D. Rus. Origami-inspired printed robots. *IEEE/ASME Transactions on Mechatronics*, 20(5):2214–2221, 2015.

[62] K. Zhang, C. Qiu, and J. S. Dai. An extensible continuum robot with integrated origami parallel modules. *Journal of Mechanisms and Robotics*, 8(3):031010,

2016.

[63] H. Shigemune, S. Maeda, Y. Hara, N. Hosoya, and S. Hashimoto. Origami robot: A self-folding paper robot with an electrothermal actuator created by printing. *IEEE/ASME Transactions on Mechatronics*, (99):1–9, 2016.

[64] Y. Jung and J. Kim. Flutter speed estimation for folding wing system. In *Proceedings of the 18th International Conference on Composite Materials*, 2011.

[65] M. P. Snyder, B. Sanders, F. E. Eastep, and G. J. Frank. Vibration and flutter characteristics of a folding wing. *Journal of Aircraft*, 46(3):791–799, 2009.

[66] D. H. Lee and T. A. Weisshaar. Aeroelastic studies on a folding wing configuration. In *46th AIAA/ASME/ASCE/AHS/ASC Structures, Structural Dynamics & Materials Conference*, volume 1996, pages 1–13, 2005.

[67] G. Bunget and S. Seelecke. BATMAV: a biologically inspired micro air vehicle for flapping flight: kinematic modeling. In *Proceedings of the 15th International Symposium on Smart Structures and Materials & Nondestructive Evaluation and Health Monitoring*, page 69282F. International Society for Optics and Photonics, 2008.

[68] G. Bunget and S. Seelecke. BATMAV: a 2-DOF bio-inspired flapping flight platform. In *Proceedings of the SPIE Smart Structures and Materials+ Nondestructive Evaluation and Health Monitoring*, page 76433B. International Society for Optics and Photonics, 2010.

[69] P. E. I. Pounds. Paper plane: Towards disposable low-cost folded cellulose-substrate UAVs. In *2012 Australasian Conference on Robotics and Automation*. Australian Robotics and Automation Association (ARAA), 2012.

[70] Q.-T. Truong, B. W. Argyoganendro, and H. C. Park. Design and demonstration of insect mimicking foldable artificial wing using four-bar linkage systems. *Journal of Bionic Engineering*, 11(3):449 – 458, 2014.

[71] S. Fischer, K. Drechsler, S. Kilchert, and A. Johnson. Mechanical tests for foldcore base material properties. *Composites Part A: Applied Science and Manufacturing*, 40(12):1941 – 1952, 2009.

[72] S. Heimbs, J. Cichosz, M. Klaus, S. Kilchert, and A. F. Johnson. Sandwich structures with textile-reinforced composite foldcores under impact loads. *Composite Structures*, 92(6):1485 – 1497, 2010.

[73] S Heimbs, S Kilchert, S Fischer, M Klaus, E Baranger, et al. Sandwich structures with folded core: mechanical modeling and impact simulations. In *SAMPE Europe international conference, Paris*, pages 324–31, 2009.

[74] M. Klaus and H.-G. Reimerdes. Numerical investigation of different strength after impact test procedures. In *Proceedings of the IMPLAST 2010 conference*, Providence, RI, 2010.

[75] A. F. Johnson. Novel hybrid structural core sandwich materials for aircraft applications. In *Proceedings of the 11th Euro-Japanese Symposium on Composite Materials*, Porto, Portugal, 9–11 September 2008.

[76] M. Grzeschik. Performance of foldcores mechanical properties and testing. In *Proceedings of the ASME 2013 International Design Engineering Technical Conference and Computers and Information in Engineering Conference IDETC/CIE*, pages No. DETC2013–13324, pp. V06BT07A042, Portland, OR, 2013. American Society of Mechanical Engineers.

[77] J. M. Gattas and Z. You. Quasi-static impact response of alternative origami-core sandwich panels. In *Proceedings of the ASME 2013 International Design Engineering Technical Conference and Computers and Information in Engineering Conference IDETC/CIE*, pages No. DETC2013–12681, pp. V06BT07A032, Portland, OR, 2013. American Society of Mechanical Engineers.

[78] S. Fischer. Realistic fe simulation of foldcore sandwich structures. *International Journal of Mechanical and Materials Engineering*, 10(1):1–11, 2015.

[79] R. Sturm and S. Fischer. Virtual design method for controlled failure in foldcore sandwich panels. *Applied Composite Materials*, 22(6):791–803, 2015.

[80] R. K. Fathers, J. M. Gattas, and Z. You. Quasi-static crushing of eggbox, cube, and modified cube foldcore sandwich structures. *International Journal of Mechanical Sciences*, 101102:421 – 428, 2015.

[81] J. M. Gattas and Z. You. The behaviour of curved-crease foldcores under low-velocity impact loads. *International Journal of Solids and Structures*, 53:80–91, 2015.

[82] J. Ma and Z. You. The origami crash box. *Origami 5: Fifth International Meeting of Origami Science, Mathematics, and Education*, pages 277–290, 2011.

[83] J. Ma and Z. You. A novel origami crash box with varying profiles. In *Proceedings of the ASME 2013 International Design Engineering Technical Conferences and Computers and Information in Engineering Conference IDETC/CIE*, pages No. DETC2013–13495, pp. V06BT07A048. American Society of Mechanical Engineers, 2013.

[84] S. S. Tolman, I. L. Delimont, L. L. Howell, and D. T. Fullwood. Material selection for elastic energy absorption in origami-inspired compliant corrugations. *Smart Materials and Structures*, 23(9):094010, 2014.

[85] J. Ma and Z. You. Energy absorption of thin-walled square tubes with a prefolded origami pattern–Part I: Geometry and numerical simulation. *Journal of Applied Mechanics*, 81(1):011003, 2014.

[86] A. P. Thrall and C. P. Quaglia. Accordion shelters: A historical review of origami-like deployable shelters developed by the US military. *Engineering Structures*, 59:686 – 692, 2014.

[87] F. J. Martínez-Martín and A. P. Thrall. Honeycomb core sandwich panels for origami-inspired deployable shelters: Multi-objective optimization for minimum weight and maximum energy efficiency. *Engineering Structures*, 69:158–167, 2014.

[88] C. P. Quagli, Z. C. Ballard, and A. P. Thrall. Parametric modelling of an air-liftable origami-inspired deployable shelter with a novel erection strategy. *Mobile and Rapidly Assembled Structures IV*, 136:23, 2014.

[89] C. P. Quaglia, N. Yu, A. P. Thrall, and S. Paolucci. Balancing energy efficiency and structural performance through multi-objective shape optimization: Case study of a rapidly deployable origami-inspired shelter. *Energy and Buildings*, 82:733 – 745, 2014.

[90] C. P. Quaglia, A. J. Dascanio, and A. P. Thrall. Bascule shelters: A novel erection strategy for origami-inspired deployable structures. *Engineering Structures*, 75:276 – 287, 2014.

[91] M. D. Tumbeva, Y. Wang, M. M. Sowar, A. J. Dascanio, and A. P. Thrall. Quilt pattern inspired engineering: Efficient manufacturing of shelter topologies. *Automation in Construction*, 63:57 – 65, 2016.

[92] M. Schenk and S. D. Guest. Geometry of Miura-folded metamaterials. *Proceedings of the National Academy of Sciences*, 110(9):3276–3281, 2013.

[93] K. Fuchi, A. R. Diaz, E. J. Rothwell, R. O. Ouedraogo, and J. Tang. An origami tunable metamaterial. *Journal of Applied Physics*, 111(8):084905, 2012.

[94] J. L. Silverberg, A. A. Evans, L. McLeod, R. C. Hayward, T. Hull, C. D. Santangelo, and I. Cohen. Using origami design principles to fold reprogrammable mechanical metamaterials. *Science*, 345(6197):647–650, 2014.

[95] E. T. Filipov, T. Tachi, and G. H. Paulino. Origami tubes assembled into stiff, yet reconfigurable structures and metamaterials. *Proceedings of the National Academy of Sciences*, 112(40):12321–12326, 2015.

[96] V. Brunck, F. Lechenault, A. Reid, and M. Adda-Bedia. Elastic theory of origami-based metamaterials. *Physical Review E*, 93(3):033005, 2016.

[97] X. Zhou, S. Zang, and Z. You. Origami mechanical metamaterials based on the Miura-derivative fold patterns. *Proceedings of the Royal Society A: Mathematical, Physical and Engineering Sciences*, 472(2191):20160361, 2016.

[98] Y. Shen, Y. Pang, J. Wang, H. Ma, Z. Pei, and S. Qu. Origami-inspired metamaterial absorbers for improving the larger-incident angle absorption. *Journal of Physics D: Applied Physics*, 48(44):445008, 2015.

[99] W. Jiang, H. Ma, M. Feng, L. Yan, J. Wang, J. Wang, and S. Qu. Origami-inspired building block and parametric design for mechanical metamaterials. *Journal of Physics D: Applied Physics*, 49(31):315302, 2016.

[100] M. A. E. Kshad and H. E. Naguib. Characterization of origami shape memory metamaterials (SMMM) made of bio-polymer blends. In *Proceedings of SPIE Smart Structures and Materials+ Nondestructive Evaluation and Health Monitoring*, page 98000H. International Society for Optics and Photonics, 2016.

[101] Y Zhao, MS Nandra, and YC Tai. A MEMS intraocular origami coil. In *Proceedings of the 16th International Solid-State Sensors, Actuators and Microsystems Conference (TRANSDUCERS)*, pages 2172–2175. IEEE, 2011.

[102] C. Yoon, R. Xiao, J. Park, J. Cha, T. D. Nguyen, and D. H. Gracias. Functional stimuli responsive hydrogel devices by self-folding. *Smart Materials and Structures*, 23(9):094008, 2014.

[103] A. Vorob'ev, P. Vaccaro, K. Kubota, S. Saravanan, and T. Aida. Array of micromachined components fabricated using micro-origami method. *Japanese Journal of Applied Physics*, 42(6S):4024, 2003.

[104] J. M. Z. Ocampo, P. O. Vaccaro, T. Fleischmann, T.-S. Wang, K. Kubota, T. Aida, T. Ohnishi, A. Sugimura, R. Izumoto, M. Hosoda, and S. Nashima. Optical actuation of micromirrors fabricated by the micro-origami technique. *Applied Physics Letters*, 83(18):3647–3649, 2003.

[105] T. G. Leong, A. M. Zarafshar, and D. H. Gracias. Three-dimensional fabrication at small size scales. *Small*, 6(7):792–806, 2010.

[106] J. Rogers, Y. Huang, O. G. Schmidt, and D. H. Gracias. Origami MEMS and NEMS. *MRS Bulletin*, 41(02):123–129, 2016.

[107] A. Efimovskaya, D. Senkal, and A. M. Shkel. Miniature origami-like folded MEMS TIMU. In *Proceedings of Transducers-2015 18th International Confer-*

ence on Solid-State Sensors, Actuators and Microsystems (TRANSDUCERS), pages 584–587. IEEE, 2015.

[108] Y. Morikawa, S. Yamagiwa, H. Sawahata, M. Ishida, and T. Kawano. An origami-inspired ultrastretchable bioprobe film device. In *Proceedings of the 2016 IEEE 29th International Conference on Micro Electro Mechanical Systems (MEMS)*, pages 149–152. IEEE, 2016.

[109] G. J. Hayes, Y. Liu, J. Genzer, G. Lazzi, and M. D. Dickey. Self-folding origami microstrip antennas. *IEEE Transactions on Antennas and Propagation*, 62(10):5416–5419, 2014.

[110] K. Kuribayashi, K. Tsuchiya, Z. You, D. Tomus, M. Umemoto, T. Ito, and M. Sasaki. Self-deployable origami stent grafts as a biomedical application of Ni-rich TiNi shape memory alloy foil. *Materials Science and Engineering: A*, 419(12):131 – 137, 2006.

[111] C. L. Randall, E. Gultepe, and D. H. Gracias. Self-folding devices and materials for biomedical applications. *Trends in Biotechnology*, 30(3):138–146, 2012.

[112] R. Fernandes and D. H. Gracias. Self-folding polymeric containers for encapsulation and delivery of drugs. *Advanced Drug Delivery Reviews*, 64(14):1579–1589, 2012.

[113] Y. Wang, L. Ge, P. Wang, M. Yan, J. Yu, and S. Ge. A three-dimensional origami-based immuno-biofuel cell for self-powered, low-cost, and sensitive point-of-care testing. *Chemical Communications*, 50(16):1947–1949, 2014.

[114] K. Kuribayashi and S. Takeuchi. Foldable Parylene origami sheets covered with cells: Toward applications in bio-implantable devices. In *Origami 5:*

Fifth International Meeting of Origami Science, Mathematics, and Education, page 385. CRC Press, 2011.

[115] B. J. Edmondson, L. A. Bowen, C. L. Grames, S. P. Magleby, L. L. Howell, and T. C. Bateman. Oriceps: Origami-inspired forceps. In *Proceedings of the ASME 2013 Conference on Smart Materials, Adaptive Structures and Intelligent Systems SMASIS*. American Society of Mechanical Engineers, 2013.

[116] A. Lebée. From folds to structures, a review. *International Journal of Space Structures*, 30(2):55–74, 2015.

[117] N. Turner, B. Goodwine, and M. Sen. A review of origami applications in mechanical engineering. *Proceedings of the Institution of Mechanical Engineers, Part C: Journal of Mechanical Engineering Science*, page 0954406215597713, 2015.

[118] C. Lauff, T. W. Simpson, Z. Frecker, M.and Ounaies, S. Ahmed, P. von Lockette, R. Strzelec, R. Sheridan, and J.-M. Lien. Differentiating bending from folding in origami engineering using active materials. In *Proceedings of the ASME 2014 International Design Engineering Technical Conferences and Computers and Information in Engineering Conference IDETC/CIE*, pages No. DETC2014–34702, pp. V05BT08A040. American Society of Mechanical Engineers, 2014.

[119] S. M. Felton, K. P. Becker, D. M. Aukes, and R. J. Wood. Self-folding with shape memory composites at the millimeter scale. *Journal of Micromechanics and Microengineering*, 25(8):085004, 2015.

[120] P. K. Kumar and D. C. Lagoudas. Introduction to shape memory alloys. In *Shape Memory Alloys: Modeling and Engineering Applications*, pages 1–51. Springer, 2008.

[121] S.-M. Belcastro and T. C. Hull. A mathematical model for non-flat origami. In *Origami 3: Third International Meeting of Origami Mathematics, Science, and Education*, pages 39–51, 2002.

[122] H. Shimanuki, J. Kato, and T. Watanabe. Construction of 3-D paper-made objects from crease patterns. In *Proceedings of MVA2005 IAPR Conference on Machine Vision Applications, May 16-18, 2005, Tsukuba Science City, Japan*, pages 35–38, 2005.

[123] M. I. Frecker. Recent advances in optimization of smart structures and actuators. *Journal of Intelligent Material Systems and Structures*, 14(4-5):207–216, 2003.

[124] R. G. Loewy. Recent developments in smart structures with aeronautical applications. *Smart Materials and Structures*, 6(5):R11, 1997.

[125] D. J. Hartl and D. C. Lagoudas. Aerospace applications of shape memory alloys. *Proceedings of the Institution of Mechanical Engineers, Part G: Journal of Aerospace Engineering*, 221(4):535–552, 2007.

[126] Z. Guo, H. Yu, and L.-B. Wee. Design of a novel compliant differential shape memory alloy actuator. In *Proceedings of the 2013 IEEE/RSJ International Conference on Intelligent Robots and Systems (IROS)*, pages 4925–4930. IEEE, 2013.

[127] D. Hartl, K. Lane, and R. Malak. Design of a massively reconfigurable origami space structure incorporating shape memory alloys. In *Proceedings of the ASME 2012 International Mechanical Engineering Congress and Exposition IMECE*, pages No. IMECE2012–86391, pp. 115–122. American Society of Mechanical Engineers, 2012.

[128] E. Peraza Hernandez, D. Hartl, R. Malak, and D. Lagoudas. Analysis and optimization of a shape memory alloy-based self-folding sheet considering material uncertainties. In *Proceedings of the ASME 2015 Conference on Smart Materials, Adaptive Structures and Intelligent Systems SMASIS*, pages No. SMASIS2015–9001, pp. V001T01A013. American Society of Mechanical Engineers, 2015.

[129] Q. Li. *Intelligent Stimuli-Responsive Materials: From Well-Defined Nanostructures to Applications*. John Wiley & Sons, Inc., Hoboken, New Jersey, 2013.

[130] S. Ahmed, C. Lauff, A. Crivaro, K. McGough, R. Sheridan, M. Frecker, P. von Lockette, Z. Ounaies, T. Simpson, J.-M. Lien, and R. Strzelec. Multi-field responsive origami structures: preliminary modeling and experiments. In *Proceedings of the ASME 2013 International Design Engineering Technical Conference and Computers and Information in Engineering Conference IDETC/CIE*, pages No. DETC2013–12405, pp. V06BT07A028, Portland, OR, 4–7 August 2013.

[131] P. von Lockette and R. Sheridan. Folding actuation and locomotion of novel magneto-active elastomer (MAE) composites. In *Proceedings of the ASME 2013 Conference on Smart Materials, Adaptive Structures, and Intelligent Systems SMASIS*, pages No. SMASIS2013–3222, pp. V001T01A020, 16–18 September 2013.

[132] M. Budimir. Piezoelectric anisotropy and free energy instability in classic perovskites. Technical report, Materiaux, Ecole Polytechnique Fédérale de Lausane, 2006.

[133] J. Lee, J. G. Boyd IV, and D. C. Lagoudas. Effective properties of three-phase electro-magneto-elastic composites. *International Journal of Engineering Science*, 43(10):790–825, 2005.

[134] P. Tan and L. Tong. Modeling for the electro-magneto-thermo-elastic properties of piezoelectric-magnetic fiber reinforced composites. *Composites Part A: Applied Science and Manufacturing*, 33(5):631–645, 2002.

[135] C. Y. K. Chee, L. Tong, and G. P. Steven. A review on the modelling of piezoelectric sensors and actuators incorporated in intelligent structures. *Journal of Intelligent Material Systems and Structures*, 9(1):3–19, 1998.

[136] C. M. Wayman and H. K. D. H. Bhadeshia. Phase transformations, nondiffusive. *Physical Metallurgy*, 2:1507–1554, 1983.

[137] D. A. Porter, K. E. Easterling, and M. Sherif. *Phase Transformations in Metals and Alloys (Third Edition)*. CRC Press, Taylor & Francis Group, Boca Raton, FL, 2009.

[138] R. Kainuma, Y. Imano, W. Ito, Y. Sutou, H. Morito, S. Okamoto, O. Kitakami, K. Oikawa, A. Fujita, T. Kanomata, and K. Ishida. Magnetic-field-induced shape recovery by reverse phase transformation. *Nature*, 439(7079):957–960, 2006.

[139] B. Kiefer and D. C. Lagoudas. Magnetic field-induced martensitic variant reorientation in magnetic shape memory alloys. *Philosophical Magazine*, 85(33-35):4289–4329, 2005.

[140] I. Karaman, B. Basaran, H. E. Karaca, A. I. Karsilayan, and Y. I. Chumlyakov. Energy harvesting using martensite variant reorientation mechanism in a NiM-

nGa magnetic shape memory alloy. *Applied Physics Letters*, 90(17):172505, 2007.

[141] A. Lendlein and S. Kelch. Shape-memory polymers. *Angewandte Chemie International Edition*, 41(12):2034–2057, 2002.

[142] P. T. Mather, X. Luo, and I. A. Rousseau. Shape memory polymer research. *Annual Review of Materials Research*, 39:445–471, 2009.

[143] Y. Liu, H. Du, L. Liu, and J. Leng. Shape memory polymers and their composites in aerospace applications: A review. *Smart Materials and Structures*, 23(2):023001, 2014.

[144] M. D. Hager, S. Bode, C. Weber, and U. S. Schubert. Shape memory polymers: Past, present and future developments. *Progress in Polymer Science*, 4950:3 – 33, 2015. Self-Healing Polymers.

[145] G McKnight and C Henry. Variable stiffness materials for reconfigurable surface applications. In *Proceedings of SPIE*, volume 5761, pages 119–126, 2005.

[146] T. Hino and T. Maeno. Development of a miniature robot finger with a variable stiffness mechanism using shape memory alloy. In *International Simposium on Robotics and Automation*, pages 25–27, 2004.

[147] K. Ikuta. Micro/miniature shape memory alloy actuator. In *Proceedings of the 1990 IEEE International Conference on Robotics and Automation*, pages 2156–2161. IEEE, 1990.

[148] K. A. Williams, G. T. C. Chiu, and R. J. Bernhard. Dynamic modelling of a shape memory alloy adaptive tuned vibration absorber. *Journal of Sound and Vibration*, 280(1):211–234, 2005.

[149] D. Damjanovic and R. E. Newnham. Electrostrictive and piezoelectric materials for actuator applications. *Journal of Intelligent Material Systems and Structures*, 3(2):190–208, 1992.

[150] R. E. Newnham and G. R. Ruschau. Smart electroceramics. *Journal of the American Ceramic Society*, 74(3):463–480, 1991.

[151] L. L. Howell. Compliant mechanisms. In *Encyclopedia of Nanotechnology*, pages 457–463. Springer, 2012.

[152] H. Greenberg, M. Gong, S. Magleby, and L. Howell. Identifying links between origami and compliant mechanisms. *Mechanical Sciences*, 2:217–225, 2011.

[153] K. A. Seffen. Compliant shell mechanisms. *Philosophical Transactions of the Royal Society A: Mathematical, Physical and Engineering Sciences*, 370(1965):2010–2026, 2012.

[154] N. Lobontiu. *Compliant Mechanisms: Design of Flexure Hinges*. CRC Press LLC, Boca Raton, Florida, 2003.

[155] G. K. Ananthasuresh and S. Kota. Designing compliant mechanisms. *Mechanical Engineering*, 117(11):93–96, 1995.

[156] K.-J. Lu and S. Kota. Design of compliant mechanisms for morphing structural shapes. *Journal of Intelligent Material Systems and Structures*, 14(6):379–391, 2003.

[157] K. Otsuka and C. M. Wayman. *Shape Memory Materials*. Cambridge University Press, Cambridge, 1999.

[158] M. Behl, J. Zotzmann, and A. Lendlein. Shape-memory polymers and shape-changing polymers. In *Shape-Memory Polymers*, pages 1–40. Springer, 2010.

[159] S. M. Felton, M. T. Tolley, B. H. Shin, C. D. Onal, E. D. Demaine, D. Rus, and R. Wood. Self-folding with shape memory composites. *Soft Matter*, 9(32):7688–7694, 2013.

[160] M. T. Tolley, S. M. Felton, S. Miyashita, D. Aukes, D. Rus, and R. J. Wood. Self-folding origami: shape memory composites activated by uniform heating. *Smart Materials and Structures*, 23(9):094006, 2014.

[161] R. W. Mailen, Y. Liu, M. D. Dickey, M. Zikry, and J. Genzer. Modelling of shape memory polymer sheets that self-fold in response to localized heating. *Soft Matter*, 11(39):7827–7834, 2015.

[162] D. Davis, B. Chen, M. D. Dickey, and J. Genzer. Self-folding of thick polymer sheets using gradients of heat. *Journal of Mechanisms and Robotics*, 8(3):031014, 2016.

[163] Y. Lee, H. Lee, T. Hwang, J.-G. Lee, and M. Cho. Sequential folding using light-activated polystyrene sheet. *Scientific Reports*, 5:16544, 2015.

[164] R. N. Saunders, D. J. Hartl, J. G. Boyd, and D. C. Lagoudas. Modeling and development of a twisting wing using inductively heated shape memory alloy actuators. In *Proceedings of SPIE Smart Structures and Materials+ Nondestructive Evaluation and Health Monitoring*, pages 94310U–94310U–8. International Society for Optics and Photonics, 2015.

[165] R. N. Saunders, J. G. Boyd, D. J. Hartl, J. K. Brown, F. T. Calkins, and D. C. Lagoudas. A validated model for induction heating of shape memory alloy actuators. *Smart Materials and Structures*, 25(4):045022, 2016.

[166] T. J. Cognata, D. Hartl, R. Sheth, and C. Dinsmore. A morphing radiator for high-turndown thermal control of crewed space exploration vehicles. In

Proceedings of 23rd AIAA/AHS Adaptive Structures Conference, pages AIAA 2015–1509, 2015.

[167] C. L. Bertagne, R. B. Sheth, D. J. Hartl, and J. D. Whitcomb. Simulating coupled thermal-mechanical interactions in morphing radiators. In *Proceedings of SPIE Smart Structures and Materials+ Nondestructive Evaluation and Health Monitoring*, pages 94312F–94312F–10. International Society for Optics and Photonics, 2015.

[168] J. Paik, B. An, D. Rus, and R. J. Wood. Robotic origamis: Self-morphing modular robots. In *Proceedings of the 2nd International Conference on Morphological Computation ICMC*, pages EPFL–CONF–206919, Venice, Italy, 2012.

[169] E. A. Peraza Hernandez, S. Hu, H. W. Kung, D. Hartl, and E. Akleman. Towards building smart self-folding structures. *Computers & Graphics*, 37(6):730–742, 2013.

[170] D. Hartl, K. Lane, and R. Malak. Computational design of a reconfigurable origami space structure incorporating shape memory alloy thin films. In *Proceedings of the ASME 2012 Conference on Smart Materials, Adaptive Structures and Intelligent Systems SMASIS*, pages 277–285. American Society of Mechanical Engineers, 2012.

[171] T. Halbert, P. Moghadas, R. Malak, and D. Hartl. Control of a shape memory alloy based self-folding sheet. In *Proceedings of the ASME 2014 International Design Engineering Technical Conference & Computers and Information in Engineering Conference IDETC/CIE*, pages No. DETC2014–34703, pp. V05BT08A041, Buffalo, New York, 2014.

[172] Z. You and K. Kuribayashi. A novel origami stent. In *Proceedings of Summer Bioengineering Conference*, pages 0257–0258, Key Biscayne, Florida, 2003.

[173] K. Kuribayashi. A novel foldable stent graft. *Thesis, University of Oxford*, 2004.

[174] C. D. Onal, R. J. Wood, and D. Rus. An origami-inspired approach to worm robots. *IEEE/ASME Transactions on Mechatronics*, 18(2):430–438, 2013.

[175] C. D. Onal, R. J. Wood, and D. Rus. Towards printable robotics: Origami-inspired planar fabrication of three-dimensional mechanisms. In *Proceedings of the 2011 IEEE International Conference on Robotics and Automation (ICRA)*, pages 4608–4613. IEEE, 2011.

[176] D.-Y. Lee, J.-S. Kim, S.-R. Kim, J.-J. Park, and K.-J. Cho. Design of deformable-wheeled robot based on origami structure with shape memory alloy coil spring. In *Proceedings of the 10th International Conference on Ubiquitous Robots and Ambient Intelligence (URAI)*, page 120. IEEE, 2013.

[177] A. Firouzeh, Y. Sun, H. Lee, and J. Paik. Sensor and actuator integrated low profile robotic origami. In *Proceedings of the IEEE/RSJ International Conference on Intelligent Robots and Systems*, pages 4937–4944, 2013.

[178] A. Roudaut, A. Karnik, M. Löchtefeld, and S. Subramanian. Morphees: toward high shape resolution in self-actuated flexible mobile devices. In *Proceedings of the 2013 SIGCHI Conference on Human Factors in Computing Systems*, pages 593–602. ACM, 2013.

[179] A. Gomes, A. Nesbitt, and R. Vertegaal. MorePhone: a study of actuated shape deformations for flexible thin-film smartphone notifications. In *Proceedings of the SIGCHI Conference on Human Factors in Computing Systems*, pages 583–592. ACM, 2013.

[180] L. Qi, J .and Buechley. Animating paper using shape memory alloys. In *Proceedings of the 2012 SIGCHI Conference on Human Factors in Computing Systems*, pages 749–752. ACM, 2012.

[181] J. Qi and L. Buechley. Electronic popables: exploring paper-based computing through an interactive pop-up book. In *Proceedings of the Fourth International Conference on Tangible, Embedded, and Embodied Interaction*, pages 121–128. ACM, 2010.

[182] N. Koizumi, K. Yasu, A. Liu, M. Sugimoto, and M. Inami. Animated paper: A toolkit for building moving toys. *Computers in Entertainment (CIE)*, 8(2):7, 2010.

[183] R. Saunders, D. Hartl, R. Malak, and D. Lagoudas. Design and analysis of a self-folding sma-smp composite laminate. In *Proceedings of the ASME 2014 International Design Engineering Technical Conferences and Computers and Information in Engineering Conference IDETC/CIE*, pages No. DETC2014–35151, pp. V05BT08A048. American Society of Mechanical Engineers, 2014.

[184] M. T. Tolley, S. M. Felton, S. Miyashita, L. Xu, B. Shin, M. Zhou, D. Rus, and R. J. Wood. Self-folding shape memory laminates for automated fabrication. In *Proceedings of the 2013 IEEE/RSJ International Conference on Intelligent Robots and Systems (IROS)*, pages 4931–4936. IEEE, 2013.

[185] S. M. Felton, M. T. Tolley, C. D. Onal, D. Rus, and R. J. Wood. Robot self-assembly by folding: A printed inchworm robot. In *Proceedings of the 2013 IEEE International Conference on Robotics and Automation (ICRA)*, pages 277–282. IEEE, 2013.

[186] Q. Ge, C. K. Dunn, H. J. Qi, and M. L. Dunn. Active origami by 4D printing. *Smart Materials and Structures*, 23(9):094007, 2014.

[187] M. Behl, M. Y. Razzaq, and A. Lendlein. Multifunctional shape-memory polymers. *Advanced Materials*, 22(31):3388–3410, 2010.

[188] Y. Liu, J. K. Boyles, J. Genzer, and M. D. Dickey. Self-folding of polymer sheets using local light absorption. *Soft Matter*, 8(6):1764–1769, 2012.

[189] Y. Liu, M. Miskiewicz, M. J. Escuti, J. Genzer, and M. D. Dickey. Three-dimensional folding of pre-strained polymer sheets via absorption of laser light. *Journal of Applied Physics*, 115(20):204911, 2014.

[190] Y. Liu, R. Mailen, Y. Zhu, M. D. Dickey, and J. Genzer. Simple geometric model to describe self-folding of polymer sheets. *Physical Review E*, 89(4):042601, 2014.

[191] A. P. Lee, D. R. Ciarlo, P. A. Krulevitch, S. Lehew, J. Trevino, and M. A. Northrup. A practical microgripper by fine alignment, eutectic bonding and SMA actuation. *Sensors and Actuators A: Physical*, 54(1):755–759, 1996.

[192] P. Krulevitch, A. P. Lee, P. B. Ramsey, J. C. Trevino, J. Hamilton, and M. A. Northrup. Thin film shape memory alloy microactuators. *Journal of Microelectromechanical Systems*, 5(4):270–282, 1996.

[193] K. E. Laflin, C. J. Morris, T. Muqeem, and D. H. Gracias. Laser triggered sequential folding of microstructures. *Applied Physics Letters*, 101(13):131901, 2012.

[194] K. Kalaitzidou and A. J. Crosby. Adaptive polymer particles. *Applied Physics Letters*, 93(4):041910, 2008.

[195] B. Simpson, G. Nunnery, R. Tannenbaum, and K. Kalaitzidou. Capture/release ability of thermo-responsive polymer particles. *Journal of Materials Chemistry*, 20(17):3496–3501, 2010.

[196] S. Zakharchenko, N. Puretskiy, G. Stoychev, M. Stamm, and L. Ionov. Temperature controlled encapsulation and release using partially biodegradable thermo-magneto-sensitive self-rolling tubes. *Soft Matter*, 6(12):2633–2636, 2010.

[197] G. Stoychev, N. Puretskiy, and L. Ionov. Self-folding all-polymer thermoresponsive microcapsules. *Soft Matter*, 7(7):3277–3279, 2011.

[198] G. Stoychev, S. Zakharchenko, S. Turcaud, J. W. C. Dunlop, and L. Ionov. Shape-programmed folding of stimuli-responsive polymer bilayers. *ACS nano*, 6(5):3925–3934, 2012.

[199] K. Fuchi, T. H. Ware, P. R. Buskohl, G. W. Reich, R. A. Vaia, T. J. White, and J. J. Joo. Topology optimization for the design of folding liquid crystal elastomer actuators. *Soft Matter*, 11(37):7288–7295, 2015.

[200] K. Fuchi, P. R. Buskohl, T. Ware, R. A. Vaia, T. J. White, G. W. Reich, and J. J. Joo. Inverse design of LCN films for origami applications using topology optimization. In *Proceedings of the ASME 2014 Conference on Smart Materials, Adaptive Structures and Intelligent Systems SMASIS*, pages No. SMASIS2014–7497, pp. V001T01A011. American Society of Mechanical Engineers, 2014.

[201] L. T. de Haan, V. Gimenez-Pinto, A. Konya, T.-S. Nguyen, J. Verjans, C. Sánchez-Somolinos, J. V. Selinger, R. L. B. Selinger, D. J. Broer, and A. P. H. J. Schenning. Accordion-like actuators of multiple 3D patterned liquid crystal polymer films. *Advanced Functional Materials*, 24(9):1251–1258, 2014.

[202] B. An, N. Benbernou, E. D. Demaine, and D. Rus. Planning to fold multiple objects from a single self-folding sheet. *Robotica*, 29(1):87–102, 2011.

[203] B. An and D. Rus. Designing and programming self-folding sheets. *Robotics and Autonomous Systems*, 62(7):976–1001, 2014.

[204] E. A. Peraza-Hernandez, D. J. Hartl, K. R. Frei, and E. Akleman. Connectivity of shape memory alloy-based self-folding structures. In *Proceedings of the 22nd AIAA/ASME/AHS Adaptive Structures Conference, in AIAA SciTech*, page 1415, National Harbor, Maryland, 2014.

[205] E. Peraza Hernandez, D. Hartl, R. Malak, E. Akleman, O. Gonen, and H. Kung. Design tools for patterned self-folding reconfigurable structures based on programmable active laminates. *Journal of Mechanisms and Robotics*, 8(3):031015, 2016.

[206] P. Moghadas, R. Malak, and D. Hartl. Reinforcement learning for control of a shape memory alloy based self-folding sheet. In *Proceedings of the ASME 2015 International Design Engineering Technical Conferences and Computers and Information in Engineering Conference IDETC/CIE*, pages No. DETC2015–46980, pp. V05BT08A044. American Society of Mechanical Engineers, 2015.

[207] T. R. Halbert. An improved algorithm for sequential information-gathering decisions in design under uncertainty. Master's thesis, Texas A&M University, College Station, TX, USA, 2015.

[208] T. Halbert, E. Peraza Hernandez, R. Malak, and D. Hartl. Numerically validated reduced-order model for laminates containing shape memory alloy wire meshes. *Journal of Intelligent Material Systems and Structures*, page 1045389X15595295, 2015.

[209] E. Peraza-Hernandez, D. Hartl, and D. Lagoudas. Modeling of shape memory alloy wire meshes using effective lamina properties for improved analysis efficiency. In *Proceedings of the ASME 2013 Conference on Smart Mate-*

rials, Adaptive Structures and Intelligent Systems SMASIS 2013, pages No. SMASIS2013–3094, pp. V001T01A009. American Society of Mechanical Engineers, 2013.

[210] A. C. Powledge. Experimental characterization and validated multi-fidelity analysis of reconfigurable curvature in shape memory alloy composite sheets. Master's thesis, Texas A&M University, College Station, TX, USA, 2015.

[211] V. Brailovski, S. Prokoshkin, P. Terriault, and F. Trochu. *Shape Memory Alloys: Fundamentals, Modeling and Applications*. Université du Québec. École de technologie supérieure, Québec, Canada, 2003.

[212] L. G. Machado and M. A. Savi. Medical applications of shape memory alloys. *Brazilian Journal of Medical and Biological Research*, 36(6):683–691, 2003.

[213] N. B. Morgan. Medical shape memory alloy applications–the market and its products. *Materials Science and Engineering: A*, 378(1):16–23, 2004.

[214] J. M. Jani, M. Leary, A. Subic, and M. A. Gibson. A review of shape memory alloy research, applications and opportunities. *Materials & Design*, 56:1078–1113, 2014.

[215] G. Esquivel, D. Weiser, D. Hartl, and D. Whitten. POP-OP: A shape memory-based morphing wall. *International Journal of Architectural Computing*, 11(3):347–362, 2013.

[216] J. Berry and J. H. Seo. Incorporation of shape memory polymers in interactive design. In *Proceedings of the 21st International Symposium of Electronic Art ISEA*, 2015.

[217] C. Schwesig, I. Poupyrev, and E. Mori. Gummi: a bendable computer. In *Proceedings of the SIGCHI Conference on Human Factors in Computing Systems*,

pages 263–270. ACM, 2004.

[218] J.-S. Park, T.-W. Kim, D. Stryakhilev, J.-S. Lee, S.-G. An, Y.-S. Pyo, D.-B. Lee, Y. G. Mo, D.-U. Jin, and H. K. Chung. Flexible full color organic light-emitting diode display on polyimide plastic substrate driven by amorphous indium gallium zinc oxide thin-film transistors. *Applied Physics Letters*, 95(1):013503–013503, 2009.

[219] B. Lahey, A. Girouard, W. Burleson, and R. Vertegaal. PaperPhone: understanding the use of bend gestures in mobile devices with flexible electronic paper displays. In *Proceedings of the SIGCHI Conference on Human Factors in Computing Systems*, pages 1303–1312. ACM, 2011.

[220] A. Minuto and A. Nijholt. Smart material interfaces as a methodology for interaction: a survey of SMIs' state of the art and development. In *Proceedings of the Second International Workshop on Smart Material Interfaces: Another Step to a Material Future*, pages 1–6. ACM, 2013.

[221] A. Gomes and R. Vertegaal. PaperFold: Evaluating shape changes for viewport transformations in foldable thin-film display devices. In *Proceedings of the Ninth International Conference on Tangible, Embedded, and Embodied Interaction*, pages 153–160. ACM, 2015.

[222] D. Tan, M. Kumorek, A. A. Garcia, A. Mooney, and D. Bekoe. Projectagami: A foldable mobile device with shape interactive applications. In *Proceedings of the 33rd Annual ACM Conference Extended Abstracts on Human Factors in Computing Systems*, pages 1555–1560. ACM, 2015.

[223] L.-W. Kang, M.-F. Weng, C.-L. Jheng, C.-Y. Tseng, S. K. Ramesh, A. Gureja, H.-C. Hsu, and C.-H. Yeh. Content-aware image retargeting for image display on foldable mobile devices. *Procedia Computer Science*, 56:104–110, 2015.

[224] H. Meng and G. Li. A review of stimuli-responsive shape memory polymer composites. *Polymer*, 54(9):2199–2221, 2013.

[225] Y. Liu, J. Genzer, and M. D. Dickey. "2D or not 2D": Shape-programming polymer sheets. *Progress in Polymer Science*, 52:79–106, 2016.

[226] A. Mata, A. J. Fleischman, and S. Roy. Characterization of polydimethylsiloxane (PDMS) properties for biomedical micro/nanosystems. *Biomedical Microdevices*, 7(4):281–293, 2005.

[227] F. Schneider, J. Draheim, R. Kamberger, and U. Wallrabe. Process and material properties of polydimethylsiloxane (PDMS) for optical MEMS. *Sensors and Actuators A: Physical*, 151(2):95–99, 2009.

[228] A. Ben-Naim. *Hydrophobic Interactions*. Plenum Press, New York, 1980.

[229] V. Luchnikov, L. Ionov, and M. Stamm. Self-rolled polymer tubes: Novel tools for microfluidics, microbiology, and drug-delivery systems. *Macromolecular Rapid Communications*, 32(24):1943–1952, 2011.

[230] L. Ionov. Nature-inspired stimuli-responsive self-folding materials. *Intelligent Stimuli-responsive Materials: From Well-defined Nanostructures to Applications*, pages 1–16, 2013.

[231] K. Kumar, B. Nandan, V. Luchnikov, F. Simon, A. Vyalikh, U. Scheler, and M. Stamm. A novel approach for the fabrication of silica and silica/metal hybrid microtubes. *Chemistry of Materials*, 21(18):4282–4287, 2009.

[232] K. Kumar, B. Nandan, V. Luchnikov, E. B. Gowd, and M. Stamm. Fabrication of metallic microtubes using self-rolled polymer tubes as templates. *Langmuir*, 25(13):7667–7674, 2009.

[233] K. Kumar, V. Luchnikov, V. Nandan, V. Senkovskyy, and M. Stamm. Formation of self-rolled polymer microtubes studied by combinatorial approach. *European Polymer Journal*, 44(12):4115 – 4121, 2008.

[234] V. Luchnikov, K. Kumar, and M. Stamm. Toroidal hollow-core microcavities produced by self-rolling of strained polymer bilayer films. *Journal of Micromechanics and Microengineering*, 18(3):035041, 2008.

[235] W. Guo, M. Li, and J. Zhou. Modeling programmable deformation of self-folding all-polymer structures with temperature-sensitive hydrogels. *Smart Materials and Structures*, 22(11):115028, 2013.

[236] H. He, J. Guan, and J. L. Lee. An oral delivery device based on self-folding hydrogels. *Journal of Controlled Release*, 110(2):339–346, 2006.

[237] H. He, X. Cao, and L. J. Lee. Design of a novel hydrogel-based intelligent system for controlled drug release. *Journal of Controlled Release*, 95(3):391–402, 2004.

[238] T. S. Shim, S.-H. Kim, C.-J. Heo, H. C. Jeon, and S.-M. Yang. Controlled origami folding of hydrogel bilayers with sustained reversibility for robust microcarriers. *Angewandte Chemie*, 124(6):1449–1452, 2012.

[239] J. Guan, H. He, D. J. Hansford, and L. J. Lee. Self-folding of three-dimensional hydrogel microstructures. *The Journal of Physical Chemistry B*, 109(49):23134–23137, 2005.

[240] K.-U. Jeong, J.-H. Jang, D.-Y. Kim, C. Nah, J. H. Lee, M.-H. Lee, H.-J. Sun, C.-L. Wang, S. Z. D. Cheng, and E. L. Thomas. Three-dimensional actuators transformed from the programmed two-dimensional structures via

bending, twisting and folding mechanisms. *Journal of Materials Chemistry*, 21(19):6824–6830, 2011.

[241] N. Bassik, A. Brafman, A. M. Zarafshar, M. Jamal, D. Luvsanjav, F. M. Selaru, and D. H. Gracias. Enzymatically triggered actuation of miniaturized tools. *Journal of the American Chemical Society*, 132(46):16314–16317, 2010.

[242] J. S. Randhawa, T. G. Leong, N. Bassik, B. R. Benson, M. T. Jochmans, and D. H. Gracias. Pick-and-place using chemically actuated microgrippers. *Journal of the American Chemical Society*, 130(51):17238–17239, 2008.

[243] S. Zakharchenko, E. Sperling, and L. Ionov. Fully biodegradable self-rolled polymer tubes: a candidate for tissue engineering scaffolds. *Biomacromolecules*, 12(6):2211–2215, 2011.

[244] A. V. Prinz and V. Y. Prinz. Application of semiconductor micro-and nanotubes in biology. *Surface Science*, 532:911–915, 2003.

[245] Z. Suo. Theory of dielectric elastomers. *Acta Mechanica Solida Sinica*, 23(6):549–578, 2010.

[246] R. Shankar, T. K. Ghosh, and R. J. Spontak. Dielectric elastomers as next-generation polymeric actuators. *Soft Matter*, 3(9):1116–1129, 2007.

[247] Y. Bar-Cohen and Q. Zhang. Electroactive polymer actuators and sensors. *MRS bulletin*, 33(03):173–181, 2008.

[248] W.-C. Chuang, H.-L. Lee, P.-Z. Chang, and Y.-C. Hu. Review on the modeling of electrostatic MEMS. *Sensors*, 10(6):6149–6171, 2010.

[249] K. McGough, S. Ahmed, M. Frecker, and Z. Ounaies. Finite element analysis and validation of dielectric elastomer actuators used for active origami. *Smart Materials and Structures*, 23(9):094002, 2014.

[250] S. Ahmed, Z. Ounaies, and M. Frecker. Investigating the performance and properties of dielectric elastomer actuators as a potential means to actuate origami structures. *Smart Materials and Structures*, 23(9):094003, 2014.

[251] H. Okuzaki, T. Saido, H. Suzuki, Y. Hara, and H. Yan. A biomorphic origami actuator fabricated by folding a conducting paper. *Journal of Physics: Conference Series*, 127(1):012001, 2008.

[252] E. Smela, O. Inganäs, and I. Lundström. Controlled folding of micrometer-size structures. *Science*, 268(5218):1735–1738, 1995.

[253] E. W. H. Jager, O. Inganäs, and I. Lundström. Microrobots for micrometer-size objects in aqueous media: Potential tools for single-cell manipulation. *Science*, 288(5475):2335–2338, 2000.

[254] B. Balakrisnan, A. Nacev, and E. Smela. Design of bending multi-layer electroactive polymer actuators. *Smart Materials and Structures*, 24(4):045032, 2015.

[255] W. Sun, F. Liu, Z. Ma, C. Li, and J. Zhou. Soft mobile robots driven by foldable dielectric elastomer actuators. *Journal of Applied Physics*, 120(8):084901, 2016.

[256] A. Diaz, J. I. Castillo, J. A. Logan, and W.-Y. Lee. Electrochemistry of conducting polypyrrole films. *Journal of Electroanalytical Chemistry and Interfacial Electrochemistry*, 129(1):115–132, 1981.

[257] A. F. Diaz and B. Hall. Mechanical properties of electrochemically prepared polypyrrole films. *IBM Journal of Research and Development*, 27(4):342–347, 1983.

[258] M. Farshad and A. Benine. Magnetoactive elastomer composites. *Polymer Testing*, 23(3):347–353, 2004.

[259] P. von Lockette. Fabrication and performance of magneto-active elastomer composite structures. In *Proceedings of the ASME 2014 Conference on Smart Materials, Adaptive Structures and Intelligent Systems SMASIS*, pages No. SMASIS2014–7590, pp. V001T01A019. American Society of Mechanical Engineers, 2014.

[260] B. M. Cowan. Magnetically induced actuation and optimization of the Miura-ori structure. Master's thesis, The Pennsylvania State University, 2015.

[261] A. Crivaro, R. Sheridan, M. Frecker, T. W. Simpson, and P. Von Lockette. Bistable compliant mechanism using magneto active elastomer actuation. *Journal of Intelligent Material Systems and Structures*, page 1045389X15620037, 2015.

[262] L. Bowen, K. Springsteen, H. Feldstein, M. Frecker, T. W. Simpson, and P. von Lockette. Development and validation of a dynamic model of magneto-active elastomer actuation of the origami waterbomb base. *Journal of Mechanisms and Robotics*, 7(1):011010, 2015.

[263] L. Bowen, K. Springsteen, M. Frecker, and T. Simpson. Optimization of a dynamic model of magnetic actuation of an origami mechanism. In *ASME 2015 International Design Engineering Technical Conferences and Computers and Information in Engineering Conference IDETC/CIE*, pages No. DETC2015–47458, pp. V05BT08A05. American Society of Mechanical Engineers, 2015.

[264] L. Bowen, K. Springsteen, M. Frecker, and T. Simpson. Trade space exploration of magnetically actuated origami mechanisms. *Journal of Mechanisms and Robotics*, 8(3):031012, 2016.

[265] T. Tachi. Simulation of rigid origami. *Origami 4, Fourth International Meeting of Origami Science, Mathematics, and Education*, pages 175–187, 2009.

[266] T. A. Evans, R. J. Lang, S. P. Magleby, and L. L. Howell. Rigidly foldable origami gadgets and tessellations. *Royal Society Open Science*, 2(9), 2015.

[267] T. Ida, H. Takahashi, M. Marin, A. Kasem, and F. Ghourabi. Computational origami system Eos. *Origami 4: Proceedings of 4th International Conference on Origami, Science, Mathematics and Education*, pages 285–293, 2009.

[268] H. Huzita. Axiomatic development of origami geometry. In *Proceedings of the First International Meeting of Origami Science and Technology*, pages 143–158, 1989.

[269] R. C. Alperin and R. J. Lang. One-, two-, and multi-fold origami axioms. *Origami 4: Proceedings of 4th International Conference on Origami, Science, Mathematics and Education*, pages 371–393, 2009.

[270] T. Hull. *Project origami: Activities for Exploring Mathematics*. CRC Press, Boca Raton, FL, 2012.

[271] A. Kasem, F. Ghourabi, and T. Ida. Origami axioms and circle extension. In *Proceedings of the 2011 ACM Symposium on Applied Computing*, pages 1106–1111. ACM, 2011.

[272] F. Ghourabi, T. Ida, H. Takahashi, M. Marin, and A. Kasem. Logical and algebraic view of Huzita's origami axioms with applications to computational origami. In *Proceedings of the 2007 ACM Symposium on Applied Computing*, pages 767–772. ACM, 2007.

[273] W. Wu and Z. You. Modelling rigid origami with quaternions and dual quaternions. *Proceedings of the Royal Society of London A: Mathematical, Physical and Engineering Sciences*, 466(2119):2155–2174, 2010.

[274] E. D. Demaine and M. L. Demaine. Recent results in computational origami. In *Proceedings of the 3rd International Meeting of Origami Science, Math, and Education*, pages 3–16. Citeseer, 2001.

[275] M. S. Moses, M. K. Ackerman, and G. S. Chirikjian. Origami rotors: Imparting continuous rotation to a moving platform using compliant flexure hinges. In *Proceedings of the ASME 2013 International Design Engineering Technical Conference and Computers and Information in Engineering Conference IDETC/CIE*, pages No. DETC2013–12753, pp. V06BT07A037, Portland, OR, 2013. American Society of Mechanical Engineers.

[276] S.-M. Belcastro and T. C. Hull. Modelling the folding of paper into three dimensions using affine transformations. *Linear Algebra and its Applications*, 348(13):273 – 282, 2002.

[277] N. Watanabe and K. Kawaguchi. The method for judging rigid foldability. *Origami 4: Proceedings of 4th International Conference on Origami, Science, Mathematics and Education*, pages 165–174, 2009.

[278] T. Tachi. Generalization of rigid foldable quadrilateral mesh origami. In *Proceedings of the Symposium of the International Association for Shell and Spatial Structures (50th. 2009. Valencia): Evolution and Trends in Design, Analysis and Construction of Shell and Spatial Structures*. Editorial de la Universitat Politécnica de Valencia, 2009.

[279] Z. Abel, J. Cantarella, E. D. Demaine, D. Eppstein, T. C. Hull, J. S. Ku, R. J. Lang, and T. Tachi. Rigid origami vertices: Conditions and forcing sets. *arXiv preprint arXiv:1507.01644*, 2015.

[280] S. Liu, Y. Chen, and G. Lu. The rigid origami patterns for flat surface. In *Proceedings of the ASME 2013 International Design Engineering Techni-*

cal Conferences and Computers and Information in Engineering Conference IDETC/CIE, pages No. DETC2013–12947, pp. V06BT07A039. American Society of Mechanical Engineers, 2013.

[281] T. Tachi. Geometric considerations for the design of rigid origami structures. In *Proceedings of the International Association for Shell and Spatial Structures (IASS) Symposium*, volume 12, pages 458–460, 2010.

[282] T. Tachi. Designing freeform origami tessellations by generalizing Resch's patterns. *Journal of Mechanical Design*, 135(11):111006, 2013.

[283] T. Tachi. Freeform origami tessellations by generalizing Resch's patterns. In *Proceedings of the ASME 2013 International Design Engineering Technical Conferences and Computers and Information in Engineering Conference IDETC/CIE*, pages No. DETC2013–12326, pp. V06BT07A025. American Society of Mechanical Engineers, 2013.

[284] J. M. Gattas, W. Wu, and Z. You. Miura-base rigid origami: Parameterizations of first-level derivative and piecewise geometries. *Journal of Mechanical Design*, 135(11):111011, 2013.

[285] K. Wang and Y. Chen. Folding a patterned cylinder by rigid origami. *Origami 5: Fifth International Meeting of Origami Science, Mathematics, and Education*, pages 265–276, 2011.

[286] X.-Y. Li, T. Ju, Y. Gu, and S.-M. Hu. A geometric study of V-style pop-ups: Theories and algorithms. In *ACM SIGGRAPH 2011 Papers*, SIGGRAPH '11, pages 98:1–98:10, New York, NY, USA, 2011. ACM.

[287] S. N. Le, S.-J. Leow, T.-V. Le-Nguyen, C. Ruiz, and K.-L. Low. Surface and contour-preserving origamic architecture paper pop-ups. *IEEE Transactions*

on Visualization and Computer Graphics, 20(2):276–288, 2014.

[288] P. M. Reis, F. López Jiménez, and J. Marthelot. Transforming architectures inspired by origami. *Proceedings of the National Academy of Sciences*, 112(40):12234–12235, 2015.

[289] R. J. Lang. *Origami In Action: Paper Toys That Fly, Flag, Gobble and Inflate!* St. Martin's Griffin, New York, 1997.

[290] Y. Qin and J. Dai. Four motion branches of an origami based eight bar spatial mechanism. In *Proceedings of the ASME 2013 International Design Engineering Technical Conference and Computers and Information in Engineering Conference IDETC/CIE*, pages No. DETC2013–12584, pp. V06BT07A030, Portland, OR, 2013.

[291] L. A. Bowen, C. L. Grames, S. P. Magleby, L. L. Howell, and R. J. Lang. A classification of action origami as systems of spherical mechanisms. *Journal of Mechanical Design*, 135(11):111008, 2013.

[292] L. A. Bowen, C. L. Grames, S. P. Magleby, R. J. Lang, and L. L. Howell. An approach for understanding action origami as kinematic mechanisms. In *Proceedings of the ASME 2013 International Design Engineering Technical Conference and Computers and Information in Engineering Conference IDETC/CIE*, pages No. DETC2013–13407, pp. V06BT07A044, Portland, OR, 2013. American Society of Mechanical Engineers.

[293] L. A. Bowen, W. L. Baxter, S. P. Magleby, and L. L. Howell. A position analysis of coupled spherical mechanisms found in action origami. *Mechanism and Machine Theory*, 77:13–24, 2014.

[294] E. R. Leal and J. S. Dai. From origami to a new class of centralized 3-DOF parallel mechanisms. In *Proceedings of the ASME 2007 International Design Engineering Technical Conferences and Computers and Information in Engineering Conference IDETC/CIE*, pages 1183–1193. American Society of Mechanical Engineers, 2007.

[295] G. Wei and J. S. Dai. Origami-inspired integrated planar-spherical overconstrained mechanisms. *Journal of Mechanical Design*, 136(5):051003, 2014.

[296] I. L. Delimont, S. P. Magleby, and L. L. Howell. Evaluating compliant hinge geometries for origami-inspired mechanisms. *Journal of Mechanisms and Robotics*, 7(1):011009, 2015.

[297] B. G. Winder, S. P. Magleby, and L. L. Howell. Kinematic representations of pop-up paper mechanisms. *Journal of Mechanisms and Robotics*, 1(2):021009, 2009.

[298] G. Wei and J. S. Dai. Geometry and kinematic analysis of an origami-evolved mechanism based on artmimetics. In *Proceedings of the 2009 ASME/IFToMM International Conference on Reconfigurable Mechanisms and Robots ReMAR*, pages 450–455. IEEE, 2009.

[299] B. H. Hanna, S. P. Magleby, R. J. Lang, and L. L. Howell. Force–deflection modeling for generalized origami waterbomb-base mechanisms. *Journal of Applied Mechanics*, 82(8):081001, 2015.

[300] A. Yellowhorse and L. L. Howell. Creating rigid foldability to enable mobility of origami-inspired mechanisms. *Journal of Mechanisms and Robotics*, 8(1):011011, 2016.

[301] W. Gao, K. Ramani, and R. J. Cipra. Reconfigurable foldable spatial mechanisms and robotic forms inspired by kinetogami. In *Proceedings of the ASME 2012 International Design Engineering Technical Conferences and Computers and Information in Engineering Conference IDETC/CIE*, pages No. DETC2012–71403, pp. 1161–1168. American Society of Mechanical Engineers, 2012.

[302] T. Evans. Deployable and foldable arrays of spatial mechanisms. Master's thesis, Brigham Young University-Provo, 2015.

[303] T. Hull. Configuration spaces for flat vertex folds. *Origami 4: Proceedings of 4th International Conference on Origami, Science, Mathematics and Education*, pages 361–370, 2009.

[304] T. Hull. The combinatorics of flat folds: A survey. In *Origami 3: Third International Meeting of Origami Mathematics, Science, and Education*, pages 29–38, 2002.

[305] G. Konjevod. Integer programming models for flat origami. *Origami 4: Proceedings of 4th International Conference on Origami, Science, Mathematics and Education*, pages 207–216, 2009.

[306] T. Kawasaki. On the relation between mountain-creases and valley-creases of a flat origami. In *Proceedings of the 1st International Meeting of Origami Science and Technology*, pages 229–237, 1989.

[307] T. Tachi. Freeform rigid-foldable structure using bidirectionally flat-foldable planar quadrilateral mesh. In *Advances in Architectural Geometry*, pages 87–102. Springer, Vienna, 2010.

[308] M. Bern and B. Hayes. The complexity of flat origami. In *Proceedings of the Seventh Annual ACM-SIAM Symposium on Discrete Algorithms (Society for Industrial and Applied Mathematics)*, volume 96, pages 175–183, 1996.

[309] J. Justin. Towards a mathematical theory of origami. In *Proceedings of the 2nd International Meeting of Origami Science and Scientific Origami*, pages 15–29, 1994.

[310] T. Hull. On the mathematics of flat origamis. *Congressus Numerantium*, pages 215–224, 1994.

[311] J. Mitani. ORIPA (origami pattern editor), available at: `http://mitani.cs.tsukuba.ac.jp/oripa/`. 2012.

[312] J. Mitani. A method for designing crease patterns for flat-foldable origami with numerical optimization. *J. Geom. Graphics*, 15(2):195–201, 2011.

[313] T. Tachi. Rigid origami simulator, available at `http://www.tsg.ne.jp/TT/software/`. 2007.

[314] T. Tachi. Freeform origami, available at `http://www.tsg.ne.jp/TT/software/`. 2013.

[315] T Tachi. Freeform variations of origami. *Journal for Geometry and Graphics*, 14(2):203–215, 2010.

[316] A. Kasem, T. Ida, H. Takahashi, M. Marin, and F. Ghourabi. E-origami system Eos. In *Proceedings of the Annual Symposium of Japan Society for Software Science and Technology, JSSST, Tokyo, Japan (September 2006)*, 2006.

[317] T. Ida, H. Takahashi, M. Marin, and F. Ghourabi. Modeling origami for computational construction and beyond. In *Computational Science and Its Applications–ICCSA 2007*, pages 653–665. Springer, 2007.

[318] A. Kasem and T. Ida. Computational origami environment on the web. *Frontiers of Computer Science in China*, 2(1):39–54, 2008.

[319] M. Schenk and S. D. Guest. Origami folding: A structural engineering approach. *Origami 5: Fifth International Meeting of Origami Science, Mathematics, and Education*, pages 291–304, 2011.

[320] A. R. Diaz. Origami folding and bar frameworks. In *Proceedings of the ASME 2014 International Design Engineering Technical Conferences and Computers and Information in Engineering Conference IDETC/CIE*, pages No. DETC2014–34149, pp. V05BT08A031. American Society of Mechanical Engineers, 2014.

[321] A. A. Evans, J. L. Silverberg, and C. D. Santangelo. Lattice mechanics of origami tessellations. *Physical Review E*, 92(1):013205, 2015.

[322] S. Pellegrino and C.R. Calladine. Matrix analysis of statically and kinematically indeterminate frameworks. *International Journal of Solids and Structures*, 22(4):409–428, 1986.

[323] E. Demaine, M. Demaine, D. Koschitz, and T. Tachi. Curved crease folding: a review on art, design and mathematics. In *Proceedings of the IABSE-IASS Symposium: Taller, Longer, Lighter (IABSE-IASS2011), London, England, Sept*, pages 20–23. Citeseer, 2011.

[324] E. D Demaine, M. L. Demaine, D. A. Huffman, D. Koschitz, and T. Tachi. Characterization of curved creases and rulings: Design and analysis of lens tessellations. *Origami 6: I. Mathematics*, pages 209–230, 2015.

[325] M. A. Dias, L. H. Dudte, L. Mahadevan, and C. D. Santangelo. Geometric mechanics of curved crease origami. *Physical Review Letters*, 109(11):114301,

2012.

[326] J. M. Gattas and Z. You. Miura-base rigid origami: Parametrizations of curved-crease geometries. *Journal of Mechanical Design*, 136(12):121404, 2014.

[327] M. Kilian, S. Flöry, Z. Chen, N. J. Mitra, A. Sheffer, and H. Pottmann. Curved folding. *ACM Transactions on Graphics (TOG)*, 27(3):75, 2008.

[328] G. Epps and S. Verma. Curved folding: Design to fabrication process of Robo-Fold. In *Shape Modeling International*, pages 75–83, 2013.

[329] M. A. Dias and C. D. Santangelo. The shape and mechanics of curved-fold origami structures. *EPL (Europhysics Letters)*, 100(5):54005, 2012.

[330] C. Tang, P. Bo, J. Wallner, and H. Pottmann. Interactive design of developable surfaces. *ACM Transactions on Graphics (TOG)*, 35(2):12, 2016.

[331] D. Koschitz. Designing with curved creases. In *Advances in Architectural Geometry 2016*, pages 82–103. vdf Hochschulverlag AG an der ETH Zürich, 2016.

[332] K. C. Francis, L. T. Rupert, R. J. Lang, D. C. Morgan, S. P. Magleby, and L. L. Howell. From crease pattern to product: Considerations to engineering origami-adapted designs. In *Proceedings of the ASME 2014 International Design Engineering Technical Conferences and Computers and Information in Engineering Conference IDETC/CIE*, pages No. DETC2014–34031, pp. V05BT08A030. American Society of Mechanical Engineers, 2014.

[333] K. Fuchi and A. R. Diaz. Origami design by topology optimization. *Journal of Mechanical Design*, 135(11):111003, 2013.

[334] Y. L. Kergosien, H. Gotoda, and T. L. Kunii. Bending and creasing virtual paper. *Computer Graphics and Applications, IEEE*, 14(1):40–48, 1994.

[335] J. Solomon, E. Vouga, M. Wardetzky, and E. Grinspun. Flexible developable surfaces. *Computer Graphics Forum*, 31(5):1567–1576, 2012.

[336] H.-D. Hwang and S.-H. Yoon. Constructing developable surfaces by wrapping cones and cylinders. *Computer-Aided Design*, 58:230 – 235, 2015. Solid and Physical Modeling 2014.

[337] C. Schreck, D. Rohmer, S. Hahmann, M.-P. Cani, S. Jin, C. C.L. Wang, and J.-F. Bloch. Nonsmooth developable geometry for interactively animating paper crumpling. *ACM Transactions on Graphics (TOG)*, 35(1):10, 2015.

[338] L. Zhu, T. Igarashi, and J. Mitani. Soft folding. *Computer Graphics Forum*, 32(7):167–176, 2013.

[339] S. Miyazaki, T. Yasuda, S. Yokoi, and J.-I. Toriwaki. An origami playing simulator in the virtual space. *Journal of Visualization and Computer Animation*, 7(1):25–42, 1996.

[340] K. Saito, A. Tsukahara, and Y. Okabe. New deployable structures based on an elastic origami model. *Journal of Mechanical Design*, 137(2):021402, 2015.

[341] Y. Nakada, Y. Fujieda, T. Mori, H. Iwai, K. Nakaya, R. Uehara, and M. Yamabe. On a stiffness model for origami folding. In *Proceedings of the ASME 2015 International Design Engineering Technical Conferences and Computers and Information in Engineering Conference IDETC/CIE*, pages No. DETC2015–46731, pp. V05BT08A039. American Society of Mechanical Engineers, 2015.

[342] S. Heimbs. Virtual testing of sandwich core structures using dynamic finite element simulations. *Computational Materials Science*, 45(2):205–216, 2009.

[343] J. Ma and Z. You. Energy absorption of thin-walled beams with a pre-folded origami pattern. *Thin-Walled Structures*, 73:198–206, 2013.

[344] J. Song, Y. Chen, and G. Lu. Axial crushing of thin-walled structures with origami patterns. *Thin-Walled Structures*, 54:65–71, 2012.

[345] Y. Li and Z. You. Thin-walled open-section origami beams for energy absorption. In *Proceedings of the ASME 2014 International Design Engineering Technical Conferences and Computers and Information in Engineering Conference IDETC/CIE*, pages No. DETC2014–35204, pp. V003T01A014. American Society of Mechanical Engineers, 2014.

[346] C. Qiu, V. Aminzadeh, and J. S. Dai. Kinematic analysis and stiffness validation of origami cartons. *Journal of Mechanical Design*, 135(11):111004, 2013.

[347] C. Qiu, V. Aminzadeh, and J. S. Dai. Kinematic and stiffness analysis of an origami-type carton. In *Proceedings of the ASME 2013 International Design Engineering Technical Conferences and Computers and Information in Engineering Conference IDETC/CIE*, pages No. DETC2013–12343, pp. V06BT07A026, Portland, OR, 2013. American Society of Mechanical Engineers.

[348] H. Yasuda, Z. Chen, and J. Yang. Multitransformable leaf-out origami with bistable behavior. *Journal of Mechanisms and Robotics*, 8(3):031013, 2016.

[349] T. Tachi. Interactive form-finding of elastic origami. In *Proceedings of the International Association for Shell and Spatial Structures (IASS) Symposium*, pages 1–2, 2013.

[350] C. M. Wheeler and M. L. Culpepper. Soft origami: classification, constraint, and actuation of highly compliant origami structures. *Journal of Mechanisms and Robotics*, 8(5):051012, 2016.

[351] J. N. Reddy. *Energy Principles and Variational Methods in Applied Mechanics*. John Wiley & Sons, Hoboken NJ, 2002.

[352] J. T. Oden and J. N. Reddy. *An Introduction to the Mathematical Theory of Finite Elements*. Dover Publications, Mineola, New York, 2012.

[353] J. N. Reddy. *An Introduction to the Finite Element Method*, volume 2. McGraw-Hill, New York, 1993.

[354] J. N. Reddy. *Mechanics of Laminated Composite Plates: Theory and Analysis*. CRC Press, Boca Raton, Florida, 1997.

[355] E. Carrera. Theories and finite elements for multilayered, anisotropic, composite plates and shells. *Archives of Computational Methods in Engineering*, 9(2):87–140, 2002.

[356] H. T. Y. Yang, S. Saigal, A. Masud, and R. K. Kapania. A survey of recent shell finite elements. *International Journal for Numerical Methods in Engineering*, 47(1-3):101–127, 2000.

[357] J. Ma, D. Hou, Y. Chen, and Z. You. Quasi-static axial crushing of thin-walled tubes with a kite-shape rigid origami pattern: Numerical simulation. *Thin-Walled Structures*, 100:38–47, 2016.

[358] D. Hou, Y. Chen, J. Ma, and Z. You. Axial crushing of thin-walled tubes with kite-shape pattern. In *Proceedings of the ASME 2015 International Design Engineering Technical Conferences and Computers and Information in Engineering Conference IDETC/CIE*, pages No. DETC2015–46671, pp. V05BT08A037. American Society of Mechanical Engineers, 2015.

[359] K. Yang, S. Xu, J. Shen, S. Zhou, and Y. M. Xie. Energy absorption of thin-walled tubes with pre-folded origami patterns: Numerical simulation and

experimental verification. *Thin-Walled Structures*, 103:33–44, 2016.

[360] S. Heimbs, P. Middendorf, S. Kilchert, A. F. Johnson, and M. Maier. Experimental and numerical analysis of composite folded sandwich core structures under compression. *Applied Composite Materials*, 14(5-6):363–377, 2007.

[361] E. Peraza-Hernandez, D. Hartl, E. Galvan, and R. Malak. Design and optimization of a shape memory alloy-based self-folding sheet. *Journal of Mechanical Design*, 135(11):111007, 2013.

[362] E. Peraza-Hernandez, K. Frei, D. Hartl, and D. Lagoudas. Folding patterns and shape optimization using SMA-based self-folding laminates. *Proceedings of SPIE*, 9057:90571G–90571G–13, 2014.

[363] R. J. Lang. A computational algorithm for origami design. In *Proceedings of the Twelfth Annual Symposium on Computational Geometry*, pages 98–105. ACM, 1996.

[364] John C Bowers. Skeleton structures and origami design. *Thesis, University of Massachusetts - Amherst*, 2015.

[365] R. J. Lang. The tree method of origami design. In *The Second International Meeting of Origami Science and Scientific Origami, K. Miura, ed., Seian University of Art of Design, Otsu, Japan*, pages 72–82, 1994.

[366] R. Lang. Trees and circles: An efficient algorithm for origami design. In *Proceedings of the 3rd International Meeting of Origami Science, Math, and Education*, 2001.

[367] R. J. Lang. *Origami Design Secrets: Mathematical Methods for an Ancient Art (2nd Edition)*. AK Peters, Natick, MA, 2011.

[368] R. Lang. Treemaker, available at `http://www.langorigami.com/article/treemaker`. 1998.

[369] E. D. Demaine and M. L. Demaine. Recent results in computational origami. In *Origami 3: Third International Meeting of Origami Mathematics, Science, and Education*, pages 3–16, 2002.

[370] E. D. Demaine, M. L. Demaine, and J. S.B. Mitchell. Folding flat silhouettes and wrapping polyhedral packages: New results in computational origami. *Computational Geometry*, 16(1):3–21, 2000.

[371] W. Liu and K. Tai. Optimal design of flat patterns for 3D folded structures by unfolding with topological validation. *Computer-Aided Design*, 39(10):898–913, 2007.

[372] W. Schlickenrieder. Nets of polyhedra. Master's thesis, Technische Universität Berlin, 1997.

[373] M. Bern, E. D. Demaine, D. Eppstein, E. Kuo, A. Mantler, and J. Snoeyink. Ununfoldable polyhedra with convex faces. *Computational Geometry*, 24(2):51–62, 2003.

[374] S. Takahashi, H.-Y. Wu, S. H. Saw, C.-C. Lin, and H.-C. Yen. Optimized topological surgery for unfolding 3D meshes. *Computer Graphics Forum*, 30(7):2077–2086, 2011.

[375] Z. Xi, Y. Kim, Y. J. Kim, and J.-M. Lien. Learning to segment and unfold polyhedral mesh from failures. *Computers & Graphics*, 58:139–149, 2016.

[376] M. A. Alam and I. Streinu. Star-unfolding polygons. In *International Workshop on Automated Deduction in Geometry*, pages 1–20. Springer, 2014.

[377] E. Akleman, S. Ke, Y. Wu, N. Kalantar, A. Borhani, and J. Chen. Construction with physical version of quad-edge data structures. *Computers & Graphics*, 58:172–183, 2016.

[378] Y. Forterre, J. M. Skotheim, J. Dumais, and L. Mahadevan. How the Venus flytrap snaps. *Nature*, 433(7024):421–425, 2005.

[379] M. J. Harrington, K. Razghandi, F. Ditsch, L. Guiducci, M. Rueggeberg, J. W. C. Dunlop, C. Fratzl, P.and Neinhuis, and I. Burgert. Origami-like unfolding of hydro-actuated ice plant seed capsules. *Nature Communications*, 2:337, 2011.

[380] S. Jung, P. M. Reis, J. James, C. Clanet, and J. W. M. Bush. Capillary origami in nature. *Physics of Fluids*, 21(9):091110, 2009.

[381] L. Mahadevan and S. Rica. Self-organized origami. *Science*, 307(5716):1740–1740, 2005.

[382] H. Kobayashi, B. Kresling, and J. F. V. Vincent. The geometry of unfolding tree leaves. *Proceedings of the Royal Society of London. Series B: Biological Sciences*, 265(1391):147–154, 1998.

[383] B. Kresling. Folded and unfolded nature. In *Origami Science and Art: Second International Meeting of Origami Science and Scientific Origami, Otsu, Japan*, pages 93–108, 1994.

[384] J. Rossiter and S. Sareh. Kirigami design and fabrication for biomimetic robotics. In *Proceedings of SPIE Smart Structures and Materials+ Nondestructive Evaluation and Health Monitoring*, page 90550G. International Society for Optics and Photonics, 2014.

[385] B. Kresling. Origami-structures in nature: lessons in designing "smart" materials. *MRS Proceedings*, 1420, 2012.

[386] A. R. Studart and R. M. Erb. Bioinspired materials that self-shape through programmed microstructures. *Soft Matter*, 10(9):1284–1294, 2014.

[387] D. S. A. De Focatiis and S. D. Guest. Deployable membranes designed from folding tree leaves. *Philosophical Transactions of the Royal Society of London. Series A: Mathematical, Physical and Engineering Sciences*, 360(1791):227–238, 2002.

[388] W. Li and D. A. McAdams. Novel pixelated multicellular representation for origami structures that innovates computational design and control. In *Proceedings of the ASME 2013 International Design Engineering Technical Conference and Computers and Information in Engineering Conference IDETC/CIE*, pages No. DETC2013–13231, pp. V06BT07A041, Portland, OR, 2013. American Society of Mechanical Engineers.

[389] D. A. McAdams and W. Li. A novel method to design and optimize flat-foldable origami structures through a genetic algorithm. *Journal of Computing and Information Science in Engineering*, 14(3):031008, 2014.

[390] W. Li and D. A. McAdams. Designing optimal origami structures by computational evolutionary embryogeny. *Journal of Computing and Information Science in Engineering*, 15(1):011010, 2015.

[391] T. Tachi. 3D origami design based on tucking molecule. In *Origami 4, Fourth International Meeting of Origami Science, Mathematics, and Education*, pages 259–272, 2009.

[392] K. Fuchi, P. R. Buskohl, G. Bazzan, M. F. Durstock, G. W. Reich, R. A. Vaia, and J. J. Joo. Origami actuator design and networking through crease topology optimization. *Journal of Mechanical Design*, 137(9):091401, 2015.

[393] K. Saito, A. Tsukahara, and Y. Okabe. Designing of self-deploying origami structures using geometrically misaligned crease patterns. *Proceedings of the Royal Society of London A: Mathematical, Physical and Engineering Sciences*, 472(2185), 2016.

[394] S. Ishida, T. Nojima, and I. Hagiwara. Application of conformal maps to origami-based structures: New method to design deployable circular membranes. In *Proceedings of the ASME 2013 International Design Engineering Technical Conference and Computers and Information in Engineering Conference IDETC/CIE*, pages No. DETC2013–12725, pp. V06BT07A035, Portland, OR, 2013. American Society of Mechanical Engineers.

[395] K. Zhu, C. Deshan, and O. N. N. Fernando. Snap-n-Fold: Origami pattern generation based real-life object structure. In *CHI'12 Extended Abstracts on Human Factors in Computing Systems*, pages 2345–2350. ACM, 2012.

[396] T. Tachi. Designing rigidly foldable horns using Bricard's octahedron. *Journal of Mechanisms and Robotics*, 8(3):031008, 2016.

[397] R. J. Lang, S. Magleby, and L. Howell. Single degree-of-freedom rigidly foldable cut origami flashers. *Journal of Mechanisms and Robotics*, 8(3):031005, 2016.

[398] B. J. Edmondson, R. J. Lang, M. R. Morgan, S. P. Magleby, and L. L. Howell. Thick rigidly foldable structures realized by an offset panel technique. *Origami 6: I. Mathematics*, page 149, 2015.

[399] T. Tachi. Rigid-foldable thick origami. *Origami 5: Fifth International Meeting of Origami Science, Mathematics, and Education*, pages 253–264, 2011.

[400] S. A. Zirbel, R. J. Lang, M. W. Thomson, D. A. Sigel, P. E. Walkemeyer, B. P. Trease, S. P. Magleby, and L. L. Howell. Accommodating thickness in origami-based deployable arrays. *Journal of Mechanical Design*, 135(11):111005, 2013.

[401] S. A. Zirbel, M. E. Wilson, S. P. Magleby, and L. L. Howell. An origami-inspired self-deployable array. In *Proceedings of the ASME 2013 Conference on Smart Materials, Adaptive Structures and Intelligent Systems SMASIS*, pages No. SMASIS2013–3296, pp. V001T01A026, Snowbird, UT, 2013. American Society of Mechanical Engineers.

[402] S. A. Zirbel, B. P. Trease, M. W. Thomson, R. J. Lang, S. P. Magleby, and L. H. Howell. HanaFlex: A large solar array for space applications. In *Proceedings of SPIE*, volume 9467, pages 94671C–94671C–9, 2015.

[403] J. S. Ku and E. D. Demaine. Folding flat crease patterns with thick materials. In *Proceedings of the ASME 2015 International Design Engineering Technical Conferences and Computers and Information in Engineering Conference IDETC/CIE*, pages No. DETC2015–48039, pp. V05BT08A056. American Society of Mechanical Engineers, 2015.

[404] J. S. Ku and E. D. Demaine. Folding flat crease patterns with thick materials. *Journal of Mechanisms and Robotics*, 8(3):031003, 2016.

[405] K. Saito, A. Tsukahara, and Y. Okabe. Designing of self-deploying origami structures using geometrically misaligned crease patterns. *Proceedings of the Royal Society of London A: Mathematical, Physical and Engineering Sciences*, 472(2185):20150235, 2016.

[406] G. Song and N. M. Amato. A motion-planning approach to folding: from paper craft to protein folding. *IEEE Transactions on Robotics and Automation*, 20(1):60–71, 2004.

[407] N. M. Amato, K. A. Dill, and G. Song. Using motion planning to map protein folding landscapes and analyze folding kinetics of known native structures. *Journal of Computational Biology*, 10(3-4):239–255, 2003.

[408] Z. Xi and J.-M. Lien. Folding rigid origami with closure constraints. In *Proceedings of the ASME 2014 International Design Engineering Technical Conferences and Computers and Information in Engineering Conference IDETC/CIE*, pages No. DETC2014–35556, pp. V05BT08A052. American Society of Mechanical Engineers, 2014.

[409] Z. Xi and J.-M. Lien. Folding and unfolding origami tessellation by reusing folding path. In *Proceedings of the 2015 IEEE International Conference on Robotics and Automation (ICRA)*, pages 4155–4160. IEEE, 2015.

[410] Z. Xi and J.-M. Lien. Plan folding motion for rigid self-folding machine via discrete domain sampling. In *Proceedings of the 2015 IEEE International Conference on Robotics and Automation (ICRA)*, pages 2938–2943. IEEE, 2015.

[411] R. A. Horn and C. R. Johnson. *Topics in Matrix Analysis*. Cambridge University Press, Cambridge, 1991.

[412] W.-H. Steeb and T. K. Shi. *Matrix Calculus and Kronecker Product with Applications and C++ Programs*. World Scientific Publishing, River Edge, New Jersey, 1997.

[413] W.-H. Steeb. *Problems and Solutions in Introductory and Advanced Matrix Calculus*. World Scientific Publishing, Hackensack, New Jersey, 2006.

[414] A. N. Pressley. *Elementary Differential Geometry*. Springer Science & Business Media, London, UK, 2010.

[415] C. R. Calladine. *Theory of Shell Structures*. Cambridge University Press, Cambridge, 1989.

[416] E. Akleman and J. Chen. Insight for practical subdivision modeling with discrete gauss-bonnet theorem. In *International Conference on Geometric Modeling and Processing*, pages 287–298. Springer, 2006.

[417] M. Meyer, M. Desbrun, P. Schröder, and A. H. Barr. Discrete differential-geometry operators for triangulated 2-manifolds. In *Visualization and Mathematics III*, pages 35–57. Springer, 2003.

[418] J. M. Sullivan. Curvatures of smooth and discrete surfaces. In *Discrete Differential Geometry*, pages 175–188. Springer, 2008.

[419] T. Tachi. Rigid folding of periodic origami tessellations. *Origami 6: I. Mathematics*, pages 97–108, 2015.

[420] D. Davis, R. Mailen, J. Genzer, and M. D. Dickey. Self-folding of polymer sheets using microwaves and graphene ink. *RSC Advances*, 5(108):89254–89261, 2015.

[421] J.-H. Na, A. A. Evans, J. Bae, M. C. Chiappelli, C. D. Santangelo, R. J. Lang, T. C. Hull, and R. C. Hayward. Programming reversibly self-folding origami with micropatterned photo-crosslinkable polymer trilayers. *Advanced Materials*, 27(1):79–85, 2015.

[422] J. C. Breger, C. Yoon, R. Xiao, H. R. Kwag, M. O. Wang, J. P. Fisher, T. D. Nguyen, and D. H. Gracias. Self-folding thermo-magnetically responsive soft microgrippers. *ACS Applied Materials & Interfaces*, 7(5):3398–3405, 2015.

[423] S. Pandey, C. Yoon, Z. Zhang, H. R. Kwag, J. Hong, and D. H. Gracias. Patterned soft-micropolyhedra by self-folding and molding. In *Proceedings of the 2016 IEEE 29th International Conference on Micro Electro Mechanical Systems (MEMS)*, pages 203–206. IEEE, 2016.

[424] Y. Zhang and L. Ionov. Reversibly cross-linkable thermoresponsive self-folding hydrogel films. *Langmuir*, 31(15):4552–4557, 2015.

[425] S. Zakharchenko and L. Ionov. Anisotropic liquid microcapsules from biomimetic self-folding polymer films. *ACS Applied Materials & Interfaces*, 7(23):12367–12372, 2015.

[426] B. A. Barsky and T. D. DeRose. *Geometric continuity of parametric curves*. Computer Science Division, University of California, 1984.

[427] B. A. Barsky, R. H. Bartels, and J. C. Beatty. *An Introduction to Splines for Use in Computer Graphics and Geometric Modeling*. Los Altos, Calif.: M. Kaufmann Publishers, 1987.

[428] W. Cheney and D. Kincaid. *Numerical Analysis. Mathematics of Scientific Computing*. Brooks & Cole Publishing Company, Pacific Grove, California, 1996.

[429] F. McRobie and J. Lasenby. The kinematics of large rotations using Clifford algebra. In *IUTAM-IASS Symposium on Deployable Structures: Theory and Applications*, pages 271–280. Springer, 2000.

[430] Y. Chen, R. Peng, and Z. You. Origami of thick panels. *Science*, 349(6246):396–400, 2015.

[431] M. R. Morgan, R. J Lang, S. P. Magleby, and L. L. Howell. Towards developing product applications of thick origami using the offset panel technique.

Mechanical Sciences, 7(1):69, 2016.

[432] M. Arya. *Packaging and deployment of large planar spacecraft structures*. PhD thesis, California Institute of Technology, 2016.

[433] M. Arya, N. Lee, and S. Pellegrino. Wrapping thick membranes with slipping folds. In *Proceedings of the 2nd AIAA Spacecraft Structures Conference*, page 0682, 2015.

[434] J. Erickson and S. Har-Peled. Optimally cutting a surface into a disk. *Discrete & Computational Geometry*, 31(1):37–59, 2004.

[435] T. K. Dey and H. Schipper. A new technique to compute polygonal schema for 2-manifolds with application to null-homotopy detection. *Discrete & Computational Geometry*, 14(1):93–110, 1995.

[436] F. Lazarus, M. Pocchiola, G. Vegter, and A. Verroust. Computing a canonical polygonal schema of an orientable triangulated surface. In *Proceedings of the Seventeenth Annual Symposium on Computational Geometry*, pages 80–89. ACM, 2001.

[437] P. J. Frey and P. L. George. *Mesh Generation: Application to Finite Elements. 2nd ed.* Wiley online library. London: ISTE; Hoboken, NJ: John Wiley & Sons, 2008.

[438] Y. Zheng, R. W. Lewis, and D. T. Gethin. Three-dimensional unstructured mesh generation: Part 2. Surface meshes. *Computer Methods in Applied Mechanics and Engineering*, 134(3):269 – 284, 1996.

[439] W. S. Slaughter. *The Linearized Theory of Elasticity*. Birkhäuser, Boston, 2002.

[440] G. A. Holzapfel. *Nonlinear Solid Mechanics: A Continuum Approach for Engineering*. John Wiley & Sons, LTD, Chichester, 2000.

[441] J. N. Reddy. *An Introduction to Nonlinear Finite Element Analysis: with applications to heat transfer, fluid mechanics, and solid mechanics*. Oxford University Press, Oxford, 2014.

[442] D. Lagoudas, D. Hartl, Y. Chemisky, L. Machado, and P. Popov. Constitutive model for the numerical analysis of phase transformation in polycrystalline shape memory alloys. *International Journal of Plasticity*, 3233:155 – 183, 2012.

[443] D. J. Hartl, D. C. Lagoudas, and F. T. Calkins. Advanced methods for the analysis, design, and optimization of SMA-based aerostructures. *Smart Materials and Structures*, 20(9):094006, 2011.

[444] J. L. Rohmer, E. A. Peraza Hernandez, R. E. Skelton, D. J. Hartl, and D. C. Lagoudas. An experimental and numerical study of shape memory alloy-based tensegrity/origami structures. In *Proceedings of the ASME 2015 International Mechanical Engineering Congress and Exposition IMECE 2015*, pages No. IMECE2015–51928, pp. V009T12A064, Houston, TX, 2015. American Society of Mechanical Engineers.

[445] D. J. Hartl, J. T. Mooney, D. C. Lagoudas, F. T. Calkins, and J. H. Mabe. Use of a Ni60Ti shape memory alloy for active jet engine chevron application: II. Experimentally validated numerical analysis. *Smart Materials and Structures*, 19(1):015021, 2009.

[446] D. J. Hartl, J. T. Mooney, D. C. Lagoudas, J. H. Mabe, and F. T. Calkins. Experimentally validated numerical analysis of aerostructures incorporating shape memory alloys. In *Proceedings of SPIE*, volume 6929, pages 692913–692913–11, 2008.

[447] S. D. Oehler, D. J. Hartl, R. Lopez, R. J. Malak, and D. C. Lagoudas. Design optimization and uncertainty analysis of SMA morphing structures. *Smart Materials and Structures*, 21(9):094016, 2012.

[448] E. A. Peraza Hernandez, D. J. Hartl, A. Kotz, and R. J. Malak. Design and optimization of an SMA-based self-folding structural sheet with sparse insulating layers. In *Proceedings of the ASME 2014 Conference on Smart Materials, Adaptive Structures and Intelligent Systems SMASIS*, pages No. SMASIS2014–7540, pp. V001T01A015. American Society of Mechanical Engineers, 2014.

[449] J. Solomon. *Numerical Algorithms: Methods for Computer Vision, Machine Learning, and Graphics*. CRC Press, Boca Raton, Florida, 2015.

[450] A. G. Solomou, T. T. Machairas, and D. A. Saravanos. A coupled thermomechanical beam finite element for the simulation of shape memory alloy actuators. *Journal of Intelligent Material Systems and Structures*, page 1045389X14526462, 2014.

[451] D. J. Hartl and D. C. Lagoudas. Constitutive modeling and structural analysis considering simultaneous phase transformation and plastic yield in shape memory alloys. *Smart Materials and Structures*, 18(10):104017, 2009.

[452] E. C. de Verdiere and F. Lazarus. Optimal polygonal schema on an orientable surface. In *18th European Workshop on Computational Geometry*, pages 627–636, 2002.

[453] P. Cignoni, C. Montani, and R. Scopigno. A comparison of mesh simplification algorithms. *Computers & Graphics*, 22(1):37–54, 1998.

[454] Z. J. Li, Y. Zhou, T. Yun, Z. Feng, and S. Zhang. A short review on mesh simplification. In *Applied Mechanics and Materials*, volume 568, pages 628–

633. Trans. Tech. Publ., 2014.

[455] J. N. Reddy. A simple higher-order theory for laminated composite plates. *Journal of Applied Mechanics*, 51(4):745–752, 1984.

[456] E. Carrera. Theories and finite elements for multilayered plates and shells: A unified compact formulation with numerical assessment and benchmarking. *Archives of Computational Methods in Engineering*, 10(3):215–296, 2003.

[457] D. C. Lagoudas, D. Moorthy, M. A. Qidwai, and J. N. Reddy. Modeling of the thermomechanical response of active laminates with SMA strips using the layerwise finite element method. *Journal of Intelligent Material Systems and Structures*, 8(6):476–488, 1997.

[458] S. Timoshenko et al. Analysis of bi-metal thermostats. *J. Opt. Soc. Am*, 11(3):233–255, 1925.

[459] W. M. Lai, E. Krempl, and D. Ruben. *Introduction to Continuum Mechanics*. Butterworth-Heinemann, Elsevier, Burlington, Massachusetts, 2009.

APPENDIX A

ANALYSIS OF SELF-FOLDING USING A LAMINATE WITH AN ACTIVE LAYER AND A PASSIVE LAYER

[1]The derivation of the equations used for the simplified analysis of the multilayer self-folding concept (Figure 1.4(d)) presented in Section 1.1.3 is outlined in this Appendix. For simplicity, bending of a laminated beam having one active layer and one passive layer is considered. The base analytical solution for this case is obtained from [458]. The bilayer laminate is illustrated in Figure A.1. The laminate of total thickness h_B has a layer of material I of thickness a_1^B and a layer of material II of thickness a_2^B such that:

$$a_1^B + a_2^B = h_B. \tag{A.1}$$

The width of the laminated beam is denoted as w_B so that the total cross-sectional area of the beam is $w_B h_B$. In [458], it is assumed that both materials comprising the laminate are thermoelastic. Material I has Young's modulus and thermal expansion coefficient of E_1^B and α_1^B, respectively. Likewise, material II has Young's modulus and thermal expansion coefficient of E_2^B and α_2^B, respectively. When the temperature of the laminate is uniformly altered from the reference temperature T_0 to a current temperature T, the laminate bends to a configuration having a mid-surface radius of curvature R_B (see Figure A.1) due to the unequal thermal expansion coefficients of the constituent layers (i.e. when $\alpha_1^B \neq \alpha_2^B$). The relationship between the obtained

[1]Portions of this appendix are reprinted or adapted from [3] E. A. Peraza-Hernandez, D. J. Hartl, R. J. Malak Jr, and D. C. Lagoudas. Origami-inspired active structures: a synthesis and review. Smart Materials and Structures, 23(9):094001, 2014. http://dx.doi.org/10.1088/0964-1726/23/9/094001

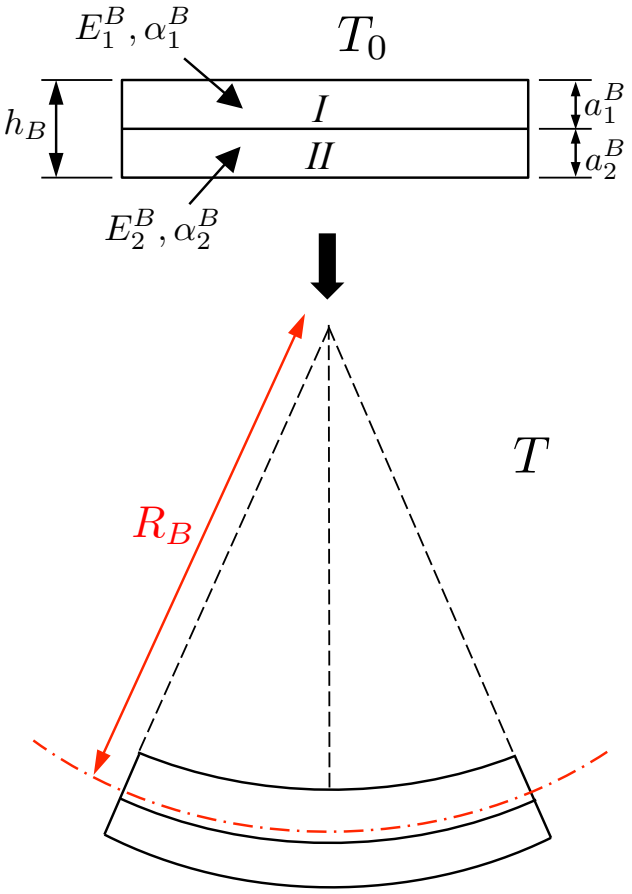

Figure A.1: Bending of a bilayer laminated beam under unequal field-induced expansion of its comprising layers. The bending radius of curvature R_B is measured at the mid-surface of the laminate.

radius of curvature R_B and the geometric and material parameters of the laminate was derived by Timoshenko [458] and is given as follows:

$$\frac{1}{R_B} = \frac{6(\alpha_2^B - \alpha_1^B)(T - T_0)(1 + m_B)^2}{h_B\Big(3(1 + m_B)^2 + (1 + m_B n_B)\big(m_B^2 + 1/(m_B n_B)\big)\Big)}, \tag{A.2}$$

where m_B and n_B are defined as follows:

$$m_B := \frac{a_1^B}{a_2^B}, \tag{A.3}$$

$$n_B := \frac{E_1^B}{E_2^B}. \tag{A.4}$$

Also let the dimensionless constants C_1^B and C_2^B be defined as follows:

$$C_1^B := \frac{3(1+m_B)^2 + (1+m_B n_B)\big(m_B^2 + 1/(m_B n_B)\big)}{6(1+m_B)^2}, \tag{A.5}$$

$$C_2^B := 2 + \frac{6h_B(a_1^B)^2 E_1^B}{E_1^B(a_1^B)^3 + E_2^B(a_2^B)^3}. \tag{A.6}$$

For the assessment of self-folding with respect to actuation strain and actuation stress, material I is assumed as the active material while material II is assumed as the passive material. In Equation (A.2), the actuation strain is assumed to be due to the thermal expansion of the constituent layers. However, the final configuration of such a laminate would be the same regardless of the physical mechanisms generating the actuation strain. Therefore, the following expressions are considered:

$$\alpha_2^B = 0, \tag{A.7}$$

$$\varepsilon^{ACT} = -\alpha_1^B(T - T_0). \tag{A.8}$$

Equation (A.7) emerges from the assumption that the passive material provides negligible strain under the applied field. Equation (A.8) implies that the active layer is deforming with a strain of ε^{ACT}. The following is obtained after substituting in Equations (A.7) and (A.8) into Equation (A.2):

$$\frac{1}{R_B} = \frac{6\varepsilon^{ACT}(1+m_B)^2}{h_B\Big(3(1+m_B)^2 + (1+m_B n_B)\big(m_B^2 + 1/(m_B n_B)\big)\Big)}. \tag{A.9}$$

The radius of curvature non-dimensionalized by the laminate thickness is then given as follows:

$$\frac{R_B}{h_B} = \frac{3(1+m_B)^2 + (1+m_B n_B)\left(m_B^2 + 1/(m_B n_B)\right)}{6\varepsilon^{ACT}(1+m_B)^2}. \tag{A.10}$$

To simplify the preceding equation, the constant C_1^B, defined in Equation (A.5), is substituted into Equation (A.10) and the following is obtained:

$$\varepsilon^{ACT} = \frac{C_1^B h_B}{R_B}. \tag{A.11}$$

Equation (A.11) provides a non-dimensional analytical expression for the assessment of the self-folding behavior of a bilayer laminate with a layer of active material and a layer of passive material. Clearly, as the actuation strain increases, the radius of curvature of the bent sheet decreases.

An assessment of the influence of effective actuation stress σ^{ACT} on the folding performance is subsequently derived. The effective actuation stress σ^{ACT} is assumed as the maximum stress experienced by the active layer. An expression for the maximum stress in the considered bilayer laminated beam was also obtained by Timoshenko [458] and is given as follows:

$$\sigma^{ACT} = \frac{P_B}{w_B a_1^B} + \frac{a_1^B E_1^B}{2R_B}, \tag{A.12}$$

where P_B is the total axial force in the active layer. It can be shown [458] that the total bending moment M_B relates to P_B and R_B as follows:

$$P_B = \frac{2M_B}{h_B}, \tag{A.13}$$

$$
\begin{aligned}
R_B &= \frac{E_1^B I_1^B + E_2^B I_2^B}{M_B} \\
&= \frac{w_B(E_1^B(a_1^B)^3 + E_2^B(a_2^B)^3)}{12M_B},
\end{aligned}
\tag{A.14}
$$

where I_1^B and I_2^B are the area moments of inertia of the cross-sections of layers I and II, respectively. The term $E_1^B I_1^B + E_2^B I_2^B$ represents the effective bending stiffness of the laminate. The moments of inertia were substituted in Equation (A.14) using the relation $I_i^B = w_B(a_i^B)^3/12$ where $i = 1, 2$. Substituting the results from Equations (A.13) and (A.14) into Equation (A.12) the following is obtained:

$$
\sigma^{ACT} = \frac{M_B}{w_B h_B a_1^B}\left(2 + \frac{6h_B(a_1^B)^2 E_1^B}{E_1^B(a_1^B)^3 + E_2^B(a_2^B)^3}\right). \tag{A.15}
$$

To simplify Equation (A.15), the constant C_2^B defined in Equation (A.6) is substituted into Equation (A.15) and the following simplified relation between actuation stress and bending moment is obtained:

$$
\sigma^{ACT} = \frac{M_B C_2^B}{w_B h_B a_1^B}. \tag{A.16}
$$

APPENDIX B

ANALYSIS OF SELF-FOLDING USING A TORSIONAL ACTUATOR

[1]The derivation of the equations used for the simplified analysis of the *torsional* concept for an active fold (Figure 1.4(b)) presented in Section 1.1.3 is summarized in this Appendix. In order to allow for a simplified analysis, only the active torsional element is contained in the analysis domain [3]. A boundary value problem of the torsional element is considered by modeling the interactions of the element with other bodies (hinge and connected faces, refer to Figure 1.4(b)) as applied moments. The active torsional element is represented as a rod of length L_T and having uniform circular cross-section of radius r_T. The rod is assumed to initially have zero stresses. The rod twists under the uniform application of the activation field which allows for the generation of actuation strains. If the rod is constrained to some degree at its ends, it is subjected to equal and opposite end-torques denoted as M_T. These torques are associated with the resistance of the sheet to fold (caused by friction at the hinge, interactions of the sheet with other bodies, the effects of gravity, etc.). The reference and current configurations of the torsional element are shown in Figure B.1.

In this analysis, the longitudinal axis of the rod is defined such that it coincides with the 1-axis. By the rotational symmetry of the problem, it is reasonable to assume that the deformation of each infinitesimal region along the longitudinal axis of the rod with thickness $\mathrm{d}X_1$ is restricted to a rigid body rotation about the 1-axis [459]. Considering a quasi-static form of the equations for conservation of linear

[1]Portions of this appendix are reprinted or adapted from [3] E. A. Peraza-Hernandez, D. J. Hartl, R. J. Malak Jr, and D. C. Lagoudas. Origami-inspired active structures: a synthesis and review. Smart Materials and Structures, 23(9):094001, 2014. http://dx.doi.org/10.1088/0964-1726/23/9/094001

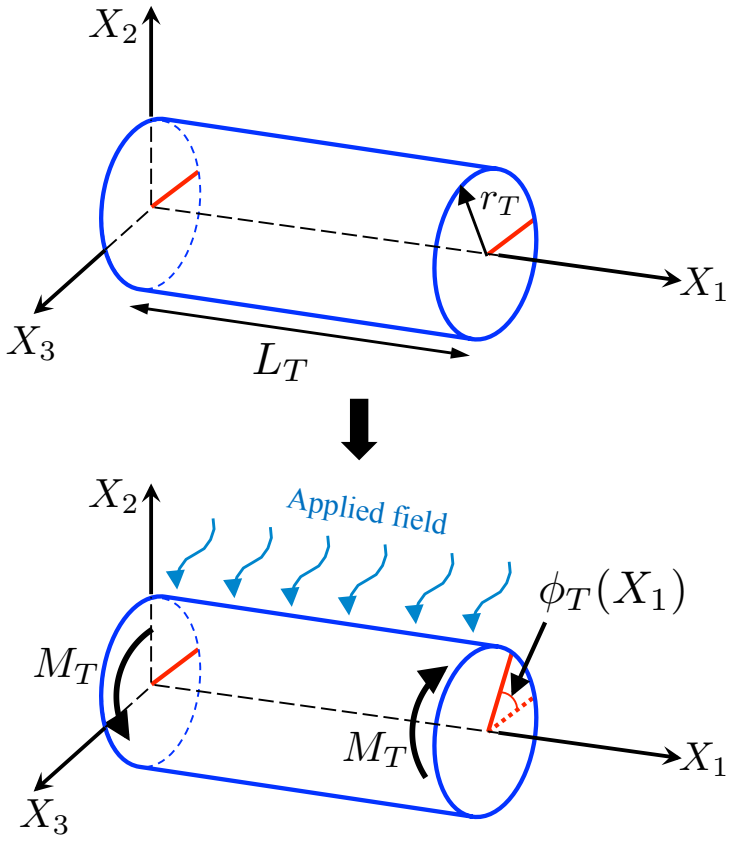

Figure B.1: Reference and current configurations of an active rod that twists under the application of a uniform field.

momentum, no body forces, and uniform actuation strains along the 1-axis, it can be determined that the *twist angle* ϕ_T varies linearly along the 1-axis [459]:

$$\frac{\mathrm{d}\phi_T}{\mathrm{d}X_1} = \text{constant} = \phi_T'. \tag{B.1}$$

Under such an assumption on the deformation of the rod, the only non-zero strains, which are due to elastic strains (denoted as ε_{ij}^{EL}) and physical mechanism-agnostic *actuation strains* (denoted ε_{ij}^{ACT}) are given by:

$$\varepsilon_{12}^{EL} + \varepsilon_{12}^{ACT} = -\frac{1}{2} X_3 \phi_T', \tag{B.2}$$

$$\varepsilon_{13}^{EL} + \varepsilon_{13}^{ACT} = \frac{1}{2} X_2 \phi_T'. \tag{B.3}$$

The corresponding non-zero stress components are the following:

$$\sigma_{12} = G_T \left(-\frac{1}{2} X_3 \phi_T' - \varepsilon_{12}^{ACT} \right), \tag{B.4}$$

$$\sigma_{13} = G_T \left(\frac{1}{2} X_2 \phi_T' - \varepsilon_{13}^{ACT} \right), \tag{B.5}$$

where G_T is the shear modulus of the active material rod that is assumed to be homogeneous and independent from the deformation of the rod. To determine the influence of the actuation stress and actuation strain of the active material on the folding performance, two different cases are explored. To relate actuation strain to the folding performance of the torsional element, it is assumed that the magnitude of the actuation shear strain far exceeds that of the elastic shear strain due to the choice of active material and/or the assumption of negligible applied moments at the fold (i.e. $\sigma_{12} = \sigma_{13} = 0$). Considering Equations (B.4) and (B.5) under this assumption:

$$\varepsilon_{12}^{ACT} = -\frac{1}{2} X_3 \phi_T', \tag{B.6}$$

$$\varepsilon_{13}^{ACT} = \frac{1}{2} X_2 \phi_T'. \tag{B.7}$$

The effective actuation strain ε^{ACT} in the rod considering the strain components

given in Equation (B.6) and (B.7) is the following:

$$\begin{aligned} \varepsilon^{ACT} &= \left(\frac{2}{3}\left(2(\varepsilon_{12}^{ACT})^2 + 2(\varepsilon_{13}^{ACT})^2\right)\right)^{1/2} \\ &= \frac{\sqrt{3}}{3}\phi_T'(X_2^2 + X_3^2)^{1/2}. \end{aligned} \tag{B.8}$$

The maximum value of ε^{ACT} occurs at $(X_2^2 + X_3^2)^{1/2} = r_T$. Therefore, the spatial derivative of twist angle along the rod longitudinal axis ϕ_T' multiplied by r_T is given by:

$$r_T\phi_T' = \sqrt{3}\,\varepsilon^{ACT}, \tag{B.9}$$

and the *total twist angle* φ_T (that is expected to translate into a fold angle) is calculated by integrating ϕ_T' over the entire length of the rod:

$$\begin{aligned} \varphi_T &= \int_0^{L_T} \phi_T'\,\mathrm{d}X_1 \\ &= \phi_T' \int_0^{L_T} \mathrm{d}X_1 = \phi_T' L_T. \end{aligned} \tag{B.10}$$

Substituting Equation (B.10) in Equation (B.9), the following relation between ε^{ACT} and the total twist angle φ_T is obtained:

$$\varepsilon^{ACT} = \frac{\sqrt{3}\,r_T\varphi_T}{3L_T}. \tag{B.11}$$

To assess the influence of actuation stress on the resulting folding response, the case in which the fold having the active torsional rod is fully constrained from folding is considered. In this case, $\phi_T(X_1) = 0$ and $\phi_T' = 0$. Considering Equations (B.2)–

(B.5) and the previous assumptions, the following is obtained:

$$\begin{aligned} \sigma_{12} &= G_T(-\varepsilon_{12}^{ACT}) \\ &= G_T\varepsilon_{12}^{EL}, \end{aligned} \tag{B.12}$$

$$\begin{aligned} \sigma_{13} &= G_T(-\varepsilon_{13}^{ACT}) \\ &= G_T\varepsilon_{13}^{EL}. \end{aligned} \tag{B.13}$$

The preceding equation corresponds to the elastic solution of the problem for which the relations between the stresses and the applied torque are given as follows [459]:

$$\sigma_{12} = -\frac{M_T X_3}{I_T}, \tag{B.14}$$

$$\sigma_{13} = \frac{M_T X_2}{I_T}, \tag{B.15}$$

where I_T is the polar second moment of the circular cross-section ($I_T = \pi r_T^4/2$). The von Mises stress $\bar{\sigma}$ in the rod is given as follows [439]:

$$\begin{aligned} \bar{\sigma} &= \left(\frac{3}{2}\left(2(\sigma_{12})^2 + 2(\sigma_{13})^2\right)\right)^{1/2} \\ &= \sqrt{3}\,\frac{M_T}{I_T}(X_2^2 + X_3^2)^{1/2}, \end{aligned} \tag{B.16}$$

and the effective actuation stress σ^{ACT} (assumed as the maximum von Mises stress in the rod) occurs at $(X_2^2 + X_3^2)^{1/2} = r_T$ and is related to the applied torque M_T as

follows:

$$\sigma^{ACT} = \frac{2\sqrt{3}\, M_T}{\pi r_T^3}. \tag{B.17}$$

Equations (B.11) and (B.17) provide an assessment of the folding performance (twist angle, applied torque) of the torsional concept for an active fold as function of actuation stress and strain of the active material.

APPENDIX C

DERIVATION OF THE CONSTRAINT FOR ORIGAMI WITH CREASED FOLDS (EQUATION (2.14)) AS A SPECIAL CASE OF THE CONSTRAINTS FOR ORIGAMI WITH SMOOTH FOLDS

[1]The constraint for origami with creased folds presented in Equation (2.14) has been derived in the literature (see [121, 276]) using an approach analogous to that taken in Section 2.2.3 to derive the constraints for origami with smooth folds (Equations (2.85) and (2.86)). The purpose here is not to reproduce such a derivation from the literature but rather derive Equation (2.14) as a special case of Equations (2.85) and (2.86) occurring when the smooth folds are degenerated to straight lines (corresponding to creased folds).

Since Equation (2.14) is already accounted for in origami with smooth folds (cf. Equation (2.85)), it is only needed to show that $\mathbf{d}^j = \mathbf{0}_3$ (Equation (2.86)) holds for origami with creased folds if the constraint presented in Equation (2.14) is met. A segment of a general path $\boldsymbol{\gamma}_j(\eta)$ enclosing an interior fold intersection (corresponding to a single point for origami with creased folds) crossing each of its incident folds once in a counterclockwise order is shown in Figure C.1. Using Figure C.1 as a reference, the vectors $\tilde{\mathbf{w}}^{jk}$ and $\tilde{\mathbf{l}}^{jk}$ (see Equations (2.81) and (2.82)) are respectively given as

[1]Portions of this appendix are reprinted or adapted from [7] E. A. Peraza Hernandez, D. J. Hartl, and D. C. Lagoudas. Kinematics of origami structures with smooth folds. Journal of Mechanisms and Robotics, 2016. Copyright © 2016 by ASME. Reproduced with permission. http://dx.doi.org/10.1115/1.4034299

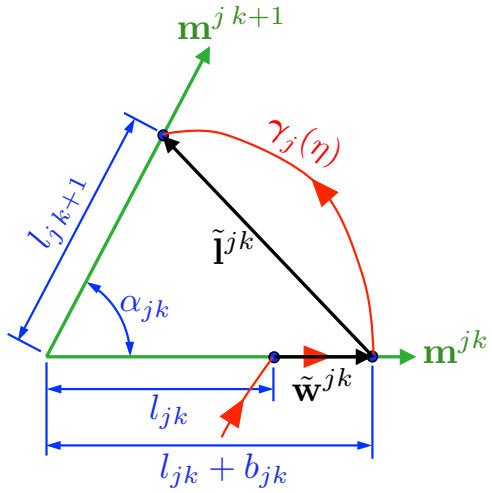

Figure C.1: Schematic showing two adjacent creased folds (along the vectors $\mathbf{m}^{jk}$ and $\mathbf{m}^{j\,k+1}$) incident to a common interior vertex. The vectors $\tilde{\mathbf{w}}^{jk}$ and $\tilde{\mathbf{l}}^{jk}$ are shown.

follows:

$$\tilde{\mathbf{w}}^{jk} = \begin{bmatrix} b_{jk} \\ 0 \\ 0 \end{bmatrix}, \tag{C.1}$$

$$\tilde{\mathbf{l}}^{jk} = \begin{cases} \begin{bmatrix} l_{j\,k+1}\cos(\alpha_{jk}) - l_{jk} - b_{jk} \\ l_{j\,k+1}\sin(\alpha_{jk}) \\ 0 \end{bmatrix}; & k = 1, \ldots, n_j - 1 \\ \begin{bmatrix} l_{j1}\cos(\alpha_{jk}) - l_{jk} - b_{jk} \\ l_{j1}\sin(\alpha_{jk}) \\ 0 \end{bmatrix}; & k = n_j \end{cases}, \tag{C.2}$$

where $l_{jk} \in \mathbb{R}_{\geq 0}$, $b_{jk} \in \mathbb{R}$, and $l_{jk} + b_{jk} \geq 0$.

Substituting Equations (C.1) and (C.2) into the expression for $\mathbf{d}^j$ provided in Equation (2.86) and utilizing the fact that $\mathbf{R}_1(\phi)\tilde{\mathbf{w}}^{jk} = \tilde{\mathbf{w}}^{jk}$ for the expression of $\tilde{\mathbf{w}}^{jk}$ in Equation (C.1), the following is obtained:

$$
\begin{aligned}
\mathbf{d}^j &= \sum_{k=1}^{n_j} \left(\left(\prod_{l=1}^{k-1} \mathbf{R}_1(\theta_{jl}) \mathbf{R}_3(\alpha_{jl}) \right) \begin{bmatrix} b_{jk} \\ 0 \\ 0 \end{bmatrix} \right) \\
&\quad + \sum_{k=1}^{n_j-1} \left(\left(\prod_{l=1}^{k-1} \mathbf{R}_1(\theta_{jl}) \mathbf{R}_3(\alpha_{jl}) \right) \mathbf{R}_1\left(\theta_{jk}\right) \begin{bmatrix} l_{j\,k+1}\cos(\alpha_{jk}) - l_{jk} - b_{jk} \\ l_{j\,k+1}\sin(\alpha_{jk}) \\ 0 \end{bmatrix} \right) \\
&\quad + \left(\prod_{l=1}^{n_j-1} \mathbf{R}_1(\theta_{jl}) \mathbf{R}_3(\alpha_{jl}) \right) \mathbf{R}_1\left(\theta_{jn_j}\right) \begin{bmatrix} l_{j1}\cos(\alpha_{jn_j}) - l_{jn_j} - b_{jn_j} \\ l_{j1}\sin(\alpha_{jn_j}) \\ 0 \end{bmatrix} \\
&= \sum_{k=1}^{n_j-1} \left(\left(\prod_{l=1}^{k-1} \mathbf{R}_1(\theta_{jl}) \mathbf{R}_3(\alpha_{jl}) \right) \mathbf{R}_1\left(\theta_{jk}\right) \begin{bmatrix} l_{j\,k+1}\cos(\alpha_{jk}) - l_{jk} \\ l_{j\,k+1}\sin(\alpha_{jk}) \\ 0 \end{bmatrix} \right) \\
&\quad + \left(\prod_{l=1}^{n_j-1} \mathbf{R}_1(\theta_{jl}) \mathbf{R}_3(\alpha_{jl}) \right) \mathbf{R}_1\left(\theta_{jn_j}\right) \begin{bmatrix} l_{j1}\cos(\alpha_{jn_j}) - l_{jn_j} \\ l_{j1}\sin(\alpha_{jn_j}) \\ 0 \end{bmatrix}.
\end{aligned}
\tag{C.3}
$$

The following equality is then used to simplify the previous expression:

$$\begin{bmatrix} l_{j\,k+1}\cos(\alpha_{jk}) \\ l_{j\,k+1}\sin(\alpha_{jk}) \\ 0 \end{bmatrix} = \mathbf{R}_3(\alpha_{jk})\mathbf{R}_1(\theta_{j\,k+1}) \begin{bmatrix} l_{j\,k+1} \\ 0 \\ 0 \end{bmatrix} \qquad \forall\, k \in \{1,\ldots,n_j-1\}. \tag{C.4}$$

Substituting Equation (C.4) into Equation (C.3), the following simplified expression is obtained:

$$\begin{aligned} \mathbf{d}^j &= \mathbf{R}_1(\theta_{j1}) \begin{bmatrix} -l_{j1} \\ 0 \\ 0 \end{bmatrix} + \left(\prod_{l=1}^{n_j-1} \mathbf{R}_1(\theta_{jl})\mathbf{R}_3(\alpha_{jl}) \right) \mathbf{R}_1\left(\theta_{jn_j}\right) \begin{bmatrix} l_{j1}\cos(\alpha_{jn_j}) \\ l_{j1}\sin(\alpha_{jn_j}) \\ 0 \end{bmatrix} \\ &= \begin{bmatrix} -l_{j1} \\ 0 \\ 0 \end{bmatrix} + \left(\prod_{l=1}^{n_j-1} \mathbf{R}_1(\theta_{jl})\mathbf{R}_3(\alpha_{jl}) \right) \mathbf{R}_1(\theta_{jn_j})\mathbf{R}_3(\alpha_{jn_j}) \begin{bmatrix} l_{j1} \\ 0 \\ 0 \end{bmatrix} \\ &= \begin{bmatrix} -l_{j1} \\ 0 \\ 0 \end{bmatrix} + \left(\prod_{l=1}^{n_j} \mathbf{R}_1(\theta_{jl})\mathbf{R}_3(\alpha_{jl}) \right) \begin{bmatrix} l_{j1} \\ 0 \\ 0 \end{bmatrix} \\ &= \begin{bmatrix} -l_{j1} \\ 0 \\ 0 \end{bmatrix} + \mathbf{R}^j \begin{bmatrix} l_{j1} \\ 0 \\ 0 \end{bmatrix}. \end{aligned} \tag{C.5}$$

The previous equation shows that $\mathbf{R}^j = \mathbf{I}_3 \Rightarrow \mathbf{d}^j = \mathbf{0}_3$ for origami with creased folds independently from the choice of the path $\boldsymbol{\gamma}_j(\eta)$. Therefore, $\mathbf{d}^j = \mathbf{0}_3$ is a redundant constraint for origami with creased folds. This result shows that the constraints for origami with creased folds are a special case of the more general constraints for origami with smooth folds.

APPENDIX D

ALTERNATIVE FORMULATION OF DESIGN METHOD CONSTRAINTS

As noted in Section 3.5, one of the objectives that may be considered during the implementation of the origami design method presented in Section 3 is to maximize the surface area efficiency E (defined in Equation (3.65)). For a given goal mesh $\mathcal{M}$, E is maximized by minimizing the area of the determined sheet design $\mathcal{S}_0$. The surface area of $\mathcal{S}_0$ is the addition of the surface areas of the trimmed mesh faces and the edge modules (see Figure 3.6). The surface areas of the trimmed mesh faces are prescribed by the given goal mesh $\mathcal{M}$ and the fold widths. Therefore, the only surface areas of $\mathcal{S}_0$ that may be altered by selecting different values of the design variables $\hat{W}_i$ and $\hat{\psi}_i$, $i = 1, \ldots, N_{\mathcal{E}}^I$, are the surface areas of the edge modules. This Appendix addresses an alternative formulation of the constraints in the origami design method presented in Section 3 allowing for reduction of the surface areas of the edge module rigid faces (as a consequence allowing for an increase in the value of E).

Referring to Figure 3.10(a), the total surface area of the rigid faces in the i^{th} edge module, denoted as $\mathtt{A}_i$, is given as follows:

$$\mathtt{A}_i = \left(\hat{W}_i - \hat{w}_i^{\mathsf{I}0} - 2\hat{w}_i^{\mathsf{E}0}\cos\left(\frac{\hat{\psi}_i}{2}\right)\right)\|\hat{\mathbf{z}}^i\|\cos\left(\frac{\hat{\psi}_i}{2}\right). \tag{D.1}$$

For simplicity in the formulation presented here, the surface area of the edge module rigid faces prior to face trimming (Section 3.3.1) and edge module trimming (Section 3.3.2.1) is considered in Equation (D.1). It is observed from Equation (D.1) that the total surface area of the rigid faces in the i^{th} edge module is linear with respect to the length design parameter $\hat{W}_i$. Thus, for a fixed value of $\hat{\psi}_i$, the total

surface area of the rigid faces in the i^{th} edge module reaches its minimum value when $\hat{W}_i$ reaches its lowest feasible value. For a fixed value of $\hat{\psi}_i$, the lowest feasible value for $\hat{W}_i$ is determined by setting the inequality constraint in Equation (3.21) to an equality constraint. The resulting equality constraint is given as follows:

$$\hat{W}_i = \hat{w}_i^{\mathsf{I0}} + 2\hat{w}_i^{\mathsf{E0}} \cos\left(\tfrac{\hat{\psi}_i}{2}\right) + \left\|\hat{\mathbf{z}}^i\right\| \sin\left(\left|\tfrac{\hat{\psi}_i}{2}\right|\right) - \begin{cases} (\hat{d}_{11}^i + \hat{d}_{21}^i)\sin\left(\tfrac{\hat{\psi}_i}{2}\right); & \hat{\psi}_i \geq 0 \\ (\hat{d}_{12}^i + \hat{d}_{22}^i)\sin\left(-\tfrac{\hat{\psi}_i}{2}\right); & \hat{\psi}_i < 0 \end{cases}, \tag{D.2}$$

cf. Equation (3.21). With this alternative formulation, the loop closure constraints (Equations (3.15) and (3.16)) and the additional constraints in Equation (D.2) provide $3N_{\mathcal{N}}^I + N_{\mathcal{E}}^I$ equality constraints. Equations (3.20) and (3.28) allowing for valid edge module geometries and self-intersection avoidance in $\mathcal{S}_\star$ provide $3N_{\mathcal{E}}^I$ inequality constraints. For numerical implementation of the present alternative formulation, the equality constraints are set to the form $\boldsymbol{h} = \mathbf{0}_{3N_{\mathcal{N}}^I + N_{\mathcal{E}}^I}$ while the inequality constraints are set to the form $\boldsymbol{g} \leq \mathbf{0}_{3N_{\mathcal{E}}^I}$. The numerical procedure outlined in Section 3.4.2 is again utilized to implement this alternative formulation for the origami design method.

Two implementation results of this alternative formulation of the design method are shown in Figures D.1 and D.2. Both examples show high values of surface area efficiency ($\mathsf{E} = 0.80$ for the example shown in Figure D.1 and $\mathsf{E} = 0.76$ for the example shown in Figure D.2).

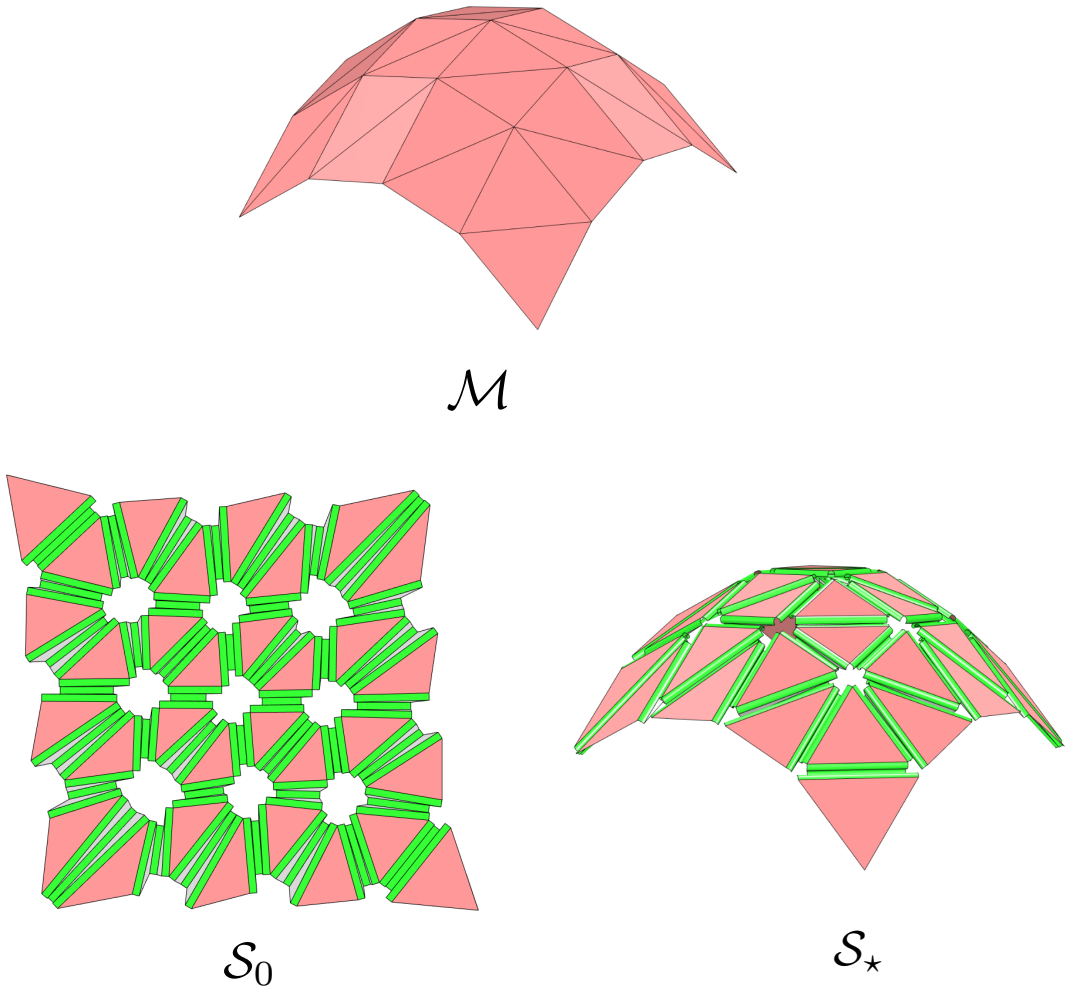

Figure D.1: Goal mesh $\mathcal{M}$ having interior nodes of positive discrete Gaussian curvature and its associated determined sheet reference configuration $\mathcal{S}_0$ obtained using the alternative formulation of the design method presented in this Appendix. The surface area efficiency for this example has a value of $\mathsf{E} = 0.80$. The folded goal configuration $\mathcal{S}_\star$ is also shown.

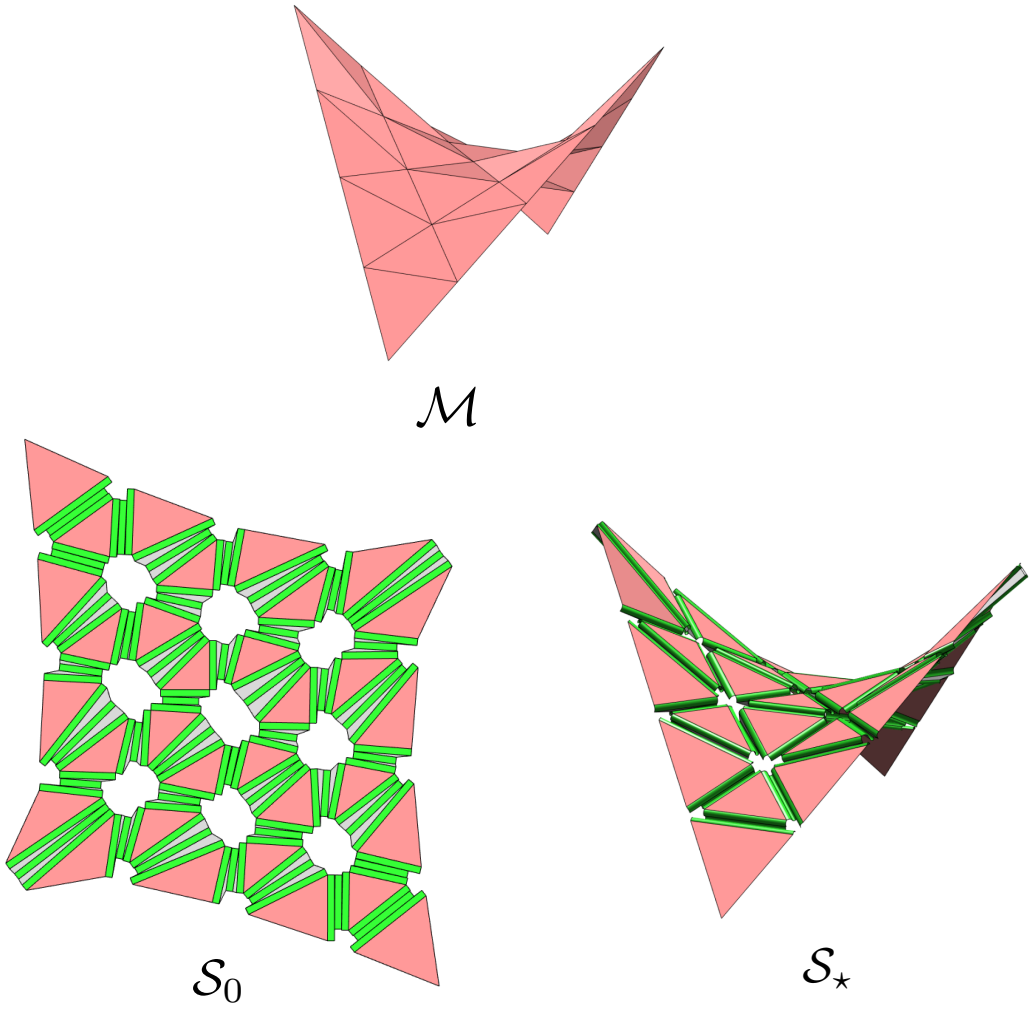

Figure D.2: Goal mesh $\mathcal{M}$ having interior nodes of negative discrete Gaussian curvature and its associated determined sheet reference configuration $\mathcal{S}_0$ obtained using the alternative formulation of the design method presented in this Appendix. The surface area efficiency for this example has a value of $\mathsf{E} = 0.76$. The folded goal configuration $\mathcal{S}_\star$ is also shown.